

Université de Montréal

# **Étude fondamentale des interactions plasma-graphène dans les plasmas Argon/B<sub>2</sub>H<sub>6</sub>**

par Pierre Vinchon

Département de physique  
Faculté des études supérieures et postdoctorales

Thèse présentée  
en vue de l'obtention du grade de Philosophiae Doctor (Ph.D.)  
en physique

Décembre, 2020

©Pierre Vinchon, 2020

Université de Montréal  
Unité académique : Département de Physique, Faculté des Arts et des Sciences

---

*Cette thèse intitulé(e)*

**Étude fondamentale des interactions plasma-graphène  
dans les plasmas Argon/B2H6**

*Présenté par*  
**Pierre Vinchon**

*A été évalué(e) par un jury composé des personnes suivantes*

**Joëlle Margot**  
Président-rapporteur

**Luc Stafford**  
Directeur de recherche

**François Schietekatte**  
Membre du jury

**Michael Bradley**  
Examinateur externe

## Résumé

Les travaux de recherche menés dans cette thèse de doctorat se sont focalisés sur la compréhension des interactions graphène-plasma dans le cas de l'exposition de graphène polycristallin à un plasma d'argon pouvant contenir du diborane ( $B_2H_6$ ). Une attention particulière est portée sur la cinétique de génération de dommage dans un plasma d'argon pur. Ainsi dans le cas d'un plasma continu, l'absence de seuil en énergie pour la génération de dommage due à un bombardement ionique est mis en évidence. Ceci ne peut s'expliquer que par une gravure à deux étapes, facilitée par la densité ionique élevée caractéristique des plasmas inductifs opérés en mode H. La caractérisation Raman des échantillons exposés au plasma montre une large distribution sur la petite zone sondée. Afin de relier ces fluctuations à l'état initial du graphène, l'imagerie Raman (RIMA) est adaptée dans le but d'extraire des données quantitatives sur l'état du graphène et utilisée pour le reste des travaux. Par la suite, l'étude temporelle des plasmas pulsés en puissance permet de trouver des conditions opératoires avec une fluence ionique drastiquement diminuée. Les traitements subséquents combinés aux analyses RIMA ont permis de suivre l'évolution de l'état du graphène et de distinguer l'état des joints du graphène des domaines de croissance. Ainsi, pour la première fois, l'autoréparation des joints de grains dans un matériau 2D est mis en évidence expérimentalement. Cet effet, théorisé dans les matériaux 3D mais difficilement observé expérimentalement, était effectivement prédis dans le cas du graphène. De plus, un contrôle fin des conditions opératoires du plasma pulsé d'argon a permis d'extraire des paramètres plasmas dans lesquels les métastables d'argons puis les photons VUV émis par les états résonants de l'argon sont les principaux vecteurs d'énergie. Suivant la même méthodologie que précédemment, ces traitements ont mis en lumière les rôles respectifs des ions, des métastables et des photons VUV dans la transmission d'énergie du graphène. Enfin, l'introduction de 5% de diborane a pour conséquence une modification radicale des paramètres physique du plasma. L'exposition de graphène à ce graphène à ce plasma démontre l'intérêt de cette technique pour l'incorporation élevé de bore tout en minimisant la génération de dommages

**Mot clés :** interactions plasma-graphène, graphène polycristallin, bilan d'énergie, synergie, auto-réparation des joins de grains

# Abstract

The research realized in this PhD thesis focuses on the understanding of plasma-graphene interactions during exposure of polycrystalline graphene films to a low-pressure argon RF plasma containing diborane ( $B_2H_6$ ). A particular attention is devoted to the kinetics driving the damage formation dynamics. In the case of a continuous, argon plasma, the absence of energy threshold for the production of ion-induced damage is demonstrated. This is explained by two-step etching, facilitated by the high number density of charged species in the H-mode of RF plasmas. Raman characterization of plasma-treated graphene films shows a wide distribution over the small area surveyed. In order to link these fluctuations to the initial state of graphene, Raman imaging (RIMA) is adapted to extract quantitative data on the state of graphene before and after plasma treatment. Subsequently, the temporal study of argon RF plasmas in the pulsed regime makes it possible to find operating conditions with a drastically reduced fluence of charged species compared to the continuous regime; in combination with RIMA studies, this allows temporally- and spatially-resolved investigations of plasma-graphene interactions. For the first time, a preferential self-healing of ion-irradiation damage at grain boundaries of graphene films is experimentally demonstrated. Moreover, by using several electrical and optical diagnostics of the argon plasma in the pulsed regime, it is possible to determine operating conditions in which either the ions, the metastables or the VUV photons emitted by the resonant states become the main energy vectors. From these experiments, the respective roles of each of these species in the physics of plasma-graphene interactions could be highlighted. Finally, the introduction of 5% of diborane into the argon plasma induces a radical modification of the physicochemical properties of the plasma. Exposure of graphene films to this highly reactive plasma reveals high boron incorporation with minimal ion and hydrogen damage.

**Keywords:** plasma-surface interactions, polycrystalline graphene, synergy effects, self-healing at grain boundaries

# Table des matières

Résumé .....	1
Abstract.....	2
Table des matières.....	3
Remerciements.....	5
Introduction.....	16
Chapitre 1 : État de l'art .....	23
1.    Le graphène .....	23
1.1.    Structure et propriétés fondamentales.....	23
1.2.    Défauts dans le graphène.....	27
1.3.    Synthèse du graphène.....	31
1.4.    Traitements post-synthèse .....	32
2.    Plasmas à base de bore.....	40
2.1.    Méthodes physiques et chimiques d'injection du bore .....	40
2.2.    Diagnostics des plasmas à base de bore.....	44
3.    Applications des plasmas de bore.....	54
Références.....	60
Chapitre 2 : Interactions plasma-graphène dans les plasmas d'argon en régime continu .....	67
1.    Article 1 : Étude des dommages d'irradiation.....	67
2.    Article 2: Spectroscopie Raman Hyperspectrale .....	92
Chapitre 3 : Interactions plasma-graphène dans les plasmas d'argon en régime pulsé .....	121
1.    Article 3 : Étude résolue spatialement des dommages d'irradiations ionique .....	121
2.    Article 4: Étude des rôles respectifs des ions, des metastables et des photons VUV ...	159
Chapitre 4. Dopage du graphène par plasma d'argon au diborane .....	160
1    Article 5: Dopage du graphène par plasma .....	190
Conclusion .....	214

# Liste des tableaux

## Chapitre 1

Tableau 1.1: Récapitulatif des défauts et de leurs énergies de formation et de migration [18].....p31

## Chapitre 2

Table 2.2.1: Comparison for various Raman parameters between untreated and plasma-treated monolayer graphene samples. The mean and standard deviations are also presented. A threshold on the G band intensity is used to remove points with no graphene (e.g. the crack and where the image is cropped on the side).....p105  
Table 2.2.2: Raman spectroscopy comparison between standard confocal measurements (with inVia setup) and Rima measurements for the treated state and untreated state of the graphene.....p118

## Chapitre 3

Table 3.1.1: Summary of the effects arising from the increase of different graphene lattice defects on the parameters of D, G and 2D bands. Data are taken from exfoliated and/or CVD-grown polycrystalline graphene films.....p143

## Chapitre 4

Table 4.1.2: Percent contribution of each sub-peak in the XPS HR scans of B1s and C1s. For B1s, the sub-peaks are: B1 (B-B), B2 (B-C), B3 (B-H), B4 (C<sub>2</sub>BO), B5 (CB<sub>2</sub>O), B6 (B-C sp<sup>2</sup>). For C1s, the sub-peaks are: C1(B-C sp<sup>3</sup>), C2(C-C sp<sup>3</sup>), C3(C-O), C4(C=O), C5(O-C=O), C6(C-C sp<sup>2</sup>), C7(B-C sp<sup>2</sup>).....p200

# Liste des figures

## Chapitre 1

Figure 1.1 : Structure hexagonale du graphène. Chaque atome de carbone possède trois voisins. Tiré de [1] .....	p23
Figure 1.2 : Formation de l'hybridation sp <sub>2</sub> et visualisation des liaisons sigma et pi dans le graphène. Tiré de [2] .....	p24
Figure 1.3 : (a) Structure de bande du graphène et (b) coupe transversale de la structure de bande, où l'énergie est représentée en fonction de la fonction d'onde k <sub>x</sub> le long de la ligne k <sub>y</sub> = 0. Tiré de [2].....	p24
Figure 1.4 : (a) Relations de dispersions théoriques du graphène présentant les différentes branches iLO, iTO, oTO, iLA, iTA, et oTA et (b) processus Raman conduisant à l'émission des principaux pics du graphène. Tiré de [9].....	p25
Figure 1.5 : Évolution du spectre Raman d'un échantillon de graphène soumis à un bombardement avec des atomes de Bores à 32 keV pour différentes doses. Tiré de [10]......	p26
Figure 1.6 : Image TEM et (b) représentation atomique d'un défaut de type Stone-Wales. Tiré de [12].....	p27
Figure 1.7 : (a) Image TEM et (b) représentation atomique d'un défaut de type lacune. Tiré de [12].....	p28
Figure 1.8 : (a) image TEM et (b) représentation atomique d'un défaut de type lacune double Tiré de [12].....	p29
Figure 1.9 : Structure autour des joints de grain du graphène consistant en une succession de paires de pentagones et d'octogones [15].....	p29
Figure 1.10 : Différentes configurations possibles en bordure de graphène (a) en bras de chaise et (b) en zigzag. Tiré de [12].....	p30
Figure 1.11 : Structure théorique d'une paire de Stone Wales inverse. Tiré de [12].....	p31
Figure 1.12 : Spectres haute résolution XPS du graphène pour deux dopages différents (a-c) et (b-d). Spectres (a) et (c) N1s avec différentes configurations, N1(pyridinic) N2 (pyrrolic) et	

N3 (quaternaire). Spectres (c) et (d) C1s avec C1 (C-C sp <sub>2</sub> ), C2 (C-C sp <sub>3</sub> ), C3 (O-C-O ou C-N) et C4 (C=C=O) .....	p35
Figure 1.13 : Évolution de AD/AG corrigé par l'énergie du laser en fonction de FWHMG. La ligne pleine est une corrélation qui décrit le cas où les défauts générés sont linéaires (1D). La ligne en pointillé représente le cas où les défauts sont ponctuels (0D). Les points sont ceux obtenus de la littérature. ....	p36
Figure 1.14: Évolution de I <sub>D</sub> /I <sub>G</sub> en fonction de I <sub>D</sub> /I <sub>G</sub> pour des échantillons traités par plusieurs méthodes afin de mettre en évidence le changement de la nature des défauts.....	p38
Figure 1.15: Distribution de la position du pic 2D en fonction de la position du pic G pour un échantillon de graphène recuit dans une atmosphère d'oxygène [51].....	p39
Figure 1.16: Schéma d'un réacteur DC-PECVD [59][60].....	p42
Figure 1.17: Profil typique d'un réacteur ECR avec (a) la configuration et (b) le profil axial des variations de champs magnétique [58]. (c) Schéma typique d'un réacteur ECR-PECVD [65]......	p43
Figure 1.18: Réacteur ICP utilisé par Ichiki et al [68] pour le dépôt de couches de BN.....	p44
Figure 1.19: Spectres OES de la plume (a) proche de la cible et (b) après expansion avec et sans atmosphère de diazote [57].....	p46
Figure 1.20: Spectre d'OES d'un plasma d'H <sub>2</sub> avec 66 ppm de B <sub>2</sub> H <sub>6</sub> et 1% de CH <sub>4</sub> [74]. .....	p47
Figure 1.21: Évolution temporelle de la raie de BH et de H $\beta$ lors de l'allumage d'un plasma MW B <sub>2</sub> H <sub>6</sub> /Ar/H <sub>2</sub> [75].....	p48
Figure 1.22 : (a) Spectres OES aux longueurs d'ondes au doublet du bore dans un plasma d'argon avec des traces de diborane ( $\diamond$ ) et un plasma H <sub>2</sub> -Ar-B <sub>2</sub> H <sub>6</sub> (64:33:3) et (b) schéma représentant la désexcitation du bore excité sur les deux niveaux fondamentaux [76]......	p49
Figure 1.23 : (a) Variation du rapport des raies du doublet du Bore avec sa densité absolue. Les lignes représentent des valeurs de rapport obtenues pour différentes conditions. (b) Évolution de la densité atomique de bore dans un plasma d'H <sub>2</sub> en fonction de la concentration de diborane injectée dans le réacteur [76].....	p49
Figure 1.24 : (a) Spectre d'absorption avec en noir, 30 ppm de B <sub>2</sub> H <sub>6</sub> dans H <sub>2</sub> à 53 mbarr sans plasma, en rouge, le plasma et vert le plasma allumé à 60 mbarr à 600W et 1000W. (b) Spectre d'absorption en pointillé d'un plasma B <sub>2</sub> H <sub>6</sub> /H <sub>2</sub> et en rouge, d'un plasma B <sub>2</sub> H <sub>6</sub> /H <sub>2</sub> /CH <sub>4</sub> .....	p50

- Figure 1.25 : Densité de B et de BH dans un plasma B2H6/Ar/H2 en fonction de (a) flux de B2H6, (b) de la pression avec un flux de 0.003 sccm [74].....p52
- Figure 1.26 : Spectre de masse dans une atmosphère de B2H6/H2 avec un substrat chauffé à (a) 400°C et (b) 800°C. (c) Diagramme d'énergie des décompositions primaires du diborane [80].....p53
- Figure 1.27 : Spectre de masse d'un plasma B2H6/He (15/85) pulsé à -6 kV [81].....p54
- Figure 1.28 : Structure cristalline du (a) h-BN, (b) w-BN, (c) r-BN et (d) c-BN [82].....p55
- Figure 1.29 : Images SEM et spectres Raman correspondant de couches de BN déposées avec (a-b) 1 sccm et (c-d) 20 sccm de  $B(OCH_3)_3$  injecté dans un plasma DC  $CH_4/H_2$  [60].....p57
- Figure 1.30 : Mesures XPS d'échantillons traités par un plasma  $B_2H_6/He$  (15/85) à 6 kV (a) après traitement (b) après nettoyage de la surface et recuit. (c) Profils SIMS des échantillons implantés au bore pour différentes dilutions dans l'hélium [81].....p58
- Figure 1.31 : Évolution de la quantité de bore atomique en fonction du temps d'exposition au plasma mesuré par XPS [66] .....p59

## Chapitre 2

- Figure 2.1.1: Sketch of the plasma apparatus used to examine plasma-graphene interactions. A scanning electron microscopy image of a typical graphene film is also shown.....p71
- Figure 2.1.2: Langmuir probe measurements of  $V_p-V_f$  and  $kT_e$  as a function of the working pressure. The corresponding RF power to obtain a constant ion density of  $1.1 \times 10^{11} \text{ cm}^{-3}$  is also plotted. Lines are guides to the eye.....p74
- Figure 2.1.3: Normalized  $ArH^+$  IEDFs from 5 to 80 mTorr (H-mode). Measurements are taken in the vicinity of the substrate-holder.....p75
- Figure 2.1.4: Populations of argon metastable ( $1s_3$  and  $1s_5$ ) and resonant ( $1s_2$  and  $1s_4$ ) states obtained by optical absorption spectroscopy as a function of pressure (same experimental conditions as in Figure 2.1.1). Lines are guides to the eye only.....p76
- Figure 2.1.5: Evolution of power fluxes to the graphene surface due to surface de-excitation of metastable and resonant atoms (Equation (4)), vacuum UV irradiation (Equation (5)), and ion bombardment (Equation (6)). Experimental conditions are the same than those used in Figures 2.1.2 and 2.1.4. Lines are guides to the eye only.....p79

- Figure 2.1.6: Raman spectrum of untreated graphene (black), plasma-treated graphene in H-mode at 5 mTorr (blue) and 80 mTorr (red). Treatment times are 15 s at 5 mTorr and 21 s at 80 mTorr to provide the same fluence of  $2.7 \times 10^{17} \text{ cm}^{-2}$  .....p80
- Figure 2.1.7: Graphene Raman data for 5 different fluence conditions in the E-mode (121 spectra recorded at different location on the graphene sample). (a)  $A_D/A_G$  ratio corrected by the laser energy  $E_L$  (2.41 eV) to the power 4 and (b) ratio of 2D over G peak intensities ( $I_{2D}/I_G$ ) as a function of FWHM(G). The top-line in (a) represents 0D defects, while the bottom line follows 1D defects (see Cançado et al [42] for more details). Stage 1 and 2 are described in the text.....p82
- Figure 2.1.8: Graphene Raman data for 4 different incident ion energy (fixed ion fluence) in the H-mode (121 spectra recorded at different location on the graphene sample). (a)  $A_D/A_G$  peak area ratio corrected by the laser energy (2.41 eV) to the power 4 and (b) ratio of 2D over G peak intensities ( $I_{2D}/I_G$ ) as a function of FWHM(G).....p83
- Figure 2.1.9:(a)  $A_D/A_G$  ratio corrected by the laser energy (2.41 eV) to the power 4 and (b)  $I_{2D}/I_G$  as a function of FWHM(G) for graphene films treated in the E-mode (purple) and in the H-mode (red and black). Data are replotted from Figures 2.1.7 and 2.1.8.....p84
- Figure 2.1.10: Graphene defect density in function of average crystallite size for plasma treatments (121 spectra each) in the H-mode (fixed ion fluence) and in the E-mode (fixed ion energy). In addition, data extracted from ion beam experiments [45] are presented as comparison.....p86
- Figure 2.2.1: Comparison raw data and PCA filtered data for untreated (a) and treated (b) graphene.....p97
- Figure 2.2.2: Comparison of Raman spectra obtained either from a conventional confocal (Renishaw inVia) mapping (a) or from the RIMA instrument (Photon etc) (b). (c) Typical spectra of the broad signal form artefacts in RIMA giving a singular line shape. Fits to the spectra and polynomial fit to the baseline are also shown. The sharp feature marked with \* is an instrument's artefact. .....p98
- Figure 2.2.3: Juxtaposition of two zones of untreated graphene. (a) 2D:G ratio, (b) D:G ratio, (c) 2D position and (d) 2D width are presented. .....p101
- Figure 2.2.4: Comparison of (a) D:G, (b) 2D:G and (c) D:D' ratios for mapping taken with RIMA (left column) and conventional confocal Raman (inVia) (right column).....p103

- Figure 2.2.5: Distribution of the variation of 2D:G ratio as a function of the initial 2D:G ratio. High quality graphene undergoes a larger decrease than what is seen in regions of low quality graphene.....p107
- Figure 2.2.6: Distribution of the variation of D:G ratio as a function of the initial D:G ratio. Higher quality graphene undergoes a larger increase of D:G values compared to lower quality graphene. The distribution of the D:G ratio is wider for initially larger D:G ratio.....p108
- Figure 2.2.7: Distribution of the variation of D:2D ratio as a function of the initial D:2D ratio. Higher quality graphene undergoes a larger increase of D:2D values compared to lower quality graphene. The distribution of the D:2D ratio is wider for initially low D:2D ratio.....p109
- Figure 2.2.S1: Mean spectra for the two regions before and after the plasma treatment process. The cubes of untreated graphene (black and red) and the cube for the treated graphene (blue) are presented.....p112
- Figure 2.2.S2: Cumulative eigenvalues of sorted principal components as a function of component index. The red line reveals the number of components retained for reconstruction as calculated from the criteria presented in the manuscript.....p112
- Figure 2.2.S3: Small sample of spectra for both the untreated (a) and the treated (b) state of the graphene. Raw data (black) and filtered data (red) are shown.....p113
- Figure 2.2.S4: Example of various curve fit with different order of polynomial baseline for a point of the untreated graphene sample. Regions of the (a) D, (b) G and (c) 2D bands are shown.....p114
- Figure 2.2.S5: Example of various curve fit with different order of polynomial baseline for a point of the plasma treated graphene sample. Regions of the (a) D, (b) G and (c) 2D bands are shown.....p115
- Figure 2.2.S6: Mean values of peak parameters for various order of the polynomial baseline subtraction for the untreated sample. Chosen polynomial order are highlighted in yellow. D' values not shown since it is too small or irrelevant for undamaged graphene.....p115
- Figure 2.2.S7: Mean values of peak parameters for various order of the polynomial baseline subtraction for the treated sample. Chosen polynomial order are highlighted in yellow.....p116
- Figure 2.2.S8: All different values of line ratio possible when considering the polynomial orders presented in Figure 2.2.S6 and Figure 2.2.S7. The ratio for the chosen order of polynomial baseline fitting is presented in red. Under each graph is presented the

maximum value of deviation (max-min) over the value in red. These percent are shown very small; thus, the order of the polynomial does not impact considerably the data in the manuscript.....p116

Figure 2.2.S9: Mean image for the image registration of an untreated zone and the same zone after plasma treatment. A criterion based on the G-band intensity is used to distinguish between specific zones within the graphene sample. Defects are therefore aligned so as to allow point by point analysis. Two basis of logical values are aligned. Points where both signal are 1 appear black; points where both signal are 0 appear white and points which values are opposite appear as grey.....p117

## Chapitre 3

Figure 3.1.1: Subsequent graphene treatments plotted in a Cançado-like graph: evolution of  $A_D/A_G \times E_L^4$  versus  $\Gamma_G$ . The colored scale is density-normalized. Green lines delimit the 0D and 1D defect-type evolutions. For clarity, black outlines highlight the 7 different sets of data. The gray dashed line delimits the 2 commonly reported stages of the amorphization trajectory.....p126

Figure 3.1.2: Evolution of band parameters mapping with plasma treatments.  $130 \times 130 \mu\text{m}^2 A_D/A_G \times E_L^4$  mappings of (a) pristine, (b) 60s and (c) 425s plasma-treated graphene. Note the color scale difference for each map.  $130 \times 130 \mu\text{m}^2$ .....p127

Figure 3.1.3: Evolution of an intensity ratio mapping with plasma treatments linked to graphene disorder.  $130 \times 130 \mu\text{m}^2 I_D/I_{2D}$  mappings of (a) pristine, (b) 60s and (c) 425s plasma-treated graphene. Note the color scale difference for each map.....p129

Figure 3.1.4: Imaging and probing of graphene boundaries. (a)  $92 \times 92 \mu\text{m}^2$  area map of Fig. 3.1.2c highlighting in red the locations of the selected GB spectra used to distinguish GBs from the rest of the graphene. (b) the Cançado-like graph extracted from Fig. 3.1.3 representing the mean evolution of each distribution with their standard deviation. The dashed ellipse highlights the 425-sec plasma treated data.....p130

Figure 3.1.5: Relevant Raman parameters highlighting the discrepancies between graphene grain and grain boundaries. The mean evolution of each parameters distribution with their standard deviation are plotted versus the total energy fluence during the subsequent plasma treatments ( $60\text{s} \leftrightarrow 0.03 \text{J}\cdot\text{cm}^{-2}$ ,  $1005\text{s} \leftrightarrow 0.75 \text{J}\cdot\text{cm}^{-2}$ ). The extracted Raman band parameters are: (a)  $I_{2D}/I_G$  and (b)  $I_D/I_{2D}$ . Values for pristine graphene are displayed as horizontal dashed lines. Pristine values are similar in (b). .....p131

- Figure 3.1.6: Schematics of preferential self-healing at GBs in plasma-treated graphene involving: (1) Formation of carbon adatoms-vacancies by plasma-generated species; (2) Preferential migration of carbon adatoms on the graphene surface; (3) Anisotropic transport of carbon adatoms along grain boundaries; (4) Defect healing at GBs; (5) Carbon adatom emission from GBs leading to defect healing in the zone of potential repair.....p132
- Figure 3.1.S1: Sketch of the plasma apparatus.....p140
- Figure 3.1.S2: (a) Electron temperature  $kT_e$  (in eV, blue) and  $V_p-V_f$  (in V, red) derived from cylindrical LP measurements. The ion energy  $E_{ion}$  may be approximated to  $(V_p-V_f)$ . (b) Argon ion, metastable and resonant densities extracted from LP measurements for ions and OAS measurements otherwise.....p142
- Figure 3.1.S3: Evolution of the power density measured in the plasma reactor at the substrate location for 4 different conditions, labelled on the x-axis. Lines are guides to the eyes highlighting the net drop in power density.....p149
- Figure 3.1.S4: Comparison between optical microscopy (left, after 1005 s of plasma treatment) and D/G area ratio extracted from RIMA imaging (right, 425 s).....p144
- Figure 3.1.S5: Evolution of (a)  $\omega_{2D}$ , (b)  $\omega_G$ , (c)  $\Gamma_{2D}$ , and (d)  $\Gamma_G$  highlighting the discrepancies between GBs and graphene grains. All parameters are plotted versus the total energy fluence accumulated during the subsequent.....p147
- Figure 3.1.S6: MD simulations of damage formation at energies below  $T_d$  plotted as a thermally-activated process (Arrhenius plot). Here, the apparent activation energy decreases with increasing value of T (linked to the energy of argon atoms). A similar behavior was observed for temperature-dependent radiation-enhanced diffusion in ion-irradiated solids[58]....p152
- Figure 3.2.1: Plasma characterization in conditions c1, c2 and c3. (a,c,e) Electron temperature  $kT_e$  (in eV, blue) and  $V_p-V_f$  (in V, red) derived from cylindrical LP measurements. The average ion energy  $E_{ion}$  is linked to  $(V_p-V_f)$ . (b,d,f) Argon positive ion, metastable and resonant densities extracted from LP measurements for ions and OAS measurements otherwise.....p165
- Figure 3.2.2: Percent contribution of positive ions, VUV-photons and metastable atoms in the total power density provided to the graphene lattice for conditions c1, c2 and c3. The results are shown for  $\xi_i=\xi_m=\xi_u=1$  and  $\xi_i=1$ ,  $\xi_m=0.085$  and  $\xi_u=0.07$ .....p169
- Figure 3.2.3: Cançado-type graphs extracted from RIMA mappings with distinctions between GDs (blue) and GBs (red) in conditions c1, c2 and c3. Lines are guide to the eye only. Green lines

delimit the 0D and 1D defect type evolutions. A vertical dotted line marks the limit between stage 1 and stage 2 of the amorphization trajectory.....p171

Figure 3.2.4: Evolution of  $I_{2D}/I_G$  (a-c-e) –related to the graphene quality– and  $I_D/I_{2D}$  (b-d-f) –related to the damage generation– as a function of the energy fluence provided by positive ions to the graphene lattice for conditions c1, c2 and c3. The results are shown for both graphene domains (blue) and graphene boundaries (red). For  $I_{2D}/I_G$ , the dashed lines correspond to the values in pristine graphene. For  $I_D/I_{2D}$ , pristine values were much below 0.1 (not shown) [13].....p173

Figure 3.2.5: (a) Evolution of  $I_{2D}/I_G$  as a function of  $I_D/I_{2D}$  for conditions c1, c2 and c3. (b) Evolution of  $I_D/I_{2D}$  as a function of  $I_D/I_{2D}$  for conditions c1, c2 and c3. The results are for GDs only, but similar values were observed for GBs (not shown for concision).....p175

Figure 3.2.6: Damage generation analysis in graphene domains as a function of (a) the energy fluence provided by positive ions and (b) the total energy fluence assuming  $\xi_i = 1$ ,  $\xi_u = 0.085$  and  $\xi_u = 0.07$ . Similar results with lower  $I_D/ I_{2D}$  values due to preferential self-healing were observed at graphene boundaries (not shown).....p177

## Chapitre 4

Figure 4.1.1: Effect of the addition of 5%  $B_2H_6$  in a nominally pure argon plasma on the power density provided to the graphene lattice. The respective contributions of positive ions, argon metastable and resonant atoms, and VUV photons are also shown. Populations of each species obtained from LP and OAS are provided in  $cm^{-3}$ .....p197

Figure 4.1.2: RGA plasma on-to-plasma off ratios for Ar and the main fragments of  $B_2H_6$ .....p198

Figure 4.1.3: (a) Normalized XPS surveys of pristine (black), BTSi (blue) and BTG (red) samples. (b) B1s and (c) C1s HR scans of BTSi. (d) B1s and (e) C1s HR scans of BTG. ....p199

Figure 4.1.4: BTG and subsequent ATG data extracted from RIMA measurements plotted in a Cançado-like [68] graph: evolution of  $A_D/A_G \times E_{laser}^4$  in function of  $\Gamma_G$ . Distributions for untreated graphene films are also displayed. The colored scale is density-normalized. Green lines delimit the 0D and 1D defect type evolutions [68]. For clarity, black outlines highlight the 6 different sets of data.....p202

Figure 4.1.5: (Left) Raw averaged spectra from the same graphene domain area (red rectangle in the inset) for pristine and BTG ( $18 \times 22 \mu m^2$ ). (right) Plot of  $\omega_{2D}$  in function of  $\omega_G$  to separate strain and p-doping levels. The  $\epsilon$  and  $n$  scales are derived from [30].....p204

Figure 4.1.6: Evolution of  $I_D/I_{2D}$  as a function of  $\Gamma_{2D}$  in ATG and BTG samples.....p205

## **Conclusion**

Figure C.1: Évolution temporelle en spectrométrie de masse des ratios plasma allumé et éteint de  $\text{H}_2^+$ ,  $\text{BH}_2^+$ ,  $\text{B}_2\text{H}_2^+$ ,  $\text{B}_2\text{H}_4^+$ ,  $\text{B}_2\text{H}_5^+$  pour un plasma généré en mode E à 30W et (1) 10 mTorr, (2) 20 mTorr, (3) 30 mTorr, (4) 40 mTorr et (5) 50 mTorr.....p218

# Remerciements

Pour commencer, j'aimerais remercier sincèrement mon directeur de recherche, le professeur Luc Stafford, pour la confiance qu'il m'a accordée tout le long de ma thèse. Son écoute, ses conseils ainsi que l'environnement exceptionnel que constitue son groupe de recherche m'ont permis de m'épanouir et de prendre confiance en tant que chercheur. Je lui suis particulièrement reconnaissant de la large liberté d'action qu'il m'a permis afin d'éprouver certaines de mes idées.

Je suis aussi particulièrement reconnaissant envers le professeur Richard Martel pour sa collaboration dans de ce projet. Il nous a donné carte blanche pour expérimenter avec le prototype RIMA ce qui a donné une nouvelle dimension à notre projet de recherche. De plus, ses conseils pour l'interprétation et la valorisation des données ont été précieux pour saisir la toute la richesse de nos résultats.

Je voudrais également remercier les membres de mon jury, les professeurs M. Bradley, J. Margot, et F. Schietekatte pour le temps consacré à l'évaluation de mon manuscrit et à la défense de ma thèse.

Je suis reconnaissant aux techniciens, Jean-Sébastien Mayer et Véronique Desjardins qui se sont toujours rendu disponible pour modifier le setup, qui a souvent eu besoin d'une attention particulière. Le projet de recherche a pu aller aussi loin grâce à leur expertise.

Cette thèse n'aurait sans doute pas été aussi agréable si je n'avais pas pu côtoyer toutes ces personnes qui ont participé à la vie de ce groupe de recherche. Je pense notamment à petit et grand Vincent, Antoine, Simon, Édouard et Sara. Dans le même registre, j'ai apprécié les pauses café toujours constructives (ou pas) et les débats qui s'en suivaient avec Julien, Maxime, Francis et Louis-Felix. Du coup, mention spéciale aux Français, Laura et Thibault qui ont su « diversifier » le groupe.

J'aimerais spécifiquement remercier les deux postdocs du groupe qui m'ont beaucoup apporté. Merci à Jacopo pour son énergie débordante et toutes ses idées qui permettent d'élargir notre vision de la recherche trop souvent (et naturellement) concentré sur notre projet de thèse. Merci à Xavier et à sa rigueur légendaire qui a été précieuse pour l'étude du graphène, un matériau bien capricieux. Je te suis également reconnaissant pour ton aide dans la fin (stressante) de ma thèse qui aurait été sans aucun doute différente sinon.

Dans la même lignée, merci à Germain, mon camarade de bureau et de thèse, pour toutes les conversations constructives et ta persistance. Réaliser des thèses si proches l'une de l'autre aurait pu être problématique, mais je pense qu'au contraire ça nous a permis de nous soutenir et de pousser encore plus loin nos recherches respectives.

D'un point de vue personnel, cette thèse a été rendue possible grâce à tout le support que j'ai reçu durant ces 5 dernières années. Je pense ainsi à mon club de rugby, le RCM, qui a beaucoup aidé à relâcher la tension de ces premières années. Merci aux amis encore ici, ou ailleurs, Seb, Axelle, Alex, Perrine, Marion, Cédric, Jb, Lucille, Thomas, Bastien, Raph, Loïc, Valentin, Arthur, Juliana, Rocio et Loïck. Merci pour tous ces moments de fou rire et ces discussions plus ou moins sérieuses qui m'ont permis de persister dans mes projets.

Je remercie aussi mes parents pour leur soutien durant toutes mes études, ce qui m'a permis de comprendre et de réaliser ce que je voulais faire. Je suis donc fier d'avoir accomplis cette thèse.

Enfin, un grand merci à celle qui partage ma vie depuis le début de cette thèse, Laura. Merci de ton soutien inconditionnel lors des bons et mauvais moments. Cette thèse n'aurait sans doute pas été la même chose sans toi. J'ai hâte de voir la suite en ta compagnie, y compris de te voir réussir avec brio tes études !

Ces remerciements sont un bien maigre reflet de toute la reconnaissance que je ressens envers les personnes qui m'ont soutenue pendant toutes ces années malgré nos différences et opinions divergentes. À mon sens, c'est ce qui a transformé cette expérience de thèse en une grande aventure humaine grâce à la diversité d'expériences autour de moi.

# Introduction

Notre mode de vie actuel repose sur de nombreuses percées scientifiques et technologiques associées de près ou de loin au domaine des matériaux et des nanomatériaux. Ceci inclut les applications électroniques, optiques et photoniques mais aussi celles destinées au domaine du stockage et de la conversion de l'énergie, de l'aéronautique et de l'aérospatial, du militaire, du médical, de la pharmaceutique, etc. Dans ce contexte, la mise au point de dispositifs toujours plus performants et miniaturisés a été rendue possible grâce à l'élaboration et à la mise en forme de nombreux matériaux et de nanomatériaux aux propriétés physiques et chimiques finement contrôlées. Parmi l'ensemble des méthodes utilisées pour la synthèse, la modification et la gravure des matériaux et des nanomatériaux, celles basées sur les plasmas produits en laboratoire s'avèrent particulièrement attrayantes pour plusieurs applications. L'intérêt croissant suscité par l'utilisation des plasmas tient à ce qu'ils mettent en présence une grande variété de particules et de rayonnements pouvant réagir de manière sélective avec la matière organique et inorganique. Dans bien des cas, ce milieu, souvent hors équilibre thermodynamique (milieu faiblement ionisé dans lequel la température des électrons est largement supérieure à celles des ions et des neutres), représente une solution économique et écologique à divers problèmes difficiles, voire impossibles à résoudre par les approches physiques ou chimiques habituelles. De plus, les procédés assistés par plasma se distinguent bien souvent des autres méthodes puisqu'ils possèdent l'avantage d'être rapides, souples, se prêtant bien à l'automatisation et respectueux de l'environnement. L'une des applications les plus spectaculaires des plasmas est sans contredit leur utilisation massive dans la reproduction de motifs sous-micrométriques dans les matériaux pour la fabrication de transistors en micro et nanoélectronique.

De nos jours, les principaux secteurs dans lesquels les plasmas jouent un rôle stratégique, faisant l'objet d'une activité intense à l'échelle internationale, sont à titre d'exemples non-limitatifs : (i) la synthèse de matériaux de pointe (diélectriques, magnétiques, couches barrières, couches intelligentes, biomatériaux, matériaux multifonctionnels, etc.) et (ii) les nanotechnologies, notamment la production et la fonctionnalisation de nanoparticules, de nanotubes et autres matériaux nanostructurés. Par exemple, le graphène (c'est-à-dire le carbone bidimensionnel monoatomique avec hybridation  $sp^2$ ) représente sans contredit l'un des

matériaux de l'heure au niveau mondial. Depuis les premières évidences expérimentales des propriétés électroniques exceptionnelles du graphène en 2004 [1], plusieurs efforts de recherche ont été consacrés au développement d'approches physiques et chimiques permettant de synthétiser des feuilles et des flocons de graphène bien définies et libres de contaminants. Ces méthodes incluent l'exfoliation micromécanique et chimique du graphite [2], la synthèse CVD (acronyme anglais pour *Chemical Vapor Deposition*) et PECVD (acronyme anglais pour *Plasma-Enhanced Chemical Vapor Deposition*) [3–6]. Ces diverses méthodes ont permis de mettre en évidence des propriétés inédites du graphène, notamment l'effet hall quantique demi-entier pour les électrons et les trous [7] et un comportement ultra-relativiste des porteurs menant à des mobilités extraordinairement élevées [8]. Puisque le graphène est aussi transparent, flexible, robuste et un excellent conducteur thermique, il s'avère fort prometteur pour plusieurs applications dont l'électronique flexible, la spintronique, les piles à haute performance et la catalyse [9–12]. Une fois fonctionnalisés avec des biomolécules (protéines, peptides, etc.), les nanomatériaux à base de graphène ouvrent également la voie à une multitude de débouchés dans le domaine des biosciences et des biotechnologies. Par exemple, des études récentes ont démontré que le graphène fonctionnalisé possède des propriétés uniques pour le développement de biocapteurs FRET (acronyme anglais pour *fluorescence resonance energy transfer*) et l'imagerie biomédicale [13].

En dépit du potentiel d'innovation immense qu'offre le graphène, il est néanmoins relativement inerte d'un point de vue chimique et possède une bande interdite (énergie de gap) nulle et difficile à ouvrir de manière significative, ce qui le rend à priori mal adapté pour l'électronique logique, l'optoélectronique, ainsi que pour les capteurs de gaz et les biocapteurs. Ceci explique sans doute les recherches intensives à l'échelle internationale visant à fonctionnaliser le graphène (et ses dérivés), soit (i) par attachement covalent de différentes fonctions chimiques, (ii) par attachement non-covalent de divers atomes et molécules via les interactions  $\pi$ , (iii) par attachement de nanoparticules (par exemple des métaux nobles, des oxydes métalliques ou des semiconducteurs), ou encore (iv) par l'incorporation d'atomes dans la couche monoatomique bidimensionnelle par dopage substitutionnel [14]. Dans ce contexte, plusieurs auteurs ont mis au point de nouvelles approches basées sur les plasmas afin de fonctionnaliser le graphène après sa croissance. Ceci inclut les plasmas hors équilibre

thermodynamique à pression réduite à base d'argon, d'hydrogène, d'oxygène, d'azote et d'ammoniac produits par des champs électriques radiofréquence dans l'optique de produire des dommages dans le graphène par irradiation ionique, de former du graphane ou de l'oxyde de graphène ou encore de réaliser un dopage substitutionnel du graphène avec des atomes d'azote [15]. Cependant, dans la majorité des travaux publiés dans la littérature scientifique, le plasma est utilisé comme un simple outil ou encore comme une « boîte noire » pour le traitement post-synthèse du graphène. Sans des études détaillées des propriétés physiques et chimiques du plasma et donc de l'ensemble des particules et des rayonnements susceptibles d'interagir avec le graphène au cours de ces traitements, il s'avère extrêmement difficile de conclure sur la nature et le rôle de l'ensemble des espèces du plasma mises en jeu et donc de parfaitement contrôler le procédé selon l'application envisagée.

Par ailleurs, en plus des plasmas à base d'hydrogène, d'oxygène, d'azote et d'ammoniac, les plasmas à base de bore pourraient également représenter une approche intéressante pour la modification post-croissance du graphène. Inspirés des travaux sur le silicium en microélectronique, on pourrait, par exemple, imaginer un dopage de type N (production d'un excès d'électrons) avec des atomes d'azote et de type P (production d'un déficit d'électrons) avec des atomes de bore. Néanmoins, les recherches sur les plasmas à base de bore demeurent dans bien des cas limités en raison des risques importants en matière de gestion des gaz associés (par exemple, le  $B_2H_6$  est pyrophorique). Ceci inclut autant les études fondamentales des propriétés physiques et chimiques de ce type de plasmas que les études appliquées en synthèse et modification des matériaux et des nanomatériaux. Avec les avancées récentes des systèmes de sécurité, on peut néanmoins noter une reprise des études fondamentales et appliquées sur ce type de plasmas hautement réactifs.

Dans ce contexte, les objectifs scientifiques et technologiques de cette thèse de doctorat peuvent être élaborés de la manière suivante :

- (i) Réaliser une étude fondamentale de pointe des interactions plasma-graphène dans les plasmas non réactifs, en particulier les plasmas d'argon à pression réduite produits par des champs électriques radiofréquences. Il s'agit ici d'identifier l'ensemble des particules et des rayonnements formés dans ce type de plasmas afin

- de mieux comprendre leurs rôles respectifs sur la dynamique de formation des dommages dans les films de graphène.
- (ii) Effectuer une étude expérimentale de pointe des plasmas à base de bore, en particulier ceux produits dans des mélanges d'argon et de B<sub>2</sub>H<sub>6</sub>. Il s'agit ici de recourir à divers diagnostics électriques et spectroscopiques des plasmas radiofréquences à pression réduite afin d'obtenir un portrait complet des principaux facteurs gouvernant l'évolution des populations des particules et des rayonnements produits dans les plasmas d'argon et de B<sub>2</sub>H<sub>6</sub>.
  - (iii) Explorer le potentiel des plasmas à base de bore pour le traitement post-croissance. Il s'agit ici de capitaliser sur le savoir et le savoir-faire obtenu dans les deux premières étapes afin d'étudier la possibilité de fonctionnaliser le graphène dans les plasmas d'argon et de B<sub>2</sub>H<sub>6</sub>.

Dans un premier temps, nous décrirons brièvement les propriétés électroniques et optiques du graphène afin de saisir toute l'originalité de ce matériau. Nous présenterons également sa réponse en spectroscopie Raman immédiatement après sa croissance puis après bombardement par des ions de hautes énergies. Nous dresserons par la suite un état de l'art dans la production et la caractérisation de plasmas à pression réduite à base de bore. Un aperçu des applications de ces plasmas hautement réactifs en synthèse et en modification de matériaux et de nanomatériaux sera également exposé.

En lien avec les objectifs de la thèse, un autre chapitre dévoilera les résultats concernant l'interaction d'un plasma RF d'argon avec les films de graphène. Après une étude approfondie des populations de l'ensemble des particules et des rayonnements obtenus à partir de plusieurs diagnostics électriques et spectroscopiques (par exemple, la sonde de Langmuir, la spectrométrie de masse, la spectroscopie optique d'émission et d'absorption), les résultats sur le traitement du graphène seront présentés sous la forme d'un article publié. De plus, afin d'obtenir une cartographie complète de l'interaction plasma graphène, une toute nouvelle méthode d'analyse quantitative des spectres Raman du graphène résolus spatialement sera aussi décrite.

Le troisième volet se penchera sur l’interaction de plasma RF d’argon en régime pulsé avec les films de graphène. Selon un choix judicieux de conditions opératoires, nous avons pu isoler les effets des ions, des métastables et des photons VUV. De plus, en capitalisant sur le potentiel d’innovation de la nouvelle méthode d’analyse des cartographies Raman, nous avons pu comparer les dommages produits dans les cristaux de graphène versus aux joints de grains. À nouveau, les résultats sont présentés sous forme d’articles publiés et récemment soumis pour publication.

Enfin, dans la dernière section, une étude détaillée des plasmas à base de bore sera d’abord présentée. Puis, inspiré de ces travaux, nous présenterons sous la forme d’un article récemment soumis pour publication un exemple d’applications de ce type de plasmas hautement réactifs pour le traitement post-croissance de films de graphène. Finalement, nous allons conclure et présenter quelques-unes des perspectives s’inscrivant dans la suite de ce travail de doctorat. Notons, pour le lecteur, que les références sont situées à la fin de chaque chapitre et/ou article plutôt qu’à la fin du document complet.

## Références

- [1] Novoselov KS, Geim A K, Morozov S V, Jiang D, Zhang Y, Dubonos S V, et al. Electric field effect in atomically thin carbon films. *Science* 2004;306:666–9. doi:10.1126/science.1102896.
- [2] Hernandez Y, Coleman JN, Wang Z, King PJ, Duesberg GS, Nicolosi V, et al. Liquid Phase Production of Graphene by Exfoliation of Graphite in Surfactant/Water Solutions. *J Am Chem Soc* 2009;131:3611–20. doi:10.1021/ja807449u.
- [3] Kim KS, Zhao Y, Jang H, Lee SY, Kim JM, Kim KS, et al. Large-scale pattern growth of graphene films for stretchable transparent electrodes. *Nature* 2009;457:706–10. doi:10.1038/nature07719.
- [4] Li X, Reina A, Jia X, Ho J, Nezich D, Son H, et al. Large-Area Synthesis of High-Quality and Uniform Graphene Films on Copper Foils. *Science* (80- ) 2009;324:1312–4.
- [5] Dato A. Graphene synthesized in atmospheric plasmas—A review. *J Mater Res* 2019;34:214–30. doi:10.1557/jmr.2018.470.
- [6] Rincón R, Melero C, Jiménez M, Calzada MD. Synthesis of multi-layer graphene and multi-wall carbon nanotubes from direct decomposition of ethanol by microwave plasma without using metal catalysts. *Plasma Sources Sci Technol* 2015;24:032005. doi:10.1088/0963-0252/24/3/032005.
- [7] Novoselov KS, Geim AK, Morozov S V., Jiang D, Katsnelson MI, Grigorieva I V., et al. Two-dimensional gas of massless Dirac fermions in graphene. *Nature* 2005;438:197–200. doi:10.1038/nature04233.
- [8] Gass MH, Bangert U, Bleloch AL, Wang P, Nair RR, Geim AK. Free-standing graphene at atomic resolution. *Nat Nanotechnol* 2008;3:676–81. doi:10.1038/nnano.2008.280.
- [9] Reina AE Al, et al Reina A, Jia X, Ho J, Nezich D, Son H, et al. Large area, few-layer graphene films on arbitrary substrates by chemical vapor deposition. *Nano Lett* 2009;9:30–5. doi:10.1021/nl801827v.
- [10] Noorden BR Van. The Trials of new carbon. *Carbon Nanotub* 2011;469:14–6. doi:Doi 10.1038/469014a.
- [11] Kim WY, Kim KS. Prediction of very large values of magnetoresistance in a graphene nanoribbon device. *Nat Nanotechnol* 2008;3:408–12. doi:10.1038/nnano.2008.163.
- [12] Lee WH, Park J, Kim Y, Kim KS, Hong BH, Cho K. Control of graphene field-effect transistors by interfacial hydrophobic self-assembled monolayers. *Adv Mater* 2011;23:3460–4. doi:10.1002/adma.201101340.

- [13] Min SK, Kim WY, Cho Y, Kim KS. Fast DNA sequencing with a graphene-based nanochannel device. *Nat Nanotechnol* 2011;6:162–5. doi:10.1038/nnano.2010.283.
- [14] Georgakilas V, Tiwari JN, Kemp KC, Perman JA, Bourlinos AB, Kim KS, et al. Noncovalent Functionalization of Graphene and Graphene Oxide for Energy Materials, Biosensing, Catalytic, and Biomedical Applications. *Chem Rev* 2016;116:5464–519. doi:10.1021/acs.chemrev.5b00620.
- [15] Robert Bigras G, Glad X, Martel R, Sarkissian A, Stafford L. Treatment of graphene films in the early and late afterglows of N<sub>2</sub> plasmas: comparison of the defect generation and N-incorporation dynamics. *Plasma Sources Sci Technol* 2018;27. doi:10.1088/1361-6595/aaedfd.

# Chapitre 1 : État de l'art

## 1. Le graphène

### 1.1. Structure et propriétés fondamentales

Le graphène se caractérise par une couche unique d'atomes de carbone disposés en hexagone (ou en nid d'abeille). Comme le montre la Figure 1.1, du fait de son organisation cristalline, chaque atome de carbone est à une distance moyenne  $a = 1.42 \text{ \AA}$  de chacun de ses trois plus proches voisins. Ainsi, le graphène peut être représenté par une feuille de carbone extrêmement fine de seulement 0.34 nm d'épaisseur.

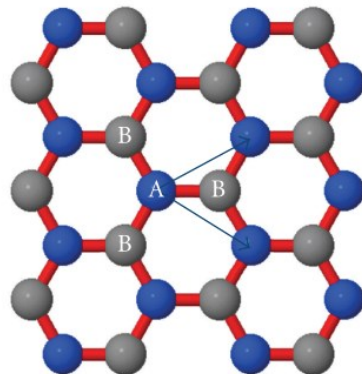


Figure 1.1 : Structure hexagonale du graphène. Chaque atome de carbone possède trois voisins. Tiré de [1].

Cette structure bien spécifique du graphène est rendue possible par l'hybridation  $sp^2$  qui permet de maintenir une structure plane en liant chaque atome de carbone avec ses trois plus proches voisins via des liaisons sigmas. Comme le montre la Figure 1.2, une autre liaison  $\pi$  se forme également hors plan.

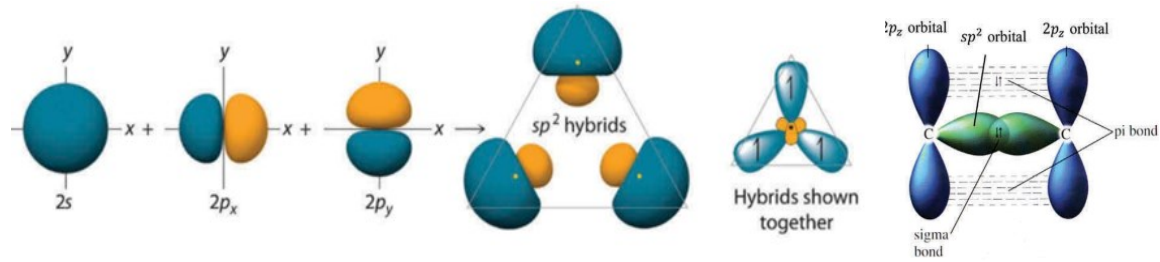


Figure 1.2 : Formation de l’hybridation  $sp^2$  et visualisation des liaisons sigma et pi dans le graphène.  
Tiré de [2].

Grâce à sa structure cristalline et la présence de liaisons  $\pi$ , le graphène possède une structure de bande remarquable [1]. En effet, c’est un semi-conducteur à gap nul (semi-métal) dû à la rencontre des bandes de conduction et de valence aux points de Dirac. La Figure 1.3 représente la première zone de Brillouin et une coupe transversale selon l’axe x de la structure de bande [2]. Sur la Figure 1.3a, on note qu’il existe deux groupes de trois points de Dirac chacun nommé  $K_-$  et  $K_+$ . La relation de dispersion proche de ces deux points est linéaire, contrairement aux semi-conducteurs classiques [1].

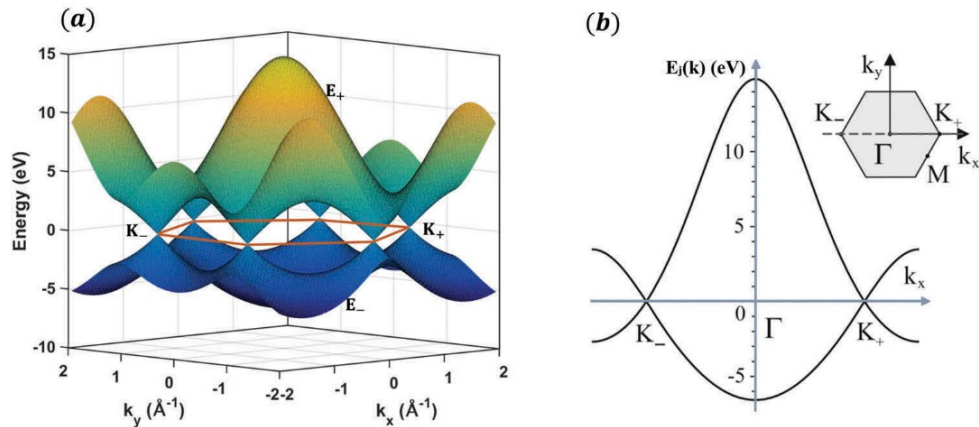


Figure 1.3 : (a) Structure de bande du graphène et (b) coupe transversale de la structure de bande, où l’énergie est représentée en fonction de la fonction d’onde  $k_x$  le long de la ligne  $ky = 0$ . Tiré de [2].

L’une des propriétés les plus spectaculaires du graphène est de posséder des électrons au niveau de Fermi dont la masse apparente est nulle ; il constitue ainsi le seul système physique

faisant apparaître des fermions de masse nulle. Par conséquent, la mobilité électronique théorique du graphène à température ambiante est de l'ordre de  $250\,000\,\text{cm}^2\cdot\text{V}^{-1}\cdot\text{s}^{-1}$  pour une densité de porteurs de  $10^{12}\,\text{cm}^{-2}$  [3,4], tout ceci combiné à une excellente conductivité thermique ( $5000\,\text{W m}^{-1}\,\text{K}^{-1}$ ) [5]. Dans ces conditions, c'est la diffusion des électrons par les phonons acoustiques du graphène qui limite les valeurs théoriques de mobilité électronique. Cependant, sur substrats de  $\text{SiO}_2$ , les phénomènes de diffusion des électrons par les phonons optiques du substrat deviennent plus importants que ceux dans le graphène; ceci limite alors la mobilité électronique à  $40,000\,\text{cm}^2\cdot\text{V}^{-1}\cdot\text{s}^{-1}$  [6]. La résistivité des films de graphène est également de  $10^{-6}\,\Omega\cdot\text{cm}$ , ce qui est plus faible que celle de l'argent (la plus faible valeur connue à ce jour à température ambiante [6]).

Le graphène possède également des propriétés vibrationnelles particulières, ce qui lui permet d'être un très bon conducteur thermique. De plus, ces propriétés jouent un rôle important en caractérisation optique puisqu'elles permettent des mesures par spectroscopie Raman [7,8]. Ainsi, il existe six relations de dispersion des phonons, trois dites Acoustiques (A) et trois autres dites Optiques (O). De chacune de ces deux branches, il existe des modes de vibrations atomiques hors plan (o) et dans le plan (i). Les vibrations atomiques hors plan sont transverses (oTA et oTO) tandis que les vibrations atomiques dans le plan peuvent être longitudinales (iLA et iLO) ou Transverses (iTA et iTA). On obtient ainsi six courbes de dispersions correspondants aux différents modes iLO, iTO, oTO, iLA, iTA, oTA présentés sur la [9].

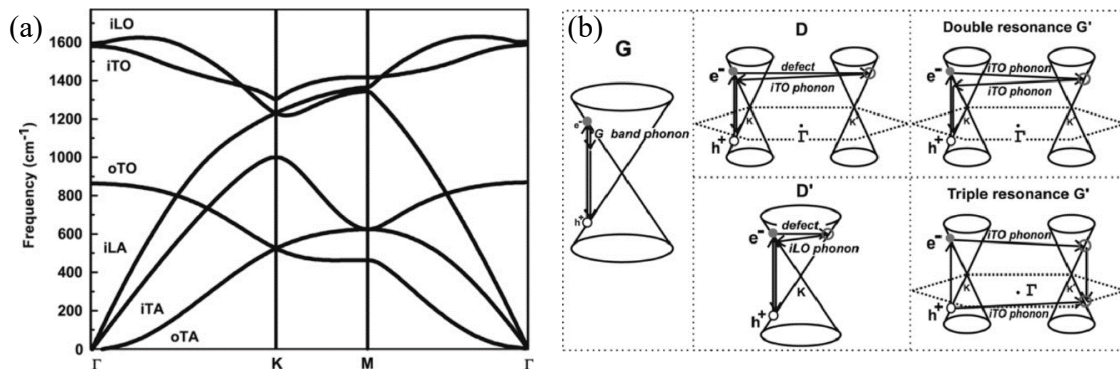


Figure 1.4 : (a) Relations de dispersions théoriques du graphène présentant les différentes branches iLO, iTO, oTO, iLA, iTA, et oTA et (b) processus Raman conduisant à l'émission des principaux pics du graphène. Tiré de [9].

Lors de l'exposition du graphène à une lumière laser (532 nm, par exemple), plusieurs réponses Raman peuvent être obtenues. Un exemple est présenté à la Figure 1.5. La bande G ( $\sim 1585$  cm $^{-1}$ ) est communément émise par tous les éléments carbonés ayant des liaisons sp $^2$ . Il s'agit d'un phénomène de premier ordre associé aux modes iTO et iLO. La bande D (1350 cm $^{-1}$ ) est liée à un processus du second ordre impliquant un phonon et un défaut dans la structure du graphène. Comme nous le verrons plus loin, ce pic Raman est couramment utilisé pour caractériser les défauts dans le graphène. La bande 2D (aussi appelé G', 2700 cm $^{-1}$ ) est aussi un phénomène du deuxième ordre et est, en principe, très faible. Cependant dans le cas du graphène parfait, sa structure permet d'obtenir une intensité supérieure à la bande G. Enfin, la bande D' (1620 cm $^{-1}$ ) apparaît de manière similaire à la bande D via un défaut dans la structure cristalline. Cependant, comme présenté dans la Figure 1.4b, un phonon iLO est impliqué dans ce cas-ci.

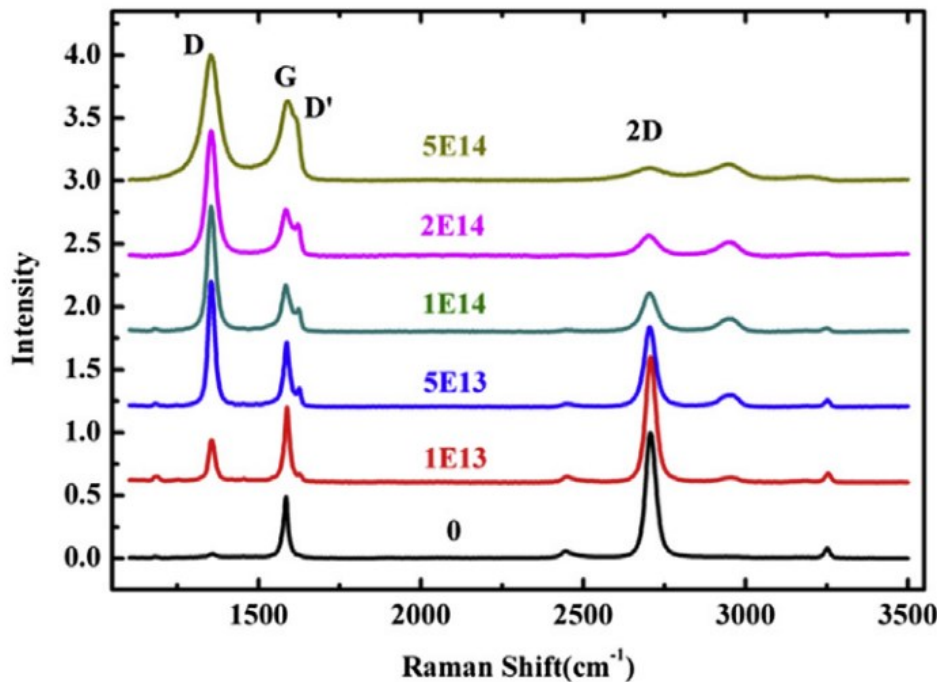


Figure 1.5: Évolution du spectre Raman d'un échantillon de graphène soumis à un bombardement avec des atomes de Boré à 32 keV pour différentes doses. Tiré de [10].

## 1.2.Défauts dans le graphène

Le graphène peut présenter des défauts dans sa structure cristalline. Ceux-ci peuvent être associés à la méthode de synthèse ou encore induits par divers traitements post-synthèse (voir détails plus bas). Ces défauts sont particulièrement importants puisqu'ils influencent directement les propriétés électroniques et optiques du graphène. Le premier type de défauts, dits de Stone-Wales, n'implique pas de perte ou d'ajout d'atomes dans la structure cristalline du graphène : il s'agit d'une simple réorganisation des atomes. Un exemple de défauts de Stone-Wales, pouvant être visualisé par Microscopie Électronique à Transmission (TEM pour *Transmission Electron Microscopy*) [11], est présenté à la Figure 1.6. Il est intéressant de noter que l'énergie de formation des défauts illustrés sur cette figure est de 5 eV [12] et que le processus peut être réversible si la même énergie est fournie au système. De plus, l'énergie de migration pour ce type de défaut est de 10 eV. Cela signifie ainsi que les défauts de Stone-Wales sont stables à température ambiante (300 K) et quasiment immobiles une fois créés.

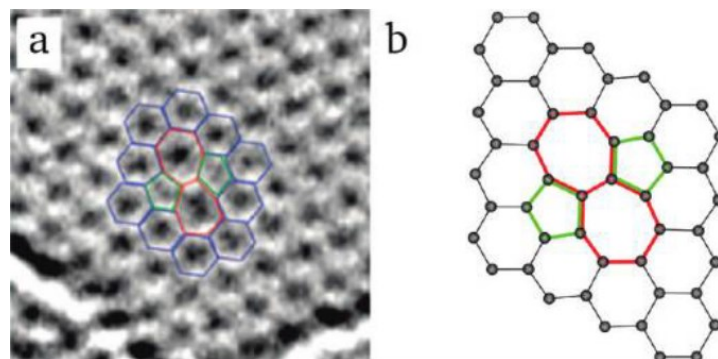


Figure 1.6 : Image TEM et (b) représentation atomique d'un défaut de type Stone-Wales. Tiré de [12].

Il existe également des défauts ponctuels caractérisés par l'absence d'un atome de carbone dans la structure cristalline du graphène. La Figure 1.7 présente un exemple d'image TEM ainsi que la disposition théorique correspondante pour de telles lacunes. Dans ces conditions, l'énergie de formation de la lacune peut être estimée à 7.5 eV tandis que l'énergie de migration est d'environ 1.3 eV [13,14]. Ces défauts sont donc très mobiles sur la surface du graphène et peuvent ainsi être considérés comme des adatomes. De plus, la liaison pendante entourée sur la

Figure 1.7b rend cet atome très réactif aux autres atomes pouvant entrer en contact avec celui-ci. Nous reviendrons sur ce point plus loin.

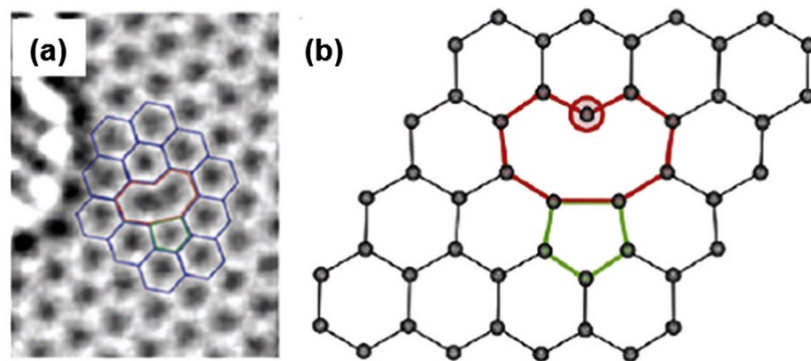


Figure 1.7 : (a) Image TEM et (b) représentation atomique d'un défaut de type lacune. Tiré de [12].

Les défauts ponctuels dans le graphène peuvent également prendre la forme de doubles lacunes. Dans ce cas, aucune liaison pendante n'est présente puisque, comme le montre la Figure 1.8, tous les atomes de carbones possèdent trois voisins. De manière assez surprenante, l'énergie de formation de ce type de défaut est assez proche de celle pour la formation d'une lacune simple, soit autour de 8 eV [13,14]. De plus, en vertu de l'absence de liaisons pendantes, les lacunes doubles sont thermodynamiquement favorisées par rapport aux lacunes simples et sont donc plus susceptibles d'être présentes à la surface du graphène. Cependant, l'énergie de migration de la double lacune est beaucoup plus élevée, soit autour de 7 eV; ces défauts sont donc beaucoup moins mobiles.

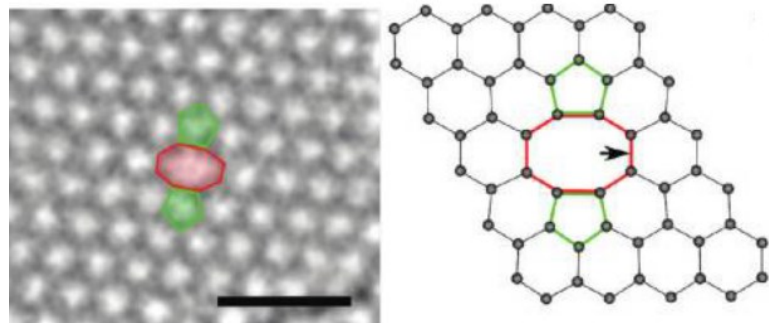


Figure 1.8 : (a) image TEM et (b) représentation atomique d'un défaut de type lacune double Tiré de [12].

Des défauts linéaires peuvent aussi être observés lors de la rencontre de deux domaines de croissance du graphène associés à des orientations cristallines distinctes. Comme le montre la Figure 1.9, on obtient alors une structure périodique d'octogones et de pentagones tout le long de la jonction entre les deux domaines [15].

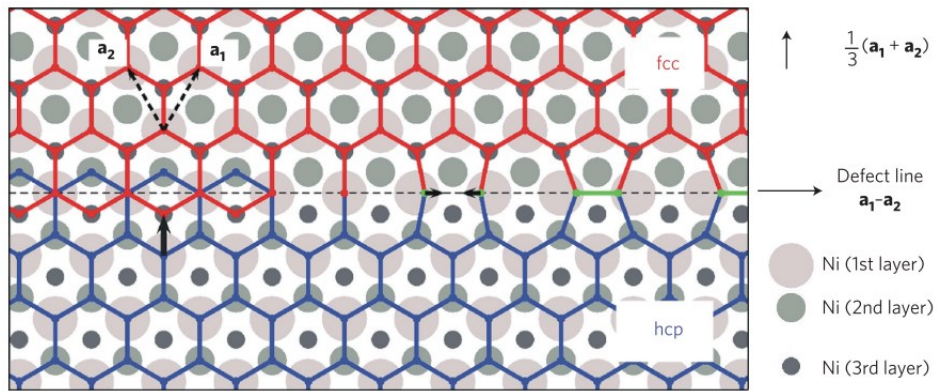


Figure 1.9 : Structure autour des joints de grain du graphène consistant en une succession de paires de pentagones et d'octogones [15].

Enfin, on peut également observer des défauts linéaires en périphérie des domaines cristallins du graphène. Comme le montre la Figure 1.10, les configurations les plus simples sont le bras de chaise (armchair) et le zigzag. Les atomes en rouge sont ceux possédant des liaisons

pendantes et donc fortement réactifs (elles peuvent ainsi être facilement passivées, par exemple par des atomes d'hydrogène [16,17]).

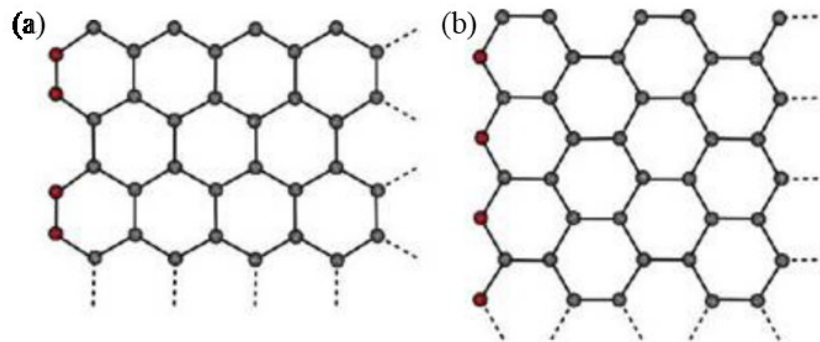


Figure 1.10 : Différentes configurations possibles en bordure de graphène (a) en bras de chaise et (b) en zigzag. Tiré de [12].

Il est important de rappeler que certains défauts, en particulier les lacunes simples, peuvent aisément migrer à la surface du graphène. Ces adatomes peuvent aussi provoquer une hybridation  $sp^3$  sur le graphène pour laquelle l'énergie de migration est similaire à celle des lacunes (1.5-2 eV) [18]. Si deux adatomes se rencontrent en un point donné à la surface du graphène, ils peuvent alors former une paire de Stone-Wales inverses comme le montre la Figure 1.11. L'énergie de formation de cette structure est de 5.8 eV et donc peu présente sur le graphène de bonne qualité.

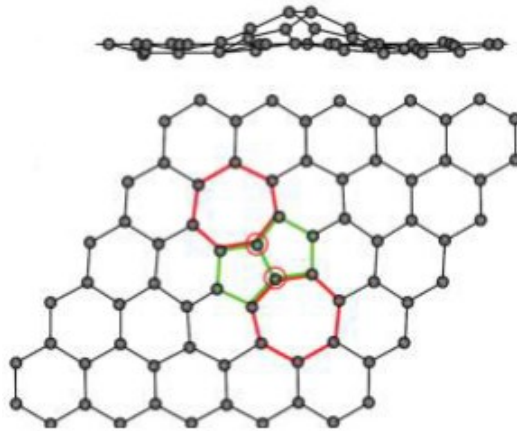


Figure 1.11: Structure théorique d'une paire de Stone Wales inverse. Tiré de [12].

Le Tableau 1.1 présente un sommaire des défauts décrits dans cette section avec leurs énergie de formation et de migration correspondante.

Tableau 1.1: Récapitulatif des défauts et de leurs énergies de formation et de migration [18].

defect type	configuration	formation energy [eV]	migration energy [eV]
Stone—Wales	55-77	4.5—5.3	10
single vacancy	5-9	7.3—7.5	1.2—1.4
double vacancy	5-8-5	7.2—7.9	7
	555-777	6.4—7.5	6
	555-6-777	7	6
adatom <sup>a</sup>		6—7	0.4
inverse SW	57-57	5.8 <sup>b</sup>	
adatom—SV pair		14	

### 1.3. Synthèse du graphène

Historiquement, le graphène a été produit pour la première fois par exfoliation [19]. Le principe de cette méthode est de briser les forces de van der Walls reliant les feuillets de graphène contenues dans le graphite [20]. Pour isoler le graphène, du ruban adhésif a été initialement utilisé mais dans la volonté d'obtenir un procédé plus stable, rapide et efficace, certaines études se sont intéressées à l'utilisation d'un agent chimique [21]. Ces méthodes

permettent d'obtenir du graphène de très haute pureté mais typiquement de relativement faibles dimensions.

Une méthode alternative introduite en 2006 est basée sur le dépôt chimique en phase vapeur (CVD pour *Chemical Vapor Deposition*) [22]. Cette technique consiste à introduire un substrat métallique (cuivre ou nickel) dans un four à haut vide ( $10^{-6}$  Torr). Un mélange de H<sub>2</sub> et de CH<sub>4</sub> est alors introduit afin d'atteindre une pression de plusieurs centaines de mTorr. Le substrat est chauffé autour de 1000°C afin que les molécules de méthane se fragmentent au contact de la surface. Le carbone peut alors migrer sur la surface pour se lier à d'autres atomes de carbone et former petit à petit le graphène [23]. Du graphène monocouche de très bonne qualité peut ainsi être obtenue sur des surfaces relativement grandes [24], de l'ordre de plusieurs centimètres. Cependant, pour des applications en micro et nanoélectronique, il est nécessaire de transférer le graphène sur un substrat de silicium. Le substrat de cuivre utilisé étant très fin, il est alors possible de retirer chimiquement le graphène et de le récupérer sur le substrat de son choix. Cependant, ceci entraîne une légère dégradation de la qualité du graphène. De plus, la couche de PMMA utilisée pour protéger le graphène lors du transfert laisse bien souvent des résidus. Pour cette raison, certaines études ont cherché à optimiser cette méthode [25] [26] ou à développer des approches alternatives [20].

### 1.3.1. Traitements post-synthèse

Au cours des dernières années, plusieurs approches basées sur la chimie des solutions ont été proposées pour attacher de manière covalente des fonctions chimiques sur le graphène [27]. À partir des travaux sur les fullerènes et les nanotubes de carbone, les espèces les plus susceptibles de réagir avec les atomes de carbone sp<sup>2</sup> du graphène sont les radicaux libres et les diénophiles. Par exemple, Kosynkin *et al.* [28] ont eu recours au sel de diazonium qui, une fois en contact avec des donneurs d'électrons, produit des radicaux libres. Ce type de traitement résulte en une diminution notable de la conductivité du graphène due au changement d'hybridation des atomes de carbone de sp<sup>2</sup> vers sp<sup>3</sup>. De manière similaire, Niyogi *et al.* [29] ont montré que l'attachement covalent de nitrophényles introduit une bande interdite dans le graphène. Toujours par voies

chimiques, des matériaux nanocomposites dérivés de la dispersion de nanostructures sur le graphène ont aussi été étudiés et appliqués à la catalyse, l'optoélectronique, les piles à combustible, etc. De manière générale, pour le dépôt de nanostructures de métaux précieux (Au, Pt, Ag) ou encore d'oxydes métalliques ( $ZnO$ ,  $TiO_2$ ,  $Fe_3O_4$ ), des précurseurs de sels métalliques sont injectés dans un solvant (avec ou sans agent oxydant) contenant des nanoplaquettes de graphène dispersées. Par exemple, Wang *et al.* [30] ont dispersé des nanoplaquettes d'oxyde de graphène dans l'eau à partir d'un stabilisant dodecyl sulfate. À cette solution, ils ont ajouté une solution de  $TiCl_3$ , résultant en un dépôt de nanoparticules de  $TiO_2$  par hydrolyse. Le nanocomposite  $TiO_2$ -graphène ainsi obtenu a démontré une nette amélioration des performances anodiques des piles de lithium due à une meilleure cinétique d'insertion/extraction du Li dans le  $TiO_2$ . De manière analogue, des nanofils de  $ZnO$  ont été déposés sur la surface d'oxyde de graphène utilisé comme composant de capteurs UV [31]. Le nanocomposite  $ZnO$ -graphène a démontré une augmentation substantielle de l'efficacité du capteur, un effet dû à l'habileté du  $ZnO$  d'absorber les photons UV ainsi qu'à la grande conductivité du graphène qui facilite le transfert de charges. Dans l'ensemble, malgré les succès indéniables des méthodes de fonctionnalisation post-croissance du graphène par voies chimiques, celles-ci sont peu versatiles, font souvent intervenir des produits nocifs pour l'être humain ainsi que son environnement et sont mal adaptées à l'automatisation en milieu industriel.

Par opposition aux approches par voies chimiques, des méthodes dites sèches beaucoup plus souples et plus vertes ont aussi été proposées pour attacher après synthèse des atomes et des molécules au graphène. Par exemple, le graphane, le graphène complètement hydrogéné, fut synthétisé en exposant le graphène à un plasma d'hydrogène [32,33]. Bien que ces modifications maintiennent la structure bidimensionnelle du graphène, la perte de conjugaison associée à la rupture des liaisons  $\pi$  au-dessus et en dessous du réseau hexagonal engendre d'importants changements de ses propriétés électroniques. En effet, la mobilité des porteurs dans le graphane est environ 3 ordres de grandeur plus faible que celle dans le graphène. Il se comporte alors comme un isolant, ouvrant la voie à une panoplie d'applications couplant graphène et graphane. Des résultats similaires ont été rapportés pour le fluoro-graphène obtenu en exposant le graphène à un jet de  $F_2$  [34]. Les mesures de photoluminescence montrent un pic d'émission à 3.8 eV attribué à la recombinaison des électrons de la bande de conduction et des trous de la bande de

valence [35], en excellent accord avec les simulations utilisant la théorie de la fonctionnelle de la densité qui suggèrent l'apparition d'un gap direct d'environ 3.1 eV [36]. Récemment, des plasmas de N<sub>2</sub> [37,38], de NH<sub>3</sub>[39], d'O<sub>2</sub> [40], de SF<sub>6</sub> [41], CF<sub>4</sub> [40,42], Ar/F<sub>2</sub> [43] et CHF<sub>3</sub> [40] ont aussi été explorés pour le traitement de monocouches et de multicouches à base de graphène.

Dans les plasmas réactifs, l'interaction plasma-graphène peut mettre en jeu une grande variété de particules (ions positifs, électrons, espèces excitées, atomes et molécules réactives, etc.) mais aussi de rayonnements (de l'ultraviolet jusqu'à l'infrarouge). Ces espèces peuvent mener à des phénomènes (i) d'attachement covalent de différentes fonctions chimiques, (ii) d'attachement non-covalent de divers atomes et molécules via les interactions  $\pi$ , (iii) d'incorporation d'atomes dans le graphène par dopage substitutionnel, ou encore (iv) d'incorporation de défauts dans le graphène associé à un apport d'énergie externe. Pour quantifier les phénomènes d'attachement et d'incorporation d'atomes par dopage substitutionnel, il est commun de recourir à la spectroscopie des photoélectrons induits par les rayons X (XPS pour *X-ray photoelectron spectroscopy*) afin d'obtenir la composition chimique du graphène et de l'environnement chimique de chacun des constituants. La Figure 1.12 présente un exemple de spectre du carbone et de l'azote avant et après traitement dans un plasma d'azote. Les auteurs note une légère diminution des liaisons C-C du signal C1s du graphène au profit d'autres liaisons comme C-O et C-N. Dans le cas des atomes d'azote, le signal N1s peut être lié à diverses configurations d'incorporation dans le graphène, par exemple, le pyrrole, le pyridine et le graphitique [38].

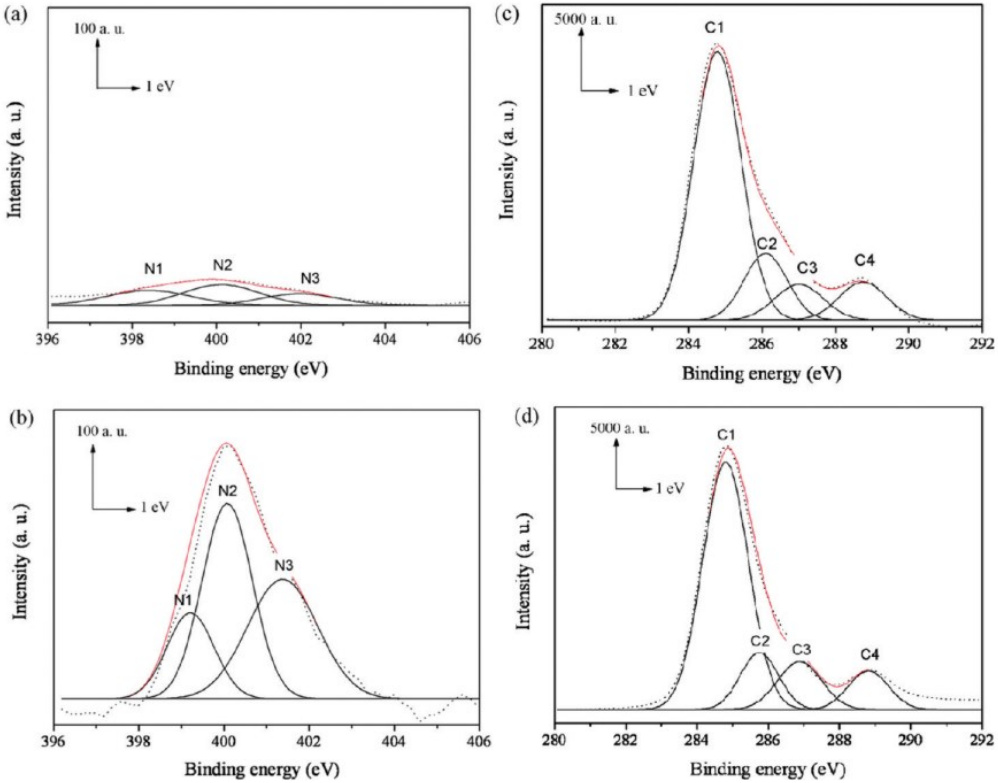


Figure 1.12 : Spectres haute résolution XPS du graphène pour deux dopages différents (a-c) et (b-d). Spectres (a) et (c) N1s avec différentes configurations, N1(pyridinique) N2 (pyrrolique) et N3 (quaternaire). Spectres (c) et (d) C1s avec C1 (C-C sp<sub>2</sub>), C2 (C-C sp<sub>3</sub>), C3 (O-C-O ou C-N) et C4 (C-C=O).

### 1.3.2. Caractérisation Raman du graphène

Plusieurs informations sur les traitements post-synthèse peuvent également être tirés de la spectroscopie Raman en étudiant l'intensité (I), la largeur à mi-hauteur (FWHM), la position (Pos) ou l'aire (A) des pics D, G, D' et 2D [44,45]. Une excellente introduction à ce vaste domaine est réalisée par Merlen *et al* [46] et permet de saisir toute la richesse d'information qu'il est possible d'extraire de la spectroscopie Raman. En particulier, pour étudier la dynamique de création des défauts, il est commun de regarder le ratio de l'intensité du pic D sur celui du pic G ( $I_D/I_G$ ) [45][47]. Une augmentation de ce rapport est typiquement liée à une augmentation de la densité de défauts dans le graphène. Cependant, ce rapport diminue après un certain niveau de défauts où on assiste à une amorphisation du graphène [44]. Afin de mieux illustrer ce phénomène, Figure 1.13 illustre la variation du ratio  $A_D/A_G$  corrigé par l'énergie du

laser en fonction de  $\text{FWHM}_G$  pour différents échantillons de graphène. De ces travaux pionniers réalisés par *Cancado et al* [48], on peut distinguer deux types de défauts. Les défauts de type lacune (0D) ou ceux qui se forment sur une ligne bien définie (1D). Dans le cas des défauts 0D, une rapide augmentation du ratio  $A_D/A_G$  est observée avec peu de variation dans  $\text{FWHM}_G$ . Cette région correspond au graphène peu endommagé et dont les propriétés sont peu affectées par la présence de défauts ponctuels. Un maximum est ensuite atteint pour une valeur de  $\text{FWHM}_G$  autour de  $25 \text{ cm}^{-1}$ . Au-delà de ce point, le ratio  $A_D/A_G$  diminue jusqu'à se stabiliser autour de 50 alors que  $\text{FWHM}_G$  continue d'augmenter.

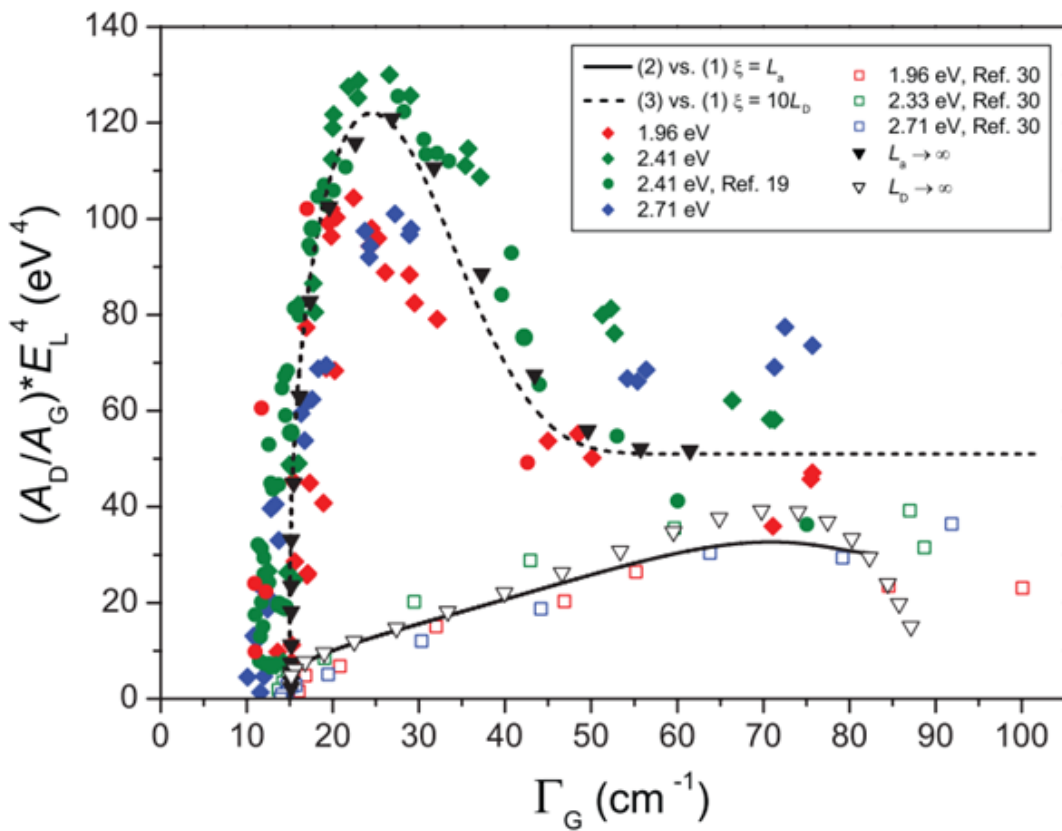


Figure 1.13 : Évolution de  $\text{AD}/\text{AG}$  corrigé par l'énergie du laser en fonction de  $\text{FWHM}_G$ . La ligne pleine est une corrélation qui décrit le cas où les défauts générés sont linéaires (1D). La ligne en pointillé représente le cas où les défauts sont ponctuels (0D). Les points sont ceux obtenus de la littérature.

Le ratio  $I_{2D}/I_G$  permet lui aussi d'évaluer la qualité du graphène et la dynamique de création des défauts. Une valeur égale ou supérieur de 2 est typiquement une confirmation d'un graphène de haute qualité et monocouche [49]. Ainsi, dès qu'une désorganisation du réseau hexagonal apparaît, il est attendu que ce ratio diminue. Ceci n'est pas forcément lié à l'apparition de lacunes mais peut aussi résulter d'autres types de défauts provoqués par un dopage du graphène [49]. Comme ce ratio est plus souvent difficile à interpréter, il est beaucoup moins utilisé dans la littérature pour l'étude de la dynamique de formation des défauts dans le graphène.

Le ratio  $I_D/I_{D'}$  est également beaucoup utilisé pour caractériser les défauts dans le graphène. En effet, *Eckmann et al* [47] [50] ont lié la valeur de ce ratio à la nature même des défauts pouvant être formés lors de la synthèse ou des traitements post-synthèse. Pour illustrer ce phénomène, la Figure 1.14 présente l'évolution du ratio  $I_D/I_G$  en fonction du ratio  $I_D/I_{D'}$  pour divers échantillons. De ces résultats obtenus sur une vaste gamme de conditions de traitements post-synthèse, les auteurs distinguent plusieurs valeurs reliées à la nature des défauts mais pas à leur densité. Ceci est particulièrement vrai dans le stage 1 où la densité des défauts est faible. Dans ce régime, les deux ratios  $I_D/I_G$  et  $I_D/I_{D'}$  augmentent de manière similaire avec la densité de défauts de sorte que le rapport  $I_D/I_{D'}$  demeure constante. Par exemple, pour  $I_D/I_{D'}=3.5$ , les défauts sont typiques de ceux trouvés en bordure de graphène. Pour  $I_D/I_{D'}=7$ , les défauts sont des lacunes (défauts 0D) alors que pour  $I_D/I_{D'}=13$ , on se rapproche d'une fonctionnalisation du graphène et donc des atomes de carbones en configuration  $sp^3$ . Il est aussi possible d'obtenir une valeur  $I_D/I_{D'}=8$ , signe de la substitution d'un atome de carbone par un atome d'une autre nature [47]. Cependant, dès que le graphène commence à être amorphisé, le comportement et les valeurs de  $I_D/I_{D'}$  deviennent plus difficile à interpréter. Il faut alors vérifier que les valeurs d'intensité de D et de D' restent bien reliées par une relation linéaire.

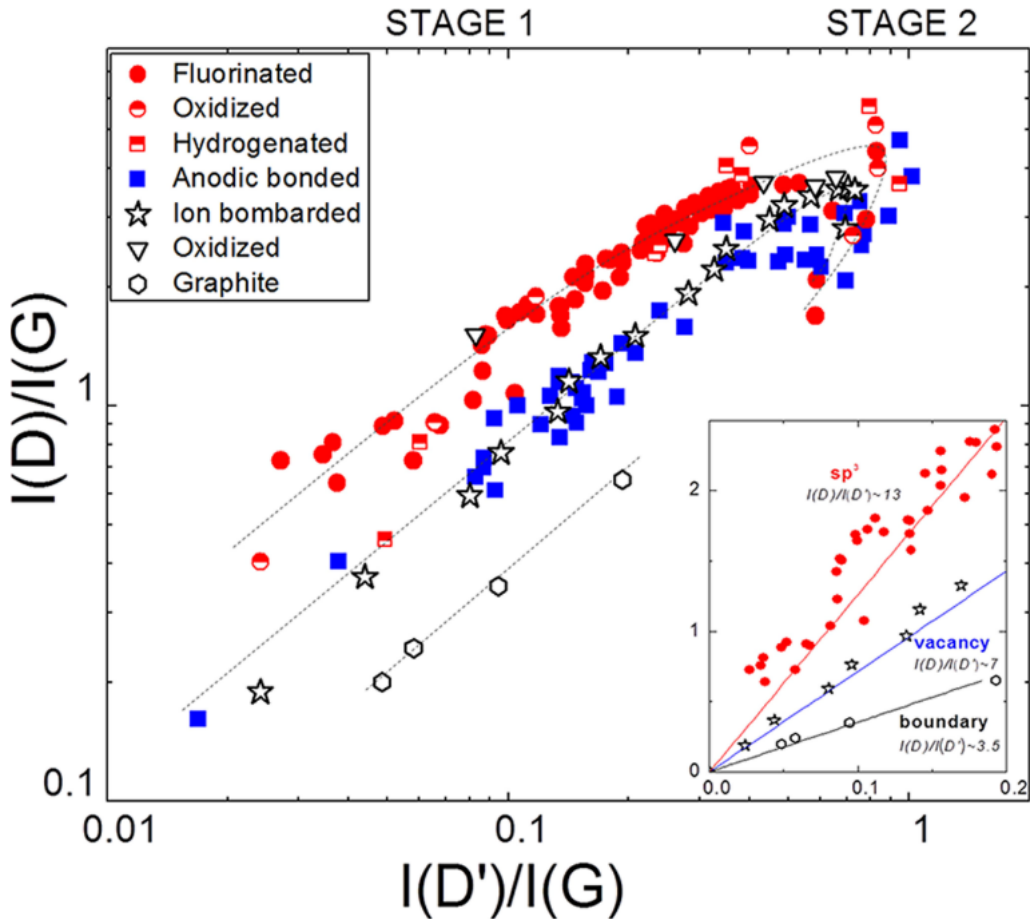


Figure 1.14 : Évolution de  $I(D)/I(G)$  en fonction de  $I(D')/I(G)$  pour des échantillons traités par plusieurs méthodes afin de mettre en évidence le changement de la nature des défauts.

Les positions des pics en spectroscopie Raman peuvent également être utilisées pour évaluer les contraintes et le niveau de dopage du graphène. En effet, Lee et al [51] ont démontré expérimentalement qu'il est possible de représenter les contraintes par la position du pic 2D et le niveau de dopage par la position du pic G. La Figure 1.15 présente l'évolution des valeurs de la Pos2D en fonction de la PosG d'un échantillon de graphène recuit à différentes températures sous atmosphère d'oxygène [51].

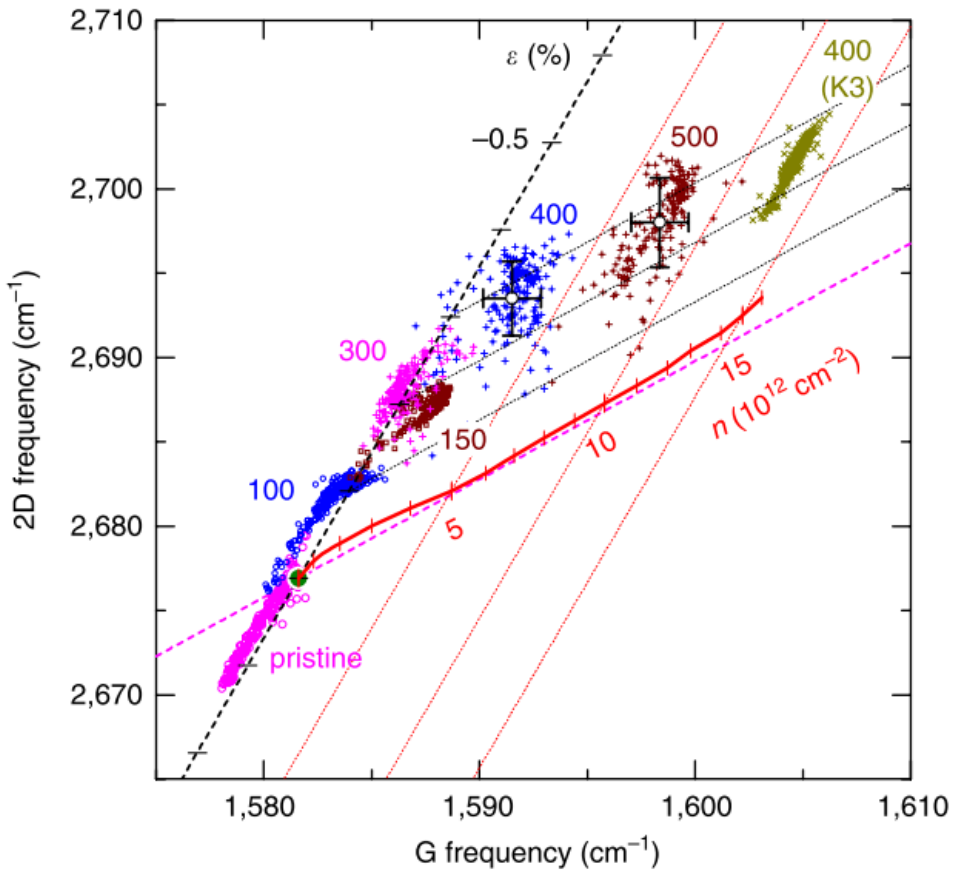


Figure 1.15 : Distribution de la position du pic 2D en fonction de la position du pic G pour un échantillon de graphène recuit dans une atmosphère d'oxygène [51].

Dans ce cas, on observe une augmentation de  $\text{Pos}_{2\text{D}}$  avec les traitements indiquant un stress compressif. Il existe aussi une distribution de  $\text{Pos}_{2\text{D}}$  pour un même échantillon indiquant que le stress diffère effectivement d'un point à un autre à la surface du graphène. L'augmentation de  $\text{Pos}_G$  est ici liée à la création de lacunes qui provoquent une augmentation de la densité de porteurs et donc une forme de dopage dans le graphène. De plus, lors d'un traitement qui impliquerait de manière simultanée un dopage et des dommages, Bruna *et al*[52] indiquent que les aires et intensités des pics D et D' diminuent à cause du dopage. Ceci peut être trompeur si l'on cherche à évaluer l'état du graphène.

Dans les plasmas réactifs comme  $\text{H}_2$ ,  $\text{N}_2$  ou  $\text{O}_2$ , les agents réactifs impliqués dans les phénomènes d'attachement ou de substitution sont typiquement les atomes d'hydrogène, d'azote ou d'oxygène créés par la fragmentation de  $\text{H}_2$ ,  $\text{N}_2$  ou  $\text{O}_2$ . Dans certains cas, l'apport de réactants

dans le graphène peut aussi résulter des ions réactifs accélérés dans la gaine ionique au voisinage du substrat, par exemple,  $H^+$ ,  $H_2^+$ ,  $N^+$ ,  $N_2^+$ ,  $O^+$  et  $O_2^+$ . Cependant, dans les plasmas non réactifs comme l'argon, il est généralement admis dans la littérature scientifique que la dynamique de formation des défauts est directement et uniquement liée aux ions d'argon. Or, selon les conditions opératoires, des espèces neutres de longues durées de vie (par exemple des atomes d'argon métastables situés à plus de 11 eV au-dessus du niveau fondamental) ou encore des rayons ultraviolets (par exemple les transitions de l'argon autour de 105 nm) peuvent représenter des réservoirs d'énergie importants pour le plasma mais aussi pour l'interaction plasma-graphène. En lien avec les objectifs spécifiques de cette thèse, nous désirons explorer la nature et le rôle respectif de l'ensemble de ces particules et de ces rayonnements mis en jeu dans les plasmas non réactifs à base d'argon.

## 2. Plasmas à base de bore

### 2.1. Méthodes physiques et chimiques d'injection du bore

Il existe plusieurs méthodes physiques et chimiques permettant d'injecter des atomes de bore dans un plasma. La première consiste à fournir un apport d'énergie externe à une cible solide à base de bore dans le but de provoquer l'éjection des atomes. Cet apport d'énergie peut provenir, par exemple, d'un faisceau laser pulsé [53]. Si l'énergie déposée par le laser pulsé est suffisamment élevée, la zone visée sera ablatée et un plasma à base de bore sera formé à la surface de la cible. Ce plasma pourra alors se propager perpendiculairement à la surface de la cible pour former une plume. À la rencontre d'un substrat, les atomes issus de cette plume pourront contribuer au dépôt d'une couche mince composée des éléments de la cible ablatée mais aussi du gaz environnant. Communément appelée PLD (acronyme anglais pour *Pulsed Laser Deposition*), cette technique est très utilisée pour le dépôt de couches minces multi-élémentaires. Dans le cas du bore, une revue exhaustive de la littérature correspondante permet de constater que la majorité des travaux reposent sur des cibles de nitrule de bore (BN). Ceci permet d'introduire des atomes de bore et d'azote atomique dans la plume et donc de déposer des couches à base de BN [54–57].

Les plasmas à base de bore peuvent également être formés en injectant un précurseur destiné au CVD (acronyme anglais pour *Chemical Vapor Deposition*) ou au PECVD (acronyme anglais pour *Plasma Enhanced Chemical Vapor Deposition*). À ce sujet, les molécules  $\text{B}_2\text{H}_6$ ,  $\text{B}(\text{CH})_3$ ,  $\text{BCl}_2$ ,  $\text{BF}_3$  et  $\text{B}(\text{OCH}_3)_3$  sont les principaux précurseurs utilisés dans la littérature. Notons qu'ils sont tous toxiques et doivent donc absolument être dilués avec un gaz vecteur (par exemple  $\text{H}_2$ ,  $\text{N}_2$  ou  $\text{Ar}$ ) lors de leurs utilisations. De plus, certains de ces précurseurs vont également introduire des éléments parfois indésirables comme le fluor ou le chlore, ce qui limite encore plus le choix de précurseur selon l'application envisagée.

Parmi l'éventail des sources à plasma dans lesquelles des précurseurs à base de bore ont été injectés, nous constatons que les sources peuvent être classées en deux catégories : les plasmas de basse et de haute densité. La première configuration repose sur l'application d'un champ électrique DC (acronyme anglais pour *Direct Current*) ou RF (radiofréquence, typiquement 13.56 MHz) entre deux électrodes de manière à produire une décharge capacitive [58]. À basse pression, les densités des espèces chargées dans la zone plasma des décharges DC et RF sont relativement faibles, typiquement entre  $10^9$  et  $10^{11} \text{ cm}^{-3}$  [58]. On parle donc de plasmas de basse densité. La particularité de ce type de décharge est que la majorité de la puissance électrique injectée dans le système est dissipée dans les gaines au voisinage des électrodes. On obtient, néanmoins, des ions positifs très énergétiques à la surface du substrat placé sur la cathode grâce à l'accélération des ions dans la gaine ionique [58]. La Figure 1.16 présente un exemple d'un tel réacteur à plasma DC destiné à la croissance de diamant dopé au bore [59][60]. Deux lignes de gaz permettent d'acheminer du  $\text{CH}_4$  pour la croissance du diamant ainsi que le précurseur contenant le bore. Dans ce cas, du dihydrogène est injecté dans du  $\text{B}(\text{OCH}_3)_3$  liquide contenu dans un barboteur afin d'introduire le bore dans le plasma.

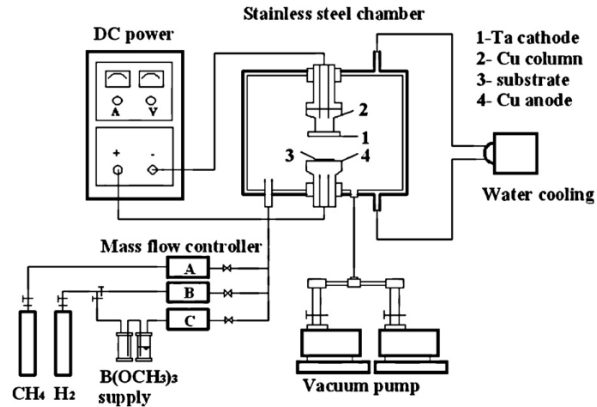


Figure 1.16: Schéma d'un réacteur DC-PECVD [59][60].

Les faibles densités de particules chargées des décharges capacitatives produites par des champs DC et RF limitent bien souvent la fragmentation des précurseurs dans le plasma. Pour combler cette lacune, des sources dites de haute densité (supérieures à  $10^{10}$ - $10^{11}$  électrons/ions par cm<sup>3</sup>) ont alors été développées [61], [62]. Dans ces systèmes, le couplage de l'énergie électrique vers les électrons du plasma n'est plus capacitif mais repose plutôt sur des interactions ondes-particules, des phénomènes de résonance ou encore de l'induction. Ceci permet alors d'obtenir des densités de particules chargées très élevées dans le plasma mais avec des chutes de potentiels plutôt faibles dans les gaines. Un premier type de réacteur à plasma de haute densité utilise des microondes en conditions de résonance cyclotronique électronique (plasmas ECR pour *Electron Cyclotron Resonance*)[63][61][64]. Dans ce cas, un champ magnétique statique est présent dans la chambre en plus des microondes. Si la fréquence cyclotronique électronique due au champ magnétique est égale à la fréquence de l'onde électromagnétique, un maximum d'absorption est alors observé [58]. Ceci facilite l'ignition de la décharge à très basses pressions pour lesquelles la fréquence de collision électron-neutre est trop faible par rapport à la fréquence d'oscillation de l'onde pour profiter du chauffage ohmique. Typiquement, un champ magnétique de 875 Gauss est nécessaire pour atteindre la condition de résonance pour une fréquence de 2.45 GHz. Plusieurs auteurs ont eu recours à des plasmas ECR pour la fragmentation de précurseurs à base de bore [65–67]. Dans la plupart des cas, les précurseurs utilisés sont soit le B<sub>2</sub>H<sub>6</sub>, soit du triméthylborane (TMB) dilué dans du dihydrogène ou de l'azote.

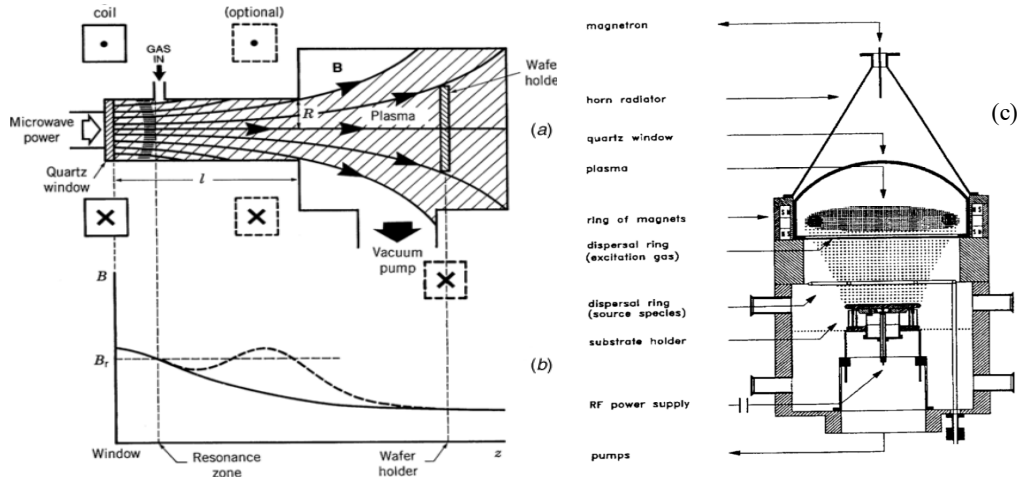


Figure 1.17: Profil typique d'un réacteur ECR avec (a) la configuration et (b) le profil axial des variations de champs magnétiques [58]. (c) Schéma typique d'un réacteur ECR-PECVD [65].

**LesError! Reference source not found.** Figures 1.17a et b présentent un exemple de réacteur ECR avec le profil axial de l'intensité du champ magnétique. La résonance est observée juste avant l'entrée dans la chambre où se trouve le substrat. La Figure 1.17c montre un autre exemple de réacteur ECR, cette fois dédié à l'étude du dépôt de couches minces de h-BN [65]. Dans ce cas, le plasma ECR est combiné avec une polarisation RF du substrat pour profiter des effets du bombardement ionique. On obtient alors un plasma hybride avec un couplage ECR pour la création et le maintien du plasma et un couplage capacitif pour le contrôle de l'énergie des ions incidents sur le substrat.

La Figure 1.18 présente un autre exemple de réacteur à plasma de haute densité utilisé pour le dépôt de couches minces à base de bore [68][69]. Dans ce cas, le plasma est produit par une bobine située autour d'un tube diélectrique et dans laquelle circule un courant RF (typiquement à 13.56 MHz) produisant un champ magnétique variable dans le temps. Dans ce type de réacteur, deux modes de fonctionnement existent. Le premier, le mode E (électrostatique), apparaît à basse puissance lorsque le plasma est maintenu par la différence de potentiel entre la bobine et les parois du réacteur reliées à la masse. Le couplage est donc capacitif, ce qui donne lieu à des plasmas de faibles densités de particules chargées. Le deuxième mode apparaît à plus haute puissance, c'est le mode H (électromagnétique). Dans ce régime, c'est le champ électrique induit par les oscillations temporelles du champ magnétique (Loi de Faraday) qui fournit la puissance

électrique aux électrons du plasma. En général, une transition E-H a lieu au démarrage du plasma avec l'augmentation de la puissance injectée [62]. Dans les conditions de Ichiki *et al.*[68] présentées à la Figure 1.18**Error! Reference source not found.**, le plasma ICP (acronyme anglais pour *Inductively Coupled Plasma*) est à nouveau combiné avec une polarisation RF du substrat pour profiter des effets du bombardement ionique.

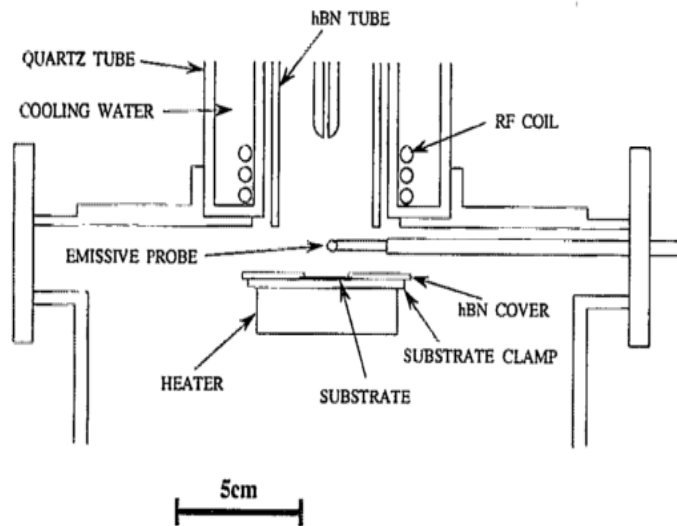


Figure 1.18: Réacteur ICP utilisé par Ichiki et al [68] pour le dépôt de couches de BN.

## 2.2.Diagnostics des plasmas à base de bore

Dans la section précédente, nous avons présenté les différentes approches pour l'incorporation du bore dans les plasmas à pression réduite. Pour les méthodes reposant sur la fragmentation d'un précurseur, nous avons classifié les réacteurs à plasma en deux catégories : basse et haute densité. À l'évidence, les cinétiques de fragmentation des précurseurs diffèrent selon le type de plasma de sorte qu'il est pertinent de s'intéresser à leurs études fondamentales pour mieux comprendre leurs propriétés physico-chimiques et ainsi mieux cibler leurs avantages et inconvénients selon l'application envisagée. Cependant, la physique des plasmas à base de bore demeure épars et peu conséquente. Ainsi, la majorité des travaux se limitent à un seul diagnostic des particules et des rayonnements sur une gamme restreinte de conditions opératoires de sorte qu'il est difficile d'obtenir un portrait complet de l'ensemble des

phénomènes physiques et chimiques mis en jeu. Dans ce contexte, nous devons restreindre notre revue de l'état de l'art à un survol des méthodes de diagnostics utilisées pour la caractérisation des plasmas à base de bore.

### 2.2.1. Spectroscopie d'émission optique

Comme son nom l'indique, la spectroscopie d'émission optique (OES pour *Optical Emission Spectroscopy*) est basée sur l'analyse de la lumière émise par les espèces présentes dans le plasma [70] [71]. En étudiant l'intensité émise par le plasma en fonction de la longueur d'onde, il devient alors possible d'étudier les populations de ces différentes espèces. À titre d'exemple, la Figure 1.19 présente des mesures OES dans un plasma produit par ablation laser d'une cible de BN. La Figure 1.19a compare des mesures avec et sans atmosphère d'azote lorsque la plume est proche de la cible de BN (région 1) tandis que la Figure 1.19b illustre des mesures enregistrées lorsque la plume atteint le substrat (région 2). De ces travaux, on peut identifier l'émission à 582.1 nm du bore atomique excité, à 345.1 nm du bore ionisé une fois et à 448.7 nm du bore ionisé deux fois. Des raies provenant d'atomes neutres et ionisés d'azote sont également observées. On remarque que dans la région 1, les intensités des raies de l'azote sont similaires avec et sans atmosphère d'azote, ce qui indique que toutes ces espèces proviennent essentiellement de la cible. Une autre observation est que la raie provenant du bore ionique est plus intense que la raie du bore neutre. L'énergie d'ionisation du bore étant de 8.3 eV, ceci va limiter la densité du bore neutre dans la plupart des plasmas. Cependant, l'énergie d'ionisation double du bore est de 25.2 eV, ce qui explique la raie peu intense observée émise pour le  $B^{2+}$ . De plus, la bande  $A^3\Pi \rightarrow X^3\Pi$  de la molécule de BN n'est pas observée entre 340 et 400 nm ; ceci indique que la couche de BN se forme principalement à la surface du substrat et non dans la phase gazeuse.

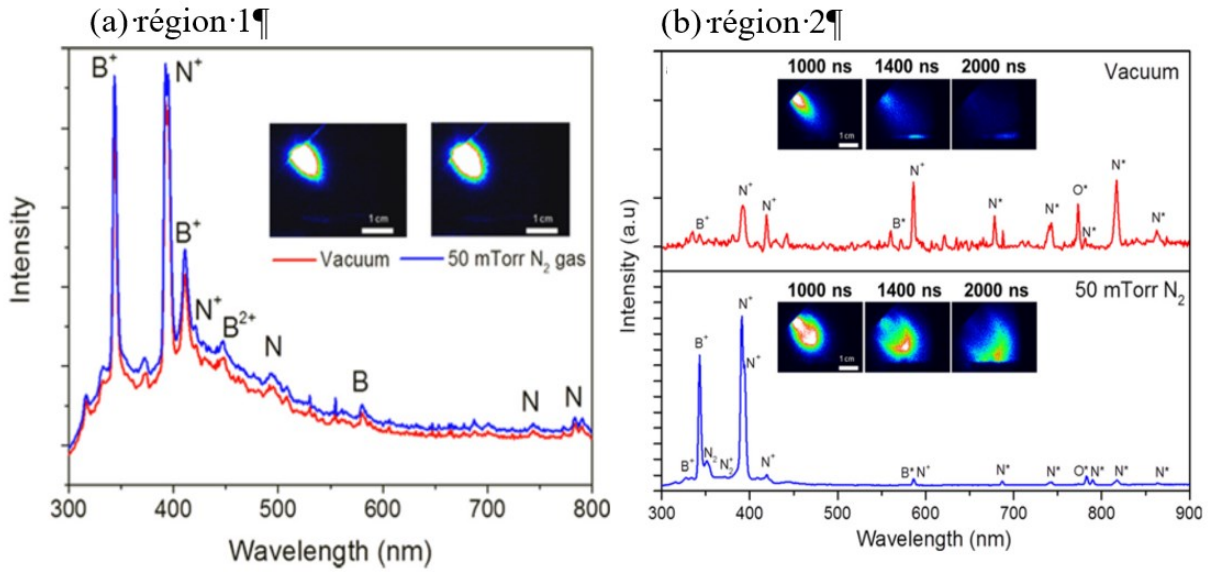


Figure 1.19 : Spectres OES de la plume (a) proche de la cible et (b) après expansion avec et sans atmosphère de diazote [57].

Dans le cas de l'injection de précurseurs dans des réacteurs de haute densité, on observe souvent, en plus des émissions du bore et de l'hydrogène atomiques, des bandes d'émission associées aux structures rovibrationnelles des précurseurs et des fragments des précurseurs [72][73]. Par exemple, la Figure 1.20 présente des mesures OES des plasmas ECR d' $H_2$  avec des traces de  $CH_4$  et de  $B_2H_6$  utilisés pour le dépôt de couches de diamant dopé au bore [74]. Dans ce type de plasmas, un problème très rapidement observé est la superposition de certaines bandes liées au BH et au CH. On note également la présence du système C<sub>2</sub>-Swan ; ceci signifie que les précurseurs sont fortement dissociés dans le plasma de haute densité de sorte que des réactions de recombinaison en phase gazeuse ou en surface peuvent avoir lieu.

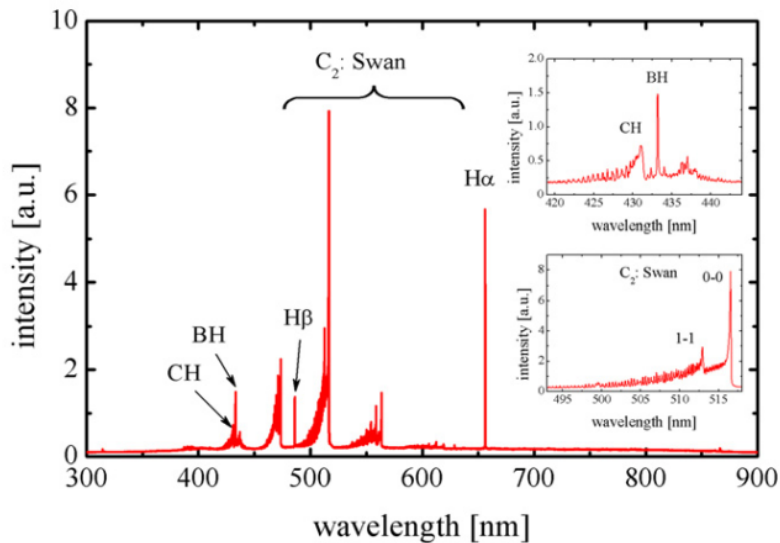


Figure 1.20 : Spectre d’OES d’un plasma d’H<sub>2</sub> avec 66 ppm de B<sub>2</sub>H<sub>6</sub> et 1% de CH<sub>4</sub> [74].

La Figure 1.21 présente l’évolution temporelle des raies de BH et de H<sub>β</sub> [75] dans un plasma ECR de B<sub>2</sub>H<sub>6</sub>/Ar/H<sub>2</sub>. En absence de diborane dans le plasma Ar/H<sub>2</sub>, seule l’émission du H<sub>β</sub> est présente, l’émission du BH étant évidemment nulle. Après injection du B<sub>2</sub>H<sub>6</sub>, on note qu’il faut attendre environ 15 min pour observer la raie du BH. De plus, il faut encore attendre une dizaine de minutes avant que le signal du BH devienne constant. Si le même plasma est produit par la suite, le temps nécessaire pour obtenir un signal stable devient beaucoup plus court. Selon les auteurs, ceci peut s’expliquer par un dépôt se formant sur les parois du réacteur et par l’obtention d’un équilibre entre les pertes et les gains de BH. Ceci est particulièrement important à considérer pour éviter les phénomènes de dérive dans les procédés qui peuvent nuire à la reproductibilité des expériences. De ces résultats, on conclut qu’il est primordial de conditionner le réacteur pendant au moins 20 min avant de réaliser des études fondamentales des propriétés physico-chimiques du plasma ou encore des traitements de surface finement contrôlés.

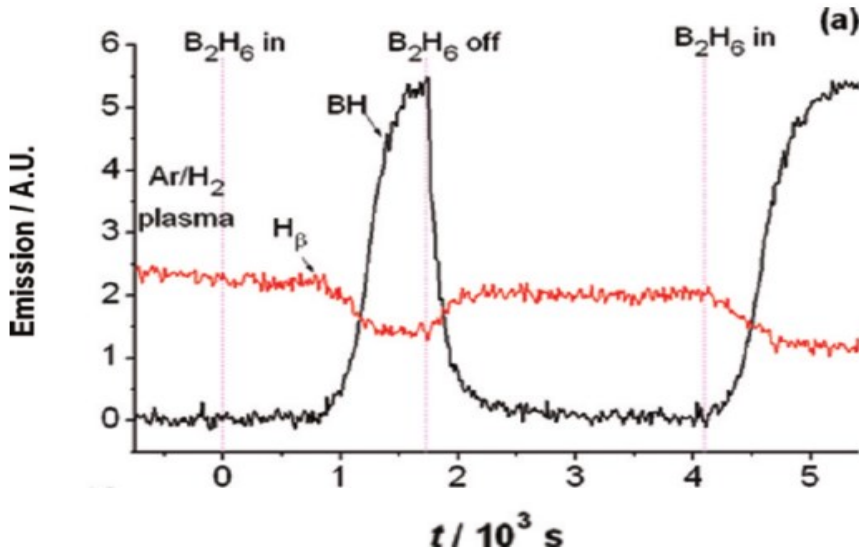


Figure 1.21: Évolution temporelle de la raie de BH et de H<sub>β</sub> lors de l'allumage d'un plasma MW B<sub>2</sub>H<sub>6</sub>/Ar/H<sub>2</sub> [75].

L'un des paramètres cruciaux dans l'étude des plasmas à base de bore est la densité du bore atomique. En effet, c'est principalement cette espèce qui risque de gouverner la dynamique d'incorporation de bore dans les processus de dépôt ou encore de dopage. Même si l'accès à cette population n'est pas aisé, une méthode a récemment été proposée pour obtenir la densité de bore atomique par OES [76]. Celle-ci repose sur l'auto-absorption des raies émises par le bore atomique excité  $3^2S_{1/2}$  (notation du couplage LS). Ce niveau émetteur est en fait un résonant dont la lumière émise peut être auto-absorbée par les atomes dans le niveau fondamental. Or, le bore neutre est un multiplet et, comme présenté sur la Figure 1.22a et b, le bore excité peut se désexciter par l'émission de deux photons à des longueurs d'ondes différentes mais très proches. La Figure 1.22a compare l'émission normalisée du doublet résonant du bore en provenance d'un plasma lorsque le diborane est présent seulement sous forme de trace et à plus haute concentration. Dans le cas de la décharge formée majoritairement d'argon, l'auto-absorption peut être négligée. Ceci n'est vraisemblablement pas le cas dans les plasmas H<sub>2</sub>-Ar-B<sub>2</sub>H<sub>6</sub> (64:33:3) dans lesquels la densité de diborane et donc de bore atomique devient plus importante.

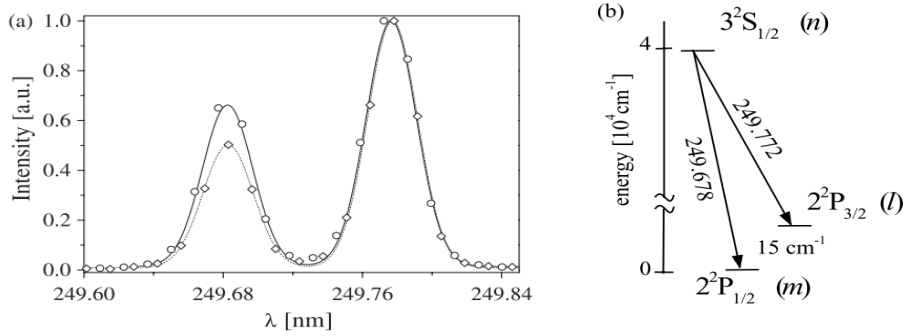


Figure 1.22 : (a) Spectres OES aux longueurs d’ondes au doublet du bore dans un plasma d’argon avec des traces de diborane ( $\diamond$ ) et un plasma  $\text{H}_2\text{-Ar-B}_2\text{H}_6$  (64:33:3) et (b) schéma représentant la désexcitation du bore excité sur les deux niveaux fondamentaux [76].

En connaissant la longueur d’absorption du plasma et la température des neutres impliqués dans l’auto-absorption, Lavrov et al. [76] ont proposé une expression entre le rapport des intensités des raies du doublet résonant et la densité d’atomes de bore dans son niveau fondamental. Les résultats sont présentés à la Figure 1.23a. De ces travaux, ils ont pu analyser l’évolution de la densité de bore atomique en fonction du pourcentage de diborane présent dans le plasma Ar-H<sub>2</sub>. Les résultats sont présentés à la Figure 1.23b.

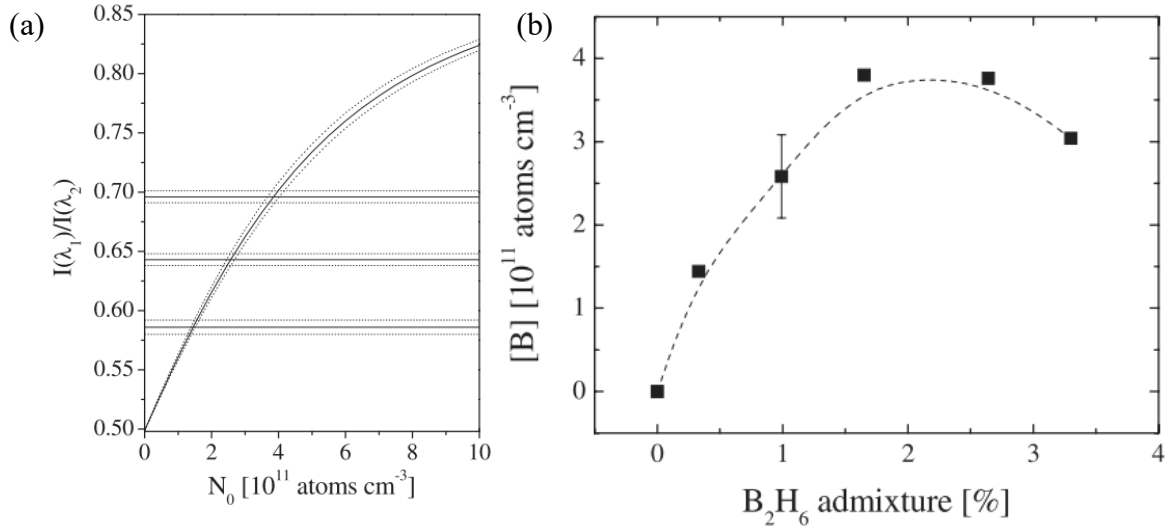


Figure 1.23 (a) Variation du rapport des raies du doublet du Bore avec sa densité absolue. Les lignes représentent des valeurs de rapport obtenues pour différentes conditions.(b) Évolution de la densité atomique de bore dans un plasma d’H<sub>2</sub> en fonction de la concentration de diborane injectée dans le réacteur [76].

Dans l'ensemble, on note que malgré les forts degrés de fragmentation du  $\text{B}_2\text{H}_6$  dans les plasmas de haute densité, la population d'atomes de bore demeure très faible par rapport aux autres espèces du plasma. Ceci peut s'expliquer par plusieurs facteurs. Premièrement, comme observé en PLD, le bore possède un potentiel d'ionisation faible (8.3 eV) de sorte qu'une bonne partie du bore peut s'ioniser. Deuxièmement, l'atome de bore est très réactif et interagit rapidement avec les diverses surfaces (dont les parois du réacteur) pour créer un dépôt mais aussi avec les autres espèces de la phase gazeuse pour former d'autres produits, par exemple du BH. De plus, cette méthode ne permet que de détecter des valeurs de densité autour de  $10^{11} \text{ cm}^{-3}$ , ce qui limite ses applications dans des conditions opératoires plus variées.

### 2.2.2. Spectroscopie d'absorption optique

La spectroscopie d'absorption optique (OAS pour *optical absorption spectroscopy*) est basée sur l'absorption d'un faisceau lumineux traversant le plasma et détecté à sa sortie. Selon la longueur d'onde absorbée, il est alors possible de remonter à la nature des molécules ou des atomes présents dans le plasma. À titre d'exemple, la Figure 1.24 présente quelques exemples de spectres d'absorption obtenus avec une diode laser à longueur d'onde variable [77]. Les mesures ont été enregistrées dans des plasmas ECR dans  $\text{B}_2\text{H}_6/\text{H}_2/\text{CH}_4$  destinés au dépôt de diamant dopé au bore [74]

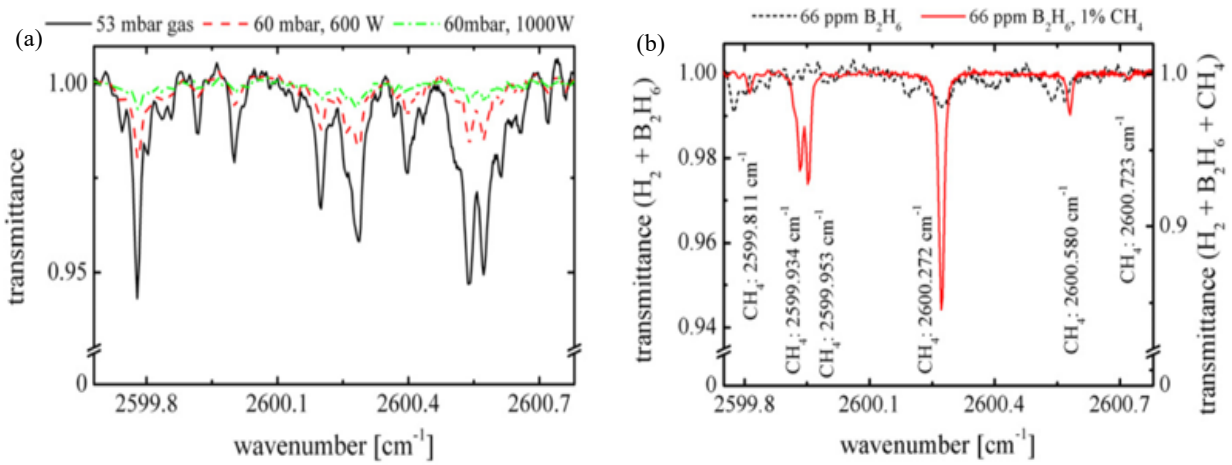


Figure 1.24 : (a) Spectre d'absorption avec en noir, 30 ppm de  $\text{B}_2\text{H}_6$  dans  $\text{H}_2$  à 53 mbarr sans plasma, en rouge, le plasma et vert le plasma allumé à 60 mbarr à 600W et 1000W. (b) Spectre d'absorption en pointillé d'un plasma  $\text{B}_2\text{H}_6/\text{H}_2$  et en rouge, d'un plasma  $\text{B}_2\text{H}_6/\text{H}_2/\text{CH}_4$ .

Sur la figure 1.24a, on observe aisément les bandes d'absorption du diborane sur la courbe noire représentant la transmission dans le cas d'un gaz composé de 30 ppm de  $B_2H_6$  dilué dans du  $H_2$  à 45 Torr. Lorsque le plasma s'allume, ces bandes deviennent moins présentes, ce qui témoigne de la forte fragmentation du précurseur par les espèces énergétiques du plasma. Cet impact devient encore plus marqué lorsque la puissance augmente de 600 à 1000W, c'est-à-dire avec l'augmentation de la densité de particules chargées du plasma. Comme pour l'OES, la Figure 1.24b montre que l'ajout de  $CH_4$  dans le plasma  $B_2H_6/H_2$  mène à une superposition des bandes d'absorption du diborane et des hydrocarbures. Les mesures deviennent alors plus difficiles à interpréter.

La spectroscopie à cavité optique est une variante de la spectroscopie d'absorption par laser mais avec une sensibilité beaucoup plus élevée [78]. Cette technique est basée sur le confinement entre deux miroirs d'une impulsion laser sensible aux transitions aux espèces recherchées. La lumière va alors parcourir l'espace entre les deux miroirs de nombreuses fois de sorte que son intensité va diminuer exponentiellement due aux pertes par absorption. Ainsi, même si l'espèce est présente sous forme de trace, son influence sur l'impulsion laser, bien que minime, peut être observée. Cette technique a notamment été utilisée sur un plasma ECR dans un mélange  $Ar-H_2-B_2H_6$  [75] pour obtenir les densités de bore présentées sur la Figure 1.25. On observe qu'avec une augmentation du débit de  $B_2H_6$  et de la pression totale, la densité de bore et de BH croît de manière, sauf à faibles débits. Les auteurs avancent que les impuretés d'airs peuvent altérer la production de ces éléments lorsque le débit de  $B_2H_6$  est faible. Ce comportement est en accord avec les mesures de *Hamann et al*[74] dans les plasmas de  $B_2H_6$  en présence de  $CH_4$ .

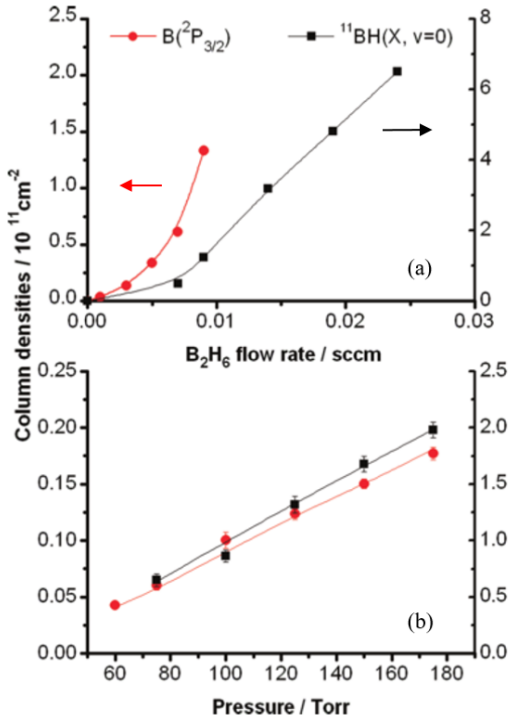


Figure 1.25 : Densité de B et de BH dans un plasma  $\text{B}_2\text{H}_6/\text{Ar}/\text{H}_2$  en fonction de (a) flux de  $\text{B}_2\text{H}_6$ , (b) de la pression avec un flux de 0.003 sccm [74].

### 2.2.3. Spectrométrie de Masse

Un spectromètre de masse (MS pour *mass spectrometer*) est un outil fonctionnant à basse pression ( $<10^{-6}$  Torr) qui extrait, ionise et sépare les espèces par l’application d’une combinaison de champs électrique et/ou magnétique [79]. Il existe de nombreux types de spectromètres de masse mais tous donnent la quantité d’éléments détectés en fonction du rapport de masse sur charge ( $m/z$ ). Il est alors possible de mesurer en temps réel l’évolution des différentes espèces, ce qui en fait une technique de choix pour l’analyse de la composition chimique de plasmas réactifs à basse pression. Il n’existe cependant pas beaucoup d’études extensives de plasmas contenant du bore par spectrométrie de masse. Une seule étude a été réalisée pour caractériser l’atmosphère d’une chambre lors de dépôts CVD sans plasma [80]. Ceux-ci étaient réalisés dans des mélanges  $\text{H}_2/\text{B}_2\text{H}_6$ . Le chauffage du substrat à haute température provoque ainsi la formation de nouvelles molécules, parfois volatiles, pouvant être détectées par MS. A titre d’exemple, la

Figure 1.26 présente un spectre de masse du mélange  $H_2/B_2H_6$  où le diborane et ses composés sont facilement identifiables à 26 amu ( $B_2H_6$ ) et à 13 amu ( $BH_3$ ).

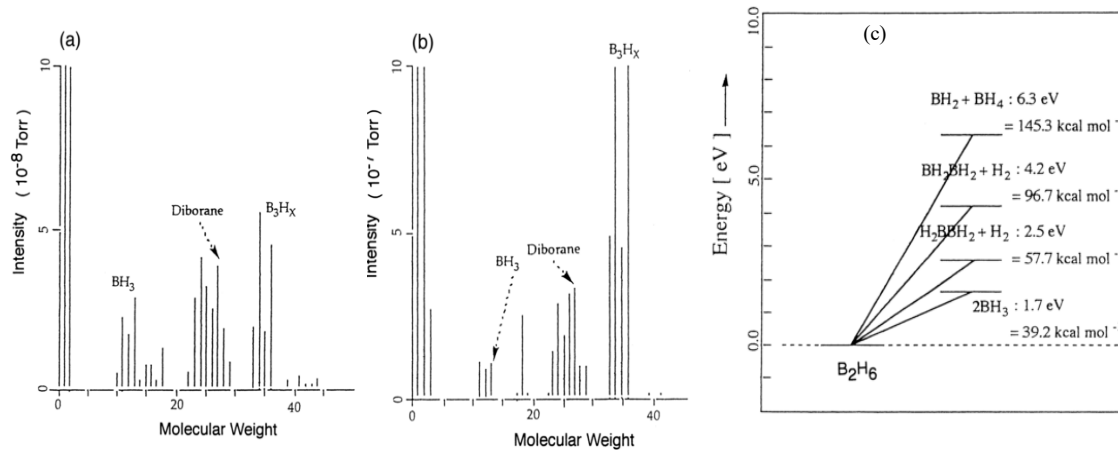


Figure 1.26 : Spectre de masse dans une atmosphère de  $B_2H_6/H_2$  avec un substrat chauffé à (a) 400°C et (b) 800°C. (c) Diagramme d'énergie des décompositions primaires du diborane [80].

Des composés plus lourds sont aussi observés, ceux-ci sont produits par des réactions ayant lieu sur le substrat chauffé. On remarque également que ces espèces sont en quantités plus importantes lorsque la température du substrat augmente de 400 à 800°C, ce qui correspond aussi à l'apparition d'un film de BN sur le substrat. Enfin, le diagramme exposé sur la Figure 1.26c présente l'énergie nécessaire pour dissocier la molécule de  $B_2H_6$ . Ainsi, dans les plasmas à pression réduite caractérisés par des températures électroniques de quelques eV, la dissociation du diborane en deux molécules de  $BH_3$  se fait facilement puisqu'uniquelement 1.7 eV est nécessaire. Les autres réactions seraient également possibles grâce à la queue énergétique de la distribution en énergie des électrons. Des mesures par MS d'un plasma contenant du bore ont été réalisées dans le cadre d'une étude sur l'immersion plasma [81]. La Figure 1.27 présente un exemple de telles mesures dans une décharge luminescente pulsée d'hélium et de  $B_2H_6$ .

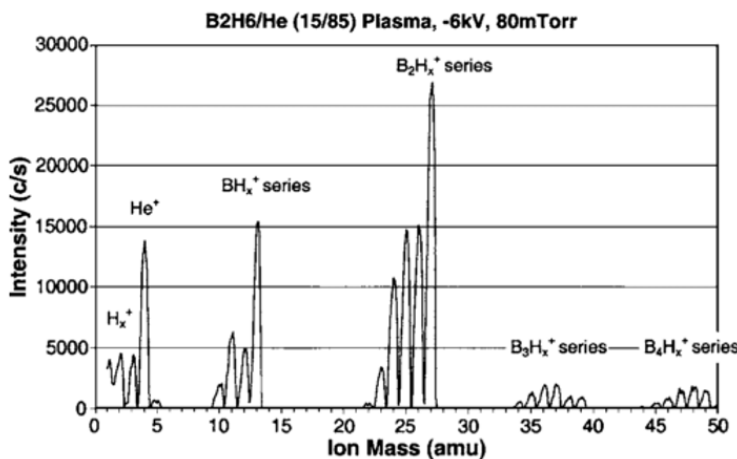


Figure 1.27 : Spectre de masse d'un plasma B<sub>2</sub>H<sub>6</sub>/He (15/85) pulsé à -6 kV [81].

Dans ce cas, on voit que les ions du type B<sub>2</sub>H<sub>x</sub> sont majoritaires et que contrairement à ce qui était observé sur la Figure 1.27a et b, les molécules du types B<sub>3</sub>H<sub>x</sub> sont peu présentes. Cependant, les études par MS demeurent peu répandues de sorte qu'il est difficile de conclure sur la cinétique réactionnelle complète de ces plasmas réactifs. En lien avec les objectifs de cette thèse de doctorat, nous comptons effectuer une étude fondamentale de pointe des caractéristiques des plasmas à base de bore en ayant recours à plusieurs méthodes de diagnostics, notamment, les sondes de Langmuir, la spectroscopie optique d'émission et d'absorption, ainsi que la spectrométrie de masse pour l'analyse des espèces neutres et chargées.

### 3. Applications des plasmas de bore

Les applications des plasmas à base de bore sont principalement concentrées autour des matériaux et des nanomatériaux. Tel que mentionné précédemment, ces plasmas permettent notamment de déposer des couches minces de BN avec un contrôle fin sur leur structure et leur composition chimique (BN, BCN). À ce sujet, rappelons que le BN peut exister sous plusieurs phases, dont les plus courantes sont présentées sur la Figure 1.28 [82]. Les phases h-BN et r-BN possèdent des liaisons sp<sup>2</sup> alors que les phases w-BN et c-BN sont liées par des liaisons sp<sup>3</sup>. La c-BN est celle la plus souvent recherchée en raison de ses propriétés proches du diamant, de sa bonne conductivité thermique, de sa large bande interdite (6.3 ± 0.2 eV) et de sa transmission

élevée de la lumière de l'ultraviolet jusqu'au visible. Ses températures d'oxydation et de graphitisation sont même supérieures à celles du diamant [9][82].

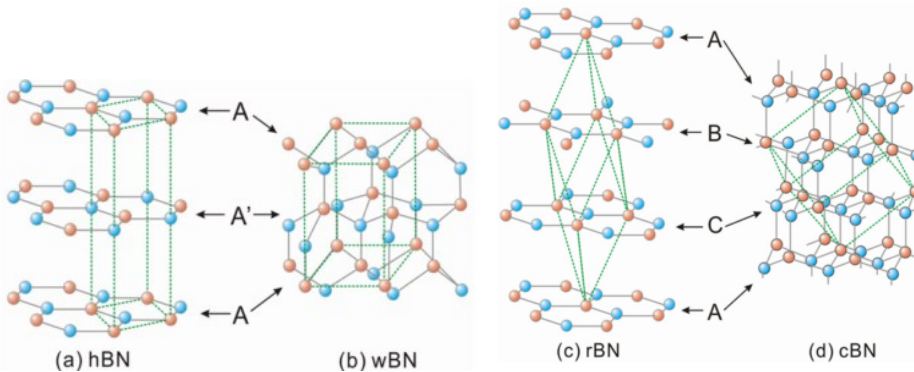


Figure 1.28 :Structure cristalline du (a) h-BN, (b) w-BN, (c) r-BN et (d) c-BN [82].

L'obtention de c-BN pur sans défaut sur des substrats communément utilisés pour les applications technologiques demeure un défi de taille. Le choix du substrat est crucial et repose sur trois critères, (1) la compatibilité en termes d'énergie de surface, (2) une largeur de maille similaire à celle du c-BN et (3) une stabilité structurelle forte pour supporter un bombardement ionique [82]. En consultant la littérature scientifique correspondante, on note que les plasmas utilisés pour le dépôt de couches minces de BN peuvent être produits de diverses manières, RF [83–85], ECR[65,86], ICP [68,69,87] et PLD [88,89]. La grande quantité d'articles centrés sur le dépôt de c-BN montre tout l'intérêt que ce matériau suscite au niveau mondial.

Le dopage des matériaux et des nanomatériaux avec du bore constitue une autre des applications des plasmas à base de bore. Il est possible d'introduire les atomes de bore durant la croissance du matériau par CVD, PECVD ou PLD, ou encore après sa croissance dans des plasmas produits en présence de précurseurs à base de bore. Une revue exhaustive de la littérature révèle que la première est surtout utilisée pour la croissance de diamant dopé au bore tandis que la seconde vise principalement le dopage du silicium et éventuellement du graphène.

La synthèse du diamant à basse pression permet d'envisager son intégration dans de nombreuses applications. En effet, les couches minces de diamant possèdent des propriétés intéressantes telles qu'une grande dureté, une conductivité thermique élevée, une inertie chimique et une large bande interdite. De telles performances sont dues à la structure cristalline

du diamant, les atomes de carbones étant liés entre eux par des liaisons covalentes  $sp^3$ . Le dopage au bore permet de contrôler la valeur de la bande interdite et ouvre alors la voie à des applications électrochimiques [60]. La croissance de ces couches peut se faire dans plusieurs types de réacteurs CVD et PECVD, mais les plus répandus sont les DC, RF et ECR. À titre d'illustration, les auteurs de la référence [60] ont eu recours à des plasmas DC à base de  $H_2/CH_4/B(OCH_3)_3$  afin d'étudier l'influence de la population de bore sur les propriétés physiques et chimiques des dépôts. Sur la Figure 1.29, on peut voir des images obtenues par microscopie électronique à balayage (SEM pour *Scanning Electron Microscopy*) couplées avec des mesures par spectroscopie Raman.

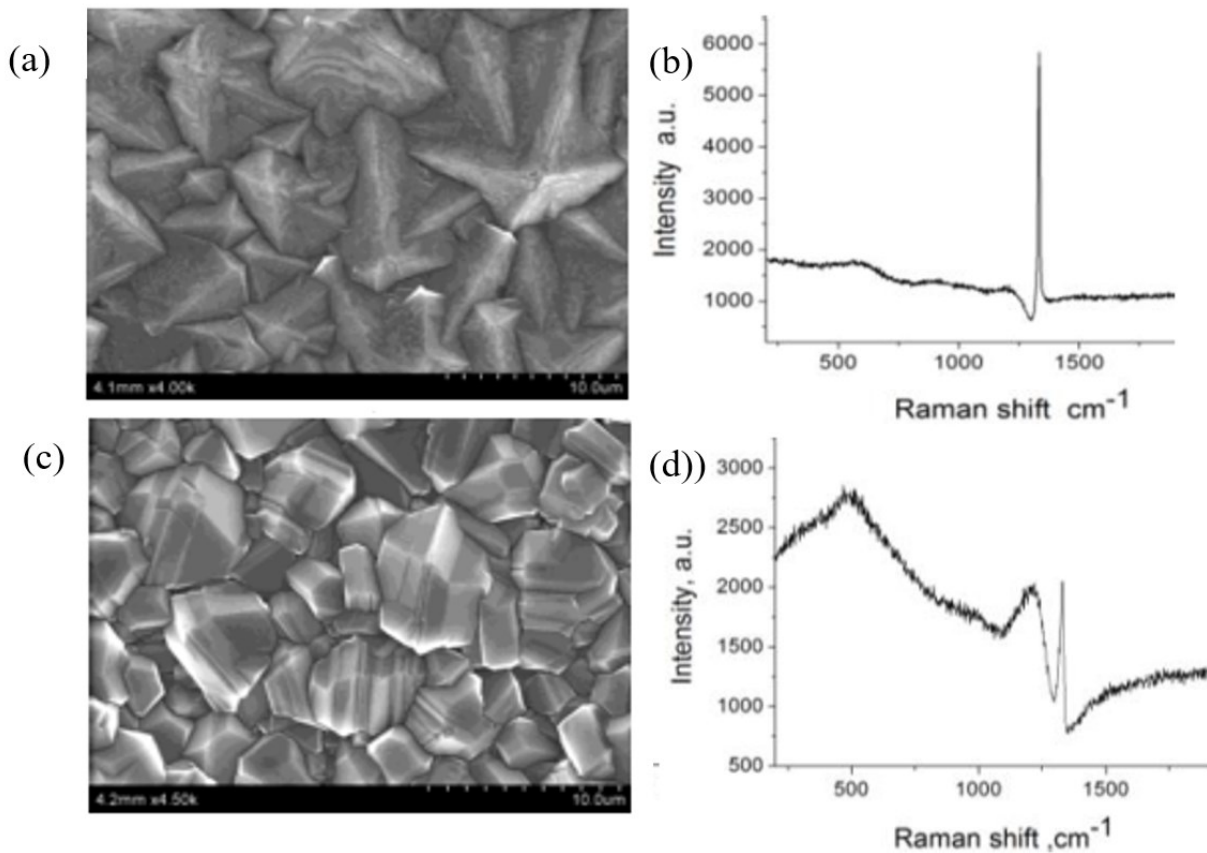


Figure 1.29 : Images SEM et spectres Raman correspondant de couches de BN déposées avec (a-b) 1 sccm et (c-d) 20 sccm de  $B(OCH_3)_3$  injecté dans un plasma DC  $CH_4/H_2$  [60].

Les images SEM montre un changement important de la morphologie du dépôt avec une augmentation de la texture (110) du diamant lorsque la concentration relative du précurseur à base de bore augmente. De plus, des macles peuvent être observées au sein de certains grains, ce qui met en évidence des phénomènes de stress. Comme ces défauts ne sont pas observés lors de dépôts classiques, les auteurs supposent que les atomes de bore provoquent ces dislocations lorsqu'une trop grosse quantité est présente dans la maille. En effet, on peut voir sur les Figures 1.29b et d, l'impact du bore sur la réponse Raman des échantillons. De ces spectres, les auteurs ont pu déterminer une concentration du bore à faible flux de  $B(OCH_3)_3$  de  $1.8 \times 10^{19} \text{ cm}^{-3}$ . À plus fort flux de précurseur dans le plasma, ils notent que la densité de bore augmente à  $1.5 \times 10^{21} \text{ cm}^{-3}$ . Ceci est en accord avec l'observation de macle sur la Figure 1.29c due à une densité trop élevée de bore. Ces résultats ont pu être confirmées sur une vaste gamme de conditions opératoires et une densité critique de bore de  $10^{20} \text{ cm}^{-3}$  au-delà de laquelle le stress cause des dislocations a pu être déterminée.

Le dopage au bore peut également s'effectuer en exposant l'objet à traiter à un plasma à base de bore après sa croissance par CVD, PECVD, ou PLD. Par exemple, en appliquant une polarisation pulsée sur le substrat à traiter, on peut accélérer des ions vers l'échantillon de telle sorte que leur pénétration dans la matière dépend de l'énergie moyenne des ions incidents. Cette méthode est communément nommée « implantation par immersion plasma ». Pour illustrer ce phénomène, les auteurs de la référence [81] ont eu recours à une décharge DC pulsée avec du diborane dilué dans de l'hélium. Dans ce système, les ions peuvent être accélérés de manière périodique jusqu'à 6 keV sur un substrat de silicium. Lors des pulses, de l'implantation, du dépôt et de la gravure peuvent avoir lieu simultanément. Le dépôt résulte de la formation d'espèces non volatiles comme  $B_2H_5$ ,  $BH_3$ , etc. Quant à la gravure, elle est principalement due aux atomes d'hydrogène et de bore qui peuvent réagir avec le silicium ou le dépôt pour produire du  $SiH_4$  ou du  $B_2H_6$ . La formation de ce dépôt est mise en évidence sur les Figures 1.30a et b où sont exposées les concentrations atomiques des espèces dans la couche avant (a) et après (b) un procédé de nettoyage de la surface de l'échantillon.

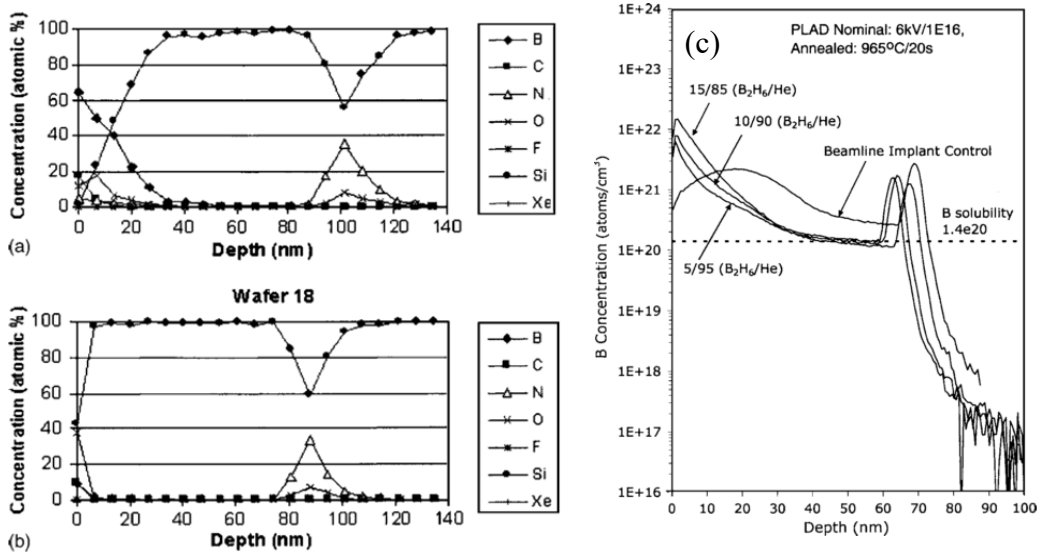


Figure 1.30 : Mesures XPS d'échantillons traités par un plasma B<sub>2</sub>H<sub>6</sub>/He (15/85) à 6 kV (a) après traitement (b) après nettoyage de la surface et recuit. (c) Profils SIMS des échantillons implantés au bore pour différentes dilutions dans l'hélium [81].

Après nettoyage, le dépôt disparait effectivement, la détection de N trahissant la présence de la couche repère de Si<sub>3</sub>N<sub>4</sub>. La Figure 1.30c présente l'évolution de la concentration de bore atomique pour différentes dilutions après nettoyage et recuit à 950°C. Les auteurs observent que la dilution n'a pas d'impact significatif sur la concentration de bore implanté et que celle-ci est similaire lors de l'utilisation d'un faisceau d'ions de bore classique. Une dilution plus élevée permet cependant de limiter le dépôt observé initialement, ce qui est évidemment privilégié.

Finalement, une seule étude à notre connaissance traite du dopage post-synthèse du graphène dans des plasmas à base de bore [90]. Dans ce cas, un plasma ECR est utilisé pour produire un plasma composé de trimethylborane et de dihydrogène. Dans ce cas, une approche XPS a été utilisée pour obtenir la quantité de bore atomique incorporée dans ou à la surface du graphène. À ce sujet, la Figure 1.31 montre l'évolution du pourcentage atomique du bore en fonction du temps de traitement. Un pourcentage atomique de bore très important est rapidement obtenu. De plus, il est précisé par les auteurs que la conductivité du graphène diminue avec le temps de traitement. Toujours selon les auteurs, ce phénomène est provoqué par des dommages importants dans la structure du graphène induite par le dopage au bore.

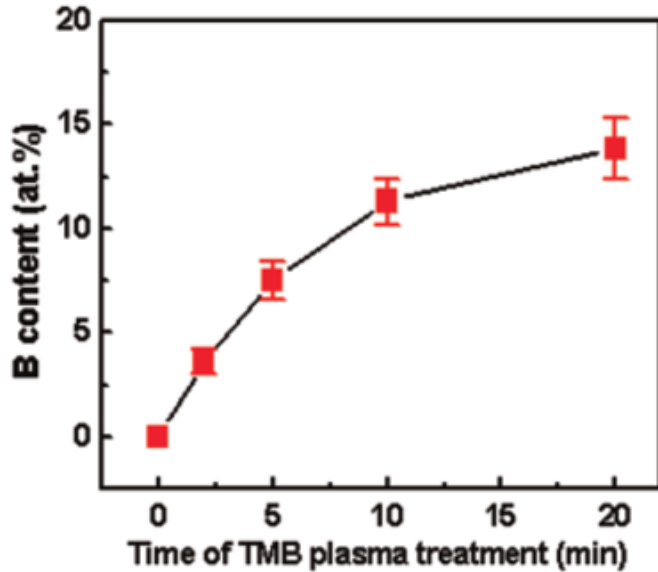


Figure 1.31 : Évolution de la quantité de bore atomique en fonction du temps d'exposition au plasma mesuré par XPS [66]

En lien avec les résultats présentés dans la référence [66], il semble clair que les plasmas à base de bore constituent une approche intéressante pour la modification post-synthèse du graphène. Cependant, très peu d'informations sont fournies sur la nature des défauts ainsi que sur leur dynamique de formation. Aucune analyse Raman n'est présentée pour renforcer les résultats et les conclusions. De plus, il n'est pas clair si les atomes de bore sont incorporés dans le plan du graphène par dopage substitutionnel, attachés de manière covalente ou non-covalente en surface, ou encore simplement liés à des contaminants de surface tel qu'observé récemment dans le cas des traitements du graphène dans des plasmas d'azote [91]. Ainsi, en lien avec les objectifs de cette thèse de doctorat, tout porte à croire que dans des conditions contrôlées d'un plasma à base de bore dont les caractéristiques physiques et chimiques sont connues, il devrait être possible de contrôler le niveau de dommage et de dopage du graphène dans ce type de plasmas selon l'application envisagée.

## Références

- [1] Cooper DR, D'Anjou B, Ghattamaneni N, Harack B, Hilke M, Horth A, et al. Experimental Review of Graphene. *ISRN Condens Matter Phys* 2012;2012:1–56. doi:10.5402/2012/501686.
- [2] Yang G, Li L, Lee WB, Ng MC. Structure of graphene and its disorders: a review. *Sci Technol Adv Mater* 2018;19:613–48. doi:10.1080/14686996.2018.1494493.
- [3] Novoselov KS, Geim AK, Morozov S V., Jiang D, Katsnelson MI, Grigorieva I V., et al. Two-dimensional gas of massless Dirac fermions in graphene. *Nature* 2005;438:197–200. doi:10.1038/nature04233.
- [4] Novoselov KS, Geim A K, Morozov S V, Jiang D, Zhang Y, Dubonos S V, et al. Electric field effect in atomically thin carbon films. *Science* 2004;306:666–9. doi:10.1126/science.1102896.
- [5] Graphene S, Balandin AA, Ghosh S, Bao W, Calizo I, Teweldebrhan D, et al. Superior Thermal Conductivity of Single-Layer Graphene. *Nano Lett* 2008;8:902–7.
- [6] Chen J-H, Jang C, Xiao S, Ishigami M, Fuhrer MS. Intrinsic and extrinsic performance limits of graphene devices on SiO<sub>2</sub>. *Nat Nanotechnol* 2008;3:206–9. doi:10.1038/nnano.2008.58.
- [7] Ferrari AC, Basko DM. Raman spectroscopy as a versatile tool for studying the properties of graphene. *Nat Publ Gr* 2013;8:235–46. doi:10.1038/nnano.2013.46.
- [8] Heller EJ, Yang Y, Kocia L, Chen W, Fang S, Borunda M, et al. Theory of Graphene Raman Scattering. *ACS Nano* 2016;10:2803–18. doi:10.1021/acsnano.5b07676.
- [9] Malard LM, Pimenta MA, Dresselhaus G, Dresselhaus MS. Raman spectroscopy in graphene. *Phys Rep* 2009;473:51–87. doi:10.1016/j.physrep.2009.02.003.
- [10] Jia K, Su Y, Chen Y, Luo J, Yang J, Lv P, et al. Effects of defects and thermal treatment on the properties of graphene. *Vacuum* 2015;116:90–5. doi:10.1016/j.vacuum.2015.03.003.
- [11] Banhart F, Kotakoski J, Krasheninnikov A V. Structural Defects in Graphene. *ACS Nano* 2011;5:26–41. doi:10.1021/nn102598m.
- [12] Banhart F, Kotakoski J, Krasheninnikov A V. Structural defects in graphene. *ACS Nano* 2011;5:26–41. doi:10.1021/nn102598m.
- [13] Krasheninnikov A V., Lehtinen PO, Foster AS, Nieminen RM. Bending the rules: Contrasting vacancy energetics and migration in graphite and carbon nanotubes. *Chem Phys Lett* 2006;418:132–6. doi:10.1016/j.cplett.2005.10.106.
- [14] El-Barbary A, Telling H, Ewels P, Heggie I, Briddon R. Structure and energetics of the vacancy in graphite. *Phys Rev B - Condens Matter Mater Phys* 2003;68:1–7.

doi:10.1103/PhysRevB.68.144107.

- [15] Lahiri J, Lin Y, Bozkurt P, Oleynik II, Batzill M. An extended defect in graphene as a metallic wire. *Nat Nanotechnol* 2010;5:326–9. doi:10.1038/nnano.2010.53.
- [16] Koskinen P, Malola S, Häkkinen H. Self-passivating edge reconstructions of graphene. *Phys Rev Lett* 2008;101:1–4. doi:10.1103/PhysRevLett.101.115502.
- [17] Koskinen P, Malola S, Häkkinen H. Evidence for graphene edges beyond zigzag and armchair. *Phys Rev B - Condens Matter Mater Phys* 2009;80:16–8. doi:10.1103/PhysRevB.80.073401.
- [18] Tsetseris L, Pantelides ST. Adatom complexes and self-healing mechanisms on graphene and single-wall carbon nanotubes. *Carbon N Y* 2009;47:901–8. doi:10.1016/j.carbon.2008.12.002.
- [19] Novoselov KS, Geim AK, Morozov S V., Jiang D, Zhang Y, Dubonos S V., et al. Electric Field Effect in Atomically Thin Carbon Films. *Science (80- )* 2004;306:666–9. doi:10.1126/science.1102896.
- [20] Singh V, Joung D, Zhai L, Das S, Khondaker SI, Seal S. Graphene based materials: Past, present and future. *Prog Mater Sci* 2011;56:1178–271. doi:10.1016/j.pmatsci.2011.03.003.
- [21] Choi W, Lahiri I, Seelaboyina R, Kang YS. Synthesis of graphene and its applications: A review. *Crit Rev Solid State Mater Sci* 2010;35:52–71. doi:10.1080/10408430903505036.
- [22] Somani PR, Somani SP, Umeno M. Planer nano-graphenes from camphor by CVD. *Chem Phys Lett* 2006;430:56–9. doi:10.1016/j.cplett.2006.06.081.
- [23] Zhang Y, Zhang L, Zhou C. Review of chemical vapor deposition of graphene and related applications. *Acc Chem Res* 2013;46:2329–39. doi:10.1021/ar300203n.
- [24] Li X, Cai W, An J, Kim S, Nah J, Yang D, et al. Large-Area Synthesis of High-Quality and Uniform Graphene Films on Copper Foils. *Science (80- )* 2009;324:1312–4. doi:10.1126/science.1171245.
- [25] Barin GB, Song Y, Gimenez IDF, Filho AGS, Barreto LS, Kong J. Optimized graphene transfer: Influence of polymethylmethacrylate (PMMA) layer concentration and baking time on grapheme final performance. *Carbon N Y* 2015;84:82–90. doi:10.1016/j.carbon.2014.11.040.
- [26] Her M, Beams R, Novotny L. Graphene transfer with reduced residue. *Phys Lett Sect A Gen At Solid State Phys* 2013;377:1455–8. doi:10.1016/j.physleta.2013.04.015.
- [27] Georgakilas V, Tiwari JN, Kemp KC, Perman JA, Bourlinos AB, Kim KS, et al. Noncovalent Functionalization of Graphene and Graphene Oxide for Energy Materials, Biosensing, Catalytic, and Biomedical Applications. *Chem Rev* 2016;116:5464–519. doi:10.1021/acs.chemrev.5b00620.
- [28] Kosynkin D V., Higginbotham AL, Sinitskii A, Lomeda JR, Dimiev A, Price BK, et al. Longitudinal unzipping of carbon nanotubes to form graphene nanoribbons. *Nature* 2009;458:872–

6. doi:10.1038/nature07872.

- [29] Niyogi S, Bekyarova E, Itkis ME, Zhang H, Shepperd K, Hicks J, et al. Spectroscopy of covalently functionalized graphene. *Nano Lett* 2010;10:4061–6. doi:10.1021/nl1021128.
- [30] Wang D, Choi D, Li J, Yang Z, Nie Z, Kou R, et al. Self-Assembled TiO<sub>2</sub> –Graphene Hybrid Nanostructures for Enhanced Li-Ion Insertion. *ACS Nano* 2009;3:907–14. doi:10.1021/nn900150y.
- [31] Chang H, Sun Z, Ho KYF, Tao X, Yan F, Kwok WM, et al. A highly sensitive ultraviolet sensor based on a facile in situ solution-grown ZnO nanorod/graphene heterostructure. *Nanoscale* 2011;3:258–64. doi:10.1039/c0nr00588f.
- [32] Elias DC, Nair RR, Mohiuddin TMG, Morozov S V., Blake P, Halsall MP, et al. Control of Graphene’s Properties by Reversible Hydrogenation: Evidence for Graphane. *Science* (80- ) 2009;323:610–3. doi:10.1126/science.1167130.
- [33] Felten A, McManus D, Rice C, Nittler L, Pireaux JJ, Casiraghi C. Insight into hydrogenation of graphene: Effect of hydrogen plasma chemistry. *Appl Phys Lett* 2014;105. doi:10.1063/1.4901226.
- [34] Withers F, Russo S, Dubois M, Craciun MF. Tuning the electronic transport properties of graphene through functionalisation with fluorine. *Nanoscale Res Lett* 2011;6:1–11. doi:10.1186/1556-276X-6-526.
- [35] Jeon KJ, Lee Z, Pollak E, Moreschini L, Bostwick A, Park CM, et al. Fluorographene: A wide bandgap semiconductor with ultraviolet luminescence. *ACS Nano* 2011;5:1042–6. doi:10.1021/nn1025274.
- [36] Samarakoon DK, Chen Z, Nicolas C, Wang XQ. Structural and electronic properties of fluorographene. *Small* 2011;7:965–9. doi:10.1002/smll.201002058.
- [37] Robert Bigras G, Glad X, Martel R, Sarkissian A, Stafford L. Treatment of graphene films in the early and late afterglows of N<sub>2</sub> plasmas: comparison of the defect generation and N-incorporation dynamics. *Plasma Sources Sci Technol* 2018;27. doi:10.1088/1361-6595/aaedfd.
- [38] Wang Y, Shao Y, Matson DW, Li J, Lin Y. Nitrogen-Doped Graphene and Its Biosensing. *ACS Nano* 2010;4:1790–8. doi:10.1063/1.4870424.
- [39] Lin YC, Lin CY, Chiu PW. Controllable graphene N-doping with ammonia plasma. *Appl Phys Lett* 2010;96. doi:10.1063/1.3368697.
- [40] Felten A, Eckmann A, Pireaux JJ, Krupke R, Casiraghi C. Controlled modification of mono- and bilayer graphene in O<sub>2</sub>, H<sub>2</sub> and CF<sub>4</sub> plasmas. *Nanotechnology* 2013;24. doi:10.1088/0957-4484/24/35/355705.
- [41] Yang H, Chen M, Zhou H, Qiu C, Hu L, Yu F, et al. Preferential and Reversible Fluorination of Monolayer Graphene. *J Phys Chem C* 2011;115:16844–8. doi:10.1021/jp204573z.

- [42] Chen M, Zhou H, Qiu C, Yang H, Yu F, Sun L. Layer-dependent fluorination and doping of graphene via plasma treatment. *Nanotechnology* 2012;23. doi:10.1088/0957-4484/23/11/115706.
- [43] Tahara K, Iwasaki T, Matsutani A, Hatano M. Effect of radical fluorination on mono- and bi-layer graphene in Ar/F<sub>2</sub> plasma. *Appl Phys Lett* 2012;101:163105. doi:10.1063/1.4760268.
- [44] Martins Ferreira EH, Moutinho MVO, Stavale F, Lucchese MM, Capaz RB, Achete CA, et al. Evolution of the Raman spectra from single-, few-, and many-layer graphene with increasing disorder. *Phys Rev B* 2010;82:125429. doi:10.1103/PhysRevB.82.125429.
- [45] Ferrari AC, Basko DM. Raman spectroscopy as a versatile tool for studying the properties of graphene. *Nat Nanotechnol* 2013;8:235–46. doi:DOI 10.1038/nnano.2013.46.
- [46] Merlen A, Buijnsters J, Pardanaud C. A Guide to and Review of the Use of Multiwavelength Raman Spectroscopy for Characterizing Defective Aromatic Carbon Solids: from Graphene to Amorphous Carbons. vol. 7. 2017. doi:10.3390/coatings7100153.
- [47] Eckmann A, Felten A, Verzhbitskiy I, Davey R, Casiraghi C. Raman study on defective graphene: Effect of the excitation energy, type, and amount of defects. *Phys Rev B - Condens Matter Mater Phys* 2013;88:1–11. doi:10.1103/PhysRevB.88.035426.
- [48] Gustavo Cançado L, Gomes da Silva M, Martins Ferreira EH, Hof F, Kampioti K, Huang K, et al. Disentangling contributions of point and line defects in the Raman spectra of graphene-related materials. *2D Mater* 2017;4:025039. doi:10.1088/2053-1583/aa5e77.
- [49] Das A, Pisana S, Chakraborty B, Piscanec S, Saha SK, Waghmare U V., et al. Monitoring dopants by Raman scattering in an electrochemically top-gated graphene transistor. *Nat Nanotechnol* 2008;3:210–5. doi:10.1038/nnano.2008.67.
- [50] Eckmann A, Felten A, Mishchenko A, Britnell L, Krupke R, Novoselov KS, et al. Probing the nature of defects in graphene by Raman spectroscopy. *Nano Lett* 2012;12:3925–30. doi:10.1021/nl300901a.
- [51] Lee JE, Ahn G, Shim J, Lee YS, Ryu S. Optical separation of mechanical strain from charge doping in graphene. *Nat Commun* 2012;3:1024–8. doi:10.1038/ncomms2022.
- [52] Bruna M, Ott AK, Ijäs M, Yoon D, Sassi U, Ferrari AC. Doping dependence of the Raman spectrum of defected graphene. *ACS Nano* 2014;8:7432–41. doi:10.1021/nn502676g.
- [53] Eason R. Pulsed Laser Deposition of Thin Films. Hoboken, NJ, USA: John Wiley & Sons, Inc.; 2006. doi:10.1002/0470052120.
- [54] Glavin NR, Muratore C, Jespersen ML, Hu J, Hagerty PT, Hilton AM, et al. Amorphous Boron Nitride: A Universal, Ultrathin Dielectric for 2D Nanoelectronics. *Adv Funct Mater* 2016;26:2640–7. doi:10.1002/adfm.201505455.

- [55] Glavin NR, Jespersen ML, Check MH, Hu J, Hilton AM, Fisher TS, et al. Synthesis of few-layer, large area hexagonal-boron nitride by pulsed laser deposition. *Thin Solid Films* 2014;572:245–50. doi:10.1016/j.tsf.2014.07.059.
- [56] Glavin NR, Muratore C, Jespersen ML, Hu J, Fisher TS, Voevodin AA. Temporally and spatially resolved plasma spectroscopy in pulsed laser deposition of ultra-thin boron nitride films. *J Appl Phys* 2015;117:165305. doi:10.1063/1.4919068.
- [57] Ying ZF, Yu D, Ling H, Xu N, Lu YF, Sun J, et al. Synthesis of BCN thin films by nitrogen ion beam assisted pulsed laser deposition from a B4C target. *Diam Relat Mater* 2007;16:1579–85. doi:10.1016/j.diamond.2007.01.021.
- [58] Lieberman MA. Principles of Plasma Discharges and Materials Processing. vol. 53. 2005. doi:10.1017/CBO9781107415324.004.
- [59] Feng Y, Lv J, Liu J, Gao N, Peng H, Chen Y. Influence of boron concentration on growth characteristic and electro-catalytic performance of boron-doped diamond electrodes prepared by direct current plasma chemical vapor deposition. *Appl Surf Sci* 2011;257:3433–9. doi:10.1016/j.apsusc.2010.11.041.
- [60] Pan M, Peng H, Zhao W, Jiang H. Morphology and Structure Properties of Boron-doped Diamond Films Prepared by Hot Cathode Direct Current Plasma Chemical Vapor Deposition. *Mater Sci* 2016;22:205–8.
- [61] Ferreira C, Moissan M. Microwave discharges: fundamentals and applications. 1993.
- [62] Chabert P, Braithwaite N. Physics of Radio-Frequency Plasmas. Cambridge: Cambridge University Press; 2011. doi:10.1017/CBO9780511974342.
- [63] Conrads H, Schmidt M. Plasma generation and plasma sources. *Plasma Sources Sci Technol* 2000;9:441–54. doi:10.1088/0963-0252/9/4/301.
- [64] Lieberman MA, Lichtenberg AJ. Principles of Plasma Discharges and Materials Processing: Second Edition. 2005. doi:10.1002/0471724254.
- [65] Kiel F, Cotarelo M, Delplancke MP, Winand R. Comparison of the properties of BN films synthesized by inductively coupled r.f. and microwave plasmas. *Thin Solid Films* 1995;270:118–23. doi:10.1016/0040-6090(95)06909-7.
- [66] Tang YB, Yin LC, Yang Y, Bo XH, Cao YL, Wang HE, et al. Tunable band gaps and p-type transport properties of boron-doped graphenes by controllable ion doping using reactive microwave plasma. *ACS Nano* 2012;6:1970–8. doi:10.1021/nn3005262.
- [67] Xu Z, Zheng R, Khanaki A, Zuo Z, Liu J. Direct growth of graphene on in situ epitaxial hexagonal boron nitride flakes by plasma-assisted molecular beam epitaxy. *Appl Phys Lett* 2015;107.

doi:10.1063/1.4936378.

- [68] Ichiki T, Yoshida T. Growth of Cubic Boron Nitride Films by Low-Pressure Inductively Coupled Plasma Enhanced Chemical Vapor Deposition. *Jpn J Appl Phys* 1994;33:4385–8. doi:10.1143/JJAP.33.4385.
- [69] Ichiki T, Momose T, Yoshida T. Effects of the substrate bias on the formation of cubic boron nitride by inductively coupled plasma enhanced chemical vapor deposition. *J Appl Phys* 1993;75:1330–4. doi:10.1063/1.356411.
- [70] Griem HR. *Principles of Plasma Spectroscopy*. vol. 36. 2011.
- [71] Fantz U. Basics of plasma spectroscopy. *Plasma Sources Sci Technol* 2006;15:S137–47. doi:10.1088/0963-0252/15/4/S01.
- [72] Rayar M, Veis P, Foissac C, Supiot P, Gicquel A. Gas temperature determination using BH (0-0) A(1)Pi -> X-1 Sigma(+) emission spectrum in a B2H6 containing plasma for doped diamond deposition. *J Phys D-Applied Phys* 2006;39:2151–9. doi:10.1088/0022-3727/39/10/027.
- [73] Osiac M, Lavrov BP, Ropcke J. Intensity distributions in R and P branches of ( 0 – 0 ) band of the A 1 → X 1 + electronic transition of the BH molecule and determination of gas temperature in non-equilibrium plasmas. *J Quant Spectrosc Radiat Transf* 2002;74:471–91.
- [74] Hamann S, Rond C, Pipa A V, Wartel M, Lombardi G, Gicquel A, et al. Spectroscopic study of H 2 microwave plasmas with small admixtures of CH 4 and B 2 H 6 used for doped diamond deposition. *Plasma Sources Sci Technol* 2014;23:045015. doi:10.1088/0963-0252/23/4/045015.
- [75] Ma J, Richley JC, Davies DRW, Ashfold MNR, Mankelevich Y a. Spectroscopic and modeling investigations of the Gas phase chemistry and composition in microwave plasma activated B2H6/CH 4/Ar/H2 mixtures. *J Phys Chem A* 2010;114:10076–89. doi:10.1021/jp104532y.
- [76] Lavrov BP, Osiac M, Pipa A V, Ropcke J. On the spectroscopic detection of neutral species in a low-pressure plasma containing boron and hydrogen. *Plasma Sources Sci Technol* 2003;12:576–89.
- [77] Röpcke J, Lombardi G, Rousseau A, Davies PB. Application of mid-infrared tuneable diode laser absorption spectroscopy to plasma diagnostics: a review. *Plasma Sources Sci Technol* 2006;15:S148–68. doi:10.1088/0963-0252/15/4/S02.
- [78] Wheeler MD, Newman SM, Orr-Ewing AJ, Ashfold MNR. Cavity ring-down spectroscopy. *J Chem Soc Faraday Trans* 1998;94:337–51. doi:10.1039/a707686j.
- [79] Hoffmann E De, Stroobant V. *Mass Spectrometry - Principles and Applications*. vol. 29. 2007. doi:10.1002/mas.20296.
- [80] Sato K, Kanda N, Ogata T, Kumashiro Y. Structures of the main precursors and initial

decomposition products of diborane chemical vapor deposition: an experimental and ab initio molecular orbital study. *Chem Phys Lett* 2000;325:453–6. doi:Doi 10.1016/S0009-2614(00)00630-8.

- [81] Qin S, McTeer A, Hu YJ. Co-gas impact of B<sub>2</sub>H<sub>6</sub> plasma diluted with helium on the plasma doping process in a pulsed glow-discharge system. *J Vac Sci Technol B Microelectron Nanom Struct* 2005;23:2272. doi:10.1116/1.2083929.
- [82] Zhang WJ, Chong YM, Bello I, Lee ST. Nucleation, growth and characterization of cubic boron nitride (cBN) films. *J Phys D Appl Phys* 2007;40:6159–74. doi:10.1088/0022-3727/40/20/S03.
- [83] Nguyen S V. Plasma-Assisted Chemical Vapor Deposition and Characterization of Boron Nitride Films. *J Electrochem Soc* 1994;141:1633. doi:10.1149/1.2054974.
- [84] Bewilogua K, Butth J, Hübsch H, Grischke M. Preparation of c-BN containing films by reactive r.f. sputtering. *Diam Relat Mater* 1993;2:1206–10. doi:10.1016/0925-9635(93)90171-W.
- [85] Kidner S, Taylor CA, Clarke R. Low energy kinetic threshold in the growth of cubic boron nitride films. *Appl Phys Lett* 1994;64:1859–61. doi:10.1063/1.111779.
- [86] Matsumoto S, Zhang W. Synthesis of boron nitride films by microwave plasma chemical vapor deposition in fluorine-containing gases. *Japanese J Appl Physics, Part 2 Lett* 2001;40:L570–2.
- [87] Teii K, Yamao R, Yamamura T, Matsumoto S. Synthesis of cubic boron nitride films with mean ion energies of a few eV. *J Appl Phys* 2007;101. doi:10.1063/1.2431401.
- [88] Acacia N, Fazio E, Neri F, Ossi PM, Trusso S, Santo N. Pulsed laser deposition of boron nitride thin films. *Radiat Eff Defects Solids* 2008;163:293–8. doi:10.1080/10420150701776522.
- [89] Reisse G, Weissmantel S. Pulsed laser deposition of hexagonal and cubic boron nitride films. *Appl Phys A Mater Sci Process* 1999;69:S749–53. doi:10.1007/s003390051521.
- [90] Tang YB, Yin LC, Yang Y, Bo XH, Cao YL, Wang HE, et al. suppData - Tunable band gaps and p-type transport properties of boron-doped graphenes by controllable ion doping using reactive microwave plasma. *ACS Nano* 2012;6:1970–8. doi:10.1021/nn3005262.
- [91] Robert Bigras G, Glad X, Vandsburger L, Charpin C, Levesque P, Martel R, et al. Low-damage nitrogen incorporation in graphene films by nitrogen plasma treatment: Effect of airborne contaminants. *Carbon N Y* 2019;144:532–9. doi:10.1016/j.carbon.2018.12.095.

# **Chapitre 2 : Interactions plasma-graphène dans les plasmas d'argon en régime continu**

## **1. Étude des dommages d'irradiation**

Dans cette section, les problématiques entourant les interactions plasma-graphène sont introduites. La littérature sur le sujet démontrant que le sujet est très riche, nous nous sommes penchés sur le cas simple de l'exposition de graphène à un plasma d'argon produit par un champs RF. Dans un premier temps, une étude exhaustive du plasma d'argon est réalisée en combinant des mesures par sonde de Langmuir, spectrométrie de masse et spectroscopie d'absorption optique. Différentes conditions de pression (5-80 mTorr) et de puissance (20-500W) sont parcourues pour estimer l'évolution des différents paramètres physiques tels que la température électronique ( $T_e$ ), le potentiel du plasma ( $V_p$ ), le potentiel flottant ( $V_f$ ) ainsi que les densités des différentes espèces (électrons, ions, métastables et résonants).

Ainsi, une première condition à faible densité d'ions (mode capacitif, E) est obtenue afin de vérifier l'évolution de l'état du graphène avec le temps de traitement. D'autres conditions sont ensuite déterminées afin de conserver la fluence des ions d'argon constante tout en variant leurs énergies (mode inductif, H). L'exposition du graphène à ces conditions nous permettra de saisir la richesse des interactions plasma-graphène. En effet, de tels plasmas permettent d'explorer des gammes d'énergie et de fluence difficile à obtenir autrement. On note alors que malgré des énergies des ions inférieures au seuil de pulvérisation (~20 eV) et de faibles temps de traitement (< 30s), des dommages considérables sont produits sur les films de graphène. Ceci est due à des phénomènes de gravure à deux étapes bien connues mais peu étudié à ce jour. De plus, nous introduisons la possibilité que les ions ne soient pas la seule espèce à pouvoir provoquer des dégâts dans le graphène. Ces travaux sont présentés sous la forme d'un article publié dans *Journal of Applied Physics*, **126**, 233302 (2019) . Pour ce travail, j'ai réalisé l'étude du plasma ainsi que la préparation et le traitement des échantillons de graphène par plasma. J'ai également rédigé la première version de l'article. X.Glad a réalisé les mesures Raman et a contribué à leurs

interprétations. J'ai été supervisé par R. Martel et L. Stafford. Le partenaire industriel A. Sarkissian a contribué à la mise au point du réacteur.

# A COMBINATION OF PLASMA DIAGNOSTICS AND RAMAN SPECTROSCOPY TO EXAMINE PLASMA-GRAPHENE INTERACTIONS IN LOW-PRESSURE ARGON RF PLASMAS

P. Vinchon<sup>1</sup>, X. Glad<sup>1</sup>, R. Martel<sup>2</sup>, A. Sarkissian<sup>3</sup> and L. Stafford<sup>1</sup>

<sup>1</sup>Département de physique, Université de Montréal, Montréal, Québec, Canada

<sup>2</sup>Département de chimie, Université de Montréal, Montréal, Québec, Canada

<sup>3</sup>Plasmionique inc., Varennes, Québec, Canada

## ABSTRACT

Graphene films were exposed to low-pressure capacitively-coupled (E-mode) and inductively-coupled (H-mode) argon radiofrequency plasmas to investigate damage formation by very low-energy ion irradiation. In the H-mode, plasma parameters were assessed by Langmuir probe and plasma sampling mass spectrometry to determine conditions of fixed ion fluence but different average ion energies. The populations of argon metastable and resonant argon atoms were also measured by optical absorption spectroscopy to determine their contribution to the total energy flux during plasma treatment. In the H-mode in which plasma-graphene interactions are dominated by ion irradiation effects, Raman spectroscopy reveals a significant rise in the D/G ratio and full width at half maximum of the G-peak as well as the onset of graphene amorphization, even at very low ion energies (between 7 and 13 eV). In the E-mode characterized by comparable ion energy but much lower ion density, significant damage is also observed; a feature ascribed to the additional energy flux linked to the de-excitation of metastable argon species on the graphene surface.

**Keywords:** graphene, damage formation, plasma-graphene interactions.

Since its discovery in 2004[1], graphene revealed itself as a promising material for a vast range of technological applications[2]. Its properties can be tailored by post-growth processing through either chemical[3] or dry plasma treatment[4–7]. The latter is commonly used to dope graphene and induce localization phenomena. Exposure to plasma-generated energetic species (ions, metastables, radicals, and UV photons) generates both defects and heteroatom incorporation throughout the graphene lattice[8,9]. However, in plasma treatment, the decoupling of physical and chemical mechanisms, such as doping and damage generation, is not trivial. Typically, damage studies on graphene are carried out using high-energy electron beams[10] or ion beams at energy above a few tens of eV[11]. Nonetheless, a few studies showed that plasma treatments may induce damage on graphite/graphene substrates although incident ions transfer less energy to the honeycomb lattice than its threshold displacement energy ( $T_d = 15\text{--}20 \text{ eV}$ )[12–15]. This effect is not yet clearly understood.

The aim of this study is to investigate plasma-graphene interactions in a low-pressure argon RF plasma characterized by significant populations of positive ions with very low energies (< 15 eV). The experimental conditions are first characterized by Langmuir probe, plasma sampling mass spectrometry, and optical absorption spectroscopy to determine the populations of energetic species (argon ions, argon metastable and resonant atoms, and UV photons). At first, the plasma conditions are kept constant while the treatment time increases to adjust the fluence of plasma-generated species. In a second step, through judicious control of the absorbed power, the ion fluence is kept constant while the pressure is changed to adjust the energy of the ions impinging on the surface. Raman spectroscopy is carried out on plasma-exposed graphene samples to examine damage formation induced by the different plasma conditions.

The setup is a planar-type inductively-coupled plasma reactor (Flarion system from Plasmionique inc.) with a spiral-shaped antenna operated at 13.56 MHz (Fig. 2.1.1). The residual pressure ( $7\times 10^{-8} \text{ Torr}$ ) is obtained by a combination of rotary and turbomolecular pumps. The argon (ultra-high purity 99.999%) mass flow rate is fixed at 20 sccm (cubic centimetres per minute at standard temperature and pressure) and the working pressure (5–80 mTorr) is adjusted by a gate valve located at the entrance of the pumping system. An automatic impedance matchbox holds the reflected power below 1 W for all conditions.

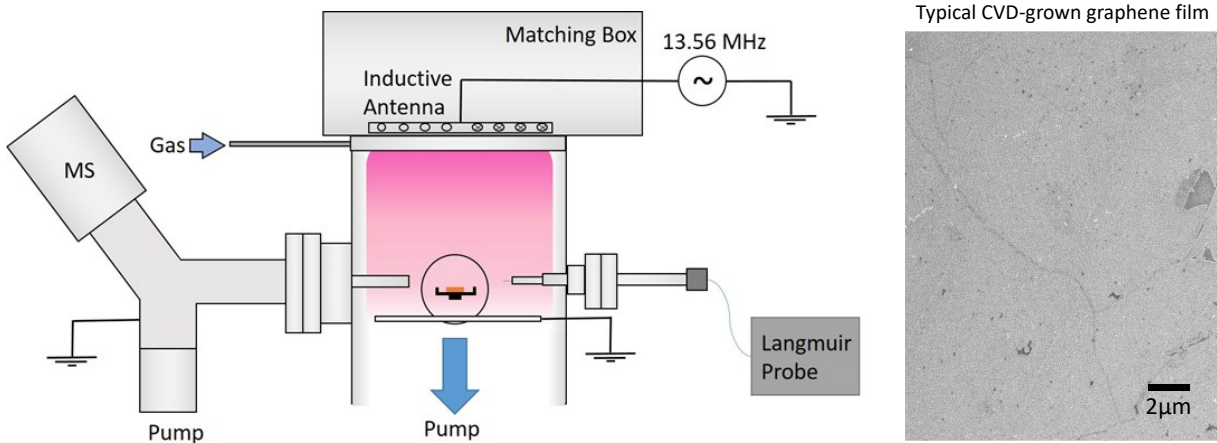


Figure 2.1.1. Sketch of the plasma apparatus used to examine plasma-graphene interactions. A scanning electron microscopy image of a typical graphene film is also shown.

Graphene films are grown on 25- $\mu\text{m}$  copper substrates by chemical vapor deposition (CVD)[16]. A typical scanning electron microscopy image of such sample is shown in Fig. 2.1.1. Before plasma treatment, the latter are transferred onto 1  $\text{cm}^2$  Si/SiO<sub>2</sub> substrates using a standard transfer procedure with Poly(methyl methacrylate) (PMMA)[17]. Note that since the graphene film lies on a dielectric material during the plasma treatment, the surface potential is floating. The substrate is placed  $\sim$ 20 cm below the antenna region and is thus exposed to the diffused region of the plasma reactor.

In order to assess the electrical parameters of the discharge, measurements were carried out with a cylindrical rf-compensated Langmuir probe (SmartProbe from Scientific Systems Ltd). The latter is placed a few centimetres above the substrate holder. Current-voltage characteristics are recorded between -60V and 20 V to extract plasma ( $V_p$ ) and floating ( $V_f$ ) potentials, positive ion density, as well as electron temperature ( $T_e$ ) assuming Maxwell electron energy distribution function.

To complete the plasma characterization, ion energy distribution functions (IEDFs) is measured with a Hiden HAL301S/2 plasma sampling mass spectrometer (MS) in SIMS+ mode

with an energy resolution of 0.05 eV. The measurements are carried out near the substrate-holder. Over the range of experimental conditions investigated, the Ar<sup>+</sup> ion signal at 40 a.m.u. always saturates. To circumvent this issue, the ArH<sup>+</sup> ion signal at 41 a.m.u. is analysed (ArH<sup>+</sup> is typically found in traces amount in argon discharges due to the degassing of the reactor walls[18]). Additionally, optical absorption spectroscopy (OAS) is performed to determine argon metastable (1s<sub>3</sub> and 1s<sub>5</sub>, Paschen's notation) and argon resonant (1s<sub>2</sub> and 1s<sub>4</sub>) populations. The setup used is described in detail by Maaloul *et al*[19].

Damage generation on graphene films is assessed by Raman spectroscopy using an inVia confocal Raman microscope system (Renishaw), a powerful tool for exhaustive studies of carbonaceous matter[20]. To prevent any heating damage, measurements are conducted at 514.5 nm (Ar laser) with a spot diameter of about 1.5 μm and a laser power below 0.5 mW. Spectra are obtained with a spectral resolution of 1 cm<sup>-1</sup>. Due to the poor homogeneity of graphene samples at a microscopic level (strain, grain boundaries, wrinkles, etc. )[21], a mapping of 121 points has been carried out on a 30×30 μm<sup>2</sup> area (x/y-step: 3 μm) .

Knowing that low-energy ions strongly impact graphite surfaces (even at energies lower than the threshold displacement energy), experimental conditions are determined such that the ion fluence  $f_{ion}$  remains constant while the ion energy,  $E_{ion}$ , varies within the very low energy range. As a first approximation, in collisionless sheaths, one may consider[14]:

:

$$E_{ion} = e(V_p - V_f), \quad (1)$$

where  $E_{ion}$  is in eV, V is in volts, and  $e$  is the absolute value of the elementary charge. Additionally, in Ar discharges,  $V_p - V_f$  is directly related to  $T_e$ [22]. Since  $T_e$  is highly pressure dependent[23], one way to change  $E_{ion}$  is to operate at different pressures. However, it also implies a modification of the ion fluence  $f_{ion}$  defined by:

$$f_{ion} = n_i v_B t_{exp}, \quad (2)$$

$$v_B = \sqrt{\frac{k T_e}{m_i}}, \quad (3)$$

is the Boltzmann constant, and  $m_i$  is the ions mass. In order to obtain a constant fluence but different  $E_{ion}$ , an approach is to fix the ion density over a large range of pressure (from 5 to 80 mTorr) by tuning the discharge power ( $P_{rf}$ ). Then, a steady fluence can be maintained by adjusting  $t_{exp}$ . In this framework, experimental conditions were determined for an ion density  $n_i = 1.1 \times 10^{11} \text{ cm}^{-3}$ : from  $p = 5 \text{ mTorr}$ ,  $P_{rf} = 500 \text{ W}$ , and  $t_{exp} = 15 \text{ s}$  to  $p = 80 \text{ mTorr}$ ,  $P_{rf} = 84 \text{ W}$ , and  $t_{exp} = 23 \text{ s}$ . The data summarized in Fig. 2.1.2 present the evolution of  $V_p - V_f$ ,  $kT_e$  and  $P_{rf}$  as a function of the working pressure. All treatments of graphene films in the inductive mode presented below were carried out in these pre-determined experimental conditions.

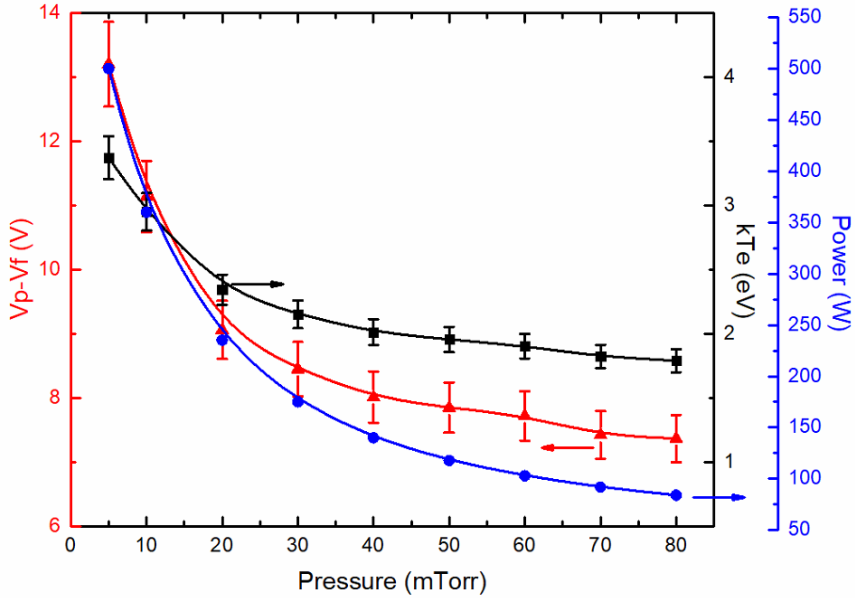


Figure 2.1.2: Langmuir probe measurements of  $V_p - V_f$  and  $kT_e$  as a function of the working pressure. The corresponding RF power to obtain a constant ion density of  $1.1 \times 10^{11} \text{ cm}^{-3}$  is also plotted. Lines are guides to the eye.

With increasing pressure, a monotonous decrease of both  $kT_e$  and  $V_p - V_f$  is observed from 3.3 eV and 13.3 V at 5 mTorr to 1.8 eV and 7.0 V at 80 mTorr, respectively. Such feature is typical for steady-state plasmas in which charged particles are predominantly created by

electron-impact excitation on ground state neutral atoms and mostly lost by ambipolar diffusion and recombination on the plasma reactor walls. In such plasmas, the drop in  $T_e$  is explained by the decrease of the electrons mean free path (mfp) with increasing pressure: this leads to a decreased electronic loss by diffusion and surface recombination and a consequently a decreased reaction rate for electron-impact ionization (and thus a decrease of  $T_e$ ) to maintain the discharge[23]. Note that in the inductive mode (H-mode) of low-pressure argon plasmas, despite a reduction of  $T_e$  with increasing pressure, the power absorbed per electron from the maintenance electric field (and thus the power dissipated per electron through elastic and inelastic collisions at steady-state) rises with increasing pressure[24]. Consequently, a lower  $P_{rf}$  value is needed at higher pressure to maintain a constant plasma density. Operation conditions are hence determined to obtain a variation of  $E_{ion}$  between 7 and 13 eV with a constant fluence of  $2.7 \times 10^{17} \text{ cm}^{-2}$ . This fluence is particularly high compared to other ion irradiation studies[25,26] but this feature is inherent to plasma treatments in inductive mode.

Due to its high ion density, the H-mode is not practical for studying the effect of fluence on graphene treatment. Hence, part of the study is done in capacitive mode (E-mode) at 40 mTorr – 20W. In this condition, a low ion density,  $n_i = 4 \times 10^8 \text{ cm}^{-3}$ , is obtained with  $E_{ion} = 7 \text{ eV}$ . Time treatment is then adjusted from 15 s up to almost an hour as to obtain a fluence variation from  $9.0 \times 10^{14} \text{ cm}^{-2}$  to  $2.1 \times 10^{17} \text{ cm}^{-2}$ . With the plasma conditions fully determined, the assumption leading to equation (1) can be further discussed. For example, it cannot be assumed that the sheath is collisionless through the whole range of pressures investigated. Indeed, the ion-neutral mfp – estimated as  $\lambda[\text{mm}] = 4.2/p[\text{Pa}][27]$  – is about 6.4 and 0.4 mm at 5 and 80 mTorr, respectively. At the highest-pressure value, the mfp compares with the average sheath width on an rf cycle (about 0.1 mm in both cases for a plasma density  $n_i = 1 \times 10^{11} \text{ cm}^{-3}$ )[27] and thus the sheath cannot be assumed collisionless. Moreover, it is known that the plasma potential,  $V_p$ , fluctuates at the rf frequency. Over the range of experimental conditions investigated, the ion transit time through the sheath is about 2.5 times greater than the rf period, which means than the ions may be affected by the instantaneous sheath voltage[28]. This would lead to bi-modal IEDFs; this is especially true below 10 mTorr where the electron energy relaxation length is greater than the distance between the substrate-holder and the rf power absorption area (20 cm).

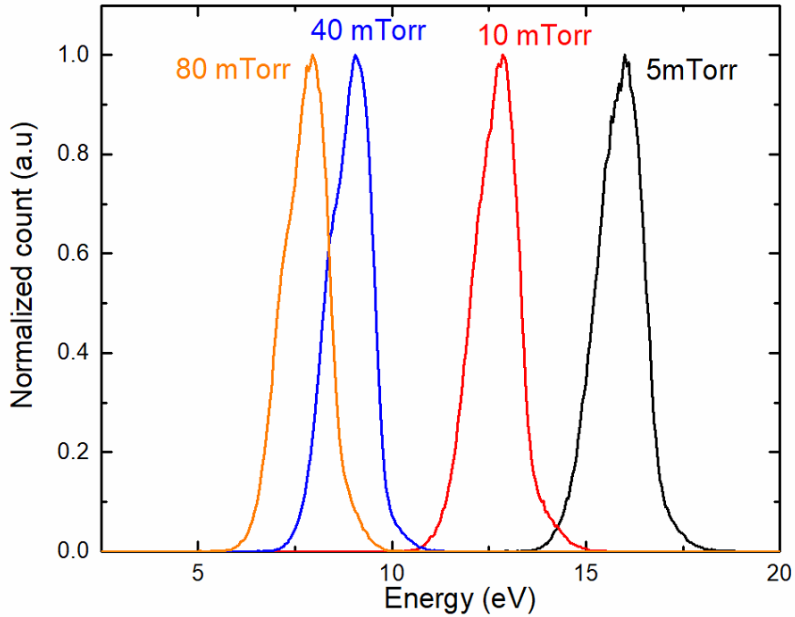


Figure 2.1.3: Normalized ArH<sup>+</sup> IEDFs from 5 to 80 mTorr (H-mode). Measurements are taken in the vicinity of the substrate-holder.

Knowing that in both ends of our pressure range, equation (1) might not be accurate, MS is carried out to assess IEDFs for various pressures. The results presented in Figure 2.1.3 show that, in our conditions, the full widths at half maximum (FWHM) are narrow ( $\sim 1.2$  eV) and only slightly modified with pressure. Bi-modal IEDFs are not observed at low pressure, confirming that the treatments are done in the diffusion region of the plasma. A weak shoulder may be distinguished towards the low-energy end of the IEDFs at 40 mTorr and above, showing the beginning of the transition towards a collisional sheath regime. Note that the charge exchange reaction  $\text{Ar}^+ + \text{Ar} \rightarrow \text{Ar} + \text{Ar}^+$  might slightly accentuate the shoulders observed at high pressure since such a reaction is not usually considered for ArH<sup>+</sup> ions. Nevertheless, the narrow FWHM of the IEDFs confirm the assumption of the monoenergetic nature of the ions, in agreement with equation (1). Additionally, in the H-mode, the average ion energy (Fig. 2.1.2) increases from 7 to 16 eV as the pressure decreases from 80 to 5 mTorr, respectively. Since the MS surface exposed to the plasma is grounded, these values are directly related to  $V_p$ . Considering  $V_f$  (about 2 V throughout the whole pressure range),  $E_{\text{ion}}$  is in good agreement with Langmuir probe measurements and ranges from 13 eV at 5 mTorr to 7 eV at 80 mTorr. In the

case of the capacitive mode (40 mTorr, 20 W), a broader distribution is obtained[29]; such broadening has been taken into account in our calculations.

To get a full picture of the physics driving plasma-graphene interactions in low-pressure argon RF plasmas, the populations of other energetic species needs to be investigated. In particular, argon metastable ( $1s^3$ ,  $1s^5$ ; noted Ar<sup>m</sup>) and resonant ( $1s^2$ ,  $1s^4$ , noted Ar\*) states have both potential energy around 11.7 eV above the ground state (Ar), albeit only resonant states can emit vacuum UV light at 104.8 and 106.4 nm (about 11.7 eV). Hence, in addition to the ion contribution, de-excitation of excited states on the graphene surface and vacuum UV irradiation of the graphene surface can both provide significant energy input to the graphene lattice during exposure to low-pressure argon plasmas. The populations of argon metastable (sum of  $1s^3$  and  $1s^5$ ) and resonant (sum of  $1s^2$  and  $1s^4$ ) states obtained by OAS are presented in Figure 2.1.4. Experimental conditions are the same than those detailed in Figure 2.1.2.

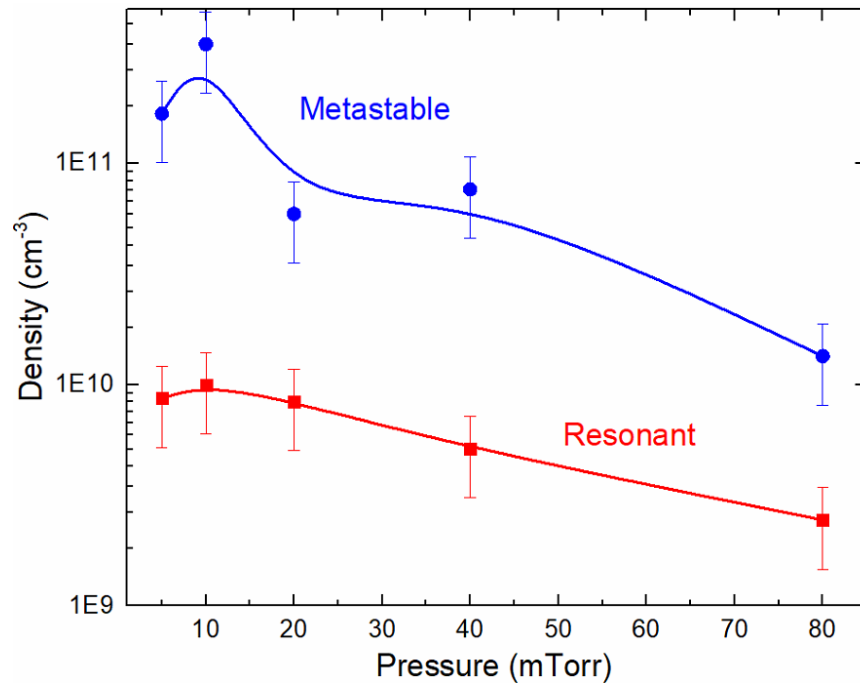


Figure 2.1.4: Populations of argon metastable ( $1s^3$  and  $1s^5$ ) and resonant ( $1s^2$  and  $1s^4$ ) states obtained by optical absorption spectroscopy as a function of pressure (same experimental conditions as in Figure 2.1.1). Lines are guides to the eye only.

At low pressure, metastable densities are of the same order of magnitude as the ion density ( $\sim 10^{11} \text{ cm}^{-3}$ ), while resonant densities are about one order of magnitude lower. However, both concentrations more or less decrease with increasing pressure. This is due to the balance between sources and losses of the probed states. The latter are mainly created by electron impact thus their density may increase with greater electron density but decrease with lower electron temperature (recall that cross sections for electron-impact excitation are energy dependent). Losses are expected to increase with rising pressure since quenching by electron or neutral species is inversely proportional to the decreasing mean-free-path (mfp). Such behaviour was already observed[30] even though experimental conditions are not strictly similar. In the E-mode (40 mTorr, 20 W), the population of metastable states is  $\sim 10^{11} \text{ cm}^{-3}$ , while the one of resonant states is  $\sim 10^8 \text{ cm}^{-3}$ , close to the value of the electron density. While resonant states are short-lived in optically thin media, metastable species have a lifetime much greater than the second in low-pressure argon plasmas[31].

From the densities determined by OAS, it is possible to estimate the power fluxes provided to the graphene substrate by metastable and resonant states as well as by vacuum UV irradiation. Piejak *et al.*[30] proposed an estimation of the power uptake following the surface de-excitation of metastable and resonant states (whose densities are noted  $N_m$  and  $N_*$ , respectively). The resulting power flux  $P_{ex}$  can be expressed as:

$$P_{ex} = 0.25\xi_m\varepsilon(N_m + N_*)\sqrt{\frac{8kT_g}{\pi M}}, \quad (4)$$

where  $\xi_m$  is the probability of energy transfer to the surface (assumed to be 1),  $\varepsilon$  is the metastable and resonant energy ( $\sim 11.7 \text{ eV}$ ),  $M$  is the argon mass, and  $T_g$  is the neutral gas temperature (assumed  $\sim 300 \text{ K}$ ). To estimate the power uptake due to vacuum UV irradiation emanating from argon  $1s_2$  and  $1s_4$  resonant states, radiation trapping needs to be considered, even at low pressure. The detailed calculation is described by Boffard *et al*[32] and the photon flux  $\Phi_\lambda$  (in  $\text{photon.s}^{-1}.\text{cm}^{-2}$ ) is given by the following relation:

$$\begin{aligned} \Phi_\lambda = & \frac{1}{2} \int_0^{z_{max}} \int_0^{r_{max}} A_{ij} \mathbf{n}_0 e^{-k_0 \sqrt{r^2+z^2}} \\ & \times \frac{z}{(r^2+z^2)^{3/2}} r dr dz, \end{aligned}, \quad (5)$$

where  $A_{ij}$  is the Einstein coefficient for spontaneous emission,  $k_0$  is the absorption coefficient at the centre of the line, and  $n_0$  is the density of resonant species (also labelled  $N_*$  in Equation (4)). Then, by multiplying  $\Phi_\lambda$  with the corresponding energy of each vacuum UV photon, an upper limit for the vacuum UV power flux is obtained.

Finally, the power flux transmitted through ion bombardment can be estimated as[33]:

$$P_{ion} = J_i(C \times E_{ion} + (\epsilon_i - \phi)) , \quad (6)$$

where  $J_i$  is the ion flux,  $E_{ion}$  is the ion kinetic energy from sheath acceleration ( $V_p - V_f$ ),  $C$  is the energy transfer coefficient through elastic collisions[33],  $\epsilon_i$  is the energy released by recombination with a substrate electron (15.76 eV), and  $\phi$  is the work function of graphene ( $\sim 4.6$  eV)[34].

Power flux values due to surface de-excitation of metastable and resonant atoms (Equation (4)), vacuum UV irradiation (Equation (5)), and ion bombardment (Equation (6)) are presented in Figure 2.1.5. Note that the experimental conditions are the same than those used in Figures 2.1.2 and 2.1.4.

As can be seen in Figure 2.1.5, ion bombardment is the dominant mechanism for all conditions displayed. However, at low pressure, vacuum UV photons combined with metastable species reveal power fluxes comparable to the ones of ion irradiation. The fluence of vacuum UV photons decreases with increasing pressure due to radiation trapping. A similar trend is observed for metastable species with a much less prominent decrease. In the E-mode, the ion power flux is  $1.6 \times 10^{-4}$  W.cm<sup>-2</sup>, the vacuum UV power flux is  $1.3 \times 10^{-4}$  W.cm<sup>-2</sup>, and the metastable power flux is  $4.9 \times 10^{-3}$  W.cm<sup>-2</sup>. Hence, considering  $\xi_m = 1$ , the total power provided to the graphene substrate mostly comes from surface de-excitation of metastable atoms.

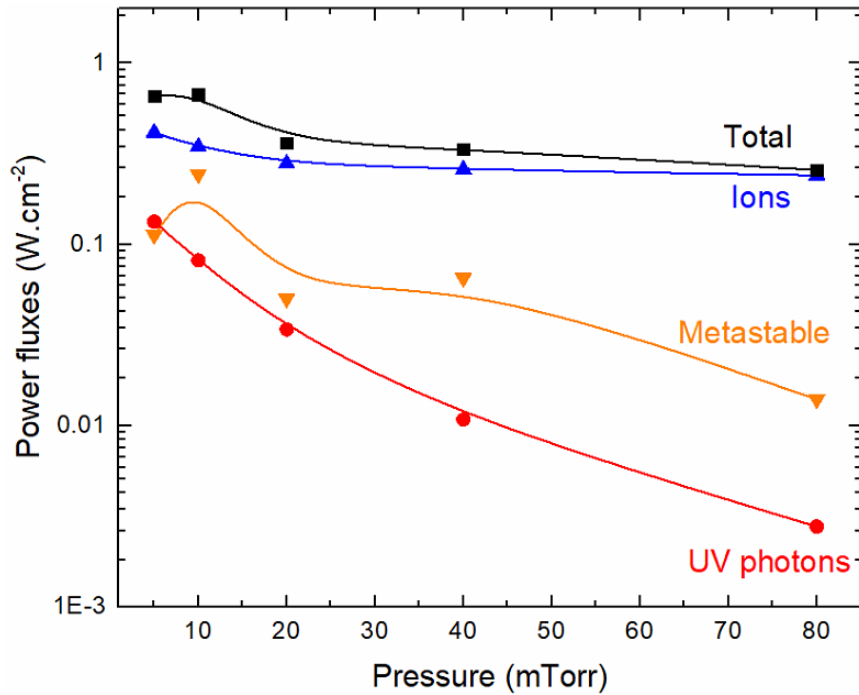


Figure 2.1.5: Evolution of power fluxes to the graphene surface due to surface de-excitation of metastable and resonant atoms (Equation (4)), vacuum UV irradiation (Equation (5)), and ion bombardment (Equation (6)). Experimental conditions are the same than those used in Figures 2.1.2 and 2.1.4. Lines are guides to the eye only.

Following each plasma treatment, graphene samples are analysed by Raman spectroscopy to assess damage generation. Typical measurements of untreated and plasma-treated graphene films are presented in Figure 2.1.6. The Lorentzian G ( $\sim 1580 \text{ cm}^{-1}$ ) and 2D ( $\sim 2700 \text{ cm}^{-1}$  at 514 nm) peaks are characteristic of defect-free single-layer graphene[20]. In addition, for defect-free monolayer graphene, the ratio of 2D over G peak intensities ( $I_{2D}/I_G$ ) is superior than 2.5. This latter value is consistent with the ratio obtained from the Raman spectrum of the pristine graphene samples used, such as the one displayed in Figure 2.1.6. When disorder grows within the lattice, the Lorentzian D ( $\sim 1350 \text{ cm}^{-1}$ ) and D' ( $\sim 1610 \text{ cm}^{-1}$ ) peaks arise. A typical approach to assess the defect density throughout the graphene lattice is to measure the ratio of D over G peak intensities ( $I_D/I_G$ )[35]. Note that the PMMA transfer from copper to Si/SiO<sub>2</sub> inevitably adds damage and leads to an  $I_D/I_G$  ratio around 0.08 for pristine graphene sample (untreated in Figure 2.1.6). After plasma treatment, a substantial rise of the D and D' peaks can be seen. In addition, while the G peak is only slightly modified, a significant drop in the 2D peak is

observed. This trend leads to a prominent increase of  $I_D/I_G$  and a considerable decrease of  $I_{2D}/I_G$ . From the results presented in Figure 2.1.6, one concludes that significant damage in graphene films occurs after plasma treatment, even for very short treatment times (21 s at 80 mTorr and 15 s at 5 mTorr) and very low ion energies (7.0 eV at 80 mTorr and 13.3 eV at 5 mTorr). The Raman spectra displayed in Figure 2.1.6 further reveals an additional contribution between the D and G peaks. Such feature can be related to the broad Gaussian G peak of amorphous carbon (a-C) at about  $1510\text{ cm}^{-1}$ ; this peak is commonly found in soot[36] or suspended graphene[37].

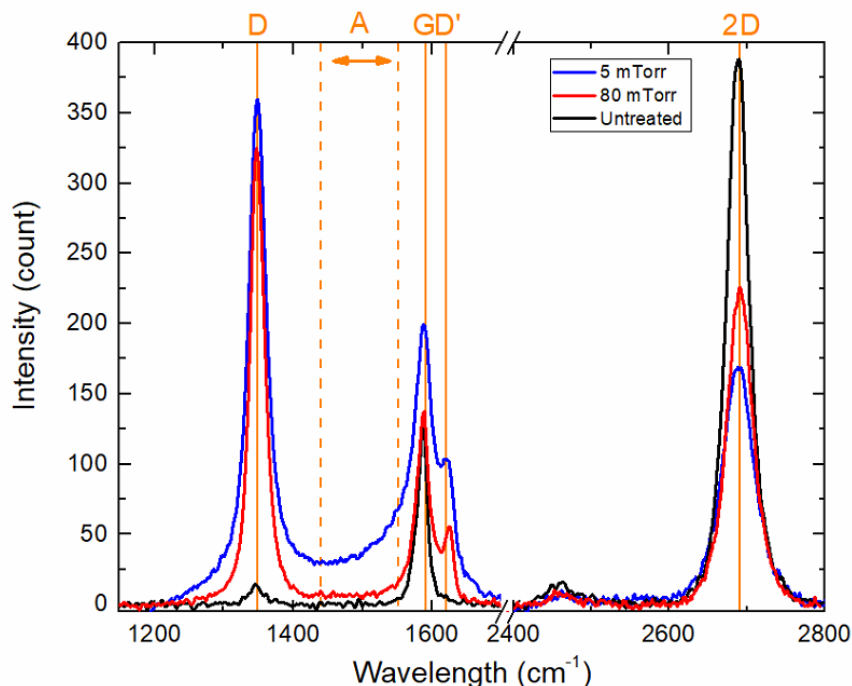


Figure 2.1.6: Raman spectrum of untreated graphene (black), plasma-treated graphene in H-mode at 5 mTorr (blue) and 80 mTorr (red). Treatment times are 15 s at 5 mTorr and 21 s at 80 mTorr to provide the same fluence of  $2.7 \times 10^{17}\text{ cm}^{-2}$ .

In order to highlight the implication of the results presented in Figure 2.1.6, recall that an Ar ion at normal incidence can transfer by elastic collisions up to 71% of its energy to a carbon atom of the graphene lattice[14], hence, up to 9.4 eV at 5 mTorr and 5.2 eV at 80 mTorr. These values being far below the threshold for direct sputtering, the removal of carbon atoms at very low ion energies can only arise through a multi-step process known as ion irradiation induced damage (I3D). In such process, a first incident ion creates a Frenkel defect, i.e. a vacancy and

an adatom. The latter is weakly bound to the lattice and can therefore easily be moved on the graphene surface or can even be desorbed by a second ion. At energy below the threshold displacement energy,  $T_d$ , of graphene ( $T_d \sim 18\text{-}22 \text{ eV}$ [38]), the formation of Frenkel pairs is expected to preferentially occur at already present defects, such as edges or grain boundaries. Additionally, very low-energy ions can induce the displacement of edge atoms ( $T_{d,\text{edge}} \sim 12 \text{ eV}$ )[39] or the generation of point defects such as bond rotation (Stone-Wales) that necessitates a formation energy of only 5 eV[38][40].

As proposed by Cançado *et al*[41], a powerful approach to monitor damage generation in graphene is to estimate the area ratio of D and G peaks ( $A_D/A_G$ ) –corrected by the laser energy  $E_L$  to the power 4– as a function of the FWHM of the G peak (FWHM(G)). In this case, it is also possible to distinguish zero- (0D) and one-dimensional (1D) defects. For the former, a strong increase of  $A_D/A_G \times E_L^4$  up to 130 with weak change in FWHM(G) is observed (stage 1[20,35], from pristine to nanocrystalline graphene, in Figure 2.1.7). With further damage in graphene films, the  $A_D/A_G$  ratio decreases while FWHM(G) increases more significantly which marks the transition from nanocrystalline graphene to amorphous carbon (stage 2 in Figure 2.1.7). 1D defects produce a weak-slope linear increase of the  $A_D/A_G$  ratio with FWHM(G). Furthermore, even more information can be extracted by plotting all measured data instead of only the mean value. A distribution is then obtained, which describes the whole surface probed by Raman spectroscopy measurements.

In this context, Figure 2.1.7 examines damage generation in graphene films through Cançado-like plots for experiments performed in the E-mode (weak ion flux). For the lowest fluence, a low peak ratio combined with a narrow G peak ( $\sim 15 \text{ cm}^{-1}$ ) is observed. As the fluence increases up to  $3.9 \times 10^{16} \text{ cm}^{-2}$ , the y-axis value increases up to 40 for FWHM(G) averages of around  $18 \text{ cm}^{-1}$ . At the highest fluence, a broader FWHM(G) distribution centred around  $30 \text{ cm}^{-1}$  with a corrected peak area ratio of 50 is observed. In such conditions, as also shown in Figure 2.1.7, the ratio of 2D over G peak intensities ( $I_{2D}/I_G$ ) monotonously decreases from about 4 at low fluence down to 0.5 at higher fluence; this latter point reveals the onset of graphene amorphization[20]. Overall, the set of data presented in Figure 2.1.7 confirms that the defect generation is progressive and increases with the fluence of plasma-generated species[42,43]. In

addition, based on Cançado-like plots, it seems that plasma-generated species produce both 0D and 1D defects, with a distribution that is rather complex to establish[43].

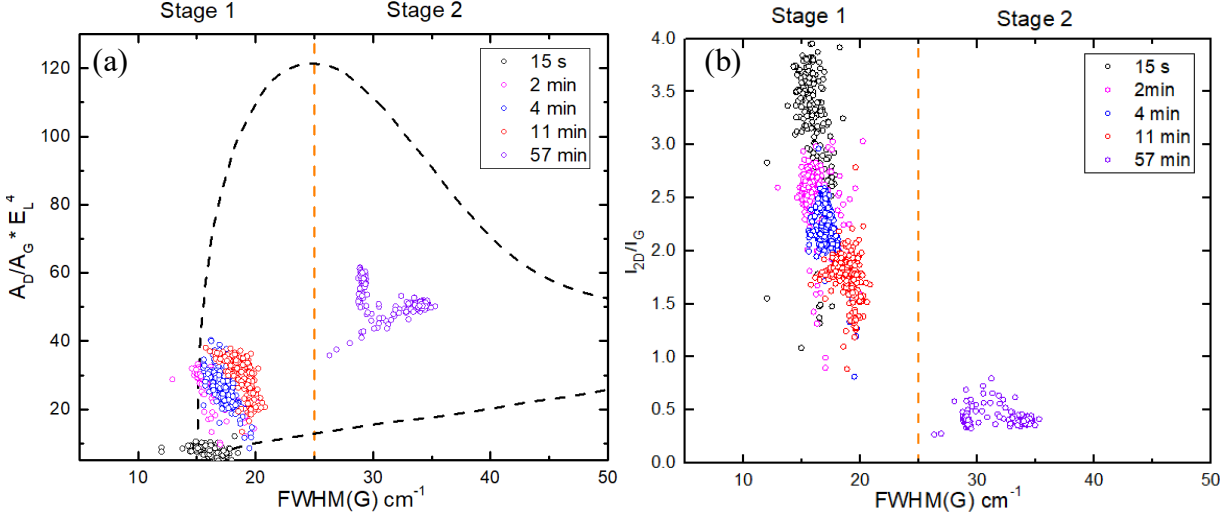


Figure 2.1.7: Graphene Raman data for 5 different fluence conditions in the E-mode (121 spectra recorded at different location on the graphene sample). (a)  $A_D/A_G$  ratio corrected by the laser energy  $E_L$  (2.41 eV) to the power 4 and (b) ratio of 2D over G peak intensities ( $I_{2D}/I_G$ ) as a function of  $FWHM(G)$ . The top-line in (a) represents 0D defects, while the bottom line follows 1D defects (see Cançado et al [42] for more details). Stage 1 and 2 are described in the text.

In line with the results presented in Figure 2.1.7, Figure 2.1.8 compares Cançado-like plots for experiments carried out in the H-mode at fixed ion fluence and varying average ion energy. As shown, high values of  $A_D/A_G$  combined with low values of  $I_{2D}/I_G$  are indicative of a significant damage generation for much lower treatment times; this behaviour is consistent with a greater density of ions in the H-mode than in the E-mode. In addition, the sample exposed to the lowest ion energy (7 eV, 80 mTorr) exhibits a rather fixed  $FWHM(G)$  ( $\sim 22$  cm<sup>-1</sup>) but a high  $A_D/A_G$  variation (from 56 to 100). With increasing  $E_{ion}$ , the extent of the corrected  $A_D/A_G$  ratios decreases (narrower distribution), while that of  $FWHM(G)$  rises and shows broader distributions. At the highest ion energy (13 eV, 5 mTorr),  $A_D/A_G$  is the lowest ( $\sim 60$ ) and  $FWHM(G)$  is the highest ( $\sim 32$  cm<sup>-1</sup>). Using the arguments detailed in Eckmann *et al.*[35], the decrease of  $I_{2D}/I_G$  down to 1 for the highest energy treatment confirms the onset of graphene amorphization ( $I_{2D}/I_G > 2.5$  for pristine graphene).

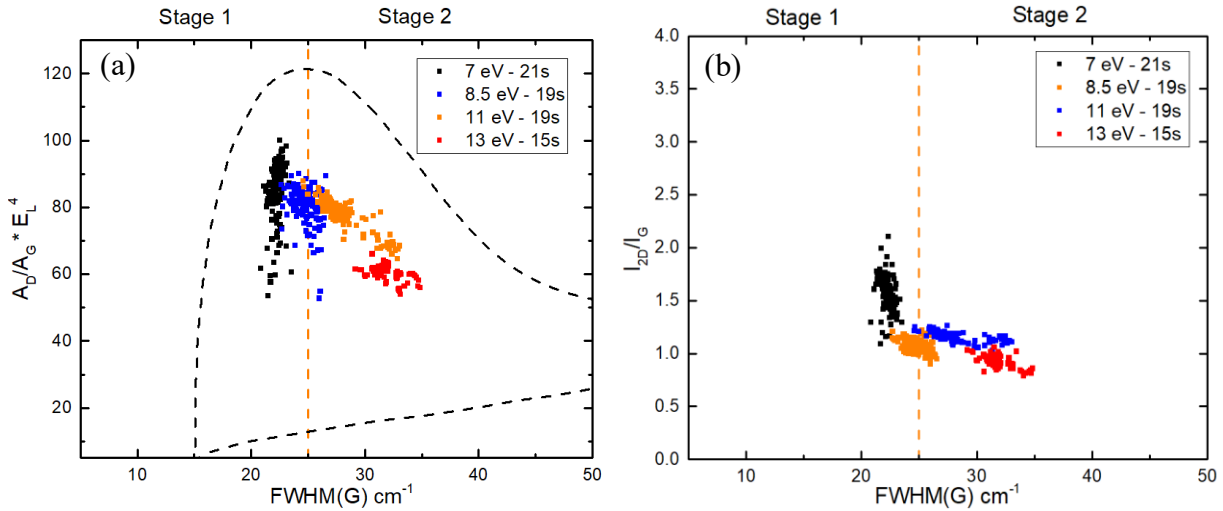


Figure 2.1.8: Graphene Raman data for 4 different incident ion energy (fixed ion fluence) in the H-mode (121 spectra recorded at different location on the graphene sample). (a)  $A_D/A_G$  peak area ratio corrected by the laser energy (2.41 eV) to the power 4 and (b) ratio of 2D over G peak intensities ( $I_{2D}/I_G$ ) as a function of  $FWHM(G)$ .

From the set of data presented in Figure 2.1.8, it seems that a difference in the ion irradiation of only a few eV at constant ion fluence can have a strong influence on the damage formation dynamics. Moreover, even if the average ion energies are low (between 7 and 13 eV), damage generation seems to gradually increase with  $E_{ion}$ . However, since no steep change is observed for neither  $A_D/A_G$  nor  $I_{2D}/I_G$  ratios, there is no evidence of an energy threshold for damage formation over the range of experimental conditions examined.

Another observation can be extracted from the distribution of the  $A_D/A_G$  and  $I_{2D}/I_G$  ratios obtained for each sample. Indeed, for all conditions, the distributions obtained are broad regarding  $A_D/A_G$ ,  $I_{2D}/I_G$  ratios and/or  $FWHM(G)$ . Since plasma treatments used in this study can be considered homogeneous and uniform over the whole surface of the graphene sample, such variations must be linked to spatial inhomogeneities in pristine graphene films (strain, grain boundaries, wrinkles, etc.)[21]. It is, however, difficult to establish links between the properties of as-grown graphene films and the subsequent damage formation at a microscopic level since Raman spectroscopy measurements can hardly be performed on the exact same micro-domains before and after plasma treatments with the inVia confocal Raman microscope system used in

this work. To distinguish those, a highly localized mapping performed over large areas is required. Such measurements are, however, very time consuming and hence hardly attainable before and after plasma treatment for a wide range of plasma conditions.

As mentioned above, for experiments realized in the H-mode, irradiation by very-low-energy ions dominates the damage formation dynamics of graphene films. However, in the E-mode, metastable species are likely to play an important role on the plasma-graphene interaction. This aspect can be examined in more details by comparing multiple sets of conditions displayed in Figure 2.1.7 and Figure 2.1.8. More specifically, Figure 2.1.9 compares Cançado-like plots for a treatment of graphene films in the E-mode with an ion energy of 7 eV and an ion fluence of  $2.1 \times 10^{17} \text{ cm}^{-2}$  with the ones for treatments in the H-mode with the minimal (7 eV) and maximal (13 eV) ion energy and a comparable ion fluence ( $2.7 \times 10^{17} \text{ cm}^{-2}$ ).

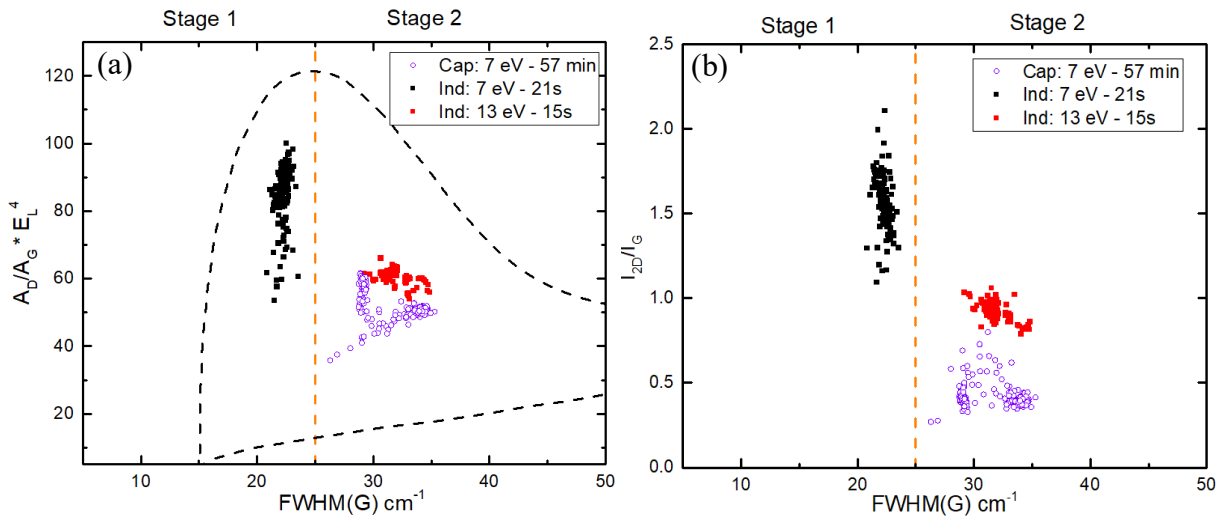


Figure 2.1.9: (a)  $A_D/A_G$  ratio corrected by the laser energy (2.41 eV) to the power 4 and (b)  $I_{2D}/I_G$  as a function of  $\text{FWHM}(G)$  for graphene films treated in the E-mode (purple) and in the H-mode (red and black). Data are replotted from Figures 2.1.7 and 2.1.8.

The results displayed in Figure 2.1.9 reveal that graphene films treated at 7 eV in the E-mode is much more damaged than those treated in the H-mode, even with the slightly lower ion fluence. While samples treated at 7 eV in the H-mode remains in stage 1, those treated at 7 eV in the E-mode are already in stage 2. This observation is strengthened with an  $I_{2D}/I_G$  around 0.5

for treatments in capacitive mode compared to  $>0.8$  for those in inductive mode. Plasma-induced damage at 7 eV in the E-mode are even more severe than those achieved at 13 eV in the H-mode. Based on the plasma characterization and power balance investigation presented above, this discrepancy can most likely be linked to the contribution of metastable species. More specifically, assuming  $\xi_m = 1$ , the power balance in E-mode is dominated by surface de-excitation of argon metastable atoms ( $4.9 \times 10^{-3}$  W.cm $^{-2}$ ) with only a small contribution of ion irradiation ( $1.6 \times 10^{-4}$  W.cm $^{-2}$ ). In contrast, ion irradiation effects in H-mode prevail with 0.1 W.cm $^{-2}$ . When considering the plasma exposure time, a total energy flux of 17.7 J.cm $^{-2}$  is provided to the graphene films in E-mode (with 0.19 J.cm $^{-2}$  provided by ion irradiation) versus 0.27 J.cm $^{-2}$  and 0.67 J.cm $^{-2}$  in H-mode at 7 eV and 13 eV, respectively. This readily explains the difference in Raman results and highlights the important contribution of metastable species in the plasma-induced modification of graphene films.

Based on *Cancado et al*[41], a further understanding of the graphene state after plasma treatment can be achieved through a determination of the average distance between nearest defects ( $L_D$ ) and the mean crystallite size ( $L_a$ ) from the set of data displayed in Figs 2.1.7a and 2.1.8a. In this framework, Figure 2.1.10 presents the evolution of the surface density of defects ( $\sigma = 1/L_D^2$ ) as a function of the mean crystallite area ( $L_a^2$ ) for all measurements presented previously. For comparison, the results obtained by *Cancado et al*[41] for a monoenergetic ion beam (70 eV) are also shown. In the E-mode, as expected, the mean value of the defect surface density sharply increases with the fluence, going from  $1 \times 10^{-3}$  nm $^{-2}$  after a treatment time of 15 s to  $\sim 200$  nm $^{-2}$  after a treatment time of 57 min. These values are comparable to those obtained using the monoenergetic ion beam. On the other hand, over the same range of conditions, the mean value of  $L_a^2$  in the plasma experiments decreases from the maximum value that can be deduced from such analysis ( $\sim 1000$  nm $^2$ ) down to  $\sim 50$  nm $^2$ . This trend was not observed by *Cancado et al*[41] such that the discrepancies between both set of experiments must be linked to the “plasma” versus “ion beam” environment. In particular, the decrease of both  $L_a$  and  $L_D$  with increasing fluence in the E-mode suggests a link between the rise of the surface density of plasma-generated defects and the decrease of the crystallite size. From *Kotakoski et al*[10], such behaviour is consistent with a coalescence of plasma-generated vacancies. Indeed,

the removal of carbon atoms by two-step physical etching combined with the additional energy uptake provided by the plasma environment can promote vacancy migration and then coalesce, thus reducing the effective crystallite size. In the E-mode, considering the typical migration energies of single (1.2-1.4 eV) and double (7 eV) vacancies on graphene[38,44], this additional energy uptake most likely comes from the de-excitation of metastable argon atoms.

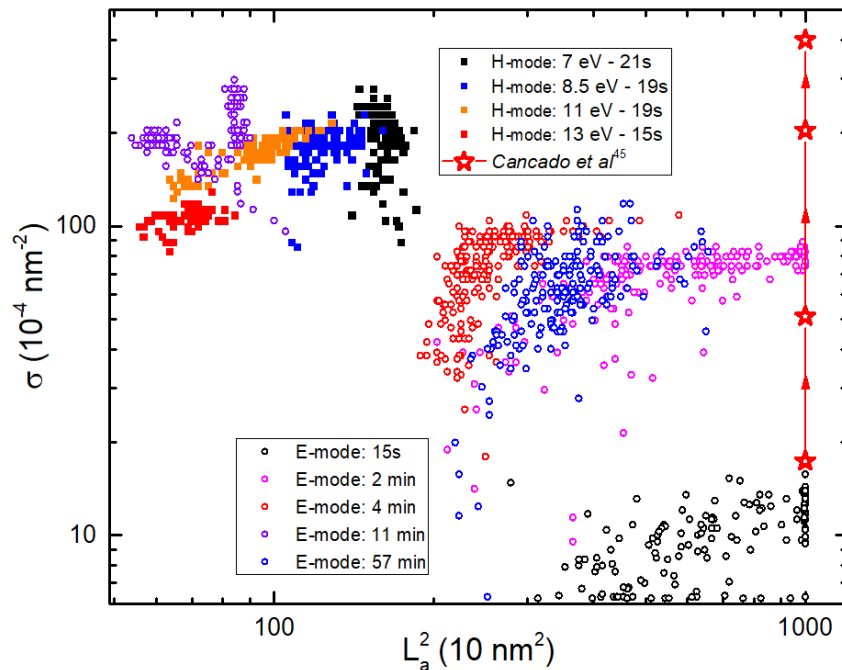


Figure 2.1.10: Graphene defect density in function of average crystallite size for plasma treatments (121 spectra each) in the H-mode (fixed ion fluence) and in the E-mode (fixed ion energy). In addition, data extracted from ion beam experiments [45] are presented as comparison.

In the H-mode, no significant change in the surface density was observed; this is consistent with the comparable fluence for all experimental conditions examined. In addition, the values are close to those obtained in the E-mode at the highest fluence ( $\sim 100\text{-}300 \text{ nm}^{-2}$ ). Moreover, as the mean ion energy increases, the mean crystallite area slightly decreases, going from  $150 \text{ nm}^2$  at 7 eV to  $70 \text{ nm}^2$  at 13 eV. In such conditions, the additional energy uptake leading to enhanced coalescence of plasma-generated vacancies could be due to either to the rise of the mean energy of the ions or the rise of the populations of metastable argon atoms (7.0 eV and  $\sim 10^{10} \text{ cm}^{-3}$  at 80 mTorr versus 13.3 eV and  $\sim 10^{11} \text{ cm}^{-3}$  at 5 mTorr; see Figures 2.1.3 and 2.1.4).

In this study, the plasma parameters of low-pressure argon inductively coupled plasmas were determined by Langmuir probe and plasma sampling mass spectroscopy to vary the average energy (from 7 to 13 eV) of ions impinging on a floating surface while maintaining a fixed ion fluence in inductive mode. In order to vary the power flux of the different species interacting with the substrate, similar conditions were determined in the capacitive mode. Plasma treatments were then carried out on CVD-grown graphene films transferred on Si/SiO<sub>2</sub> substrates and Raman spectroscopy was performed to assess the damage formation.

Our results confirm the dependence of damage generation with treatment time. They also reveal a clear and gradual increase of damage with ion energy. However, higher damage is observed in E-mode while maintaining similar ion energy and fluence than in H-mode. This result can be linked to a significant contribution of deexcitation of metastable species by the surface, which influences the damage formation dynamics of graphene films. Besides, considering the area ( $30 \times 30 \mu\text{m}^2$ ) probed by Raman spectroscopy, the highly scattered distributions observed in Cançado-like plots strengthen the need for a more spatially-resolved damage analysis technique to better understand the influence of each plasma-generated species on the pristine graphene state.

This study further shows the strong impact of relatively mild inductive plasma treatments on the structure of graphene films, even at very low ion energies (below 15 eV). This includes defect generation up to the onset of graphene amorphization. Moreover, in milder capacitive plasma treatments, ion energy and fluence are not the important parameters as metastable species becomes a significant source of damage. In contrast to conventional ion beam experiments, damage in plasma environments implies not only a rise of the surface density of defects (linked to the distance between nearest defects ( $L_D$ )) but also a reduction of the mean crystallite size ( $L_a^2$ ).

## ACKNOWLEDGMENTS

This work was financially supported by the National Science and Engineering Research Council (NSERC), PRIMA-Québec, Plasmionique inc., Photon etc, and the Fonds de Recherche du Québec—Nature et Technologies (FRQNT).

## REFERENCES

- [1] K.S. Novoselov, A.K. Geim, S. V. Morozov, D. Jiang, Y. Zhang, S. V. Dubonos, I. V. Grigorieva, A.A. Firsov, Electric Field Effect in Atomically Thin Carbon Films, *Science* (80-. ). 306 (2004) 666–669. doi:10.1126/science.1102896.
- [2] S.-M.M. Choi, S.-H.H. Jhi, Y.-W.W. Son, Effects of strain on electronic properties of graphene, *Phys. Rev. B.* 81 (2010) 081407. doi:10.1103/PhysRevB.81.081407.
- [3] J. Liu, Z. Liu, C.J. Barrow, W. Yang, Molecularly engineered graphene surfaces for sensing applications: A review, *Anal. Chim. Acta.* 859 (2015) 1–19. doi:10.1016/j.aca.2014.07.031.
- [4] M. Wojtaszek, N. Tombros, A. Caretta, P.H.M. Van Loosdrecht, B.J. Van Wees, A road to hydrogenating graphene by a reactive ion etching plasma, *J. Appl. Phys.* 110 (2011). doi:10.1063/1.3638696.
- [5] A. Dey, A. Chroneos, N.S.J. Braithwaite, R.P. Gandhiraman, S. Krishnamurthy, Plasma engineering of graphene, *Appl. Phys. Rev.* 3 (2016). doi:10.1063/1.4947188.
- [6] M. Acik, Y.J. Chabal, Nature of graphene edges: A review, *Jpn. J. Appl. Phys.* 50 (2011). doi:10.1143/JJAP.50.070101.
- [7] H.A. Mehedi, D. Ferrah, J. Dubois, C. Petit-Etienne, H. Okuno, V. Bouchiat, O. Renault, G. Cunge, High density H<sub>2</sub> and He plasmas: Can they be used to treat graphene?, *J. Appl. Phys.* 124 (2018). doi:10.1063/1.5043605.
- [8] S.H. Park, J. Chae, M.-H. Cho, J.W.J.H. Kim, K.-H. Yoo, S.W. Cho, T.G. Kim, J.W.J.H. Kim, High concentration of nitrogen doped into graphene using N 2 plasma with an aluminum oxide buffer layer, *J. Mater. Chem. C.* 2 (2014) 933–939. doi:10.1039/C3TC31773K.
- [9] M. Rybin, A. Pereyaslavtsev, T. Vasilieva, V. Myasnikov, I. Sokolov, A. Pavlova, E. Obraztsova, A. Khomich, V. Ralchenko, E. Obraztsova, Efficient nitrogen doping of graphene by plasma treatment, *Carbon N. Y.* 96 (2016) 196–202. doi:10.1016/j.carbon.2015.09.056.
- [10] J. Kotakoski, A. V. Krasheninnikov, U. Kaiser, J.C. Meyer, From point defects in graphene to two-dimensional amorphous carbon, *Phys. Rev. Lett.* 106 (2011) 1–4. doi:10.1103/PhysRevLett.106.105505.
- [11] O. Lehtinen, J. Kotakoski, a V Krasheninnikov, J. Keinonen, Cutting and controlled modification

of graphene with ion beams., *Nanotechnology*. 22 (2011) 175306. doi:10.1088/0957-4484/22/17/175306.

- [12] B. Rousseau, H. Estrade-Szwarcopf, A.L. Thomann, P. Brault, Stable C-atom displacements on HOPG surface under plasma low-energy argon-ion bombardment, *Appl. Phys. A Mater. Sci. Process.* 77 (2003) 591–597. doi:10.1007/s00339-002-1538-x.
- [13] X. Glad, L. De Poucques, J.A. Jaszczak, M. Belmahi, J. Ghanbaja, J. Bougdira, Plasma synthesis of hexagonal-pyramidal graphite hillocks, *Carbon N. Y.* 76 (2014) 330–340. doi:10.1016/j.carbon.2014.04.084.
- [14] X. Glad, L. de Poucques, J. Bougdira, Formation mechanism of graphite hexagonal pyramids by argon plasma etching of graphite substrates, *J. Phys. D. Appl. Phys.* 48 (2015) 495304. doi:10.1088/0022-3727/48/49/495304.
- [15] P. Ahlberg, F.O.L. Johansson, Z.B. Zhang, U. Jansson, S.L. Zhang, A. Lindblad, T. Nyberg, Defect formation in graphene during low-energy ion bombardment, *APL Mater.* 4 (2016). doi:10.1063/1.4945587.
- [16] S. Choubak, M. Biron, P.L. Levesque, R. Martel, P. Desjardins, No graphene etching in purified hydrogen, *J. Phys. Chem. Lett.* 4 (2013) 1100–1103. doi:10.1021/jz400400u.
- [17] A. Reina, H. Son, L. Jiao, B. Fan, M.S. Dresselhaus, Z. Liu, J. Kong, Transferring and Identification of Single- and Few-Layer Graphene on Arbitrary Substrates Transferring and Identification of Single- and Few-Layer Graphene on Arbitrary Substrates, *J. Phys. Chem. C.* 112 (2008) 17741–17744. doi:10.1021/jp807380s.
- [18] J. Tardy, J.M. Poitevin, G. Lemperiere, Glow discharge mass spectrometry of silicon DC sputtering in argon-hydrogen, *J. Phys. D. Appl. Phys.* 14 (1981) 339–346. doi:10.1088/0022-3727/14/2/025.
- [19] L. Maaloul, S. Morel, L. Stafford, Populations of metastable and resonant argon atoms in radio frequency magnetron plasmas used for deposition of indium-zinc-oxide films, *J. Vac. Sci. Technol. A Vacuum, Surfaces, Film.* 30 (2012) 021301. doi:10.1116/1.3674162.
- [20] A.C. Ferrari, J. Robertson, Interpretation of Raman spectra of disordered and amorphous carbon, *Phys. Rev. B.* 61 (2000) 14095–14107. doi:10.1103/PhysRevB.61.14095.
- [21] J. Lu, K. Zhang, X. Feng Liu, H. Zhang, T. Chien Sum, A.H. Castro Neto, K.P. Loh, Order-disorder transition in a two-dimensional boron–carbon–nitride alloy, *Nat. Commun.* 4 (2013) 1–7. doi:10.1038/ncomms3681.
- [22] D. Barton, D.J. Heason, R.D. Short, J.W. Bradley, The measurement and control of the ion energy distribution function at a surface in an RF plasma, *Meas. Sci. Technol.* 11 (2000) 1726–1731. doi:10.1088/0957-0233/11/12/312.

- [23] V.A. Godyak, R.B. Piejak, B.M. Alexandrovich, Electron energy distribution function measurements and plasma parameters in inductively coupled argon plasma, *Plasma Sources Sci. Technol.* 11 (2002) 525–543. doi:10.1088/0963-0252/11/4/320.
- [24] M. Moisan, J. Pelletier, *Microwave Excited Plasmas*, Elsevier, 1992. doi:9780444888150.
- [25] E.H. Martins Ferreira, M.V.O. Moutinho, F. Stavale, M.M. Lucchese, R.B. Capaz, C.A. Achete, A. Jorio, Evolution of the Raman spectra from single-, few-, and many-layer graphene with increasing disorder, *Phys. Rev. B.* 82 (2010) 125429. doi:10.1103/PhysRevB.82.125429.
- [26] K. Jia, Y. Su, Y. Chen, J. Luo, J. Yang, P. Lv, Z. Zhang, H. Zhu, C. Zhao, T. Ye, Effects of defects and thermal treatment on the properties of graphene, *Vacuum.* 116 (2015) 90–95. doi:10.1016/j.vacuum.2015.03.003.
- [27] P. Chabert, N. Braithwaite, *Physics of Radio-Frequency Plasmas*, Cambridge University Press, Cambridge, 2011. doi:10.1017/CBO9780511974342.
- [28] E. Kawamura, V. Vahedi, M. a Lieberman, C.K. Birdsall, Ion energy distributions in rf sheaths; review, analysis and simulation, *Plasma Sources Sci. Technol.* 8 (1999) R45–R64. doi:10.1088/0963-0252/8/3/202.
- [29] J.K. Lee, O. V. Manuilenco, N.Y. Babaeva, H.C. Kim, J.W. Shon, Ion energy distribution control in single and dual frequency capacitive plasma sources, *Plasma Sources Sci. Technol.* 14 (2005) 89–97. doi:10.1088/0963-0252/14/1/012.
- [30] R. Piejak, V. Godyak, B. Alexandrovich, N. Tishchenko, Surface temperature and thermal balance of probes immersed in high density plasma, *Plasma Sources Sci. Technol.* 7 (1999) 590–598. doi:10.1088/0963-0252/7/4/016.
- [31] H. Katori, F. Shimizu, Lifetime measurement of the 1s5 metastable state of argon and krypton with a magneto-optical trap, *Phys. Rev. Lett.* 70 (1993) 3545–3548. doi:10.1103/PhysRevLett.70.3545.
- [32] J.B. Boffard, C.C. Lin, C. Culver, S. Wang, A.E. Wendt, S. Radovanov, H. Persing, Comparison of surface vacuum ultraviolet emissions with resonance level number densities. I. Argon plasmas, *J. Vac. Sci. Technol. A Vacuum, Surfaces, Film.* 32 (2014) 021304. doi:10.1116/1.4859376.
- [33] H. Kersten, H. Deutsch, H. Steffen, G.M.W. Kroesen, R. Hippler, The energy balance at substrate surfaces during plasma processing, *Vacuum.* 63 (2001) 385–431. doi:10.1016/S0042-207X(01)00350-5.
- [34] Y.-J. Yu, Y. Zhao, S. Ryu, L.E. Brus, K.S. Kim, P. Kim, Tuning the Graphene Work Function by Electric Field Effect, *Nano Lett.* 9 (2009) 3430–3434. doi:10.1021/nl901572a.
- [35] A. Eckmann, A. Felten, A. Mishchenko, L. Britnell, R. Krupke, K.S. Novoselov, C. Casiraghi, Probing the nature of defects in graphene by Raman spectroscopy, *Nano Lett.* 12 (2012) 3925–

3930. doi:10.1021/nl300901a.

- [36] A. Sadezky, H. Muckenhuber, H. Grothe, R. Niessner, U. P??schl, Raman microspectroscopy of soot and related carbonaceous materials: Spectral analysis and structural information, *Carbon N. Y.* 43 (2005) 1731–1742. doi:10.1016/j.carbon.2005.02.018.
- [37] Y.-C. Lin, C.-C. Lu, C.-H. Yeh, C. Jin, K. Suenaga, P. Chiu, Graphene Annealing: How Clean Can It Be?, *Nano Lett.* 12 (2012) 414–419. doi:10.1021/nl203733r.
- [38] F. Banhart, J. Kotakoski, A. V. Krasheninnikov, Structural Defects in Graphene, *ACS Nano.* 5 (2011) 26–41. doi:10.1021/nn102598m.
- [39] J. Kotakoski, D. Santos-Cottin, A. V. Krasheninnikov, Stability of Graphene Edges under Electron Beam: Equilibrium Energetics versus Dynamic Effects, *ACS Nano.* 6 (2012) 671–676. doi:10.1021/nn204148h.
- [40] G. Yang, L. Li, W.B. Lee, M.C. Ng, Structure of graphene and its disorders: a review, *Sci. Technol. Adv. Mater.* 19 (2018) 613–648. doi:10.1080/14686996.2018.1494493.
- [41] L. Cançado, M. Gomes de Silva, E.H.M. Ferreira, F. Hof, Disentangling contributions of point and line defects in the Raman spectra of graphene-related materials, *2D Mater.* 4 (2017) 025039.
- [42] A. Eckmann, A. Felten, I. Verzhbitskiy, R. Davey, C. Casiraghi, Raman study on defective graphene: Effect of the excitation energy, type, and amount of defects, *Phys. Rev. B - Condens. Matter Mater. Phys.* 88 (2013) 1–11. doi:10.1103/PhysRevB.88.035426.
- [43] L. Gustavo Cançado, M. Gomes da Silva, E.H. Martins Ferreira, F. Hof, K. Kampioti, K. Huang, A. Pénicaud, C. Alberto Achete, R.B. Capaz, A. Jorio, Disentangling contributions of point and line defects in the Raman spectra of graphene-related materials, *2D Mater.* 4 (2017) 025039. doi:10.1088/2053-1583/aa5e77.
- [44] A. El-Barbary, H. Telling, P. Ewels, I. Heggie, R. Briddon, Structure and energetics of the vacancy in graphite, *Phys. Rev. B - Condens. Matter Mater. Phys.* 68 (2003) 1–7. doi:10.1103/PhysRevB.68.144107.
- [45] L.G. Cançado, A. Jorio, E.H.M. Ferreira, F. Stavale, C. a. Achete, R.B. Capaz, M.V.O. Moutinho, a. Lombardo, T.S. Kulmala, a. C. Ferrari, Quantifying defects in graphene via Raman spectroscopy at different excitation energies, *Nano Lett.* 11 (2011) 3190–3196. doi:10.1021/nl201432g.

## 2. Spectroscopie Raman Hyperspectrale

Bien que les traitements à basse pression soient reconnus pour leur reproductibilité et leur homogénéité, une grande dispersion dans les mesures a été observée dans le travail précédent. Afin de comprendre les origines physiques de telles variations, nous nous sommes tournées vers la spectroscopie Raman hyperspectrale (RIMA) développée par le groupe du Prof. Martel en collaboration avec notre partenaire industriel Photon etc. Dans ce cas, de l'imagerie Raman est réalisée avec une grande précision ( $\sim 400$  nm) sur des domaines de l'ordre de la centaine de micromètres. Ceci est indéniablement un avantage sur la spectroscopie Raman confocale classique qui nécessite un déplacement de l'échantillon pour effectuer des mesures statistiques. Cependant, à ce stade, le RIMA ne peut pas être utilisé pour l'interprétation quantitative due à la pollution des données par des artefacts intrinsèques à la méthode et la faible émission Raman du graphène. Afin d'extraire des données cohérentes, un code matlab a été développé afin d'obtenir une bonne estimation de l'état du graphène. La méthode est ensuite validée via la comparaison des valeurs extraites et celles obtenues par spectroscopie Raman classique. Cette méthode est détaillée sous la forme d'un article publié dans le journal *Review of Scientific Instruments*, **91**, 063903 (2020) à contribution égale avec G.R. Bigras. J'ai réalisé la préparation et le traitement de l'échantillon par plasma. Ainsi, j'ai participé aux mesures RIMA, au développement du code matlab pour le traitement des données ainsi qu'à l'écriture du premier jet de l'article. G.R. Bigras a contribué aux mesures RIMA, à la réalisation du code matlab ainsi qu'à l'écriture du premier jet de l'article. C. Allard a participé aux mesures RIMA tandis que X. Glad a réalisé les mesures Raman classiques de comparaison. Ce travail a été accompli sous la supervision de R. Martel et L. Stafford.

# PROBING PLASMA-TREATED GRAPHENE USING HYPERSPECTRAL RAMAN

G. Robert Bigras \*<sup>1</sup>, P. Vinchon \*<sup>1</sup>, C. Allard <sup>2</sup>, X. Glad <sup>1</sup>, R. Martel <sup>2</sup>, L. Stafford <sup>1\*\*</sup>

\* Equally credited authors \*\* Corresponding author: luc.stafford@umontreal.ca

<sup>1</sup> Département de Physique, Université de Montréal,

<sup>2</sup> Département de Chimie, Université de Montréal,

## ABSTRACT

Raman spectroscopy provides rich optical signals that can be used, after data analysis, to assess if a graphene layer is pristine, doped, damaged, functionalized, or stressed. The area being probed by a conventional Raman spectrometer is, however, limited to the size of the laser beam ( $\sim 1 \mu\text{m}$ ); hence, detailed mapping of inhomogeneities in a graphene sample requires slow and sequential acquisition of a Raman spectrum at each pixel. Studies of physical and chemical processes on polycrystalline and heterogeneous graphene films require more advanced hyperspectral Raman capable of fast imaging at high spatial resolution over hundreds of microns. Here, we compare the capacity of two different Raman imaging schemes (scanning and global) to probe graphene films modified by a low-pressure plasma treatment and present an analysis method providing assessments of the surface properties at local defects, grain boundaries and other heterogeneities. By comparing statistically initial and plasma-treated regions of graphene, we highlight the presence of inhomogeneities after plasma treatment linked to the initial state of the graphene surface. These results provided statistical results on the correlation between graphene initial state and the corresponding graphene-plasma interaction. This work further demonstrates the potential use of global hyperspectral Raman imaging with advanced Raman spectra analysis to study graphene physics and chemistry on a scale of hundreds of microns.

**Keywords:** Hyperspectral Raman imaging, graphene treatment, graphene-plasma interaction, principal component analysis filtering

Raman spectroscopy of graphene provides access to quantitative assessments of local defect density, doping state and strain levels, and, hence, represents a powerful tool for probing the quality and the chemistry of a graphene sample [1-3]. Acquiring Raman maps over macroscopic scales generates a wealth of additional information about the sample, including local heterogeneities of defects, differences in doping or stress, and helps further understand complex transformations linked to these differences. As an example, the complexity of the graphene-plasma interaction was recently highlighted by Raman mapping of polycrystalline graphene films after low-pressure argon plasma treatments [2].

The current standard Raman methods of mapping are based on scanning schemes in which the laser beam (or line) is moved pixel by pixel (or line by line). Conventional Raman are poorly adapted for macroscopic scales because the spatial resolution is limited by the beam shape and size, which is typically of around 1  $\mu\text{m}$ . Generating maps with both acceptable signal-to-noise ratio and high spatial resolution are therefore time-consuming [1]. Hyperspectral Raman Imaging (RIMA) is a global imaging scheme that has demonstrated itself to be a highly promising alternative to conventional Raman imaging schemes [1]. The instrument acquires millions of Raman spectra in a reasonable time (hours), which provides enough data for statistical analysis while allowing spatial correlation. With these advances, difficulties arise, however, when trying to evaluate quantitative values from hyperspectral Raman maps due to artefacts intrinsic to the setup and to the low density of power imposed with global illumination, which maximum value is set so as to prevent graphene damage.

Here, we present a refined data processing method for RIMA images based on Principal Component Analysis (PCA) filtering to extract the most information possible on the physics and chemistry of polycrystalline graphene films grown on copper substrates by Chemical Vapor Deposition (CVD) and then transferred on  $\text{SiO}_2$  substrates using conventional transfer methods. Through fast data handling, the method provides two-dimensional histograms of registered datasets that allow to spatially compare the Raman results of pristine graphene films with that of the same sample after a low-pressure argon plasma treatment. Thanks to the RIMA method, the characterization is facilitated by a wide field of view (hundreds of micrometers) and a good spatial resolution (tens of micrometers for a field of view of hundreds of micrometers). As

demonstrated by results on graphene plasma treatments, the method reveals itself as a promising alternative to investigate novel graphene-plasma interactions and mechanisms.

The RIMA instrument (described in details in [3], Photon Etc) relies on volumetric Bragg tunable filters (BTF) to acquire hyperspectral Raman images. Briefly, a 532 nm laser is focused at the focal length of a 100x objective, providing a field of view of  $130 \mu\text{m} \times 130 \mu\text{m}$  to the sample. The authors' custom shaping module provides the laser a flat top intensity profile, which ensures homogeneity of the laser exposition at the graphene surface. Scattered light emitted from the graphene surface is collected via the same objective and redirected towards the BTF. Gradient images are collected at a  $1024 \times 1024$  pixels charged couple device (CCD, 1024x1024 PIXIS, Princeton Instruments) for various angular position of the BTF. The final spectra are reconstructed via a wavelength rectification digital process [3]. The instrument provides spectra with a resolution of  $8 \text{ cm}^{-1}$ . Measurement were performed with  $3 \text{ cm}^{-1}$  acquisition steps; thus, the image is a 1048576 points mapping. The laser power is set to 3.5 W, which provides a power density of  $2.1 \times 10^8 \text{ W/m}^2$ , which is low enough to ensure no damage generated to the graphene sample during measurements [4].

The area probed depends on the objective used; the 100x and 50x objective provides images of  $130 \times 130 \mu\text{m}^2$  and  $260 \times 260 \mu\text{m}^2$ , respectively. Due to the high number of pixel ( $1024 \times 1024$ ), a maximum spatial resolution of 130 nm is achieved with the 100x objective. This value coincide with the diffraction limit of the setup [3]. Through binning of few pixels on the CCD camera, one can decrease the exposure time for good signal-to-noise ratio, but at the cost of a decrease of the spatial resolution. In this work, the first measurements were carried out using 1x1 binning and 100 sec of exposure time. The same region was probed after the exposure of the sample to a typical Argon ICP plasma setup (details elsewhere [2] and experimental conditions presented in Supplementary Data I) Due to time constraints, RIMA measurements of plasma-treated graphene samples were acquired using 3x3 binning and 20 sec exposure time.

For the purpose of making a comparison with conventional Raman, we present additional Raman spectra acquired using a confocal Raman spectroscopy setup (Renishaw inVia). A 514 nm argon laser was used as the source and the power at the sample position was set at 0.7

mW. The spectral resolution is  $1\text{ cm}^{-1}$ . The 100x objective of inVia provides a laser diameter of about  $1\text{ }\mu\text{m}$  on the sample. The power density ( $2.2\times10^8\text{ W/m}^2$ ) of the laser was kept below the onset of laser-induced damage in graphene films [4]. Baseline subtractions were performed using a polynomial baseline function and peak fitting was performed right afterward using a Lorentzian line shape. For sake of comparison with RIMA images of plasma-treated graphene samples,  $36\times36$  point-by-point area mappings are recorded with a step of  $4\text{ }\mu\text{m}$  to probe the uniformity of the surface. Both Raman mappings with the Renishaw and with RIMA ( $3\times3$  binning and 20 sec time exposure) took 1h30-2 hours to execute.

Principal component analysis (PCA) filtering was performed to reduce signal noise and to ease the fitting process [5,6]. Fig. 2.2.1 presents typical Raman spectra before (grey) and after (red) PCA filtering for both untreated (a) and plasma-treated (b) graphene samples. Each spectrum is taken as an observation by considering each wavenumber values as a dimension for the analysis. Following the respective subtraction of the mean value of each observation, a linear combination of the initial dimension is found to minimize the variance of the data. The obtained dimension is subtracted, and the calculation is done iteratively as many times as there are dimensions. The resulting dimensions are therefore sorted according to the contribution of the observations. The first components represent dominants features of the signal while low variance's components arise from noise in the observations. Thus, by reducing dimension numbers, one can essentially filter the data noise. In this case, the number of components chosen for the reconstruction are determined by a threshold of contribution to the cumulative signal. Components considered for the reconstruction are selected until the next component provides less than 0.05% of the cumulative signal. Additional details on the filtering process are presented in Supplementary Data II. Mean spectra of each acquisition cube, criteria on the number of components to consider and more typical spectra are presented.

Overall, an excellent matching is obtained in Fig. 2.2.1 between initial Raman spectra and reconstructed Raman signal after PCA filtering. Indeed, the sufficient number of components considered ensures that no information is lost. Some important features arise using PCA filtering. The small peak around  $1550\text{ cm}^{-1}$  was hidden in the noise for most spectra and is linked to an intrinsic artefact present in the RIMA setup [3,7]. This will be further discussed later.

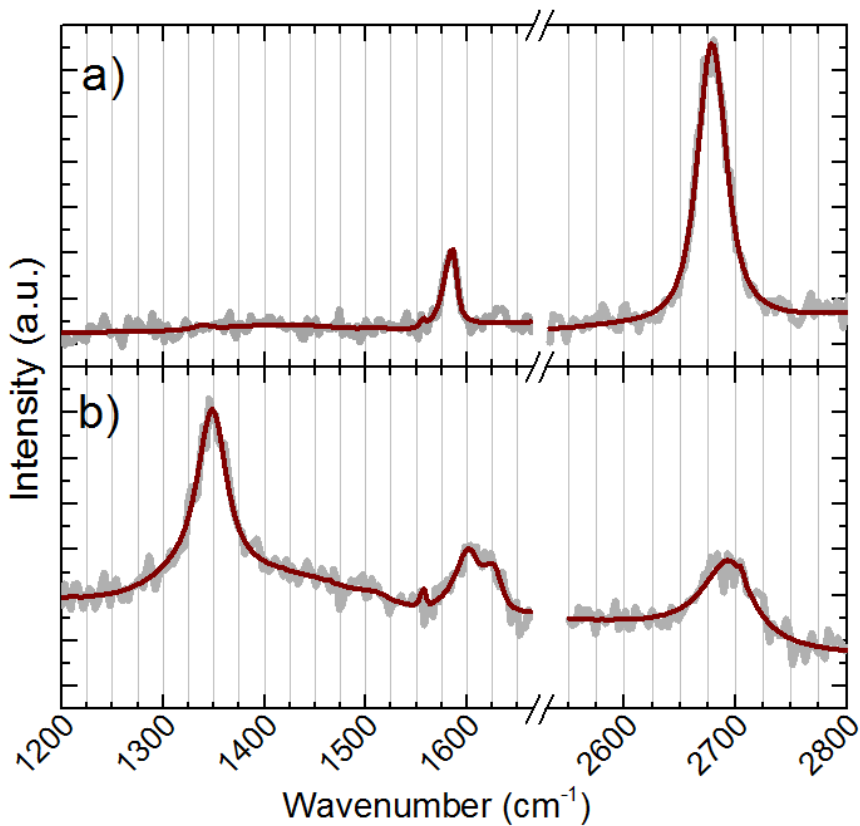


Figure 2.2.1: Comparison raw data and PCA filtered data for untreated (a) and treated (b) graphene.

After PCA filtering, Raman spectra are fitted using a nonlinear least square fitting method with normalization and centering. Each spectrum is separated in three regions (D, G&D' and 2D regions of graphene). A precise baseline subtraction is mandatory to obtain quantitative analysis of the Raman measurements and to remove residual contributions, such as fluorescence from the substrate and other intrinsic artefacts (e.g. beam inhomogeneities, fluorescence from optical components). The shape of the RIMA artefact changes over the surface of the camera. This explains the variation of the curvature's amplitude of the baseline between points taken at different position (see Fig. 2.2.1 for example). Additionally, an increase of exposure time naturally increases the ratio between the Raman signal and this baseline. The method ensures a good baseline subtraction as long as the line shape of each bands is chosen wisely so that no bands are neglected. Polynomial curves are used for baseline fitting with an order chosen to be the smallest possible while keeping good fitting results. For each acquisition cube, fitting of the

three regions is performed for a large number of orders for the polynomial baseline subtraction. Order that are clearly too low are automatically discarded. From the remaining orders, one is selected as the optimal for the fit. It is chosen low enough to make sure there is no overfitting, but also high enough to allow the baseline to have the curvature necessary to best follow the profile of the artefact. Overall, the error introduced by the choice of the order is show small (at most 12%) (Supplementary Data III). Figs. 2.2.2a-b present a comparison between typical Raman spectra obtained at a given position using both RIMA and Renishaw inVia.

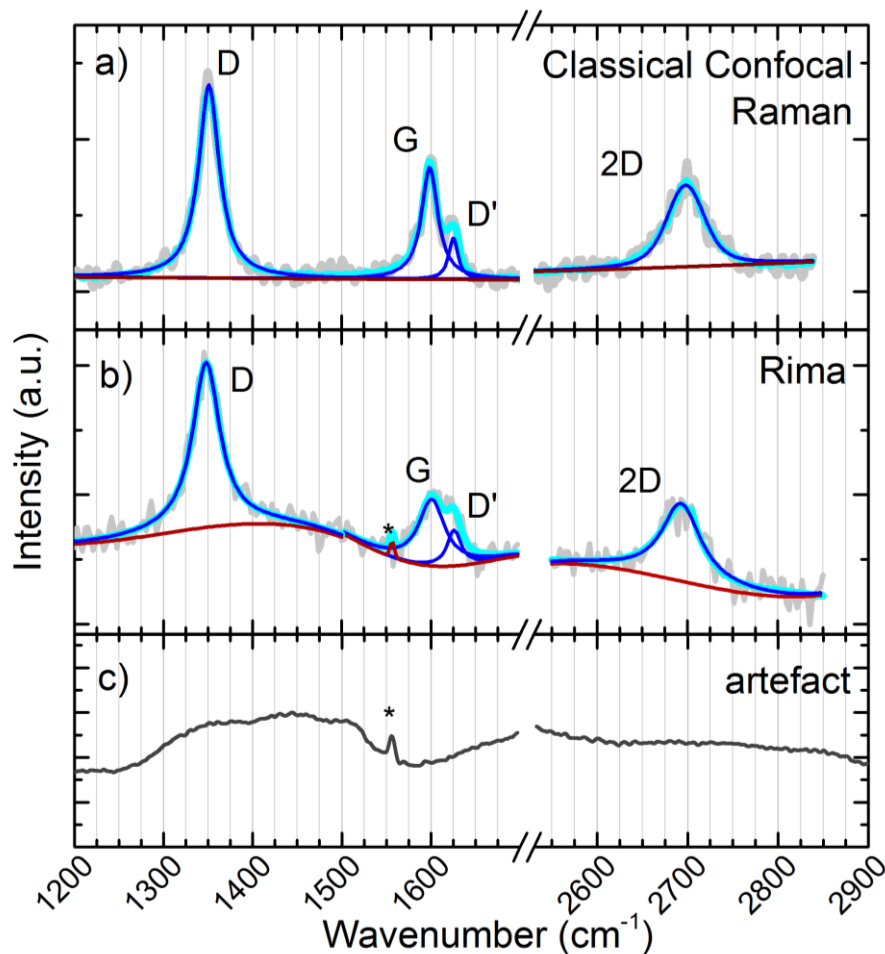


Figure 2.2.2: Comparison of Raman spectra obtained either from a conventional confocal (Renishaw inVia) mapping (a) or from the RIMA instrument (Photon etc) (b). (c) Typical spectra of the broad signal form artefacts in RIMA giving a singular line shape. Fits to the spectra and polynomial fit to the baseline are also shown. The sharp feature marked with \* is an instrument's artefact.

Overall, the spectra are alike in terms of linewidths and intensity ratios (see Section 3.2 for additional discussion). Fig 2.2.2c presents a Raman spectrum of bare cleaned SiO<sub>2</sub> (cleaned during 30 min in acetone at 60°C followed by three rinses in IPA for 10 min). Since SiO<sub>2</sub> has

no Raman peak in this spectral range, the resulting spectrum is only composed of parasitic lights (fluorescence and artefacts). It is worth highlighting that the data displayed in Fig. 2.2.2c were recorded at the same position on the CCD as that of the RIMA spectrum in Fig. 2.2.2b. A similar profile was actually obtained, which supports the conclusion that the baseline in the G&D' region on Fig. 2.2.2b is extrinsic to the graphene signal. Since graphene is present on only one of the samples, this comparison indicates, however, that the absolute intensity and shape of background signals vary from pixel to pixel, which makes baseline subtractions arduous. The nature of the artefacts is still under investigation, but it is currently believed to arise from fluorescence in the objectives.

Fitting parameters for the spectra (intensity, position, line width) can easily be presented either as maps or histograms. Already, these results are of interest for doping, strain and defect assessments [3,10]. Furthermore, the huge dataset provided by the RIMA cube gives access to extremely detailed statistical distributions and allows for a precise registration of the measurements taken on the same region before and after plasma treatments. To proceed, an image of logical value is extracted via a criterion on band parameters chosen for each measurements. Typically, a threshold on the absolute G-band intensity is used because it highlights distinguishable features from CVD-grown polycrystalline graphene films such as cracks and defects. Then an alignment using only rotation and translation of these two logical masks (0 or 1) are used to define a transform process that can be applied to band parameters to establish point-by-point behavior. Typical mean images are extracted as a confirmation (Supplementary Data IV) As discussed in Section 3.3, results show that the method allows a direct correlation of graphene initial properties with that of the resulting plasma-treated sample. At first, RIMA was used to study untreated graphene films. The large field of view enables a quantitatively evaluation of the graphene uniformity. Two areas were chosen alongside each other with a clear crack overlapping in the two selected regions. This is done to access the ability to extract band parameters from the raw data without any distortion on the output, but also to demonstrate the ability of the RIMA to probe area larger than the actual field of view of the setup. Systematic variations of intensity ratios due to an incorrect data processing would be made visible when aligning the two images. Measuring two zones also enable to probe variations of the signal that range over a single field of view. This crack and others small defects facilitate

the alignment of the two sets of data after processing. Hence, it is possible to obtain an image of all parameters used to fit graphene peaks. For examples, Fig. 2.2.3 presents images of intensity peak ratio of the D over G bands (D:G), 2D over G bands (2D:G) as well as the position and FWHM of the 2D band for the two stitched areas.

Overall the sample reveal an average D:G value of 0-0.1 with some small spots where the local signal rises up to 0.3. These damaged areas of around 500 nm wide are spread on the regions. These are also aligned on well-defined lines. Looking at the overlapping area between the two regions, a fairly good stitching is obtained. The values of the point defects and the background of graphene with low defect density have a good match. The 2D:G mapping shows a much larger variation; its values are contained between 1 and 4, with a mean value of around 2.5. There are clear disparities between several areas on the same region. These distinct areas are absent of the D:G mapping and thus 2D:G ratio can provide additional meaningful information. The last two mappings show 2D bands features. Peak positions show variations of strain around defect points identified in the D:G mappings. . In the case of the 2D bandwidth, a maximum value below  $45\text{ cm}^{-1}$  is observed while the mean value is around  $32\text{ cm}^{-1}$ . Consequently, it rules out possible bilayer presence on the pristine graphene. Furthermore, lines can be noticed that seem to define domains between graphene grains [9]. It is interesting to note that such domains are not observed when imaging band intensities ratio.

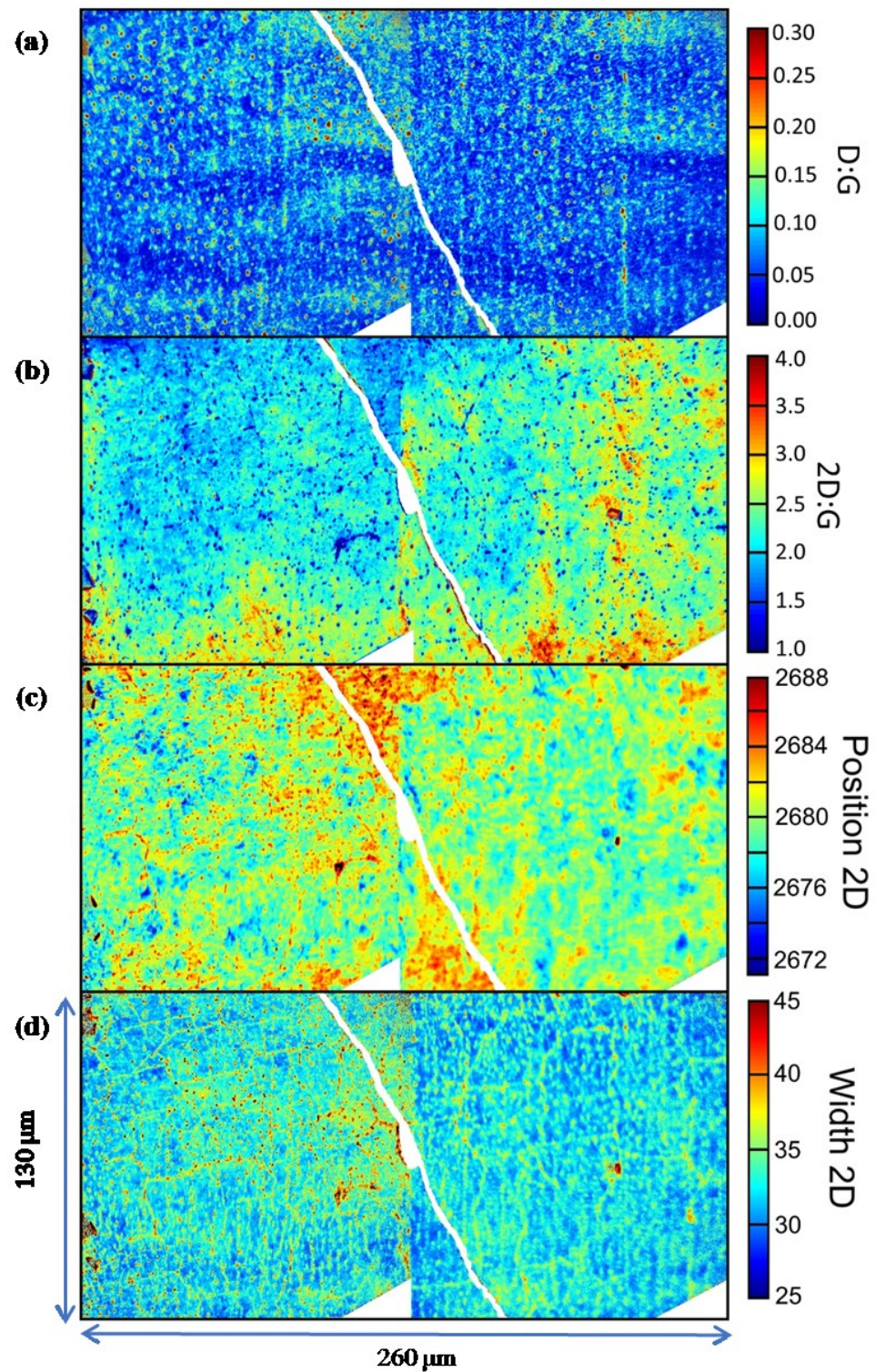


Figure 2.2.3: Juxtaposition of two zones of untreated graphene. (a) 2D:G ratio, (b) D:G ratio, (c) 2D position and (d) 2D width are presented.

This will be further discussed in Section 3.2. The values of the overall parameters of the fits are latter presented in Section 3.2 Tab. 1. All those values are expected for CVD-grown polycrystalline graphene films [1]. Ultimately, the overall good stitching of the two images underlines the coherence of the RIMA method over the whole surface probed by the measurements. Still, some discrepancies are noted and might originated from the non-flat laser irradiation of the probed area. Although the beam-shaping module enable a laser profile as flat as possible, some variations of the intensity are still present of the side (~15% variation across the field view[3]). This change in the ratio between the Raman bands and the singularly shaped background alters the polynomial baseline subtraction leading to slight variation at the edges. Yet, these variations are very small. Consequently, the level of details enabled by the high spatial resolution combined with the large field view opens the way to better understanding of graphene properties and processing.

The same sample presented in Section 3.1 was exposed to the argon ICP plasma and the same region was then measured in order to follow its evolution following the low-pressure plasma treatment (graphene-plasma interaction is dominated by very-low-energy ion irradiation [2]). For simplicity, only the left most region displayed in Fig. 2.2.3 was characterized. In order to consolidate measurements made by RIMA, the region was analyzed with a conventional confocal Raman system (Renishaw inVia). A high-resolution mapping of 1296 points was completed with a step of 4  $\mu\text{m}$  to evaluate local states of the graphene in a processing time comparable to the one of RIMA measurements.

Fig. 2.2.4 presents D:G, 2D:G and D:D' ratios images of the same region evaluated by RIMA and by conventional confocal Raman. Compared to the untreated spectra, there is a clear increase of D:G ratio evaluated by both methods from 0.2 up to 3.5. Both methods further present a gradient of the peak ratio on the whole region from 3.5 down to 1. With RIMA images, some domains can be observed delimited by thin lines with low values of D:G around 1 with higher values in the center from 1.5 to 3. Such patterns can hardly be observed with classical Raman mapping. In the case of the 2D:G ratio, both approaches display a low value below 1.4 down to 0.2 with a gradient across the region.

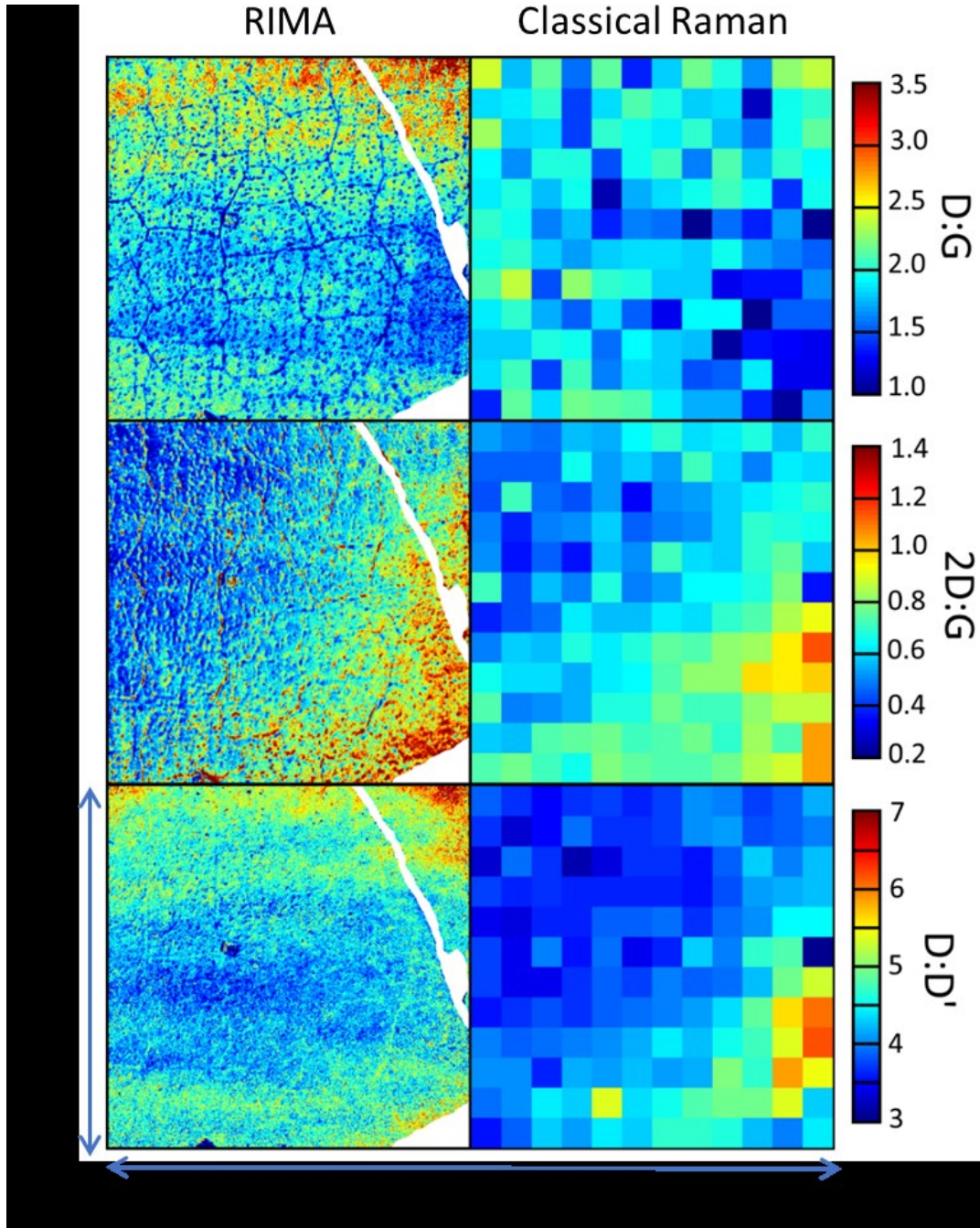


Figure 2.2.4: Comparison of (a)  $D:G$ , (b)  $2D:G$  and (c)  $D:D'$  ratios for mapping taken with RIMA (left column) and conventional confocal Raman (inVia) (right column).

The shape, orientation and intensity of the gradient are in good agreements and therefore confirms the fitting methods of the acquired datasets with RIMA. The  $2D:G$  ratio map also shows the same domains obtained with  $D:G$  ratio. This time, they are delimited by higher value of  $2D:G$ . Finally, the  $D:D'$  ratio values vary between 3 and 7. However, the gradient determined

with the two techniques are quite different. Values from the upper part of RIMA image are higher ( $>6$ ) than those with low-resolution Raman ( $\sim 3$ ). This discrepancy might arise from the difficulty to fit the D' peak, given its low value and its proximity with the G peak. The singular shape of the artifact in this spectral range is also cumbersome.

It is interesting to note that domains highlighted by the 2D linewidth of the untreated graphene (Fig. 2.2.3) clearly appear on maps of the D:G and 2D:G peak ratios after plasma exposure. The delimitation of domain growth given by a low value of D:G and a high value of 2D:G suggests that these domain lines are affected differently by the plasma treatment than the rest of graphene. Domain boundaries are typically interpreted as dislocations and hence, these defect lines are *a priori* more resistant to plasma irradiation. Giving larger 2D:G and lower D:G, the apparent resistance of these boundaries requires more testing by, for example, varying the approach angle of the bombarding ions to compensate the curvature around those dislocations [9]. To adequately show the effect of the plasma on the state of CVD-grown polycrystalline graphene films, it is relevant to examine the evolution of other band parameters. Table 2.2.1 summarizes mean values of different parameters of interest along with the standard deviations obtained before and after plasma treatment within the studied area. Correction are applied on the band parameters obtained with the confocal setup to take into account the different excitation energy of both setup (Supplementary Data VI).

First, results obtained from RIMA and InVia measurements on the same area of the treated sample are compared. Fig. 2.2.4 demonstrated that the behavior of the band parameters is coherent between both methods; gradient of similar amplitude are obtained. Nevertheless, the value themselves slightly differ from a method to the other. Geometric concerns are key to explain these variations. Indeed, the 1  $\mu\text{m}$  diameter of the spot for the laser irradiation in the case of standard confocal signal is quite large compared to the average distance between graphene boundaries and spots increased disorder (2-4  $\mu\text{m}$ ) (low D:G at Fig. 2.2.4.a). This implies that random measurements taken over this area will be affected by those regions. Besides, those domains present much stronger Raman intensity (2-3 times the signal of graphene domains) and therefore the value of these points is altered. This play an important role in explaining the discrepancies between the two methods.

Table 2.2.1 : Comparison for various Raman parameters between untreated and plasma-treated monolayer graphene samples. The mean and standard deviations are also presented. A threshold on the G band intensity is used to remove points with no graphene (e.g. the crack and where the image is cropped on the side)

Expression	inVia not corrected		inVia corrected		Rima Treated		Rima Untreated	
	Mean	STD	Mean	STD	Mean	STD	Mean	STD
2D:G	0.79	0.18	-		0.66	0.19	2.3	0.4
D:G	1.65	0.31	1.89	0.36	2.10	0.46	0.089	0.047
D:D'	3.77	4.08	-	-	4.35	0.42	-	-
D:2D	2.21	0.67	-	-	3.39	1.25	0.04	0.02
$\Gamma_G$	23.69	3.28	23.69	3.28	26.91	3.53	12.9	1.7
$\Gamma_{2D}$	50.22	4.61	50.22	4.61	61.64	6.34	31.4	1.5
$\Gamma_D$	30.31	3.43	30.31	3.43	34.72	1.24	22.8	2.5
$\omega_G$	1595.9	2.1	1596.4	2.1	1600.3	1.2	1587.2	1.3
$\omega_{2D}$	2697.5	2.4	2705.8	2.4	2688.0	3.2	2679.8	1.5
$\omega_D$	1350.8	1.3	1355.0	1.3	1348.5	0.3	1343.6	2.5

The rather destructive effect of the low-pressure plasma treatment examined in this study is observed by a decrease of 2D:G ratio with the simultaneous increase of the D:G ratio and D:2D. 2D:G values below 1 indicates that the graphene is starting to undergo a transition towards amorphization [10,11]. The D:D' peak ratio of 4.4 indicates that the nature of the defects is a combination of vacancy and boundaries defects [10]. This is only true if the graphene is at the beginning of the amorphous stage, which is believed to be the case since the 2D:G ratio is still high enough. For both RIMA and conventional Raman, spectra show no sign of a broad Raman band between the D and the G band characteristic of amorphous carbons [12]. Furthermore, the broadening of the peaks width of all bands further supports high damage generated by the plasma treatment [13]. The increase of the 2D and D mean positions suggests the presence of a variation of strain and/or doping of the graphene sample [14]. However, the increase of the G band position being much larger than the increase of 2D band position implies significant p-doping levels probably due to the creations of holes by the ion bombardment.

However, one must be cautious when extracting values of doping and strain. Indeed, the dependence of bands energy on the doping level and the strain is strongly dependent on the state

of the graphene. Damaged [15] and pristine [14,16] graphene reveal different G and 2D band shifts as a function of charge carrier modification. Additionally, graphene from CVD grown [17] and exfoliated [14,16] graphene also reveal different line-shifts behavior when subjected to strain. Further investigation on a per sample basis are needed to extract strain and doping mapping from RIMA measurements.

The comparison between untreated and plasma-treated states of the graphene sample goes beyond the mere analysis of the mean values and standard deviations. As discussed in Section 2.1, the high number of points and good spatial resolution in RIMA maps allow easy registration of the same zone for subsequent measurements. By following the process described above, one can easily link the final state of a sample to the graphene properties taken before plasma treatment at the exact same position. Achieving the same registration precision with a conventional confocal Raman setup would require excessively long acquisition (very high spatial resolution) and RIMA is therefore clearly distinct for that purpose.

The method of characterization presented above is, to our knowledge, absent in the literature, even though the unique correlations this method can provide are numerous. Using the dataset of both states of the same graphene sample, one can present the results of the plasma treatment as a double-histogram of two functions of the Raman parameters. The number of available output distribution is enormous. On one hand, we would like to focus on D:G, 2D:G, D:D' or  $\Gamma_G$  parameters to highlight the effect of plasma-induced damage. On the other hand, it seems interesting to explore the variation of the G band position versus the initial position of the 2D band to study strain effect on doping. Clearly, a whole new analysis platform for the study of graphene physics and chemistry is enabled by this method, but we will rather focus on a subset of parameters with the associated interpretation so as to demonstrate the usefulness of the method.

As an example, Fig. 2.2.5 presents the statistical distribution of the variation of 2D:G ratio ( $2D:G_{final} - 2D:G_{initial}$ ) as a function of the initial 2D:G ratio (pristine graphene film). This plot highlights a specific behavior in these histograms through a normalization along one axis to allow the visualization of the change in distribution of a first parameter (here a variation of

2D:G) as a function of another parameters (here 2D:G ratio). A straight tendency is obtained; the diminution of the 2D:G ratio is much larger for points with higher initial 2D:G ratios (i.e. higher quality graphene). This is expected since the decrease of 2D:G ratio is smaller when the state of the graphene is brought towards amorphization [10].

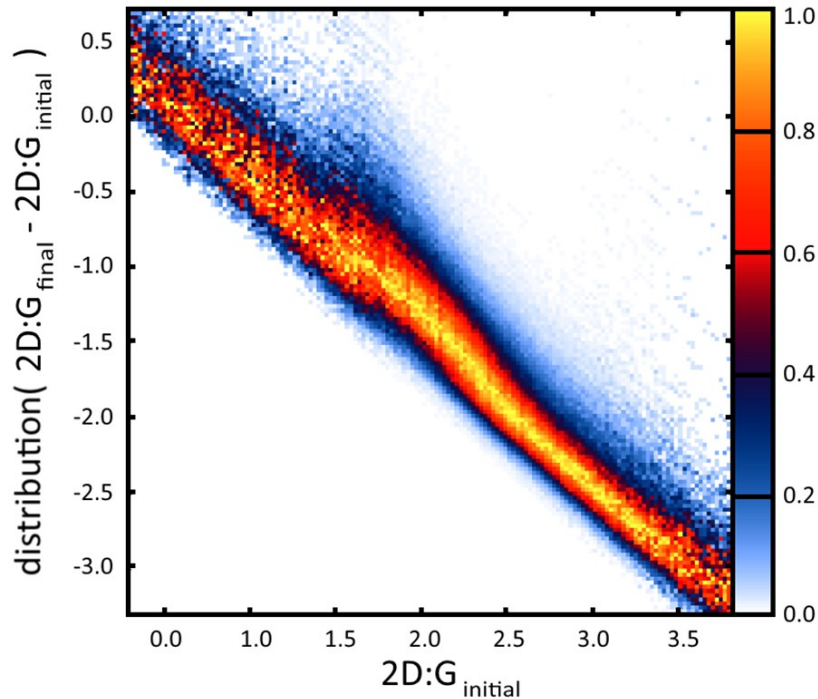


Figure 2.2.5: Distribution of the variation of 2D:G ratio as a function of the initial 2D:G ratio. High quality graphene undergoes a larger decrease than what is seen in regions of low quality graphene.

The same kind of analysis is possible using the D:G ratio and D:2D ratio. D:G is widely used in the literature, but its value is susceptible to change with doping while D:2D is independent of doping [15,16] and increases with disorder. Indeed, Fig. 2.2.6 presents the distribution of the variation of D:G ratio as a function of the initial D:G ratio. The distribution is much broader and the disparity between the variation of the D:G ratio for high quality (low initial D:G) and poor quality (high initial D:G) is much smaller. The same is done for the ratio D:2D at Fig. 2.2.7. A similar trend is observed. Initially, low damaged graphene undergoes a stronger increase of the D:2D ratio. Both results support the fact that initially-damaged graphene regions can withstand higher plasma treatment. The distribution of the D:2D increase of initially low damaged

graphene is much wider than the one of for the ratio D:G. Further works are needed to extract additional information from those distributions, which is outside the scope of this paper.

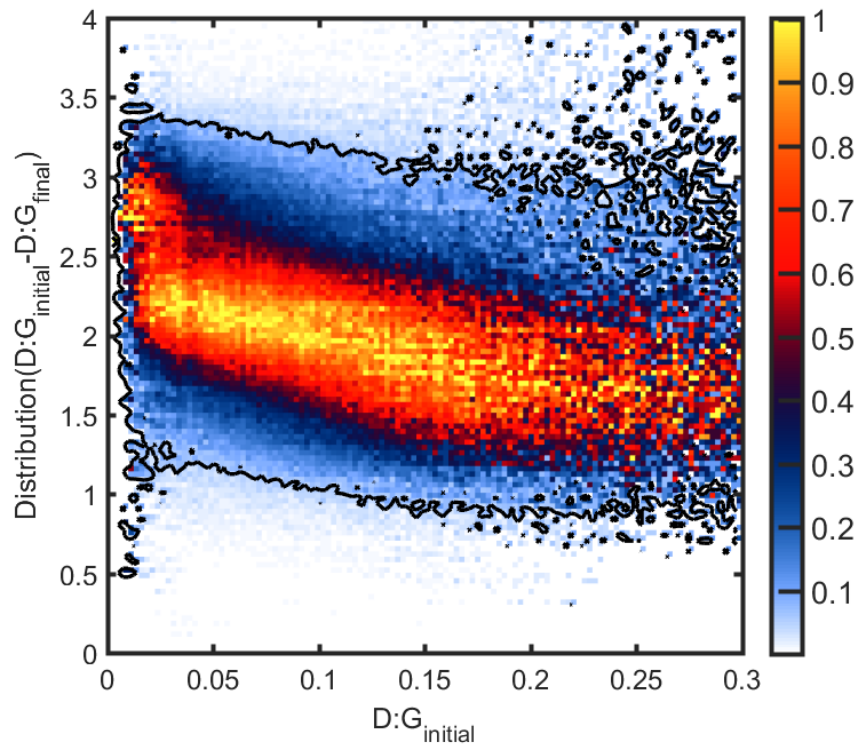


Figure 2.2.6: Distribution of the variation of D:G ratio as a function of the initial D:G ratio. Higher quality graphene undergoes a larger increase of D:G values compared to lower quality graphene. The distribution of the D:G ratio is wider for initially larger D:G ratio

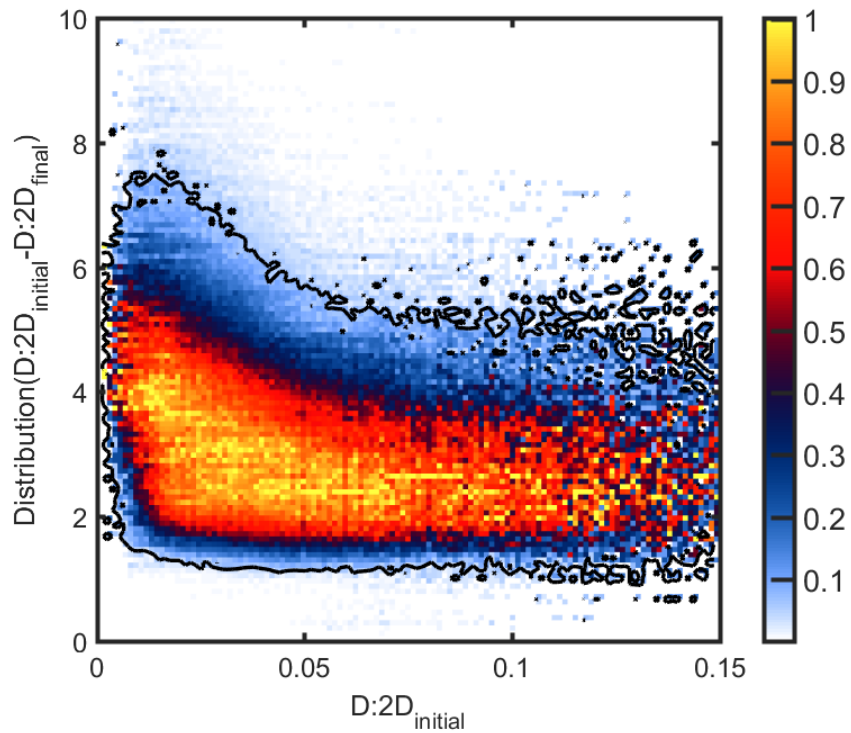


Figure 2.2.7: Distribution of the variation of D:2D ratio as a function of the initial D:2D ratio. Higher quality graphene undergoes a larger increase of D:2D values compared to lower quality graphene. The distribution of the D:2D ratio is wider for initially low D:2D ratio.

While the promises of Raman spectroscopy in the study of graphene properties are undeniable, the quantitative information it provides on damage, strain and doping remains local. By taking advantage of the high-throughput Hyperspectral Raman Imaging (RIMA) instrument recently highlighted in the literature [3], we have developed a refined method to characterize graphene on a macroscopic scale. Through careful baseline subtraction and noise filtering, high-quality distributions of band parameters became obtainable. With proper “stitching” of the Raman maps, the results show that the method adds several benefits to conventional Raman analysis by comparing registered information before and after structural or chemical modifications. Here, results with the method show how small heterogeneities (local defects, grain boundaries, *etc.*) in pristine graphene materials influence the outcomes of low-pressure plasma treatments. Graphene grain boundaries are clearly visible in the maps using the width of the 2D band for the untreated sample. After low-energy ion irradiation in a low-pressure argon plasma, these linear domains become more distinct using maps of the D:G and 2D:G ratios.

Further registration grants access to the distributions and indicates that the Raman spectra of initially-damaged graphene regions (boundaries) evolves more slowly than that of undamaged regions under plasma treatments. This new method is bound to evolve with the development of new tools capable of extracting meaningful information on graphene physics and chemistry.

## **ACKNOWLEDGMENTS**

This work was financially supported by the National Science and Engineering Research Council (NSERC), PRIMA-Québec, Plasmionique inc., Photon Etc., the Canada Research Chair and the Fonds de Recherche du Québec – Nature et Technologies (FRQNT).

## **DATA AVAILABILITY**

The data that support the findings of this study are available from the corresponding author upon reasonable request.

## SUPPLEMENTARY DATA

### I. PLASMA TREATMENT CONDITIONS

Graphene was exposed to a planar-type Inductively Induced Plasma (ICP) operated in nominally pure argon. The setup is described in detail elsewhere [2]. The residual pressure ( $1.5 \times 10^{-7}$  Torr) was obtained with an association of rotary and turbomolecular pumps. The argon mass flow was fixed at 20 sccm and the operation pressure was maintained at 5 mTorr with an injected power of 500 W. A matchbox kept the reflected power at 0 W during the whole plasma treatment. Plasma characteristics were assessed by a combination of Langmuir probe and Plasma Sampling Mass spectroscopy such that a good control of the Ions Energy Distribution Function (IEDF) following the acceleration of positive ions in the plasma sheath was obtained. In the experimental conditions investigated, the IEDF was quite narrow ( $\sim 1.2$  eV) and centered at 15 eV. Furthermore, an ion fluence of  $2.7 \times 10^{17}$  part.cm<sup>-2</sup> was achieved using an ion density of  $n_i = 1.1 \times 10^{11}$  cm<sup>-3</sup>, an ion Bohm velocity  $v_b = 2.7 \times 10^5$  cm.s<sup>-1</sup> and a plasma exposure time of 15 s. Furthermore, Optical Absorption Spectroscopy (OAS) was used to probe metastable and resonant argon species in the plasma. Again, in the experimental conditions investigated, graphene-plasma interaction is dominated by very-low-energy ion irradiation [2].

## II. PCA-ASSISTED DATA NOISE FILTERING

Before the decomposition into principal component analysis, the mean spectrum is substrate to all the spectra. Here are presented the mean spectra for the various measurements.

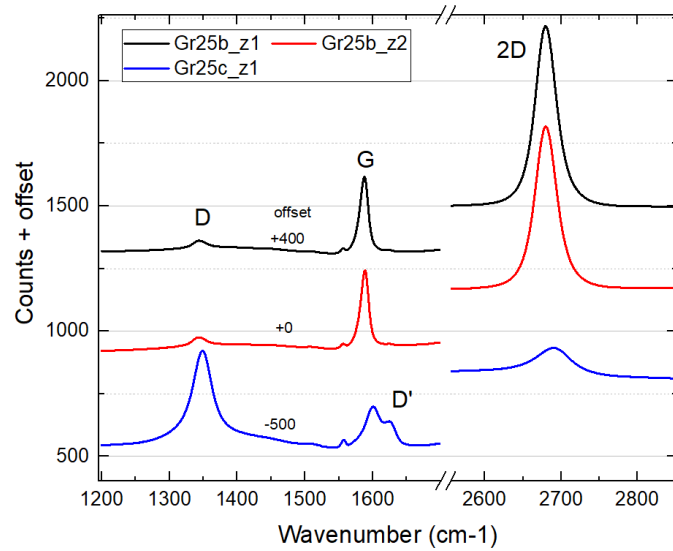


Figure 2.2.S1. Mean spectra for the two regions before and after the plasma treatment process. The cubes of untreated graphene (black and red) and the cube for the treated graphene (blue) are presented.

A graphical confirmation of the number of components to consider is shown at Figure 2.2.S2. Typically, the number of components retain should be higher than the change in curvature of the cumulative eigenvalues of the components. [19]

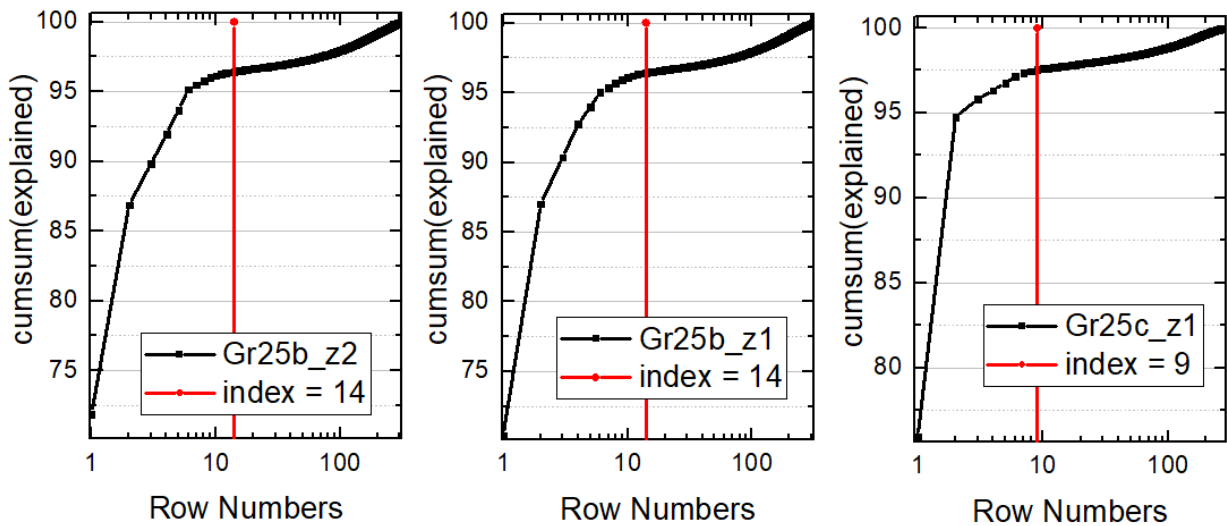


Figure 2.2.S2. Cumulative eigenvalues of sorted principal components as a function of component index. The red line reveals the number of components retained for reconstruction as calculated from the criteria presented in the manuscript.

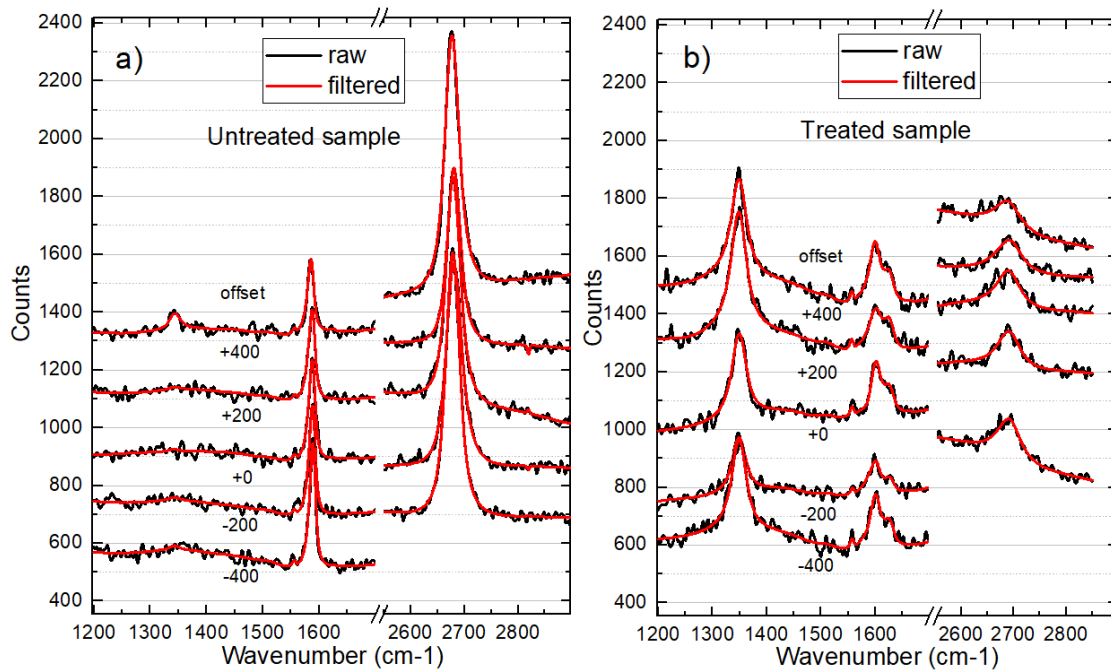


Figure 2.2.S3. Small sample of spectra for both the untreated (a) and the treated (b) state of the graphene. Raw data (black) and filtered data (red) are shown.

### III. POLYNOMIAL BASELINE SUBTRACTION

A key challenge for RIMA analysis is the subtraction of the artefact. Overfitting of the G/D' regions could induce large changes in the linewidth and intensity of the D' and G bands. To show the potential of the RIMA method without having to detail exhaustive processes, a commonly used method of baseline subtraction is chosen: polynomial fitting. More advanced methods are currently being studied and are part of another publication.

First, the fit is performed for increasing order of the polynomial baseline. Lower orders are automatically discarded when the fit clearly is inadequate. The next to polynomial order are then selected and the authors proceed to a careful study of the band parameters.

The shape of the artefact presents each band position varies drastically. Around the D band, a curve with a maximum around  $1400\text{ cm}^{-1}$  is present, while the bassline around the G and D' band contains a minimum around  $1600\text{ cm}^{-1}$ . The artefact at the 2D band as a shape that presents less curvature. The expected order of the later is thus smaller.

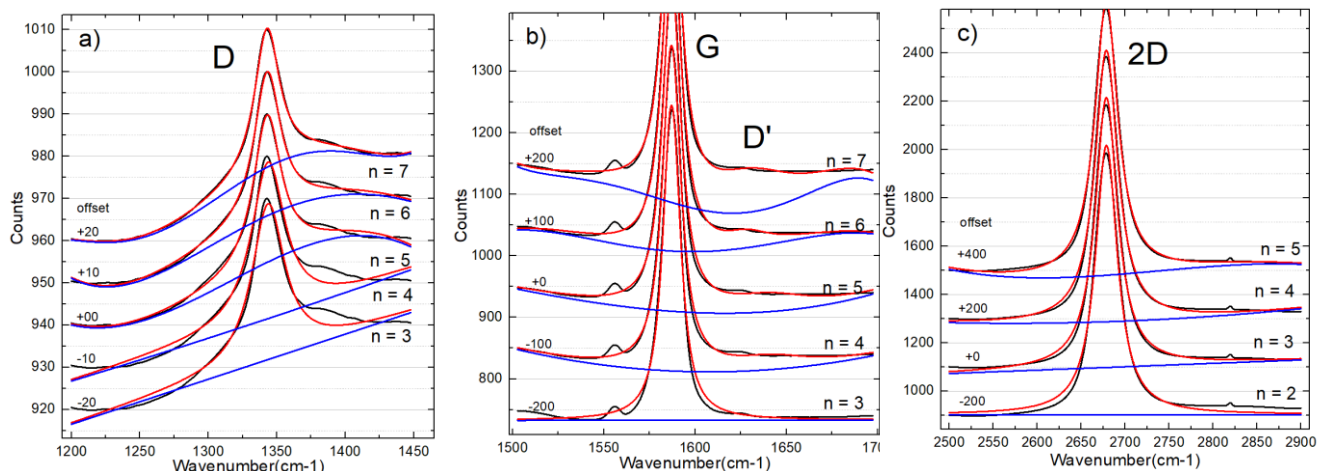


Figure 2.2.S4. Example of various curve fit with different order of polynomial baseline for a point of the untreated graphene sample. Regions of the (a) D, (b) G and (c) 2D bands are shown.

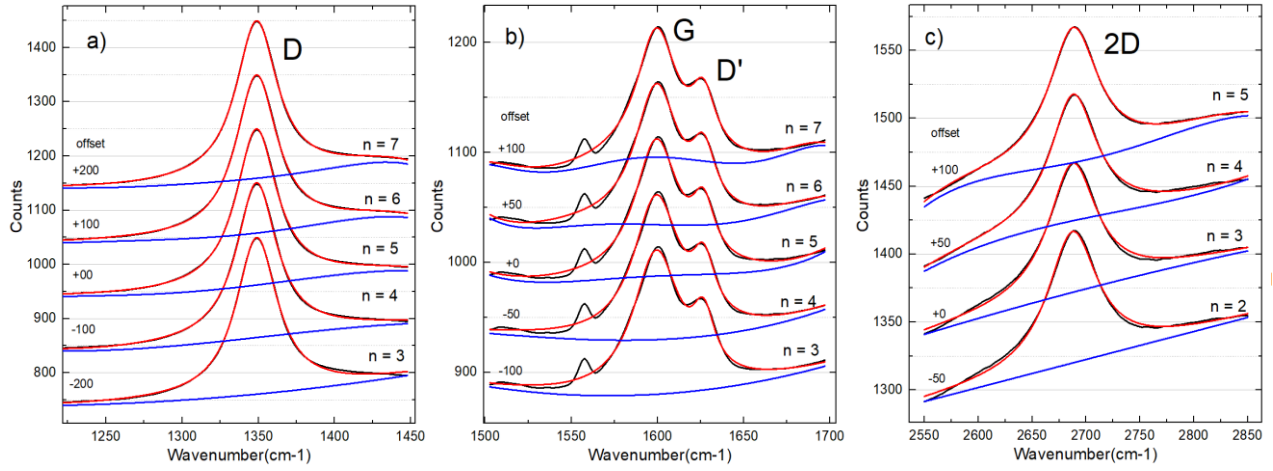


Figure 2.2.S5. Example of various curve fit with different order of polynomial baseline for a point of the plasma treated graphene sample. Regions of the (a) D, (b) G and (c) 2D bands are shown.

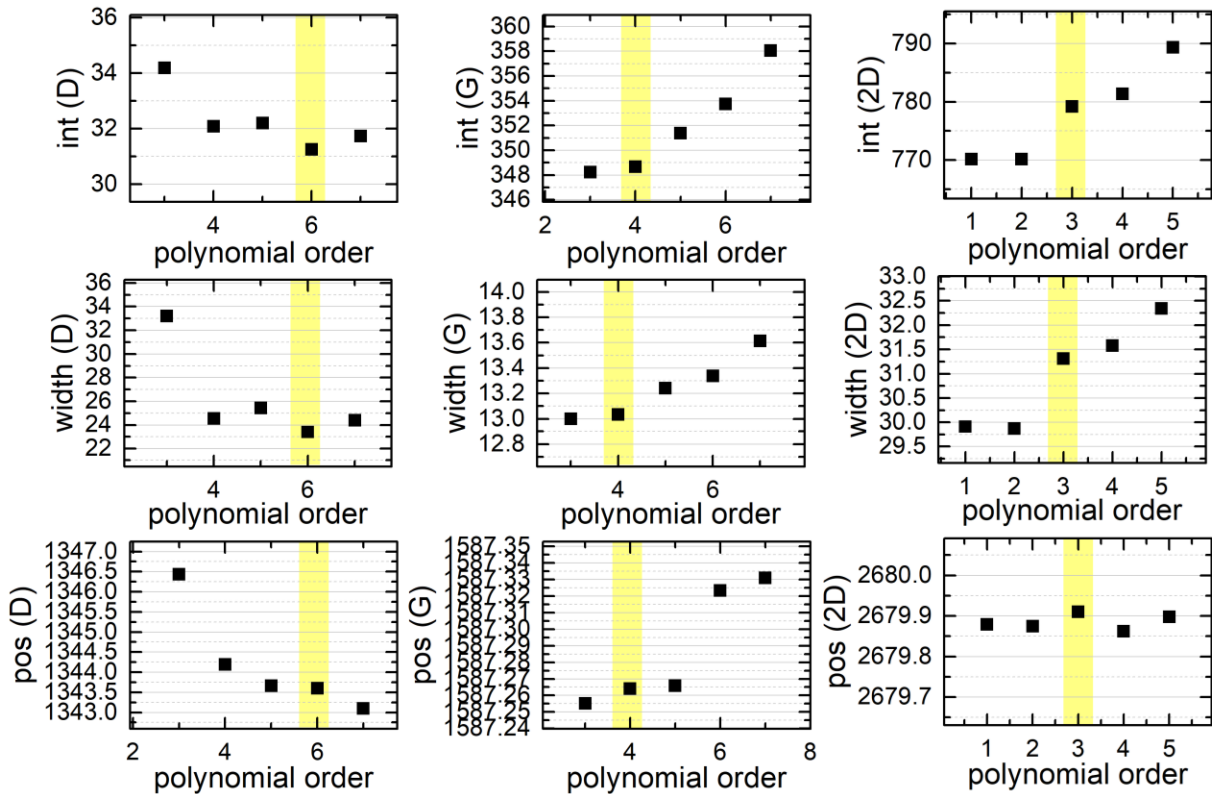


Figure 2.2.S6. Mean values of peak parameters for various order of the polynomial baseline subtraction for the untreated sample. Chosen polynomial order are highlighted in yellow. D' values not shown since it is too small or irrelevant for undamaged graphene.

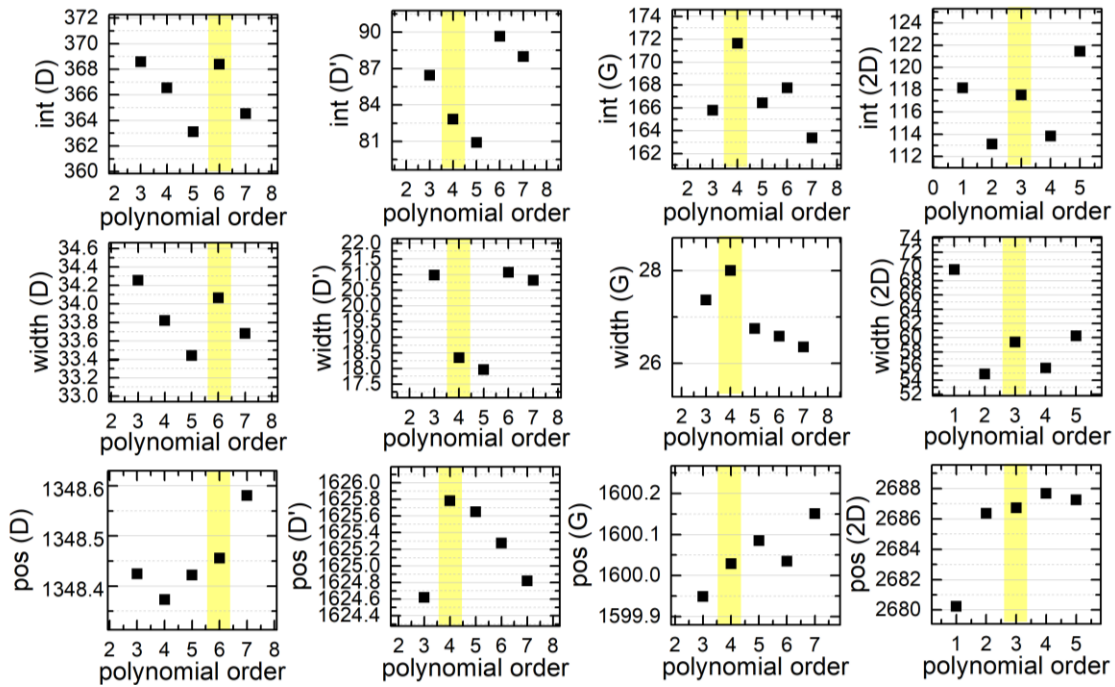


Figure 2.2.S7. Mean values of peak parameters for various order of the polynomial baseline subtraction for the treated sample. Chosen polynomial order are highlighted in yellow

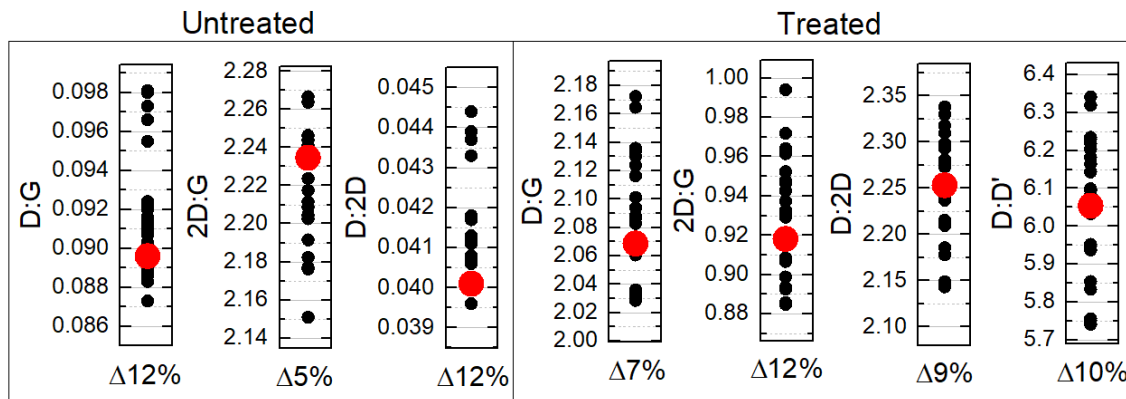


Figure 2.2.S8. All different values of line ratio possible when considering the polynomial orders presented in Figure 2.2.S6 and Figure 2.2.S7. The ratio for the chosen order of polynomial baseline fitting is presented in red. Under each graph is presented the maximum value of deviation (max-min) over the value in red. These percent are shown very small; thus, the order of the polynomial does not impact considerably the data in the manuscript.

#### IV. CUBE REGISTRATION

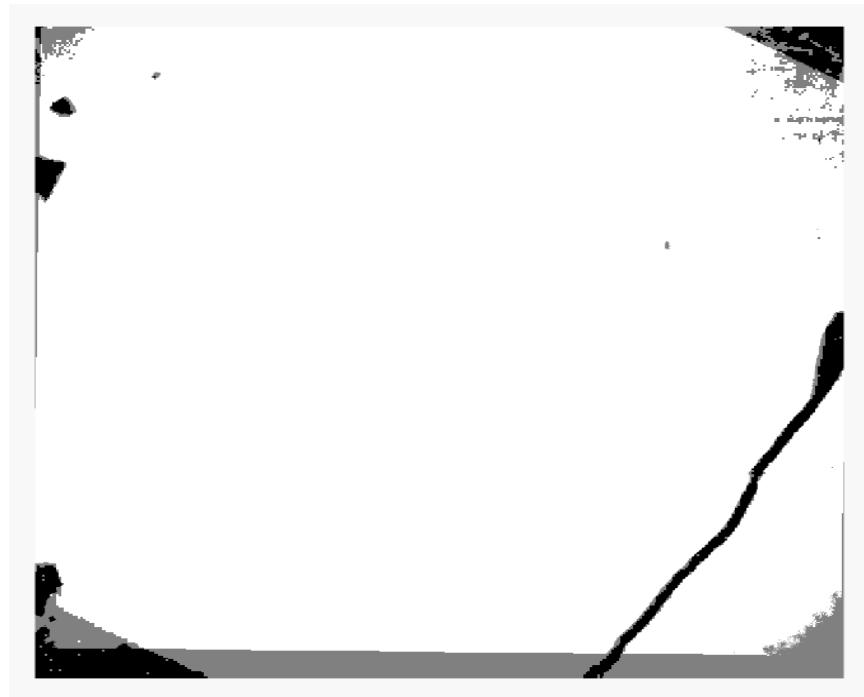


Figure 2.2.S9 - Mean image for the image registration of an untreated zone and the same zone after plasma treatment. A criterion based on the G-band intensity is used to distinguish between specific zones within the graphene sample. Defects are therefore aligned so as to allow point by point analysis. Two basis of logical values are aligned. Points where both signal are 1 appear black; points where both signal are 0 appear white and points which values are opposite appear as grey.

### III. EXCITATION ENERGY CORRECTION

To properly compare the data between the inVia and the RIMA measurements, corrections must be applied to consider the difference excitation energy (inVia : 514 nm (2.41 eV), RIMA : 532 nm (2.33 eV)).

The 2D band suffer a strong shift of  $104 \text{ cm}^{-1}/\text{eV}$ , the D a band a  $52 \text{ cm}^{-1}/\text{eV}$  shift and the G band a slight  $6 \text{ cm}^{-1}/\text{eV}$  [20] with the excitation energy. The widths of the bands are not affected by the excitation energy; no correction is required. The line ratio D:G value is higher for low excitation energy and varies with the excitation energy at the power 4 [20]. Thus a factor of  $(532/514)^4 = 1.1476$  is applied to the D:G extracted from the standard confocal setup at 514 nm. The value of the dependence of the D:D' line ratio is dependent to the nature of defects [11,21] and thus could not be corrected without further assessments. To the knowledge of the authors, the correction for the 2D:G is not discussed in the literature.

Table 2.2.2 – Raman spectroscopy comparison between standard confocal measurements (with inVia setup) and Rima measurements for the treated state and untreated state of the graphene.

Expression	inVia not corrected		inVia corrected	
	Mean	STD	Mean	STD
2D:G	0.79	0.18	-	
D:G	1.65	0.31	1.89	0.36
D:D'	3.77	4.08	-	-
D:2D			-	-
$\Gamma_G$	23.69	3.28	23.69	3.28
$\Gamma_{2D}$	50.22	4.61	50.22	4.61
$\Gamma_D$	30.31	3.43	30.31	3.43
$\omega_G$	1595.9	2.1	1596.4	2.1
$\omega_{2D}$	2697.5	2.4	2705.8	2.4
$\omega_D$	1350.8	1.3	1355.0	1.3

## REFERENCES

- [1] A.C. Ferrari, D.M. Basko, Raman spectroscopy as a versatile tool for studying the properties of graphene, *Nat. Nanotechnol.* 8 (2013) 235–246. <https://doi.org/DOI 10.1038/nano.2013.46>.
- [2] P. Vinchon, X. Glad, G. Robert-Bigras, A. Sarkissian, R. Martel, L. Stafford, Graphene under ultra-low energy ion irradiation: Investigation of the defect generation by low-pressure inductively coupled argon plasma treatments, *Submitt. J. Vac. Sci. Technol. A.* (2019).
- [3] E. Gaufrès, S. Marcet, V. Aymong, N.Y.W. Tang, A. Favron, F. Thouin, C. Allard, D. Rioux, N. Cottenye, M. Verhaegen, R. Martel, Hyperspectral Raman imaging using Bragg tunable filters of graphene and other low-dimensional materials, *J. Raman Spectrosc.* (2017). <https://doi.org/10.1002/jrs.5298>.
- [4] A. Roberts, D. Cormode, C. Reynolds, T. Newhouse-Illige, B.J. Leroy, A.S. Sandhu, Response of graphene to femtosecond high-intensity laser irradiation, *Appl. Phys. Lett.* 99 (2011) 1–4. <https://doi.org/10.1063/1.3623760>.
- [5] F. Castells, P. Laguna, L. S??rnmo, A. Bollmann, J.M. Roig, Principal component analysis in ECG signal processing, *EURASIP J. Adv. Signal Process.* 2007 (2007). <https://doi.org/10.1155/2007/74580>.
- [6] E. De la Hoz, E. De La Hoz, A. Ortiz, J. Ortega, B. Prieto, PCA filtering and probabilistic SOM for network intrusion detection, *Neurocomputing.* 164 (2015) 71–81. <https://doi.org/10.1016/j.neucom.2014.09.083>.
- [7] S. Choubak, P.L. Levesque, E. Gaufres, M. Biron, P. Desjardins, R. Martel, Graphene CVD: Interplay between growth and etching on morphology and stacking by hydrogen and oxidizing impurities, *J. Phys. Chem. C.* 118 (2014) 21532–21540. <https://doi.org/10.1021/jp5070215>.
- [8] L.G. Cançado, M. Gomes de Silva, E.H.M. Ferreira, F. Hof, Disentangling contributions of point and line defects in the Raman spectra of graphene-related materials, *2D Mater.* 4 (2017) 025039.
- [9] T. Lee, F.A. Mas'ud, M.J. Kim, H. Rho, Spatially resolved Raman spectroscopy of defects, strains, and strain fluctuations in domain structures of monolayer graphene, *Sci. Rep.* 7 (2017) 16681. <https://doi.org/10.1038/s41598-017-16969-z>.
- [10] A. Eckmann, A. Felten, A. Mishchenko, L. Britnell, R. Krupke, K.S. Novoselov, C. Casiraghi, Probing the nature of defects in graphene by Raman spectroscopy, *Nano Lett.* 12 (2012) 3925–3930. <https://doi.org/10.1021/nl300901a>.
- [11] A. Eckmann, A. Felten, I. Verzhbitskiy, R. Davey, C. Casiraghi, Raman study on defective graphene: Effect of the excitation energy, type, and amount of defects, *Phys. Rev. B.* 88 (2013) 035426. <https://doi.org/10.1103/PhysRevB.88.035426>.

- [12] A. Sadezky, H. Muckenhuber, H. Grothe, R. Niessner, U. P??schl, Raman microspectroscopy of soot and related carbonaceous materials: Spectral analysis and structural information, *Carbon N. Y.* 43 (2005) 1731–1742. <https://doi.org/10.1016/j.carbon.2005.02.018>.
- [13] Y.-B.B. Zhou, Z.-M.M. Liao, Y.-F.F. Wang, G.S. Duesberg, J. Xu, Q. Fu, X.-S.S. Wu, D.-P.P. Yu, Ion irradiation induced structural and electrical transition in graphene, *J. Chem. Phys.* 133 (2010) 234703. <https://doi.org/10.1063/1.3518979>.
- [14] J.E. Lee, G. Ahn, J. Shim, Y.S. Lee, S. Ryu, Optical separation of mechanical strain from charge doping in graphene, *Nat. Commun.* 3 (2012) 1024. <https://doi.org/10.1038/ncomms2022>.
- [15] M. Bruna, A. Ott, M. Ijas, D. Yoon, Doping dependence of the Raman spectrum of defected graphene, *ACS Nano.* 8 (2014) 7432–7441. <http://arxiv.org/abs/1405.4264>.
- [16] A. Das, S. Pisana, B. Chakraborty, S. Piscanec, S.K. Saha, U. V Waghmare, K.S. Novoselov, H.R. Krishnamurthy, a K. Geim, A.C. Ferrari, A.K. Sood, Monitoring dopants by Raman scattering in an electrochemically top-gated graphene transistor, *Nat. Nanotechnol.* 3 (2008) 210–215. <https://doi.org/10.1038/nnano.2008.67>.
- [17] M.A. Bissett, W. Izumida, R. Saito, H. Ago, Effect of Domain Boundaries on the Raman Spectra of Mechanically Strained Graphene, *ACS Nano.* 6 (2012) 10229–10238. <https://doi.org/10.1021/nn304032f>.
- [18] M.A. Bissett, M. Tsuji, H. Ago, Strain engineering the properties of graphene and other two-dimensional crystals, *Phys. Chem. Chem. Phys.* 16 (2014) 11124–11138. <https://doi.org/10.1039/c3cp55443k>.
- [19] P. Antonelli, H.E. Revercomb, L.A. Sromovsky, W.L. Smith, R.O. Knuteson, D.C. Tobin, R.K. Garcia, H.B. Howell, H.L. Huang, F.A. Best, A principal component noise filter for high spectral resolution infrared measurements, *J. Geophys. Res. D Atmos.* 109 (2004) 1–22. <https://doi.org/10.1029/2004JD004862>.
- [20] L.G. Cançado, A. Jorio, E.H.M. Ferreira, F. Stavale, C. a. Achete, R.B. Capaz, M.V.O. Moutinho, A. Lombardo, T.S. Kulmala, a. C. Ferrari, Quantifying defects in graphene via Raman spectroscopy at different excitation energies, *Nano Lett.* 11 (2011) 3190–3196. <https://doi.org/10.1021/nl201432g>.
- [21] P. Venezuela, M. Lazzeri, F. Mauri, Theory of double-resonant Raman spectra in graphene: Intensity and line shape of defect-induced and two-phonon bands, *Phys. Rev. B - Condens. Matter Mater. Phys.* 84 (2011) 1–25. <https://doi.org/10.1103/PhysRevB.84.035433>.

# **Chapitre 3 : Interactions plasma-graphène dans les plasmas d'argon en régime pulsé**

## **1. Étude résolue spatialement des dommages d'irradiations ionique**

Dans le chapitre précédent, on a pu voir l'impact impressionnant que peuvent avoir des traitements par plasma d'argon en régime continu sur le graphène malgré un temps d'exposition très court. Ceci complique l'étude des mécanismes contribuants à la génération des défauts. Puisqu'il devient difficile d'examiner les premières étapes avec de très faibles temps de traitement. Ainsi, une étude fondamentale de pointe du plasma a été réalisée dans le but de grandement diminuer l'apport d'énergie au graphène, que ce soit par les ions, les métastables et/ou les photons VUV. Pour ce faire, le plasma a été pulsé à une fréquence de 1kHz en diminuant simultanément la puissance et le rapport cyclique de la puissance radiofréquence. Une étude temporelle permet de déterminer la contribution de chaque espèce au cours du traitement du film de graphène. Par la suite, le graphène est exposé au plasma de nombreuses fois afin de générer progressivement des dommages. Entre chaque traitement, la même région est analysée par spectroscopie Raman hyperspectrale (RIMA).

Dans ce contexte, nous avons pu relier l'évolution des dommages à l'énergie apportée par l'irradiations ionique. De plus, pour la première fois à notre connaissance, nous avons noté que différences importantes selon les régions du graphène étudiées. En effet, les résultats révèlent que, dans nos conditions, les joints de grains du graphène sont plus résistants au traitement par plasma alors que ce sont les sections en théorie les plus sensibles. Ceci ne peut s'expliquer que par la capacité du graphène à se réorganiser et s'auto-réparer de manière préférentielle aux joints de grains. Or, comme ces phénomènes n'avaient jamais été explorés expérimentalement, encore moins dans les matériaux 2D comme le graphène, nous croyons qu'il s'agit d'une contribution majeure qui mérite une publication dans un journal à fort impact. Le manuscrit présenté plus bas est publié dans le journal *Nature Materials*, **20**, 49–54, (2021). Pour ce travail, j'ai effectué l'étude temporelle du plasma, les traitements par plasma du graphène ainsi que les mesures et les analyses RIMA. J'ai également développé le code matlab permettant d'identifier et d'aligner

les différentes zones étudiées. Enfin, j'ai rédigé une première version de l'article. X.Glad a participé activement à l'interprétation des données et à leurs mises en forme. G.R. Bigras a contribué à l'amélioration constante du code matlab utilisé pour interprétation des données obtenues au RIMA. Ce travail a été accomplis sous la supervision de R. Martel et L. Stafford en collaboration

# PREFERENTIAL SELF-HEALING AT GRAIN BOUNDARIES IN PLASMA-TREATED GRAPHENE

P. Vinchon<sup>1†</sup>, X. Glad<sup>1†</sup>, G. Robert Bigras<sup>1</sup>, R. Martel<sup>2</sup>, L. Stafford<sup>1</sup>

<sup>1</sup>Département de Physique, Université de Montréal, Montréal, Québec, CANADA.

<sup>2</sup>Département de Chimie, Université de Montréal, Montréal, Québec, CANADA.

<sup>†</sup>Co-authors sharing the same contribution to this work

Engineering of defects located in-grain or at grain boundary is central to the development of functional materials. Although there is a surge of interest in the formation, migration, and annihilation of defects during ion and plasma irradiation of bulk materials, these processes are rarely assessed in low-dimensional materials and remain mostly unexplored spectroscopically at the micrometer scale due to experimental limitations. Here, we use a hyperspectral Raman imaging scheme providing high selectivity and diffraction-limited spatial resolution to examine plasma-induced damage in a polycrystalline graphene film. Measurements conducted before and after very low-energy (11-13eV) ion bombardment show defect generation in graphene grains following a 0D defect curve, whereas domain boundaries tend to develop as 1D defects. Damage generation at grain boundaries is slower than within the grains, a behavior ascribed to preferential self-healing. These evidences of local defect migration and structural recovery in graphene shed light on the complexity of chemical and physical processes at the grain boundaries of 2D materials.

The outstanding properties of graphene makes this 2D materials attractive for many applications [1]. Large-area graphene grown by chemical vapor deposition (CVD) is interesting for flexible electronics, but the method produces polycrystalline films in which the graphene grains are attached together by covalent carbon bonds in various configurations. Beyond 1  $\mu\text{m}$  grain size, grain boundaries (GBs) limit the electronic properties of graphene [2] and hence, significant efforts has been invested towards increasing the grain size. Theoretically, GBs are not only limiting electronic transport [3], but can also, depending on their atomic arrangement, exhibit distinct mechanical [4], magnetic [5], and chemical [6] properties. Adjusting the gas flows during CVD [7,8] can tailor geometric aspects of the grains (tilt misorientation and edge type [3,9]), but the influence of GBs is difficult to avoid completely.

Post-growth modification, either by ion bombardment or by plasma treatment, are used to engineer graphene [1,10,11]. While high-energy ions lead to a sputtering of both the 2D materials and the substrate below, low-energy ions (typically below the displacement threshold energy of 18-22eV [12]) can be used for damage generation within the honeycomb lattice [13-15]. However, the formation, migration, and annihilation of defects have been difficult to probe experimentally [16-18]. Graphene damage evolution at GBs have been studied using transmission electron microscopy, but the material is unstable, even below 80kV [19-20]. The vibrational modes of graphene are sensitive to disorders and lattice perturbations [21] such that Raman spectroscopy is a relevant technique to study damage in graphene [22-23]. Highlighting different types of defects has, however, been difficult due to the low sensitivity and restrained spatial resolution of conventional Raman systems – mapping Raman is slow and the laser diameter ( $\sim 1\mu\text{m}$ ) is much larger than the defect size (around 2.8nm for GBs [24]). Such resolution limitations can be overcome by Tip Enhanced Raman Spectroscopy [25](TERS), which enables nano-scale studies of graphene.

In this work, the advantages of the RIMA<sup>TM</sup> system (Raman IMAge from Photon Etc.) are used to study plasma-induced damage in graphene. Hyperspectral Raman imaging with RIMA<sup>TM</sup> provides global Raman mapping ( $130\times 130\mu\text{m}^2$ ) with improved sensitivity and tremendous statistics ( $10^5\text{-}10^6$  spectra over the probed area), while maintaining

diffraction-limited spatial resolution [26]. RIMA<sup>TM</sup> measurements have been performed between each of the 12 subsequent plasma treatments and Raman band parameters were extracted and analyzed. It is demonstrated that graphene domains develop ion-induced 0D defects while pixels containing GBs reveal a greater density of 1D type defects. RIMA<sup>TM</sup> analysis further highlights a surprising resilience of GBs under very-low-energy ion irradiation. Such advances in non-destructive monitoring and plasma-induced modification of in-grain defects and grain boundaries in 2D materials can significantly benefit applications. This includes the ability to control CVD growth over very-large-area substrates as well as the doping and band gap tuning by ion or plasma irradiation.

Raman mappings with RIMA<sup>TM</sup> were performed at a laser wavelength of 532nm (2.33eV) on a CVD-grown polycrystalline monolayer graphene film transferred on SiO<sub>2</sub> substrate, from t=0s (pristine) to a total cumulated treatment time of t=1005s in a pulsed, inductively-coupled argon plasma (see Method section). Plasma-graphene interaction in such plasmas involves not only argon ions accelerated in the sheath surrounding the graphene sample, but also metastable argon atoms and photons. Over the range of experimental conditions examined, the contribution for each species to the total energy fluence is 43% by ions, 16% by metastable (and resonant) species, and 41% by photons (see section S-I). Finally, for a duty cycle of 10%, incident ions impinge on the graphene sample with 11-13eV of kinetic energy for 10% of the total treatment time (plasma *on*) and 1eV for the other 90% (plasma *off*).

Raman imaging was carried out after each subsequent treatment, giving 13 measurements over the same 130×130-μm<sup>2</sup> area of the graphene sample with 3·10<sup>5</sup> points each. Raman spectrum of pristine, single-layer graphene contains mainly 2 features: G (~1580cm<sup>-1</sup>) and 2D (~2690cm<sup>-1</sup>) bands. Disorder in graphene induces the D band (~1350cm<sup>-1</sup>). The expected behavior of the G, 2D and D band parameters (position  $\omega$ , full-width at half maximum  $\Gamma$ , peak intensity I, and peak area A) with damage, strain (tensile and compressive), number of layers in *ABAB*-stacking, and p- and n-doping are summarized in Section S-II.

The relevant Raman band parameters –thoroughly extracted according to section S-II– were plotted in a Cançado-like graph [23]. The results for pristine and plasma-treated graphene are

displayed in Figure 3.1.1. One notices that weak but distinct steps in the damage generation were obtained due to chosen plasma irradiation conditions. Results show a slow but constantly increasing evolution towards amorphization following the 0D defect type curve (top green curve). The *amorphization trajectory* is usually defined in stage 1 when progressing from undisturbed graphene to nanocrystalline graphene, and in stage 2 progressing towards amorphous carbon [27,28]. The delimitation between the two stages occurs at the maximum of  $I_D/I_G$  and  $A_D/A_G$ . Interestingly, the statistically meaningful  $3 \times 10^5$ -point distribution reveals a tail at higher  $\Gamma_G$  for  $t=0$  (black arrow) progressively switching to a lower  $A_D/A_G$  tail at  $t=340s$  (such as  $0.25\text{J}\cdot\text{cm}^{-2}$ ; red arrow). This induces a notable distribution broadening from the pristine state to 340s of cumulative plasma treatment. The distribution narrows down afterwards.

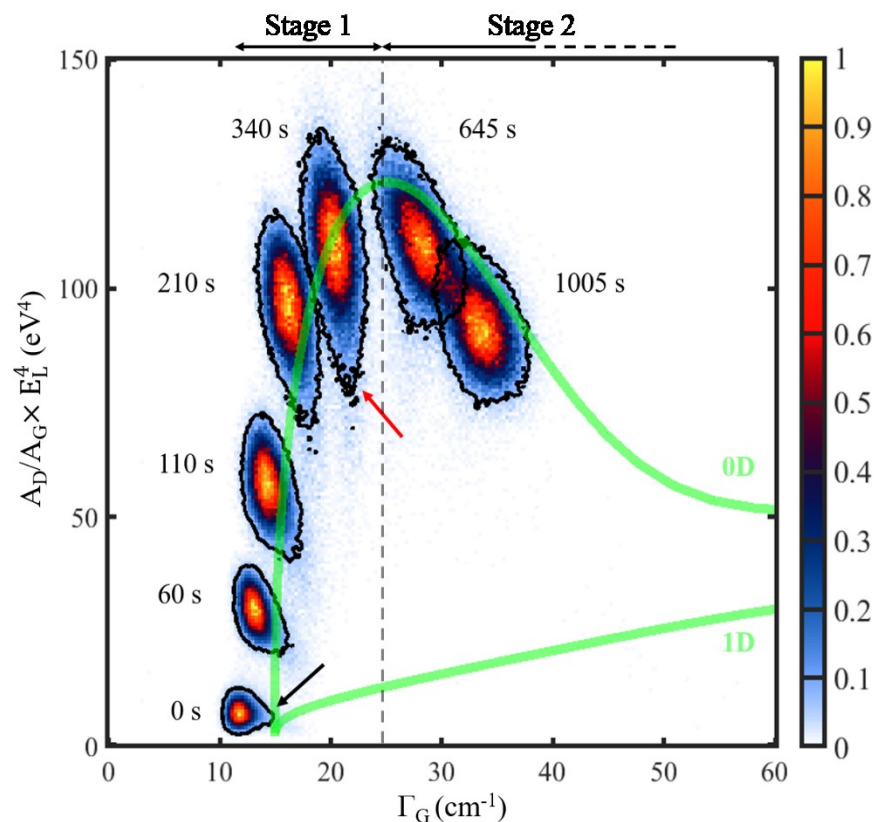


Figure 3.1.1. Subsequent graphene treatments plotted in a Cançado-like graph: evolution of  $A_D/AG \times E_L^4$  versus  $\Gamma_G$ . The colored scale is density-normalized. Green lines delimit the 0D and 1D defect-type evolutions. For clarity, black outlines highlight the 7 different sets of data. The gray dashed line delimits the 2 commonly reported stages of the amorphization trajectory.

A deeper understanding of this broadening in the statistics calls for spatially-resolved analysis. To do so, an *image registration* algorithm has been carried out to align together subsequent RIMA™ mappings. Figure 3.1.2 presents the laser-corrected  $A_D/A_G$  ratio (vertical scale of Fig. 3.1.2) for 3 cumulative times:  $t=0$ , 60 and 425s (such as 0,  $4.5 \times 10^{-2}$ , and  $0.32 \text{J}\cdot\text{cm}^{-2}$ , respectively). Figure 3.1.2a displays a great homogeneity with only local and randomly spread discrepancies exhibiting higher values; this demonstrates a good quality of CVD-grown graphene. However, figures 3.1.2b and 3.1.2c highlight continuous lines of notably lower values. This implies areas richer in 1D-type defects matching with graphene grain boundaries (GBs) [23]. This aspect was further confirmed by optical microscopy: linear discrepancies observed in RIMA™ perfectly matched with GBs (see section S-III).

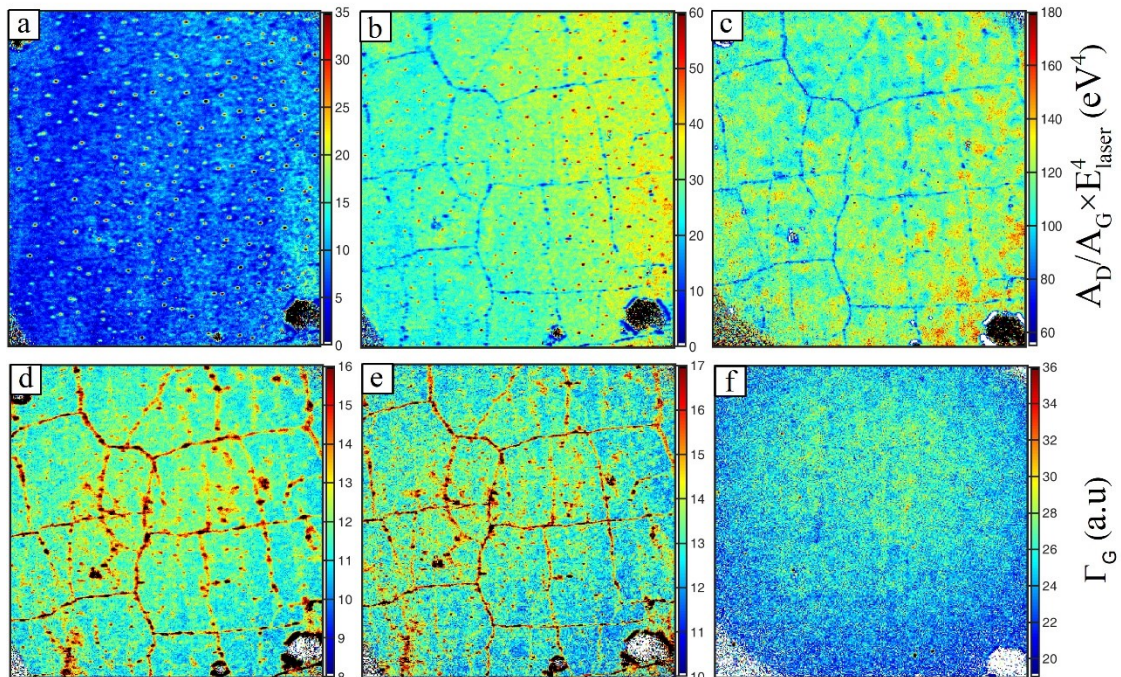


Figure 3.1.2. Evolution of band parameters mapping with plasma treatments.  $130 \times 130 \mu\text{m}^2$   $A_D/A_G \times E_L^4$  mappings of (a) pristine, (b) 60s and (c) 425s plasma-treated graphene. Note the color scale difference for each map.  $130 \times 130 \mu\text{m}^2$

Figure 3.1.2d-c displays a color map of the horizontal scale of Fig. 3.1.1 for the same area and same cumulative treatment times. Fig. 3.1.2d highlights areas of greater  $\Gamma_G$  values and thus displays a higher density of lattice disorder [23,29], especially from 1D-type defects. At  $t=0$

(Fig. 3.1.3a), GBs are discernable from graphene grains (GRs) with average values of  $\Gamma_{G,GB}=15\text{cm}^{-1}$  and  $\Gamma_{G,GR}=12\text{cm}^{-1}$ ; these are typical values for slightly-doped graphene [30]. Results are similar for  $t=60\text{s}$  (Fig. 3.1.3b) with values of  $\Gamma_{G,GB}=16.5\text{ cm}^{-1}$   $\Gamma_{G,GR}=13.5\text{cm}^{-1}$  for GBs and GRs, respectively. However, Fig. 3.1.2f ( $t=425\text{s}$ ) presents different look since the continuous lines no longer stand out and  $\Gamma_G$  has become rather homogeneous throughout the whole area probed by RIMA<sup>TM</sup> with an average value of  $25\text{ cm}^{-1}$ . This value coincides with maxima of  $I_D/I_G$  and  $A_D/A_G$ , which is often marked as the onset of graphite/graphene amorphization (Fig. 3.1.1) [27,28].

From these results, it can be seen that GBs exhibit more 1D-like defect properties than GRs, which follow exactly the 0D-type defect line. Hence, the local difference on the GBs seems linked to the broadening observed in the distribution of Fig. 3.1.1. This behavior is most likely related to the facts that graphene on SiO<sub>2</sub> is generally p-doped due to water-oxygen redox doping [31]: this influences both  $A_D/A_G$  [30] and  $\Gamma_G$  [32] (see Section S-II).  $\Gamma_G$  has also been shown to increase in CVD-grown polycrystalline graphene due to tensile or compressive strain [33,34].

To discriminate defect signals from doping and strain, the intensity ratio  $I_D/I_{2D}$ , has been evaluated because this parameter depends strongly on the damage generation [29] and only weakly on p- or n-doping of damaged graphene [32]. Figure 3.1.3 presents the values of  $I_D/I_{2D}$  of the same  $130\times130\text{ }\mu\text{m}^2$  area at  $t=0$  (a),  $60\text{s}$  (b) and  $425\text{s}$  (c). Maps in Fig. 3.1.3a and Fig. 3.1.3b indicate good homogeneity of the graphene surface even after tenfold increase of  $I_D/I_{2D}$  values after  $60\text{s}$  of plasma treatment. Nevertheless, the discrepancy between GBs and GRs is noticeable for  $t=425\text{s}$  as the former have a mean value of  $\sim 3$  while the latter average at  $\sim 5$ . This implies that the GBs are more resilient than the rest of the graphene to the damage generation in such mild, pulsed argon plasma conditions.

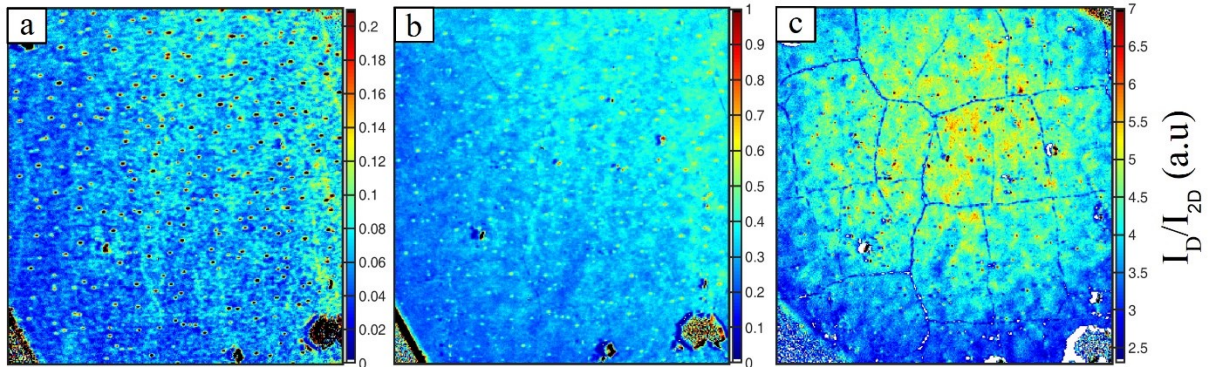


Figure 3.1.3. Evolution of an intensity ratio mapping with plasma treatments linked to graphene disorder.  $130 \times 130 \mu\text{m}^2$   $I_D/I_{2D}$  mappings of (a) pristine, (b) 60s and (c) 425s plasma-treated graphene. Note the color scale difference for each map.

Taking advantage of the characteristic Raman signatures at the GBs (Figs. 3.1.2-3), a method to extract the spectra associated with *GB-pixels* was developed (see section S-III). From the set of data displayed in Figure 3.1.1, Figure 3.1.4a presents the chosen GB-pixels whose spectroscopic data lead to the encircled points in Fig. 3.1.4b. When taking all 13 measurements into consideration, a spatially-resolved representation of the defect generation dynamics is obtained. Figure 3.1.4b reveals the strong difference between GBs and GRs to match the distribution broadening observed in Fig. 3.1.1: data from GRs follow almost perfectly the 0D-type defect line while those at GBs are shifted towards the 1D line. Note that the RIMA<sup>TM</sup> pixel size is 400nm while GBs have a characteristic width of about 2-3nm only [24]. This size difference allegedly reduces the discrepancies between both curves since one can estimate that, within a GB-pixel, a maximum of 5% of the probed atoms might be included or affected by the boundary. The distinction between GBs and GRs is no longer observable after 1005s, which means that the damaged graphene has become more homogeneous due to amorphization over the whole sample surface. It is worth mentioning that the observed GRs and GBs evolution cannot be explained by the pure geometrical superposition of 0D defects over GBs (see section S-IV); another mechanism must be considered.

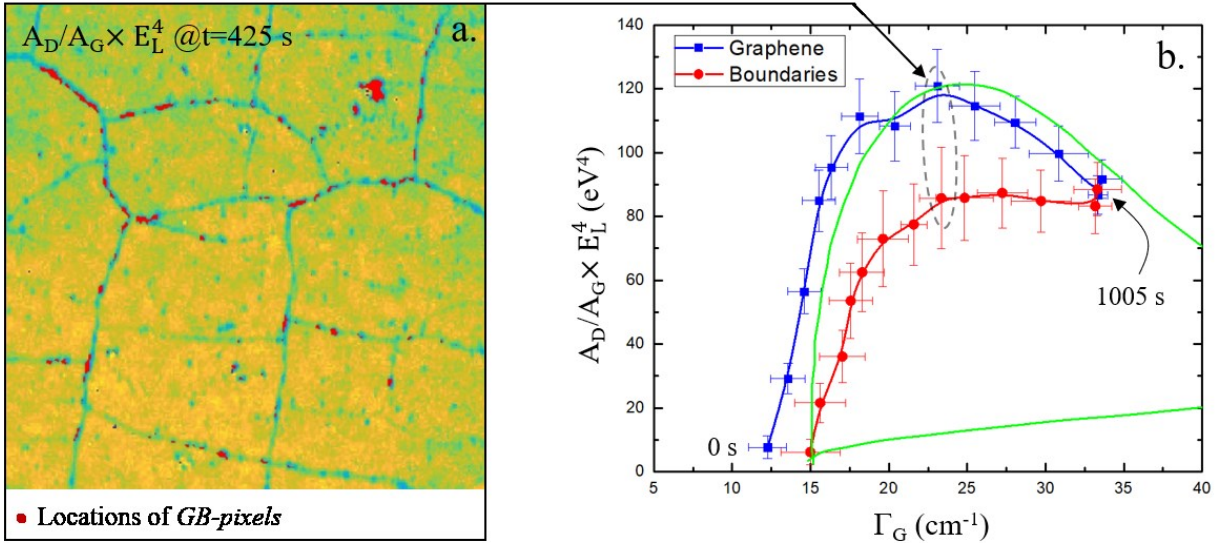


Figure 3.1.4. Imaging and probing of graphene boundaries. (a)  $92 \times 92 \mu\text{m}^2$  area map of Fig. 3.1.2c highlighting in red the locations of the selected GB spectra used to distinguish GBs from the rest of the graphene. (b) the Cançado-like graph extracted from Fig. 3.1.3 representing the mean evolution of each distribution with their standard deviation. The dashed ellipse highlights the 425-sec plasma treated data.

The aforementioned method was used to examine the evolution of other band parameters, namely  $I_{2D}/I_G$ ,  $I_D/I_{2D}$ ,  $\Gamma_{2D}$ ,  $\Gamma_G$ ,  $\omega_G$  and  $\omega_{2D}$ . Values for  $I_{2D}/I_G$  and  $I_D/I_{2D}$  are shown in Figure 3.1.5 as a function of the total energy fluence, from  $t=60\text{s}$  ( $0.03\text{J}\cdot\text{cm}^{-2}$ ) to  $t=1005\text{s}$  ( $0.75\text{J}\cdot\text{cm}^{-2}$ ). As a reference, values obtained on pristine graphene are given as horizontal dashed lines with the associated blue (GR) or red (GB) color. Additionally, the behaviors of  $\Gamma_{2D}$ ,  $\Gamma_G$ ,  $\omega_G$  and  $\omega_{2D}$  are detailed in Section S-V. These parameters are influenced by different lattice perturbations (see Section S-II), but all are associated with graphene disorder [23,29]. Focusing on their pristine values, each parameter initially reports a greater defect density and/or a different defect-type for GBs versus GRs. In Fig. 3.1.6a, the initially high  $I_{2D}/I_G$  ratios, which is relatively lower at GBs, is also consistent with morphological differences between GB and GR regions. Indeed, a lower  $I_{2D}/I_G$  value at GBs is characteristic of structural defects, such as wrinkles and defective boundaries (see section S-V). To avoid interdependencies and focus solely on defect formation, Fig. 3.1.5b displays the evolution of  $I_D/I_{2D}$  [29-32]. With rising energy fluence, both signals at the GRs and GBs show a monotonous increase of  $I_D/I_{2D}$  due to rising density of defects. Yet, GBs show a different behavior characterized with a weaker slope. A definite distinction is

further seen between total energy fluences of 0.16 and 0.57 J.cm<sup>-2</sup>, which is just before convergence of I<sub>D</sub>/I<sub>2D</sub> at 0.66 J.cm<sup>-2</sup>. This behavior before reaching a homogeneous density of defects throughout the whole analyzed area (amorphization) is consistent with a lower rate of damage generation at GBs with respect to the rest of the graphene film.

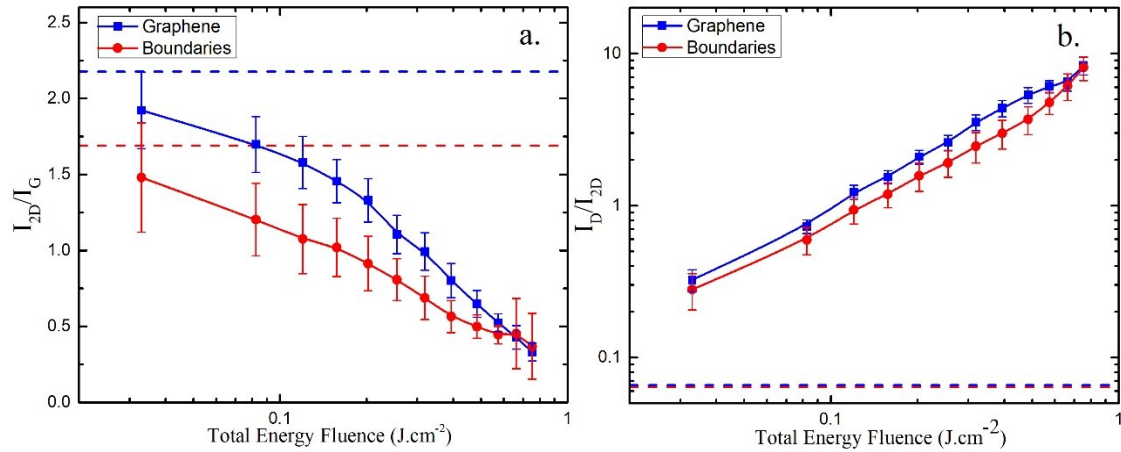


Figure 3.1.5. Relevant Raman parameters highlighting the discrepancies between graphene grain and grain boundaries. The mean evolution of each parameters distribution with their standard deviation are plotted versus the total energy fluence during the subsequent plasma treatments ( $60\text{s} \leftrightarrow 0.03\text{J}\cdot\text{cm}^{-2}$ ,  $1005\text{s} \leftrightarrow 0.75\text{J}\cdot\text{cm}^{-2}$ ). The extracted Raman band parameters are: (a)  $I_{2D}/I_G$  and (b)  $I_D/I_{2D}$ . Values for pristine graphene are displayed as horizontal dashed lines. Pristine values are similar in (b).

After plasma treatment, the evolution of all Raman features –especially  $I_D/I_{2D}$ – demonstrates different damage formation/annihilation dynamics between GBs and GRs. More specifically, limited damage is observed at GBs compared with GRs. Due to their positive enthalpy as compared with GRs [35], GBs have been shown to be highly sensitive to irradiation processes, especially by reactive atoms [36,37] or high-energy electrons [19]. Under ion irradiation (between 1 eV and 1 keV), a preferential etching of GBs has been suggested [13,38], which is clearly inconsistent with the results. This statement holds considering that GBs are not flat. In such conditions, lower binding energies and thus enhanced defect production rates are expected [39]. Therefore, a preferential adatoms-vacancies recombination at GBs, as illustrated in Figure 3.1.6, appears as key to explain their resilience.

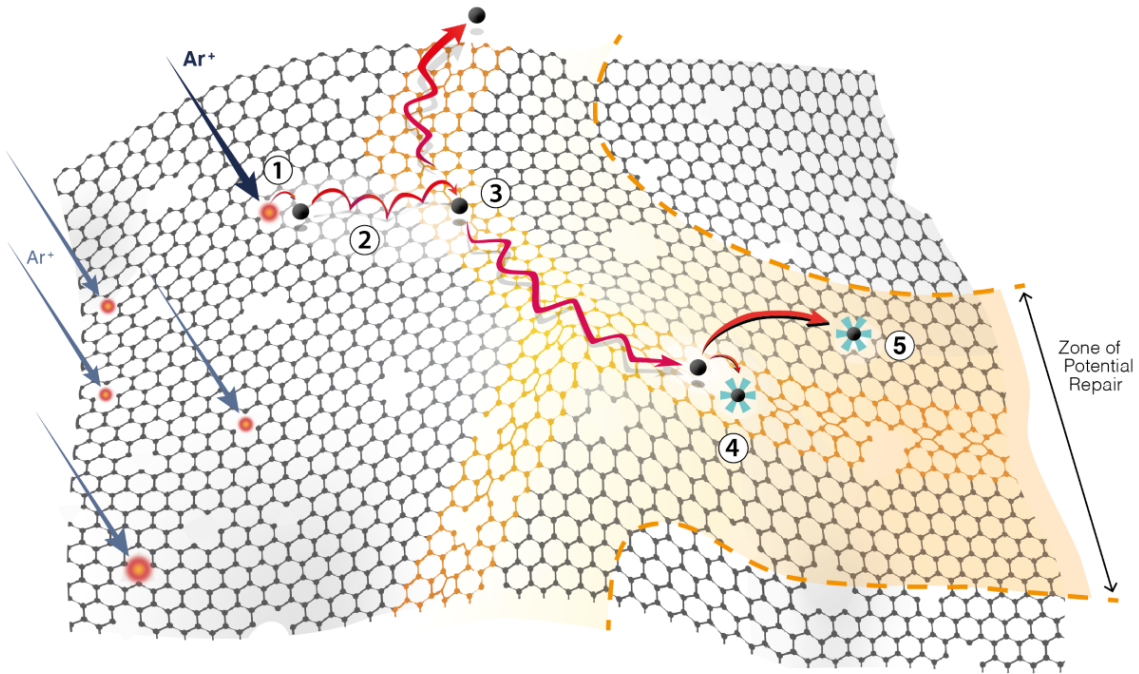


Figure 3.1.6. Schematics of preferential self-healing at GBs in plasma-treated graphene involving: (1) Formation of carbon adatoms-vacancies by plasma-generated species; (2) Preferential migration of carbon adatoms on the graphene surface; (3) Anisotropic transport of carbon adatoms along grain boundaries; (4) Defect healing at GBs; (5) Carbon adatom emission from GBs leading to defect healing in the zone of potential repair

Considering the 11-13eV argon ion flux and additional energy uptakes provided by plasma-generated species (for example, the surface recombination of argon ions and the surface deexcitation of argon metastable species that represents an instantaneous energy release of 15.8 and 11.6eV, respectively), the plasma treatment yields to significant damage in the graphene lattice, in particular carbon adatom/vacancy pairs (Frenkel pairs). The current level of knowledge on the physics driving such damage formation by very-low energy ion irradiation is summarized in Section S-VI [12,13,15]. While a single vacancy requires  $\sim$ 1.3 eV for migration on a graphene surface, a carbon adatom only needs 0.4 eV to diffuse [12]. Thus, carbon adatoms on graphene are considered as mobile species under plasma irradiation and can adopt different migration paths that should eventually cross 0D or 1D type defects. In a first case scenario, annihilation can naturally occur at a 0D defect site [40]. Upon contact with grain boundaries (1D defects), carbon adatoms become highly mobile alongside the boundary [41,42], triggering an anisotropic transport responsible of an imbalance in the spatial distribution of carbon adatoms

[43]. Hence, a second scenario can be inferred in which an accumulation or excess of carbon adatoms at the GBs enhances the annihilation probability at defects/vacancies near the GBs. Locally, the interstitial emission from this imbalance of adatom population in the zone of potential repair further contributes to the healing of vacancies near GBs [18]. The GB processes illustrated in Figure 3.1.6, which are supported by both calculations [44,45] and experiments [42,46,47], provide the main conditions to explain a preferential self-healing reported here at GBs.

Preferential self-healing of radiation damage at GBs was first theorized on bulk Cu [18] and predicted to have a pronounced effect on graphene [42]. A similar signature was observed on highly oriented pyrolytic graphite (HOPG) in very similar argon plasma etching conditions where hexagonal graphite pyramids were reported to form preferentially along GBs [48]. Their formation mechanism was ascribed to a greater etching rate at the GBs, suggesting preferential erosion at GBs as compared with graphene grains. Since domain boundaries are generally of the same type (such as 5-7 ring chains) in HOPG [49], the results presented in this study reveal, however, a completely different explanation to this behavior.

Because of their positive enthalpies with respect to the undisturbed honeycomb lattice, grain boundaries found in graphite or graphene were often assumed to be subject to faster and stronger lattice disorder under plasma irradiation. The five-order-of-magnitude size difference between grains and grain boundaries has made difficult, however, the experimental assessment of such difference during CVD growth and post-growth modifications of graphene films. Capitalizing on the innovative nature of the RIMA<sup>TM</sup> system, damage generation induced by 12 subsequent plasma treatments in well-controlled conditions was analyzed. While a synergistic plasma effect is present due to the simultaneous energy input by ions, metastable species, and VUV photons, the main contribution to the damage generation is the 11-13eV ion flux. Thorough the analyses of 8 different Raman features related to the D, G and 2D bands, plasma-induced defect generation in graphene grains and grain boundaries were compared. In accordance with recent literature, a lattice reconstruction mechanism occurring preferentially at domain boundaries and induced by preferential atom migration and adatoms-vacancies recombination was revealed.

Such preferential self-healing at grain boundaries in plasma processing of materials as well as in radiation damage studies of 2D materials represent an exciting research field which could lead to refined defect engineering.

Advances in Raman monitoring of plasma-graphene interactions together with the peculiar evolution of graphene grains and grain boundaries during ion and plasma irradiation open a window for fundamental and applied studies on the structure, properties, and control of grains and grain boundaries. This includes detailed analysis of CVD-growth processes of graphene films over large area substrates as well as ion- and plasma-assisted processes for doping, band gap tuning, and layer-by-layer etching of low-dimensional materials. This study further suggests revisiting the mechanism for the formation of chemically doped graphene film under mild plasma treatments using argon mixed with either traces of N- or B-bearing gases, especially the latter since B-adatoms have a migration barrier on graphene far below that of C-adatoms [50]. More generally, these results provide insights on the future of the design and engineering of 2D materials and call for a better integration of an important but too often marginalized feature of polycrystalline materials: the grain boundaries.

## ACKNOWLEDGMENTS

This work was financially supported by the National Science and Engineering Research Council (NSERC), PRIMA-Québec, Plasmionique Inc., Photon Etc., the Fonds de Recherche du Québec - Nature et Technologies (FRQNT), and the Canada Research Chair program (L. Stafford and R. Martel). The authors thank Carl Charpin for providing the CVD-grown graphene samples and Charlotte Allard for technical support with RIMA<sup>TM</sup> measurements.

## AUTHOR CONTRIBUTIONS

P.V., X.G. are equally contributing first authors. P.V. performed all experimental measurements. X.G., P.V. participated in the initial writing of the manuscript. G.R.B. developed the code used for the analysis of RIMA data. All authors contributed to the design of experiments and data interpretation and manuscript revision. L.S. and R.M. provided funding and supervised the study.

## REFERENCES

- [1] A. Zurutuza, C. Marinelli, Challenges and opportunities in graphene commercialization, *Nat. Nanotechnol.* 9 (2014) 730–734. doi:10.1038/nnano.2014.225.
- [2] K. Balasubramanian, T. Biswas, P. Ghosh, S. Suran, A. Mishra, R. Mishra, R. Sachan, M. Jain, M. Varma, R. Pratap, S. Raghavan, Reversible defect engineering in graphene grain boundaries, *Nat. Commun.* 10 (2019) 1–9. doi:10.1038/s41467-019-09000-8.
- [3] O. V. Yazyev, S.G. Louie, Electronic transport in polycrystalline graphene, *Nat. Mater.* 9 (2010) 806–809. doi:10.1038/nmat2830.
- [4] R. Grantab, V.B. Shenoy, R.S. Ruoff, Anomalous Strength Characteristics of Tilt Grain Boundaries in Graphene, *Science* (80-. ). 330 (2010) 946–948. doi:10.1126/science.1196893.
- [5] J. Červenka, M.I. Katsnelson, C.F.J. Flipse, Room-temperature ferromagnetism in graphite driven by two-dimensional networks of pointdefects, *Nat. Phys.* 5 (2009) 840–844. doi:10.1038/nphys1399.
- [6] S. Malola, H. Häkkinen, P. Koskinen, Structural, chemical, and dynamical trends in graphene grain boundaries, *Phys. Rev. B - Condens. Matter Mater. Phys.* 81 (2010) 1–6. doi:10.1103/PhysRevB.81.165447.
- [7] A.W. Tsen, L. Brown, R.W. Havener, J. Park, Polycrystallinity and stacking in CVD graphene, *Acc. Chem. Res.* 46 (2013) 2286–2296. doi:10.1021/ar300190z.
- [8] A.W. Tsen, P.Y. Huang, R.W. Havener, C.S. Ruiz-Vargas, D.A. Muller, L. Brown, M.P. Levendorf, J. Park, F. Ghahari, P. Kim, Tailoring electrical transport across grain boundaries in polycrystalline graphene, *Science* (80-. ). 336 (2012) 1143–1146. doi:10.1126/science.1218948.
- [9] K.W. Clark, X.G. Zhang, I. V. Vlassiouk, G. He, R.M. Feenstra, A.P. Li, Spatially resolved mapping of electrical conductivity across individual domain (Grain) boundaries in graphene, *ACS Nano.* 7 (2013) 7956–7966. doi:10.1021/nn403056k.
- [10] V. Georgakilas, J.N. Tiwari, K.C. Kemp, J.A. Perman, A.B. Bourlinos, K.S. Kim, R. Zboril, Noncovalent Functionalization of Graphene and Graphene Oxide for Energy Materials, Biosensing, Catalytic, and Biomedical Applications, *Chem. Rev.* 116 (2016) 5464–5519. doi:10.1021/acs.chemrev.5b00620.
- [11] Z. Xiang, Q. Dai, J.F. Chen, L. Dai, Edge Functionalization of Graphene and Two-Dimensional Covalent Organic Polymers for Energy Conversion and Storage, *Adv. Mater.* (2016) 6253–6261. doi:10.1002/adma.201505788.
- [12] F. Banhart, J. Kotakoski, A. V. Krasheninnikov, Structural Defects in Graphene, *ACS Nano.* 5 (2011) 26–41. doi:10.1021/nn102598m.

- [13] P. Ahlberg, F.O.L. Johansson, Z.B. Zhang, U. Jansson, S.L. Zhang, A. Lindblad, T. Nyberg, Defect formation in graphene during low-energy ion bombardment, *APL Mater.* 4 (2016). doi:10.1063/1.4945587.
- [14] P. Vinchon, X. Glad, G. Robert-Bigras, R. Martel, A. Sarkissian, L. Stafford, A combination of plasma diagnostics and Raman spectroscopy to examine plasma-graphene interactions in low-pressure argon radiofrequency plasmas, *J. Appl. Phys.* 126 (2019) 233302. doi:10.1063/1.5125143.
- [15] A. V. Krasheninnikov, F. Banhart, Engineering of nanostructured carbon materials with electron or ion beams, *Nat. Mater.* 6 (2007) 723–733. doi:10.1038/nmat1996.
- [16] X. Zhang, K. Hattar, Y. Chen, L. Shao, J. Li, C. Sun, K. Yu, N. Li, M.L. Taheri, H. Wang, J. Wang, M. Nastasi, Radiation damage in nanostructured materials, *Prog. Mater. Sci.* 96 (2018) 217–321. doi:10.1016/j.pmatsci.2018.03.002.
- [17] K. Nordlund, S.J. Zinkle, A.E. Sand, F. Granberg, R.S. Averback, R.E. Stoller, T. Suzudo, L. Malerba, F. Banhart, W.J. Weber, F. Willaime, S.L. Dudarev, D. Simeone, Primary radiation damage: A review of current understanding and models, *J. Nucl. Mater.* 512 (2018) 450–479. doi:10.1016/j.jnucmat.2018.10.027.
- [18] X.M. Bai, A.F. Voter, R.G. Hoagland, M. Nastasi, B.P. Uberuaga, Efficient annealing of radiation damage near grain boundaries via interstitial emission, *Science* (80-. ). 327 (2010) 1631–1634. doi:10.1126/science.1183723.
- [19] S. Kurasch, J. Kotakoski, O. Lehtinen, V. Skákalová, J. Smet, C.E. Krill, A. V. Krasheninnikov, U. Kaiser, Atom-by-atom observation of grain boundary migration in graphene, *Nano Lett.* 12 (2012) 3168–3173. doi:10.1021/nl301141g.
- [20] J. Kotakoski, C. Mangler, J.C. Meyer, Imaging atomic-level random walk of a point defect in graphene, *Nat. Commun.* 5 (2014) 2–6. doi:10.1038/ncomms4991.
- [21] R. Beams, L. Gustavo Cançado, L. Novotny, Raman characterization of defects and dopants in graphene, *J. Phys. Condens. Matter.* 27 (2015) 083002. doi:10.1088/0953-8984/27/8/083002.
- [22] L. Gustavo Cançado, M. Gomes da Silva, E.H. Martins Ferreira, F. Hof, K. Kampioti, K. Huang, A. Pénicaud, C. Alberto Achete, R.B. Capaz, A. Jorio, Disentangling contributions of point and line defects in the Raman spectra of graphene-related materials, *2D Mater.* 4 (2017) 025039. doi:10.1088/2053-1583/aa5e77.
- [23] M.M. Lucchese, F. Stavale, E.H.M. Ferreira, C. Vilani, M.V.O. Moutinho, R.B. Capaz, C.A. Achete, A. Jorio, Quantifying ion-induced defects and Raman relaxation length in graphene, *Carbon N. Y.* 48 (2010) 1592–1597. doi:10.1016/j.carbon.2009.12.057.
- [24] J. Ribeiro-Soares, M.E. Oliveros, C. Garin, M. V. David, L.G.P. Martins, C.A. Almeida, E.H.

- Martins-Ferreira, K. Takai, T. Enoki, R. Magalhães-Paniago, A. Malachias, A. Jorio, B.S. Archanjo, C.A. Achete, L.G. Cançado, Structural analysis of polycrystalline graphene systems by Raman spectroscopy, *Carbon N. Y.* 95 (2015) 646–652. doi:10.1016/j.carbon.2015.08.020.
- [25] R. Beams, Tip-enhanced Raman scattering of graphene, *J. Raman Spectrosc.* 49 (2018) 157–167. doi:10.1002/jrs.5211.
- [26] E. Gaufrès, S. Marcet, V. Aymong, N.Y.-W. Tang, A. Favron, F. Thouin, C. Allard, D. Rioux, N. Cottenye, M. Verhaegen, R. Martel, Hyperspectral Raman imaging using Bragg tunable filters of graphene and other low-dimensional materials, *J. Raman Spectrosc.* 49 (2018) 174–182. doi:10.1002/jrs.5298.
- [27] A. Eckmann, A. Felten, A. Mishchenko, L. Britnell, R. Krupke, K.S. Novoselov, C. Casiraghi, Probing the nature of defects in graphene by Raman spectroscopy, *Nano Lett.* 12 (2012) 3925–3930. doi:10.1021/nl300901a.
- [28] A.C. Ferrari, J. Robertson, Raman spectroscopy of amorphous, nanostructured, diamon-like carbon, and nanodiamond, *Philosophical Trans. Math. Phys. Eng. Sci.* 363 (2004) 2477–2512. doi:10.1080/037454809495909.
- [29] Y.-B. Zhou, Z.-M. Liao, Y.-F. Wang, G.S. Duesberg, J. Xu, Q. Fu, X.-S. Wu, D.-P. Yu, Ion irradiation induced structural and electrical transition in graphene, *J. Chem. Phys.* 133 (2010) 234703. doi:10.1063/1.3518979.
- [30] A. Das, S. Pisana, B. Chakraborty, S. Piscanec, S.K. Saha, U. V. Waghmare, K.S. Novoselov, H.R. Krishnamurthy, A.K. Geim, A.C. Ferrari, A.K. Sood, Monitoring dopants by Raman scattering in an electrochemically top-gated graphene transistor, *Nat. Nanotechnol.* 3 (2008) 210–215. doi:10.1038/nnano.2008.67.
- [31] P.L. Levesque, S.S. Sabri, C.M. Aguirre, J. Guillemette, M. Siaj, P. Desjardins, T. Szkopek, R. Martel, Probing charge transfer at surfaces using graphene transistors, *Nano Lett.* 11 (2011) 132–137. doi:10.1021/nl103015w.
- [32] M. Bruna, A.K. Ott, M. Ijäs, D. Yoon, U. Sassi, A.C. Ferrari, Doping Dependence of the Raman Spectrum of Defected Graphene, *ACS Nano.* 8 (2014) 7432–7441. doi:10.1021/nn502676g.
- [33] M.A. Bissett, W. Izumida, R. Saito, H. Ago, Effect of domain boundaries on the Raman spectra of mechanically strained graphene, *ACS Nano.* 6 (2012) 10229–10238. doi:10.1021/nn304032f.
- [34] Y. Wang, Y. Wang, C. Xu, X. Zhang, L. Mei, M. Wang, Y. Xia, P. Zhao, H. Wang, Domain-boundary independency of Raman spectra for strained graphene at strong interfaces, *Carbon N. Y.* 134 (2018) 37–42. doi:10.1016/j.carbon.2018.03.069.
- [35] C. Ophus, A. Shekhawat, H. Rasool, A. Zettl, Large-scale experimental and theoretical study of

- graphene grain boundary structures, *Phys. Rev. B - Condens. Matter Mater. Phys.* 92 (2015). doi:10.1103/PhysRevB.92.205402.
- [36] R. Yang, L. Zhang, Y. Wang, Z. Shi, D. Shi, H. Gao, E. Wang, G. Zhang, An anisotropic etching effect in the graphene basal plane, *Adv. Mater.* 22 (2010) 4014–4019. doi:10.1002/adma.201000618.
- [37] G. Diankov, M. Neumann, D. Goldhaber-Gordon, Extreme monolayer-selectivity of hydrogen-plasma reactions with graphene, *ACS Nano.* 7 (2013) 1324–1332. doi:10.1021/nn304903m.
- [38] T. Larionova, T. Koltsova, E. Bobrynska, A. Smirnov, I. Eliseyev, V. Davydov, O. Tolochko, Comparative characterization of graphene grown by chemical vapor deposition, transferred to nonconductive substrate, and subjected to Ar ion bombardment using X-ray photoelectron and Raman spectroscopies, *Diam. Relat. Mater.* 76 (2017) 14–20. doi:10.1016/j.diamond.2017.04.001.
- [39] M. Kabir, K.J. Van Vliet, Kinetics of Topological Stone–Wales Defect Formation in Single-Walled Carbon Nanotubes, *J. Phys. Chem. C.* 120 (2016) 1989–1993. doi:10.1021/acs.jpcc.5b11682.
- [40] J. Chen, T. Shi, T. Cai, T. Xu, L. Sun, X. Wu, D. Yu, Self healing of defected graphene, *Appl. Phys. Lett.* 102 (2013) 103–107. doi:10.1063/1.4795292.
- [41] L.F. Huang, M.Y. Ni, G.R. Zhang, W.H. Zhou, Y.G. Li, X.H. Zheng, Z. Zeng, Modulation of the thermodynamic, kinetic, and magnetic properties of the hydrogen monomer on graphene by charge doping, *J. Chem. Phys.* 135 (2011) 064705. doi:10.1063/1.3624657.
- [42] B. Wang, Y. Puzyrev, S.T. Pantelides, Strain enhanced defect reactivity at grain boundaries in polycrystalline graphene, *Carbon N. Y.* 49 (2011) 3983–3988. doi:10.1016/j.carbon.2011.05.038.
- [43] A. Hashimoto, K. Suenaga, A. Gloter, K. Urita, S. Iijima, Direct evidence for atomic defects in graphene layers, *Nature.* 430 (2004) 870–873. doi:10.1038/nature02817.
- [44] L.J. Zhou, Z.F. Hou, L.M. Wu, Y.F. Zhang, First-principles studies of lithium adsorption and diffusion on graphene with grain boundaries, *J. Phys. Chem. C.* 118 (2014) 28055–28062. doi:10.1021/jp5102175.
- [45] T. Botari, R. Paupitz, P. Alves Da Silva Autreto, D.S. Galvao, Graphene healing mechanisms: A theoretical investigation, *Carbon N. Y.* 99 (2016) 302–309. doi:10.1016/j.carbon.2015.11.070.
- [46] T.H. Liu, G. Gajewski, C.W. Pao, C.C. Chang, Structure, energy, and structural transformations of graphene grain boundaries from atomistic simulations, *Carbon N. Y.* 49 (2011) 2306–2317. doi:10.1016/j.carbon.2011.01.063.
- [47] S.U. Yu, B. Park, Y. Cho, S. Hyun, J.K. Kim, K.S. Kim, Simultaneous visualization of graphene grain boundaries and wrinkles with structural information by gold deposition, *ACS Nano.* 8 (2014) 8662–8668. doi:10.1021/nn503550d.

- [48] X. Glad, L. de Poucques, J. Bougdira, Formation mechanism of graphite hexagonal pyramids by argon plasma etching of graphite substrates, *J. Phys. D. Appl. Phys.* 48 (2015) 495304. doi:10.1088/0022-3727/48/49/495304.
- [49] P. Simonis, C. Goffaux, P.A. Thiry, L.P. Biro, P. Lambin, V. Meunier, STM study of a grain boundary in graphite, *Surf. Sci.* 511 (2002) 319–322. doi:10.1016/S0039-6028(02)01511-X.
- [50] J. Kotakoski, A. V. Krasheninnikov, Y. Ma, A.S. Foster, K. Nordlund, R.M. Nieminen, B and N ion implantation into carbon nanotubes: Insight from atomistic simulations, *Phys. Rev. B - Condens. Matter Mater. Phys.* 71 (2005) 1–6. doi:10.1103/PhysRevB.71.205408.
- [51] L. Maaloul, S. Morel, L. Stafford, Populations of metastable and resonant argon atoms in radio frequency magnetron plasmas used for deposition of indium-zinc-oxide films, *J. Vac. Sci. Technol. A Vacuum, Surfaces, Film*. 30 (2012) 021301. doi:10.1116/1.3674162.
- [52] S. Choubak, P.L. Levesque, E. Gaufres, M. Biron, P. Desjardins, R. Martel, Graphene CVD: Interplay between growth and etching on morphology and stacking by hydrogen and oxidizing impurities, *J. Phys. Chem. C*. 118 (2014) 21532–21540. doi:10.1021/jp5070215.
- [53] Y.-C. Lin, C.-C. Lu, C.-H. Yeh, C. Jin, K. Suenaga, P. Chiu, Graphene Annealing: How Clean Can It Be?, *Nano Lett.* 12 (2012) 414–419. doi:10.1021/nl203733r.
- [54] G. Robert Bigras, P. Vinchon, C. Allard, X. Glad, R. Martel, L. Stafford, Probing plasma-treated graphene using hyperspectral Raman, *Rev. Sci. Instrum.* 91 (2020) 063903. doi:10.1063/5.0006556.

## SUPPLEMENTARY INFORMATION

### S-I. PLASMA CHARACTERIZATION

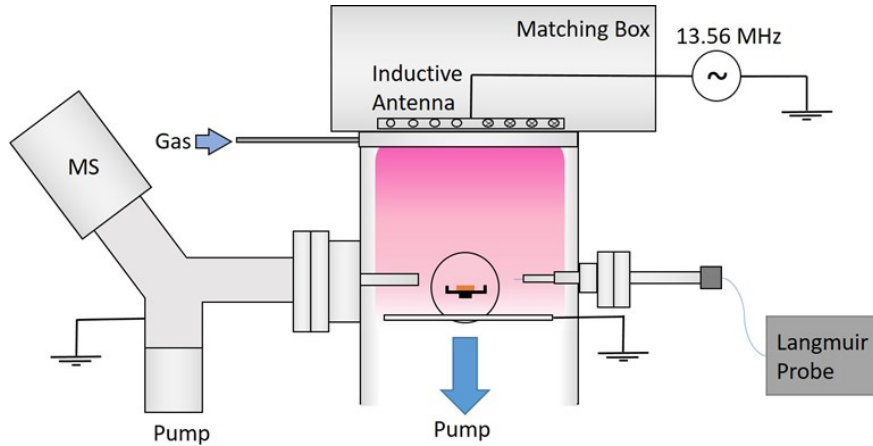


Figure 3.1.S1. Sketch of the plasma apparatus

A previous study [1] showed that argon plasmas can easily generate tremendous damage on CVD-grown polycrystalline graphene films despite a very-low ion energy and short-time treatment. Indeed, the high population of charged species in inductive mode (H-mode) of a low-pressure argon plasma induces elevated ion flux ( $10^{17} \text{ cm}^{-2}\cdot\text{s}^{-1}$ ) and thus very high ion fluences compared to ion bombardment with typical ion guns ( $10^{11}\text{-}10^{15} \text{ cm}^{-2}$ ) [2]. Aiming at thoroughly studying the defect formation dynamics in graphene films, intermediate treatment steps were required. Thus, it was needed to find plasma conditions leading to a weaker damage generation (smaller energy fluence) while ensuring a minimal contribution from argon metastable species to the total energy flux as their deexcitation on the surface of graphene can have a strong influence on the graphene defect formation dynamics [1].

To circumvent this issue, the energy fluence provided to the graphene films is reduced by first lowering pressure and RF input power as much as possible while keeping the power coupling in the inductive mode. This is primordial as it has been shown that the metastable states dominates the energy flux in capacitive mode (arising at very low RF input power and/or higher pressure) [1]. Thus, conditions with a pressure of 5 mTorr at 100 W were selected. Additionally,

to decrease the energy fluence even further, the discharge was ignited in pulsed mode. The mildest conditions were found for a frequency of 1 kHz (period  $T = 1$  ms) with a duty cycle DC = 10%, i.e. a pulse duration  $\tau = 100$   $\mu$ s ( $10\% \times T$ ).

In these pulsed argon plasma conditions, Figure 3.1.S2 of the supplementary data presents the temporal evolution of (a)  $T_e$  and  $(V_p - V_f)$ , as well as (b)  $n_i$ ,  $n(\text{Ar}^m)$  and  $n(\text{Ar}^*)$  over a period  $T$ . At the beginning of the RF power pulse, a sharp increase of  $T_e$  and  $(V_p - V_f)$  up to respectively 3.5 eV and 12 V is observed. Both parameters slowly decrease within the duration of the pulse down to 2.9 eV and 10 V, respectively. These values are close to the ones observed in continuous mode [1]. The sharp  $T_e$  increase is due to an imbalance between electron energy gains and losses before reaching a quasi-steady-state regime [3]. The same behavior is observed for  $(V_p - V_f)$  as this parameter is expected to be proportional to  $T_e$  in low-pressure argon plasmas [4]. Immediately after switching off the RF power,  $T_e$  and  $(V_p - V_f)$  values decrease rapidly and then stabilise during the rest of the period at around 0.5 eV and 1 V, respectively. Non-null values can only be explained by the presence of a temporal afterglow (post-discharge) [5]. This is confirmed by the results presented in Fig. 3.1.S2b of the supplementary data, as  $n_i$ ,  $n(\text{Ar}^m)$  and  $n(\text{Ar}^*)$  maintain significant proportion of their *plasma-on* values during the post-discharge [6]. Metastable density is barely affected by the pulse and stays at around  $1 \times 10^{10}$  cm<sup>-3</sup> for the whole period. The slight increase observed is related to Ar<sup>m</sup> sources greater than losses during plasma *on* phase, while the balance changes in the afterglow; the steady decrease is due to deexcitation by electron quenching [6] and diffusion to the walls. Regarding the ion density, it rises sharply from  $8 \times 10^8$  cm<sup>-3</sup> to  $3 \times 10^9$  cm<sup>-3</sup> and then reaches a plateau. At the pulse end in the absence of a creation mechanism, the plasma monotonously declines back to its previous value due to losses by diffusion to the walls [7]. The population of resonant species is greatly affected by the power pulse since it increases rapidly up to  $2 \times 10^9$  cm<sup>-3</sup> at plasma *on* before quickly dropping down to about  $3 \times 10^8$  cm<sup>-3</sup> in the post-discharge. Such behavior is explained by the very low-pressure conditions, which prevent VUV to be absorbed and reemitted by the gas phase, their mean-free-path being rather large at such a low pressure [8]. Note that the increasing noise seen at plasma *off* is due to the detection limit of the OAS method.

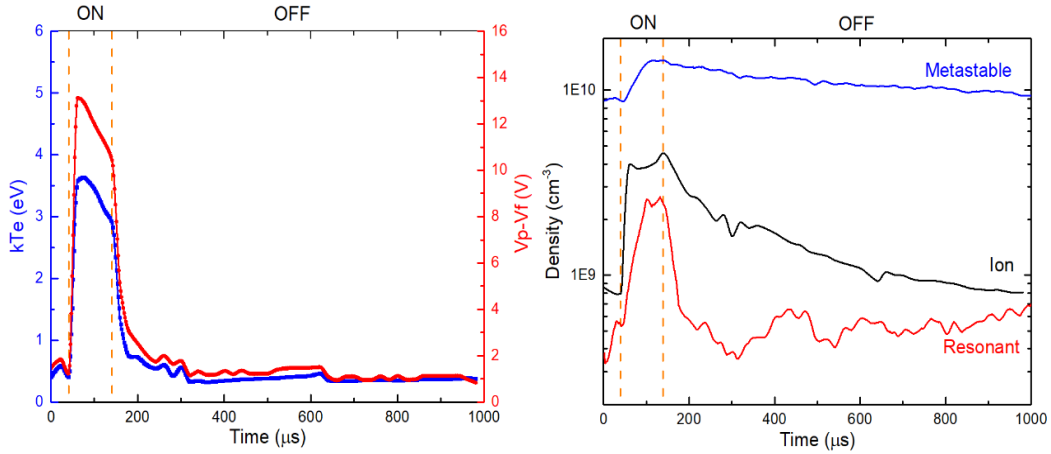


Figure 3.1.S2. (a) Electron temperature  $kT_e$  (in eV, blue) and  $V_p-V_f$  (in V, red) derived from cylindrical LP measurements. The ion energy  $E_{ion}$  may be approximated to  $(V_p-V_f)$ . (b) Argon ion, metastable and resonant densities extracted from LP measurements for ions and OAS measurements otherwise.

Based on the data presented in Fig. 3.1.S2 of the supplementary data, the contribution of each species in the total power fluxes can be obtained. The results are shown in Fig. 3.1.S3 of the supplementary data for different pulsed conditions as compared with the continuous ( $DC = 100$ ) plasma used in [1]. While VUV photons take a greater part of the total power flux, the ratio between the ion and metastable contributions has not changed between  $5mTorr\text{-}500W\text{-}DC100$  and  $5mTorr\text{-}100W\text{-}1KHz\text{-}DC10$ . Between these two conditions, however, the power density drastically drops by about 3 orders of magnitude. This lower power density in pulsed argon plasma conditions allows a much more progressive study of the damage formation dynamics in graphene films since longer plasma treatment times ( $\sim 80$  s for each of the 12 subsequent treatments leading to a total treatment time of 1005 s) can be used to achieve comparable energy fluence as in continuous plasma conditions (single treatment of 15 s). Note that the total fluence is of the same order as the ablation threshold of graphene [9].

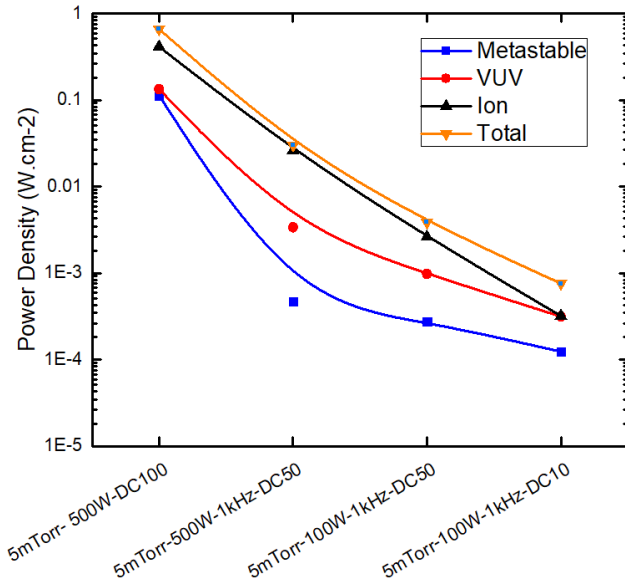


Figure 3.1.S3. Evolution of the power density measured in the plasma reactor at the substrate location for 4 different conditions, labelled on the x-axis. Lines are guides to the eyes highlighting the net drop in power density.

## S-II. EVOLUTION OF SELECTED RAMAN BAND PARAMETERS

Table 3.1.1. Summary of the effects arising from the increase of different graphene lattice defects on the parameters of D, G and 2D bands. Data are taken from exfoliated and/or CVD-grown polycrystalline graphene films.

Band		Doping		Strain $\epsilon$		Damage	# of layers (Bernal stacking)
		p	n	<0 (compr.)	>0 (tensile)		
G	$\omega_G$	↑ <sup>10,11</sup>	↑ <sup>10,11</sup>	↑ <sup>12,13*</sup>	↓ <sup>12–15</sup>	↑ <sup>16,17</sup>	
	$\Gamma_G$	↓ <sup>11</sup>	↓ <sup>11</sup>	↑ <sup>18</sup>	↑ <sup>14</sup>	↑ <sup>17,19</sup>	
D	$\omega_D$			↑ <sup>12,13</sup>	↓ <sup>12,13</sup>		
	$\Gamma_D$					↑ <sup>19,20</sup>	
D/G	$A_p/A_G$	↓ <sup>10</sup>	↓ <sup>10</sup>			↑ then ↓ <sup>16,17</sup>	
2D	$\omega_{2D}$	↑ <sup>11</sup>	= then ↓ <sup>11</sup>	↑↑ <sup>12,13</sup>	↓↓ <sup>12–15</sup>		↑ <sup>21,22</sup>
	$\Gamma_{2D}$			↑ <sup>18</sup>	↑ <sup>14,23</sup>	↑ <sup>19</sup>	↑ <sup>21,22</sup>
2D/G	$I_{2D}/I_G$	↓ <sup>11</sup>	↓ <sup>11</sup>			↓ <sup>19,20</sup>	↓ <sup>21,22</sup>
D/2D	$I_D/I_{2D}$	= <sup>10</sup>	= <sup>10</sup>			↑↑ <sup>19,20</sup>	
	$A_p/A_{2D}$	= <sup>10</sup>	= <sup>10</sup>			↑↑ <sup>24</sup>	

\*A different behavior has been observed for grain boundaries, *i.e.* nanocrystalline CVD-grown graphene as compared with exfoliated graphene [18]

### S-III. DISTINGUISHING GRAIN BOUNDARIES FROM GRAPHENE DOMAINS

To efficiently process the sheer number of spectra obtained via the RIMA system, an improved method based on Principal Component Analysis (PCA) filtering has been carried out [25]. It allows for the subtraction of intrinsic RIMA baseline (polynomial fit) and artefacts for the  $3 \times 10^5$  spectra. This number of spectra is roughly 3-order of magnitude improvement from previous data obtained by conventional confocal Raman microscopy <sup>1</sup>.

As a mean to study the local dynamics of the defect generation, a method aimed at thoroughly distinguishing the local spectra obtained at GBs from those at graphene domains was developed. Figs. 3.1.2-4 of the main manuscript and Fig 3.1.S4 the supplementary data show that GBs are easily distinguishable depending on the selected Raman band parameters. By scanning the mappings of chosen Raman band parameters and isolating pixels presenting local non-uniformity, the so-called *GB-pixels* for all 12 plasma treatment times were extracted. Note that the number of GB-pixels necessarily vary depending on the chosen Raman band parameter but at least 1000 pixels attributed to GBs were selected within the central  $92 \times 92 \mu\text{m}^2$  area from the previous figures. The error bars shown are statistical values defined by the interval of two standard deviations (i.e. 68.2% of the distribution of all the extracted values).

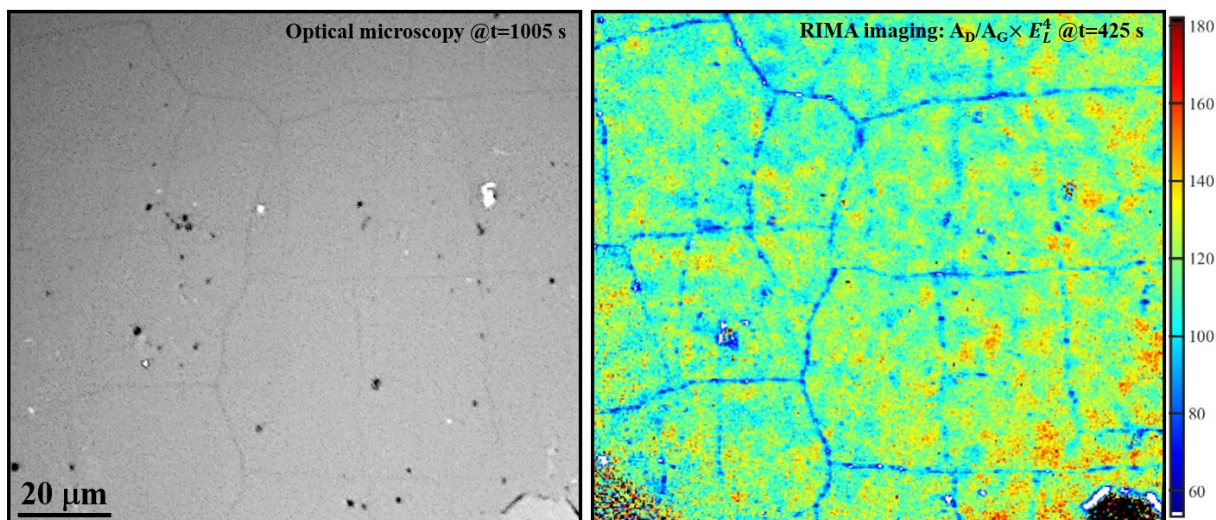


Figure 3.1.S4. Comparison between optical microscopy (left, after 1005 s of plasma treatment) and D/G area ratio extracted from RIMA imaging (right, 425 s).

Optical microscopy was further performed using an OMAX microscope at a  $\times 600$  magnification. As can be seen in Figure 3.1.S4 of the supplementary data, the linear discrepancies observed in the Raman mappings perfectly match the grain boundaries (GBs) discernable on the optical micrograph. The *sharpen* process in imageJ [26] was applied in the picture to highlight GBs.

## S-IV. GEOMETRIC CONSIDERATIONS ON GRAPHENE RAMAN SIGNATURE

In this section, the expected Raman signature of GBs during 0D defect generation is examined. The model proposed by Cançado *et al.* [27] explicitly takes into account the case of a point defect falling into a 1D line. Indeed, in appendix C of the corresponding article, the determination of  $(A_D/A_G) \times E_L^4$  is proposed to be the sum of three contributions (C.1) :

$$\left(\frac{A_D}{A_G}\right) E_L^4 = \left(\frac{A_D}{A_G}\right)_{0D}^{(S)} + \left(\frac{A_D}{A_G}\right)_{1D}^{(S)} + \left(\frac{A_D}{A_G}\right)_{0D,1D}^{(A)} \quad (\text{C.1})$$

where  $(A_D/A_G)_{0D}^{(S)}$  is the contribution term from structural deformation of 0D defects,  $(A_D/A_G)_{1D}^{(S)}$  is the term from structural deformation of 1D defects, and  $(A_D/A_G)_{0D,1D}^{(A)}$  is the term from the activated region around both 0D and 1D defects.

In this framework, Cançado *et al.* indicate that the loss of surface area of defective 1D defects ( $A_B$ ) over the total surface ( $A_T$ ) is detailed by the rate equation (C.6):

$$\frac{dA_B}{dN} = -\pi r_s^2 \frac{A_B}{A_T} \quad (\text{C.6})$$

where  $N$  is the number of 0D defects and  $r_s$  is the radius of the structurally damaged area. Cançado *et al.* carry out this geometrical consideration over the calculation of the total contribution of the defective area of the 1D defects. In the end, contribution by 1D line defects is estimated as the following (see equation C.9):

$$\left(\frac{A_D}{A_G}\right)_{1D}^{(S)} = C_S^{1D} \frac{4l_S(L_a-l_S)}{L_a^2} e^{-\pi r_s^2 \sigma} \quad (\text{C.9})$$

where  $C_S^{1D}$  is the Raman response from 1D defects,  $l_S$  is the width of the 1D line,  $L_a$  is the crystallite size and  $\sigma$  is the surface density of 0D defects. The term  $e^{-\pi r_s^2 \sigma}$  arises from the integration of equation C.6. This term decreases the contribution of the 1D-type defects in the total Raman response as the surface density of point defects increases.

It is worth noting that the way these mechanisms are considered, the structurally damage area of 0D defects has precedence over the defective 1D area. Since the Raman response of  $(A_D/A_G) \times E_L^4$  is higher for 0D defects (51 eV<sup>4</sup> versus 30.3 eV<sup>4</sup> – table 3.1 of the same article, values fitted from experimental data), 0D defects consequently lead to a higher value of  $(A_D/A_G) \times E_L^4$ .

Cançado *et al.* used the same considerations for the term of the activated area (third term of C.1.). Indeed, the equation C.14 in ref. [27] depends on the covering of structurally damaged 1D defects ( $f_{S,1D}$ ).

Therefore, the creation of point defects (0D) in the vicinity of grain boundaries (1D) would quickly favor a typical 0D-type signature. Thus, when 0D defects are created in a location where there is already a 1D defect (the grain boundary), spectral change towards a 0D-type defect signature will be observed in the Raman response of RIMA.

Regarding the possibility of a point defect arising within –or *on top*– of a GB, it is taken into account by the model and should increase the contributions of 0D defects –greatly increasing  $A_D/A_G$ – and should decrease the ones of 1D defects –which are responsible for a significantly milder increase of  $A_D/A_G$ . Therefore, the 0D defects do *overwrite* 1D defects and thus cause an increase of the  $A_D/A_G$  ratio.

## S-V. HINTS ON THE NATURE OF THE GRAIN BOUNDARIES

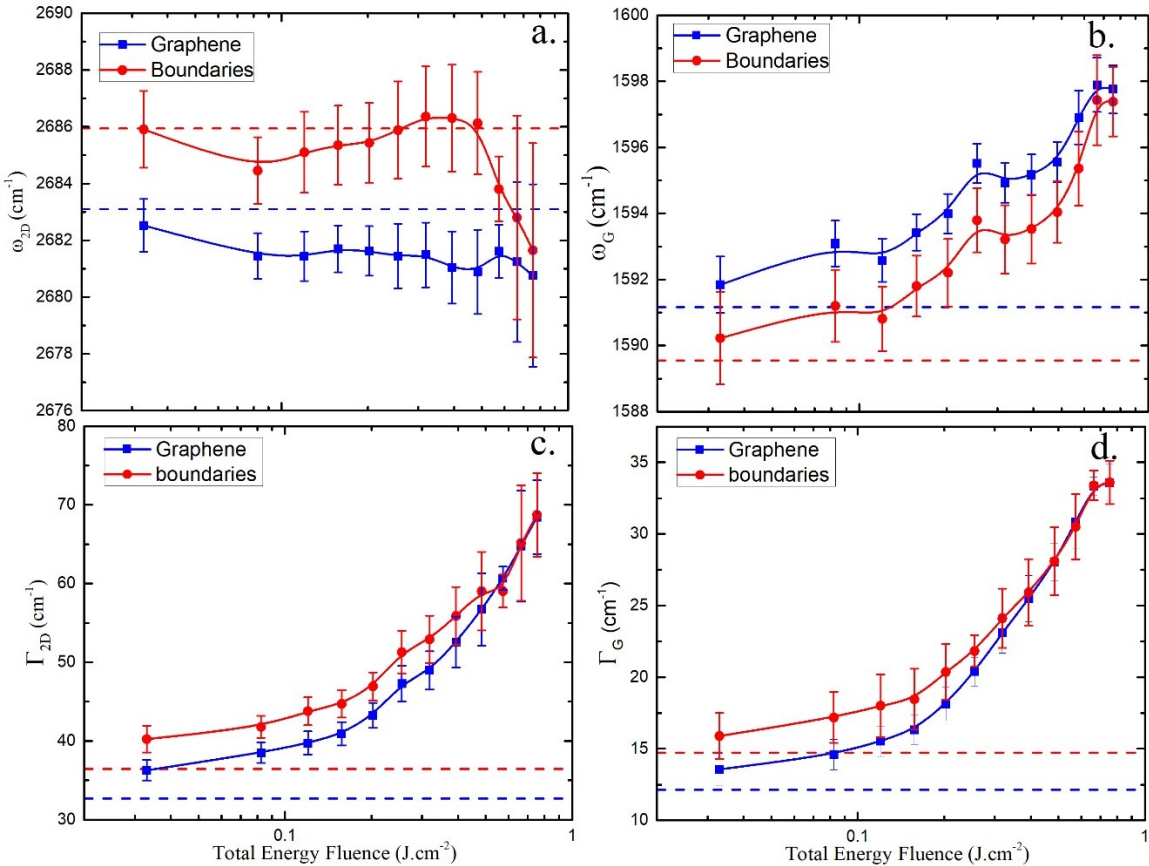


Figure 3.1.S5. Evolution of (a)  $\omega_{2D}$ , (b)  $\omega_G$ , (c)  $\Gamma_{2D}$ , and (d)  $\Gamma_G$  highlighting the discrepancies between GBs and graphene grains. All parameters are plotted versus the total energy fluence accumulated during the subsequent

Figure 3.1.S5 presents the evolution of the 2D and G bands positions. Regarding graphene in its pristine state,  $\omega_{2D}$  value at GBs is at least  $3 \text{ cm}^{-1}$  greater than at the grains. Knowing that this parameter is strongly linked with compressive ( $\varepsilon < 0$ ) or tensile ( $\varepsilon > 0$ ) strains in graphene (see Table S1) [12,14,28], it shows therefore that GBs are subject to a compressive strain. Indeed, CVD-grown graphene on copper exhibits a compressive strain after cooling due to a difference in thermal expansion between graphene and Cu [29]. Such effect may even be enhanced after transfer to  $\text{SiO}_2$  [30] and expected to be contained within the GBs [31]. The pristine value of  $\omega_G$  is smaller within GBs ( $1589 \text{ cm}^{-1}$ ) than within GR ( $1591 \text{ cm}^{-1}$ ) which is expected for CVD-graphene GBs under compressive strain or Stone-Wales defects [18,32].

Moreover, overlapping layers or wrinkles (found at the domain boundaries) are also known to induce a blueshift of the 2D band [21,33,34]. Such results are the definitive proof that the method carried out here is capable of disentangling signals at graphene domains from that at their boundaries. Note that local doping could also explain a shift in the G and 2D peaks position, but n- and p-doping would only lead to an increase of  $\omega_G$ . Significant differences between GBs and GR can also be seen for  $\Gamma_{2D}$  and  $\Gamma_G$ . For example,  $\Gamma_{2D,GB}$  is about  $4 \text{ cm}^{-1}$  wider than  $\Gamma_{2D,GR}$ . This results from the difference in morphology at the boundary of two graphene domains: overlapping layers, wrinkles or defective boundaries such as 5-7 ring chains [21,32,33] (see also discussion related to Figure 3.1.S5).

When comparing the evolution of both  $\omega_G$  and  $\omega_{2D}$ , graphene domains and their boundaries present similar behaviors, which are constant  $\Delta\omega_G$  and  $\Delta\omega_{2D}$  –i.e. a constant strain difference– up until  $t = 765 \text{ s}$  ( $0.57 \text{ J}\cdot\text{cm}^{-2}$ ). This sudden gap reduction in the data might coincide with strain relaxation in GBs, possibly due to the high defect density evidenced by the monotonous increase of  $\omega_G$  within the whole probed area [16,17]. Note that the position of the 2D band is seen to slightly increase within the GBs between 160 and 525 s ( $0.12$  to  $0.39 \text{ J}\cdot\text{cm}^{-2}$ ) of cumulative plasma treatments which could be associated with an increase of compressive strain due to adatoms incorporation, such as in inverse Stone-Wales defects [35].

A supplementary proof of GBs nature as defective 1D lines stitched grains can be found by a careful look at the results in Figure 3.1.S5a. Indeed, a high 2D/G intensity ratio is typically obtained with high-quality monolayer graphene whereas increasing disorder [19] and number of layers (*ABAB*-stacking) reduces this ratio [36]. Furthermore, due to the irregular graphene growth by CVD process on polycrystalline copper substrates [37], each grain is formed with a specific orientation, which may lead to overlapping layers at GBs. However, this angular shift within the basal plane leads to higher  $I_{2D}/I_G$  values [33,36]. Hence, the smaller value of  $I_{2D}/I_G$  at GBs (Fig. 3.1.S5b) rules out bilayer stacking as one of the main morphological differences. A lower  $I_{2D}/I_G$  value at GBs is therefore characteristic of structural defects, such as wrinkles and defective boundaries [38].

## S-VI. DAMAGE FORMATION BY VERY LOW-ENERGY ARGON IONS

The different contributions from the energetic plasma species have been detailed previously in section S-II. Metastable species only represent 16% of the total energy fluence provided to the graphene sample compared to ions and VUV photons (43 and 41%, respectively). Among those, the Ar<sup>+</sup> species (11-13 eV at plasma on and 1 eV during the post-discharge of the pulsed argon plasma) impinge the surface at normal incidence due to the potential drop in the sheath surrounding the graphene sample and, thus, transfer a significant part of the energy. Regarding VUV photons, the graphene photo-absorption at 11.7 eV is expected to be very weak [39]. Additionally, the results presented in Fig. 3.1.5b confirm that the 11-13-eV ions are the main energy input responsible for the damage generation since the defects observed by Raman are mainly 0D [17].

Considering an energy of 11-13eV for the argon ions impinging onto the graphene substrate, each incident ion transfers a maximum of 8-10 eV to the graphene lattice during the plasma-*on* time. Theoretical first-principles estimates of T<sub>d</sub>, *i.e.* the minimum energy to be transferred to a carbon atom before leaving its lattice position without immediate recombination with a vacancy, give 8-22eV,<sup>40</sup> which is consistent with the 18-20 eV values obtained by electron-beam experiments.<sup>41,42</sup> Over the range of experimental conditions investigated, despite clear evidences of 0D defect formation by Raman spectroscopy, the energy of argon ions thus seems too small to produce any significant damage by ballistic ejection of carbon atoms. However, a significant rise of the D:G ratio was also observed in graphene exposed to a beam of very-low-energy argon ions (1-2 eV range, both single (15.8eV) and double ionization (43.4eV)) [43]. This suggests that during ion irradiation of graphene, in addition to the energy provided by knock-on collisions, additional energy transfer processes linked to surface recombination of positive ions also needs to be considered. Such phenomena is more complex in plasma environments due to the simultaneous impingement of a collection of energetic particles characterized by various energy transfer time scales. This so-called plasma synergistic effect [44,45] includes, for example, the surface recombination of argon ions as in ion beam experiments but also the surface deexcitation of metastable argon atoms [46]. While recombination and deexcitation surface processes leading to electron excitation in the graphene lattice are extremely fast

(~fs),[47,48] electron energy relaxation phenomena (for example, through electron-phonon coupling) are comparatively much slower (~a few ps) [49,50].

In this context, Molecular Dynamics (MD) simulations were carried out to examine the damage formation dynamics by very-low-energy argon ions. In order to simulate the contribution of additional energy uptakes by plasma species (e.g., the surface recombination of argon ions and the deexcitation of argon metastable species, which represent instantaneous energy releases of 15.8 and 11.6eV, respectively), simulations were performed at various temperatures in the 300-3000K range. It is worth mentioning here that this “temperature” is an expression of the “transitionary state of graphene” occurring as a result of additional energy uptake (electron excitation) and subsequent energy dissipation phenomena (electron-phonon coupling). Hence, it does not represent the “actual temperature” of the graphene substrate under steady-state conditions, but rather a “transitionary vibration dynamics” in graphene after an instantaneous electron excitation. Since the knock-on collision occurs at the fs time scale and energy relaxation at the few ps time scale [47-50], the choice made is to fix the “graphene temperature” at the time scale MD simulations.

MD simulations were carried out with the open-source code LAMMPS. A three-body ZBL/Tersoff potential was used for the pristine graphene lattice [51-54], whereas a Lennard-Jones potential [52,54] was used to describe the argon-carbon interaction. As in comparable MD studies reported in the literature, the model system consists of a suspended graphene slab with 8530 carbon atoms ( $22 \times 22 \text{ nm}^2$ ). Graphene was first minimised and then heated up to 300K during 10ps in a N-P-T (constant Number-Pressure-Temperature) environment. Since energy transfers due to surface recombination of argon ions cannot be considered in LAMMPS (only argon-carbon collisions are considered), the system was manually heated up to a given temperature. For that respect, graphene obtained at 300K was progressively heated for 50ps in a N-P-T environment to attain the desired temperature of each simulation. The graphene was subsequently relaxed for another 50ps at this temperature. To avoid any edge effects, each simulation consisted of a random introduction of one argon atom (with a fixed kinetic energy,  $E_{\text{ion}}$ ) close to the center of the simulation domain in order. Every simulation lasted for 1ps and

were produced in an N-V-E (constant Number-Volume and Energy) environment. To obtain statistics in a reasonable time, 200 collisions were simulated for each set of conditions.

From each simulation image, the damage probability was assessed as follows. The difference in the z direction of each carbon atom with respect to its closest neighbors was compared with the mean position of all carbon atoms in the graphene lattice. A carbon adatom is confirmed when the difference for the suspected carbon adatom generated by the knock-on collision is higher than the mean value plus six times the standard deviation. This method permits to avoid wrongly defining as adatoms the carbon atoms found within the ripples of our suspended graphene model. Therefore, the probability for damage formation in such simulations is linked to the formation of carbon adatoms/vacancy pairs (Frenkel pairs), and not to simple bond rotations (Stones Wales defects).

Figure 3.1.S6 presents the probability for defect formation in monolayer graphene as a function of “graphene temperature” for various values of the energy transferred to the graphene lattice through argon-carbon collisions  $T = 4 m_C m_{Ar}/(m_C + m_{Ar})^2$ , where  $m_C$  and  $m_A$  are the masses of carbon and argon atoms, respectively. While more or less temperature-independent behavior is observed at 22.5eV (i.e. above  $T_d=18-22$ eV [35,40-42]), a significant rise with temperature is observed for 17.8 and 15.5eV (i.e. below  $T_d=18-22$ eV [35,40-42]). In the latter conditions, damage formation can therefore appear at energies below  $T_d$ , which is in very good agreement with the study of Ahlberg et al. [43] and consistent with our experimental data obtained in both pulsed and continuous plasma conditions.

It is worth highlighting that the probability for defect formation for  $T < T_d$  at reasonable “graphene temperatures” (below 1000K) [47-50] remains very small (at most 1%). Such low probability is important as it prevents graphene amorphization. Considering a fluence of positive ions of  $9 \times 10^{15}$  part.cm<sup>-2</sup> for 60s and  $1.5 \times 10^{17}$  part.cm<sup>-2</sup> for 1005s, this corresponds to a defect concentration of at most  $9 \times 10^{13}$  part.cm<sup>-2</sup> for 60s and at most  $1.5 \times 10^{15}$  part.cm<sup>-2</sup> for 1005s. While the former is much lower than the surface atomic density of carbon atoms in the graphene lattice ( $\sim 3.8 \times 10^{15}$  part.cm<sup>-2</sup>), the latter becomes much closer. This result is therefore in very good agreement with the expected transition from stage 1 (from undisturbed graphene to

nanocrystalline graphene) to stage 2 (progression towards amorphous carbon) with increasing plasma treatment time [55,56].

The results presented in Figure 3.1.S6 are also consistent with a study of electron-graphene collisions by Kotakosky and co-workers recently published in Scientific Reports [57]. The authors have shown that the minimum energy that needs to be transferred to a carbon atom to leave its lattice position without immediate recombination with the vacancy is not an absolute value, but rather present an energy distribution function [57]. In addition, the broadening rises with increasing graphene temperature due to the corresponding increase in the vibration dynamics of carbon atoms in the graphene lattice.

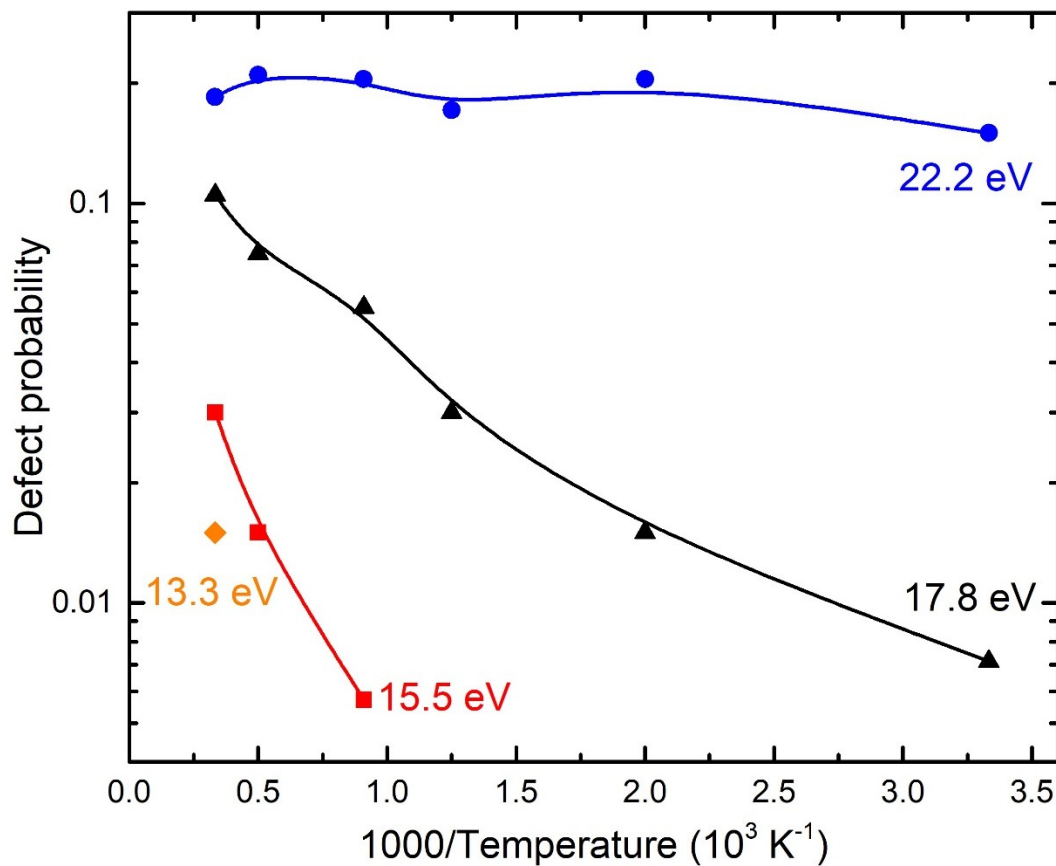


Figure 3.1.S6. MD simulations of damage formation at energies below  $T_d$  plotted as a thermally-activated process (Arrhenius plot). Here, the apparent activation energy decreases with increasing value of  $T$  (linked to the energy of argon atoms). A similar behavior was observed for temperature-dependent radiation-enhanced diffusion in ion-irradiated solids.[58]

## S-VII. PREFERENTIAL MIGRATION OF CARBON ADATOMS

The formation and migration energies of various defects are of critical importance in radiation-damage studies of graphene. An extensive review of those values is presented by *Banhart et al* [35]. It is commonly accepted that the threshold energy for carbon adatoms ejection from created defects is  $T_d = 18\text{-}20 \text{ eV}$  [35]. Even though argon ions can only transfer 8 eV to carbon atoms by knock-on collisions, these positively charged species can also neutralise on the surface, transmitting a potential energy of 15.8 eV to the graphene lattice. Furthermore, argon metastable and VUV photon can deliver around 11.5 eV to the surface. All those potential energies lead to a reduction of the threshold energy for defect formation, referenced as the plasma synergetic effect inherent to plasma processing.

Considering argon ions as initiator for defect formation in low-pressure argon plasmas, the creation of Stone-Wales defects ( $E_F(\text{SW}) = 6.4\text{-}7.9 \text{ eV}$ ) [59-61] appears the most probable, involving only bond rotation and no ballistic ejection of carbon atoms. A subsequent argon ion impinging the same location can produce a carbon adatom due to the already fragile structure. On the other hand, considering the plasma synergetic effect lowering the various energy thresholds, it is possible to consider Frenkel pair formation ( $E_F(\text{FP}) = 14 \text{ eV}$ ) as a possible outcome (see S-VII). This adatom-vacancy pair is stable unless some energy is provided.

While single vacancy requires  $\sim 1.3 \text{ eV}$  for migration on graphene surfaces, a carbons adatom only needs 0.4 eV to diffuse [35]. As for a Stones-Wales defect, it demands 10 eV to move [41], which makes such defect essentially immobile with respect to other species. Hence, carbon adatoms and single vacancies are the species with the highest probability to diffuse on the graphene surface. The energy necessary for such migration is provided locally in both time and space by the non-equilibrium plasma through ions, metastable and VUV photons. In this framework, jump frequencies can be estimated through an Arrhenius equation  $f = A \exp\left(-\frac{E_a}{k_B T}\right)$ , [62] where  $A$  is a pre-factor depending of the studied species,  $E_a$  is the activation energy, and  $k_B T$  is the thermal energy. In the case of carbon adatoms, the pre-factor for surface diffusion on graphene can be estimated at  $3.7 \times 10^{12} \text{ s}^{-1}$  [63]. Since the pre-factor for the displacement of single vacancies is of the same order of magnitude ( $1.2 \times 10^{12} \text{ s}^{-1}$ ) [62], the

jump frequency of carbon adatoms and single vacancies become mostly linked to the corresponding values of  $E_a$ . Since carbon adatoms on graphene have a much lower activation energy (0.4 eV) compared to single vacancies (1.5 eV), it results in a higher mobility for carbon adatoms than single vacancies. For example, at room temperature ( $T = 300$  K), the jump frequency for carbon adatoms and vacancies can be estimated as  $7.6 \times 10^5$  s $^{-1}$  and  $7.9 \times 10^{-14}$  s $^{-1}$ , respectively.

## S-VIII. REFERENCES

- [1] Vinchon, P. *et al.* A combination of plasma diagnostics and Raman spectroscopy to examine plasma-graphene interactions in low-pressure argon radiofrequency plasmas. *J. Appl. Phys.* **126**, 233302 (2019).
- [2] Martins Ferreira, E. H. *et al.* Evolution of the Raman spectra from single-, few-, and many-layer graphene with increasing disorder. *Phys. Rev. B* **82**, 125429 (2010).
- [3] Lieberman, M. A. & Lichtenberg, A. J. *Principles of Plasma Discharges and Materials Processing: Second Edition. Principles of Plasma Discharges and Materials Processing: Second Edition* (2005). doi:10.1002/0471724254
- [4] Barton, D., Heason, D. J., Short, R. D. & Bradley, J. W. The measurement and control of the ion energy distribution function at a surface in an RF plasma. *Meas. Sci. Technol.* **11**, 1726–1731 (2000).
- [5] Tang, X. & Manos, D. M. Time-resolved electrostatic probe studies of a pulsed inductively-coupled plasma. *Plasma Sources Sci. Technol.* **8**, 594–602 (1999).
- [6] Sushkov, V., Do, H. T., Cada, M., Hubicka, Z. & Hippler, R. Time-resolved tunable diode laser absorption spectroscopy of excited argon and ground-state titanium atoms in pulsed magnetron discharges. *Plasma Sources Sci. Technol.* **22**, (2013).
- [7] Celik, Y. *et al.* Recombination and enhanced metastable repopulation in the argon afterglow. *Phys. Rev. E - Stat. Nonlinear, Soft Matter Phys.* **85**, 1–12 (2012).
- [8] Golubovskii, Y., Gorchakov, S. & Uhrlandt, D. Transport mechanisms of metastable and resonance atoms in a gas discharge plasma. *Plasma Sources Sci. Technol.* **22**, (2013).
- [9] Zhang, W. *et al.* Ti:sapphire femtosecond laser direct micro-cutting and profiling of graphene. *Appl. Phys. A Mater. Sci. Process.* **109**, 291–297 (2012).
- [10] Bruna, M. *et al.* Doping dependence of the Raman spectrum of defected graphene. *ACS Nano* **8**, 7432–7441 (2014).
- [11] Das, A. *et al.* Monitoring dopants by Raman scattering in an electrochemically top-gated graphene

- transistor. *Nat. Nanotechnol.* **3**, 210–215 (2008).
- [12] Zabel, J. *et al.* Raman Spectroscopy of Graphene and Bilayer under Biaxial Strain: Bubbles and Balloons. *Nano Lett.* **12**, 617–621 (2012).
- [13] Lee, J. E., Ahn, G., Shim, J., Lee, Y. S. & Ryu, S. Optical separation of mechanical strain from charge doping in graphene. *Nat. Commun.* **3**, 1024 (2012).
- [14] Wang, Y. *et al.* Domain-boundary independency of Raman spectra for strained graphene at strong interfaces. *Carbon N. Y.* **134**, 37–42 (2018).
- [15] Ni, Z. H. *et al.* Uniaxial Strain on Graphene: Raman Spectroscopy Study and Band-Gap Opening. *ACS Nano* **2**, 2301–2305 (2008).
- [16] Ferrari, A. C. & Robertson, J. Interpretation of Raman spectra of disordered and amorphous carbon. *Phys. Rev. B* **61**, 14095–14107 (2000).
- [17] Gustavo Cançado, L. *et al.* Disentangling contributions of point and line defects in the Raman spectra of graphene-related materials. *2D Mater.* **4**, 025039 (2017).
- [18] Bissett, M. A., Izumida, W., Saito, R. & Ago, H. Effect of domain boundaries on the Raman spectra of mechanically strained graphene. *ACS Nano* **6**, 10229–10238 (2012).
- [19] Zhou, Y.-B. *et al.* Ion irradiation induced structural and electrical transition in graphene. *J. Chem. Phys.* **133**, 234703 (2010).
- [20] Jia, K. *et al.* Effects of defects and thermal treatment on the properties of graphene. *Vacuum* **116**, 90–95 (2015).
- [21] Ferrari, A. C. *et al.* Raman spectrum of graphene and graphene layers. *Phys. Rev. Lett.* **97**, 1–4 (2006).
- [22] Malard, L. M. M., Pimenta, M. A. A., Dresselhaus, G. & Dresselhaus, M. S. S. Raman spectroscopy in graphene. *Phys. Rep.* **473**, 51–87 (2009).
- [23] Frank, O. *et al.* Raman 2D-band splitting in graphene: Theory and experiment. *ACS Nano* **5**, 2231–2239 (2011).
- [24] Venezuela, P., Lazzeri, M. & Mauri, F. Theory of double-resonant Raman spectra in graphene: Intensity and line shape of defect-induced and two-phonon bands. *Phys. Rev. B - Condens. Matter Mater. Phys.* **84**, 1–25 (2011).
- [25] Vinchon, P. *et al.* Hyperspectral Raman Imaging of plasma treated monolayer graphene. *Submitt. to Rev. Sci. Instruments* (2019).
- [26] Rasband, W. ImageJ image processing program. *National Institutes of Health* (2019).
- [27] Cançado, L., Gomes de Silva, M., Ferreira, E. H. M. & Hof, F. Disentangling contributions of point and line defects in the Raman spectra of graphene-related materials. *2D Mater.* **4**, 025039 (2017).

- [28] Lee, J. U., Yoon, D. & Cheong, H. Estimation of young's modulus of graphene by Raman spectroscopy. *Nano Lett.* **12**, 4444–4448 (2012).
- [29] Zhang, Y. *et al.* Defect-like structures of graphene on copper foils for strain relief investigated by high-resolution scanning tunneling microscopy. *ACS Nano* **5**, 4014–4022 (2011).
- [30] Larsen, M. B. B. S., Mackenzie, D. M. A., Caridad, J. M., Bøggild, P. & Booth, T. J. Transfer induced compressive strain in graphene: Evidence from Raman spectroscopic mapping. *Microelectron. Eng.* **121**, 113–117 (2014).
- [31.] Wang, B., Puzyrev, Y. & Pantelides, S. T. Strain enhanced defect reactivity at grain boundaries in polycrystalline graphene. *Carbon N. Y.* **49**, 3983–3988 (2011).
- [32] Shirodkar, S. N. & Waghmare, U. V. Electronic and vibrational signatures of Stone-Wales defects in graphene: First-principles analysis. *Phys. Rev. B - Condens. Matter Mater. Phys.* **86**, 1–10 (2012).
- [33] Park, K. D., Raschke, M. B., Atkin, J. M., Lee, Y. H. & Jeong, M. S. Probing Bilayer Grain Boundaries in Large-Area Graphene with Tip-Enhanced Raman Spectroscopy. *Adv. Mater.* **29**, 1–6 (2017).
- [34] Kim, K. *et al.* Raman Spectroscopy Study of Rotated Double-Layer Graphene: Misorientation-Angle Dependence of Electronic Structure. *Phys. Rev. Lett.* **108**, 246103 (2012).
- [35] Banhart, F., Kotakoski, J. & Krasheninnikov, A. V. Structural Defects in Graphene. *ACS Nano* **5**, 26–41 (2011).
- [36] Ni, Z., Wang, Y., Yu, T. & Shen, Z. Raman spectroscopy and imaging of graphene. *Nano Res.* **1**, 273–291 (2008).
- [37] Nie, S., Wofford, J. M., Bartelt, N. C., Dubon, O. D. & McCarty, K. F. Origin of the mosaicity in graphene grown on Cu(111). *Phys. Rev. B - Condens. Matter Mater. Phys.* **84**, 1–7 (2011).
- [38] Ogawa, Y. *et al.* Structure and transport properties of the interface between CVD-grown graphene domains. *Nanoscale* **6**, 7288–7294 (2014).
- [39] Trevisanutto, P. E., Holzmann, M., Côté, M. & Olevano, V. Ab initio high-energy excitonic effects in graphite and graphene. *Phys. Rev. B - Condens. Matter Mater. Phys.* **81**, 3–6 (2010).
- [40] Yazyev, O. V., Tavernelli, I., Rothlisberger, U. & Helm, L. Early stages of radiation damage in graphite and carbon nanostructures: A first-principles molecular dynamics study. *Phys. Rev. B* **75**, 115418 (2007).
- [41] Banhart, F. Irradiation effects in carbon nanostructures. *Reports Prog. Phys.* **62**, 1181–1221 (1999).
- [42] Smith, B. W. & Luzzi, D. E. Electron irradiation effects in single wall carbon nanotubes. *J. Appl. Phys.* **90**, 3509–3515 (2001).

- [43] Ahlberg, P. *et al.* Defect formation in graphene during low-energy ion bombardment. *APL Mater.* **4**, (2016).
- [44] Rousseau, B., Estrade-Szwarckopf, H., Thomann, A.-L. & Brault, P. Stable C-atom displacements on HOPG surface under plasma low-energy argon-ion bombardment. *Appl. Phys. A Mater. Sci. Process.* **77**, 591 (2003).
- [45] Allain, J. P. & Shetty, A. Unraveling atomic-level self-organization at the plasma-material interface. *J. Phys. D. Appl. Phys.* **50**, 283002 (2017).
- [46] Bard, A. Self-assembled monolayers exposed by metastable argon and metastable helium for neutral atom lithography and atomic beam imaging. *J. Vac. Sci. Technol. B Microelectron. Nanom. Struct.* **15**, 1805 (1997).
- [47] Tomadin, A., Brida, D., Cerullo, G., Ferrari, A. C. & Polini, M. Nonequilibrium dynamics of photoexcited electrons in graphene: Collinear scattering, Auger processes, and the impact of screening. *Phys. Rev. B* **88**, 035430 (2013).
- [48] Su, C. *et al.* Engineering single-atom dynamics with electron irradiation. *Sci. Adv.* **5**, 1–12 (2019).
- [49] Lazzeri, M., Piscanec, S., Mauri, F., Ferrari, A. C. & Robertson, J. Electron Transport and Hot Phonons in Carbon Nanotubes. *Phys. Rev. Lett.* **95**, 236802 (2005).
- [50] Butscher, S., Milde, F., Hirtschulz, M., Malić, E. & Knorr, A. Hot electron relaxation and phonon dynamics in graphene. *Appl. Phys. Lett.* **91**, 17–20 (2007).
- [51] Bellido, E. P. & Seminario, J. M. Molecular dynamics simulations of ion-bombarded graphene. *J. Phys. Chem. C* **116**, 4044–4049 (2012).
- [52] Wei, X. L., Zhang, K. W., Wang, R. Z., Liu, W. L. & Zhong, J. X. Modified morphology of graphene sheets by Argon-atom bombardment: Molecular dynamics simulations. *J. Nanosci. Nanotechnol.* **11**, 10863–10867 (2011).
- [53] Wu, X., Zhao, H. & Murakawa, H. The joining of graphene sheets under Ar ion beam irradiation. *J. Nanosci. Nanotechnol.* **14**, 5697–5702 (2014).
- [54] Li, W., Liang, L., Zhao, S., Zhang, S. & Xue, J. Fabrication of nanopores in a graphene sheet with heavy ions: A molecular dynamics study. *J. Appl. Phys.* **114**, (2013).
- [55] Ferrari, A. C. & Robertson, J. Raman spectroscopy of amorphous, nanostructured, diamon-like carbon, and nanodiamond. *Philosophical Trans. Math. Phys. Eng. Sci.* **363**, 2477–2512 (2004).
- [56] Eckmann, A. *et al.* Probing the nature of defects in graphene by Raman spectroscopy. *Nano Lett.* **12**, 3925–3930 (2012).
- [57] Chirita Mihaila, A. I., Susi, T. & Kotakoski, J. Influence of temperature on the displacement threshold energy in graphene. *Sci. Rep.* **9**, 1–7 (2019).

- [58] Marton, D., Fine, J. & Chambers, G. P. Temperature-dependent radiation-enhanced diffusion in ion-bombarded solids. *Phys. Rev. Lett.* **61**, 2697–2700 (1988).
- [59] Li, L., Reich, S. & Robertson, J. Defect energies of graphite: Density-functional calculations. *Phys. Rev. B - Condens. Matter Mater. Phys.* **72**, 1–10 (2005).
- [60] Ma, J., Alfè, D., Michaelides, A. & Wang, E. Stone-Wales defects in graphene and other planar s p<sub>2</sub>-bonded materials. *Phys. Rev. B - Condens. Matter Mater. Phys.* **80**, 1–4 (2009).
- [61] Kotakoski, J., Krasheninnikov, A. V., Kaiser, U. & Meyer, J. C. From point defects in graphene to two-dimensional amorphous carbon. *Phys. Rev. Lett.* **106**, 1–4 (2011).
- [62] Wadey, J. D. *et al.* Mechanisms of monovacancy diffusion in graphene. *Chem. Phys. Lett.* **648**, 161–165 (2016).
- [63] Krasheninnikov, A. V. *et al.* Adsorption and migration of carbon adatoms on zigzag carbon nanotubes. *Carbon N. Y.* **42**, 1021–1025 (2004).

## **2. Étude des rôles respectifs des ions, des metastables et des photons VUV**

Dans l'optique d'étudier les mécanismes de génération de défauts sur le graphène, de nouvelles conditions opératoires du plasma RF ont été explorées. En effet, l'étude temporelle de ces plasmas combinée à un contrôle fin des paramètres opératoires permet de favoriser certaines espèces qui sont souvent négligées lors des interactions plasma-surface. Une condition particulière a permis de favoriser la densité de métastable et donc d'étudier leur impact sur le graphène. Une autre configuration a permis d'avantagez la contribution des photons VUV issus des niveaux résonants. À ceci s'ajoute les mesures présentées précédemment où les ions sont prédominants. La même méthodologie est appliquée pour les deux nouvelles conditions afin d'identifier le rôle respectif des ions, des métastables et des photons VUV lors de l'exposition au plasma d'argon du graphène. Ces résultats sont présentés sous la forme d'un article en préparation finale soumis à *Journal of Physics D* (JPhysD-126700). À notre avis, ce travail présente la première démonstration expérimentale de l'apport d'énergie des métastables et des photons VUV dans l'interaction plasma-graphène. Pour ce travail, ma contribution personnelle se situe dans l'étude temporelle du plasma pour les différentes conditions, les traitements par plasma du graphène ainsi que les mesures et analyses RIMA. J'ai également développé le code matlab permettant d'identifier et d'aligner les différentes zones étudiées. Enfin, j'ai rédigé une première version de l'article. X.Glad a participé activement à l'interprétation des données et à leurs mises en forme. G.R. Bigras a contribué à l'amélioration constante du code matlab utilisé pour interprétation des données obtenues au RIMA. Ce travail a été accomplis sous la supervision de R. Martel et L. Stafford, en collaboration avec notre partenaire industriel A. Sarkissian.

**PLASMA-GRAPHENE INTERACTIONS: RESPECTIVE ROLES OF  
POSITIVE IONS, VACUUM-ULTRAVIOLET PHOTONS,  
AND METASTABLE SPECIES**

P. Vinchon<sup>1</sup>, X. Glad<sup>1</sup>, G. Robert Bigras<sup>1</sup>, A. Sarkissian<sup>2</sup>, R. Martel<sup>3</sup>, L. Stafford<sup>1</sup>

<sup>1</sup>Département de Physique, Université de Montréal, Montréal, Québec, CANADA.

<sup>2</sup>Plasmionique Inc, Varennes, Québec, CANADA.

<sup>3</sup>Département de Chimie, Université de Montréal, Montréal, Québec, CANADA.

**ABSTRACT**

This study compares the impact of different plasma environments on the damage formation dynamics of polycrystalline monolayer graphene films on SiO<sub>2</sub>/Si substrates and investigates the combined effects often observed in low-pressure argon plasmas. After careful characterization of the discharge properties by Langmuir probes and optical absorption spectroscopy, three operating conditions were selected to promote graphene irradiation by either positive ions, metastable species, or vacuum-ultraviolet (VUV) photons. In all cases, hyperspectral Raman imaging of graphene reveals plasma-induced damage. In addition, defect generation is systematically slower at grain boundaries than within the grains, a behavior ascribed to a preferential self-healing of plasma-induced defects at grain boundaries. The evolution of selected Raman band parameters is also correlated with the energy fluence provided to the graphene lattice by very-low-energy ions. From such correlation, it is shown that the presence of VUV photons enhances the defect formation dynamics through additional energy transfer. On the other hand, the presence of metastable species first impedes the defect generation and then promotes it for higher lattice disorder. While this impediment can be linked to an enhanced defect migration and self-healing at nanocrystallite boundaries in graphene, such effect vanishes in more heavily-damaged films.

Plasma-surface interactions are at the core of new and cutting-edge technologies, especially regarding the ever-growing field of nanotechnology [1]. Development of low-dimensional materials are possible by plasma processes, e.g. carbon nanotubes [2,3], graphene [3–5], cosmic dust analogues [6], vertically-aligned nanostructures [7–11], etc. The intrinsic properties of the plasma state further allow for numerous applications in post-growth processing of nanomaterials, for example of monolayer graphene films [12–15]. Such a vast area of applications in materials processing is made possible by the versatility of plasma discharges and the numerous energetic species found within the gas phase, such as positive ions, electrons, photons, radicals and long-lived metastable states.

Depending on the nature of the plasma gas (molecular or atomic), plasma-surface interactions can induce a number of atomic-scale phenomena, including chemical and physical etching. In the former, radicals created by plasma dissociation of a reactive gas interact with the substrate surface to create new, weakly-bound chemical groups. Chemical etching by plasma-generated hydrogen atoms has been thoroughly studied in carbonaceous materials for nuclear fusion applications since graphite is a good candidate for the plasma-facing components [16–20]. In physical etching, the atom ejection is obtained through knock-on collisions with the positive ions impinging onto the surface following their acceleration in the plasma sheath. This process requires the incoming ion to transfer sufficient momentum to overcome the binding energy of the surface atoms and, thus, an energy threshold is defined for different ion-surface atom couples. For example, to eject a carbon atom from its lattice in graphite/graphene, an energy of 18–22 eV [21,22] is required; this is possible with argon ions above 25–30 eV. However, these thresholds have been found to be lowered in plasma environments as compared with conventional ion beams [23]. Indeed, physical etching has been shown to occurred on graphite/graphene surfaces in discharges with very low-energy impinging argon ions ( $E_{ion} < 15$  eV) [11,24]. This often-called “synergy plasma effect” is thought to be due to the simultaneous fluxes of other plasma-generated species which also interact with the surface, such as vacuum ultraviolet (VUV) photons or metastable states.

In this study, the combined plasma effects are explored in details for polycrystalline monolayer graphene films through fine-tuning of the operating conditions of a low-pressure

argon plasma so as to promote surface irradiation by either positive ions, VUV photons or metastable species. Inspired by recent development in Raman spectroscopy [25,26], plasma-treated graphene is analyzed by hyperspectral Raman imaging and the results are used to examine with a high selectivity the damage formation dynamics.

The apparatus is a low-pressure RF plasma system, which has been described in details elsewhere [24]. The versatility of RF plasmas at low pressure allows for a large array of possible plasma conditions and this is a critical feature in this study. The power supply (R601 Seren IPS Inc.) is operated at 13.56 MHz between 20 and 100 W in pulsed mode (frequency  $f = 1$  kHz, duty cycle DC = 10 – 50%) and is coupled with an automatic matching box to ensure minimal power reflection. To avoid the presence of contaminants during the plasma treatment, the pumping system allows a base pressure of  $5 \times 10^{-8}$  Torr ( $6.7 \times 10^{-6}$  Pa) before injecting a flow of ultra-high-purity (99.999 %) argon. Before inserting the graphene sample using a load lock, the species on the reactor walls are desorbed using a 30-min argon plasma with the exact same conditions used for plasma treatment. The substrate holder is at a floating potential and is placed at the center of the reactor at 20 cm below the planar spiral-shaped RF antenna (in the diffused plasma region).

Plasma conditions are carefully selected after characterization by time-resolved Langmuir probe (LP) and optical absorption spectroscopy (OAS) measurements recorded a few centimeters above the substrate holder. The former has been carried out using a cylindrical rf-compensated Langmuir probe (LP) from Scientific systems Ltd and the latter using a low-pressure argon lamp, a Princeton Instruments Isoplane spectrometer with a  $300 \text{ gr} \cdot \text{mm}^{-1}$  grating, and a PI-MAX4 intensified charged-coupled device camera. The whole procedure for both techniques is described in previous studies [13,24,27]. LP measurements permit the estimations of the electron temperature,  $T_e$ , assuming Maxwellian electron energy distribution function and of the positive ion density,  $n_i$ . Here,  $T_e$  is related to the energy of the ions,  $E_{\text{ion}}$ , obtained following their acceleration in the plasma sheath [28] – linked to the difference between plasma and floating potentials ( $V_p - V_f$ ) – and considered monoenergetic over the whole range of experimental conditions investigated [24]. The densities of argon  $1s_3$  and  $1s_5$  (Paschen's notation) metastable states, noted  $n(\text{Ar}^m)$ , as well as  $1s_2$  and  $1s_4$  resonant states,  $n(\text{Ar}^*)$ , are

determined using OAS. These long-lived energetic plasma species lie around 11.6 eV above the argon ground state Ar<sup>0</sup> [29]. These plasma parameters are then used to estimate the total power flux provided to the graphene lattice in each of the three selected plasma conditions, as presented in Section 3.1.

Graphene films are grown by chemical vapor deposition (CVD) on copper foils in a controlled CH<sub>4</sub>/H<sub>2</sub> environment leading to high-quality polycrystalline monolayer graphene films [30]. The latter are then transferred on SiO<sub>2</sub>/Si substrates with a 300-nm thick top SiO<sub>2</sub> layer using the standard PMMA transfer procedure [31]. Each graphene film is then exposed to subsequent argon plasma treatments, each in one of the three plasma conditions described below. Between each argon plasma treatment, damage formation in graphene is assessed by hyperspectral Raman spectroscopy using the RIMA (Raman IMAge) system [25,26]. RIMA provides a uniform laser illumination ( $\lambda_{\text{laser}} = 532 \text{ nm}$ ) over a wide area ( $130 \times 130 \mu\text{m}^2$ ) while keeping a high selectivity and diffraction-limited spatial resolution ( $\sim 390 \text{ nm}$ ). The spectral resolution of  $3 \text{ cm}^{-1}$  permits to extract meaningful data through a noise filtering technique; this method is extensively detailed elsewhere [26].

Inspired by previous works on plasma-graphene interactions [13,24], the argon plasma is pulsed at 1 kHz to reduce the fluence of plasma-generated species and thus to induce conditions of low-damage generation within the graphene films. This is of great importance since these conditions of using subsequent treatments and analysis allow for a well-controlled study on the influence of the plasma on the defect formation. For the sake of studying the respective roles of positive ions, VUV photons, and metastable species in plasma-graphene interactions, the operating parameters of the reactor such as RF power, pressure and duty cycle of the RF power have been adapted to promote one species over the others. Thus, three sets of conditions have been selected.

In a previous study [13], argon plasma treatments were carried out in conditions where positive ions dominated the damage generation. The latter are thus defined as conditions *cI*: 5 mTorr, 100 W, DC = 10%, inductive mode (H-mode). This coupling mode of the RF plasma provides high number densities of charged species and a relatively low T<sub>e</sub>, which ensures

rather low populations of metastable and resonant argon atoms [13,32]. To enhance the contribution of these species, the plasma density needs to be low and  $T_e$  has to be high [13]. Moreover in the low-pressure regime,  $Ar^m$  density typically grows with increasing pressure [29]. A plasma operated at low power and moderate pressure answers all of these requirements. Thus, *c2* condition is chosen as: 40 mTorr, 20 W, DC = 10%, capacitive mode (E-mode) of the RF plasma. Finally, an environment dominated by VUV photons requires a reduction of both  $n_i$  and  $n(Ar^m)$ . The former requires to operate the discharge in E-mode, while the latter condition is met, according to the literature [29,33], at around 5 mTorr (optically thin plasma for VUV photons). This leads to the last conditions, *c3*: 5 mTorr, 20 W, DC = 50%, E-mode of the RF plasma. The higher duty cycle has been chosen experimentally so as not to see a drop of the number density of resonant states after the plasma extinction, as discussed below.

Figure 3.2.1 presents the time-resolved evolution of  $T_e$  and  $(V_p - V_f)$  (Figure 3.2.1 a-c-e), as well as  $n_i$ ,  $n(Ar^m)$  and  $n(Ar^*)$  (Figure 3.2.1 b-d-f) for all three conditions over a period  $T = 1$  ms ( $f = 1$  kHz) of the injected RF power. Figures 3.2.1a and 3.2.1b report the results related to *c1*. A sharp increase of  $T_e$  and  $E_{ion} = e \cdot (V_p - V_f)$  is observed at plasma ignition up to 3.5 eV and 12 V, respectively. This is followed by a slow decrease down to 2.9 eV and 10 eV by the end of the pulse; comparable values were observed for a continuous plasma in similar operating conditions [24]. As the RF power is cut off,  $T_e$  and  $E_{ion}$  both drop drastically due to electron diffusive cooling [34] to stabilize around 0.4 eV and 1 eV, respectively. As detailed in [13], non-null values are the evidence of a temporal afterglow[35], which is confirmed by the presence of excited and ionized species as presented in Figure 3.2.1b. In the latter,  $n_i$ ,  $n(Ar^*)$  and  $n(Ar^m)$  – initially at  $8.0 \times 10^8 \text{ cm}^{-3}$ ,  $5.2 \times 10^8 \text{ cm}^{-3}$  and  $9.0 \times 10^9 \text{ cm}^{-3}$ , respectively – increase at *plasma-on* to reach a plateau around  $4.0 \times 10^9 \text{ cm}^{-3}$ ,  $2.5 \times 10^9 \text{ cm}^{-3}$ , and  $1.5 \times 10^{10} \text{ cm}^{-3}$ , respectively.

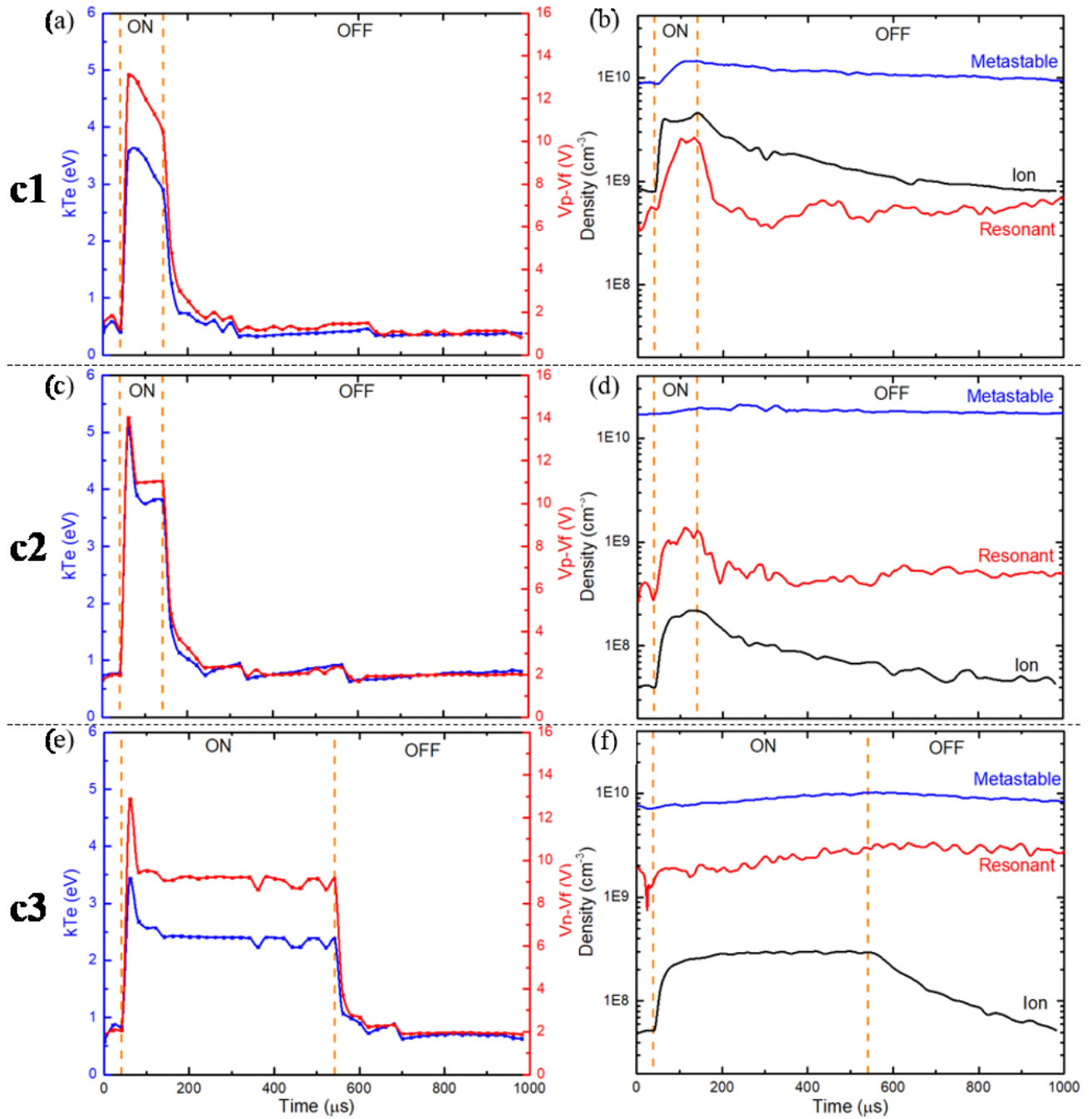


Figure 3.2.4. Plasma characterization in conditions c1, c2 and c3. (a,c,e) Electron temperature  $kT_e$  (in eV, blue) and  $V_p-V_f$  (in V, red) derived from cylindrical LP measurements. The average ion energy  $E_{\text{ion}}$  is linked to  $(V_p-V_f)$ . (b,d,f) Argon positive ion, metastable and resonant densities extracted from LP measurements for ions and OAS measurements otherwise.

However, while both ion and resonant state densities steeply increase at the beginning of the pulse,  $1s_3$  and  $1s_5$  states density briefly decrease before seeing a moderate increase. Such

behavior is explained by the quenching of metastable states due to electron-impact ionization and electron-impact excitation toward 2p states [36,37]. Note that the slope of the rising resonant states density is weaker than the one of the ion density due to the same phenomenon.

After the pulse, a sudden drop in  $T_e$  down to 1 eV prevents energetic species creation by direct electron-impact from the ground state  $\text{Ar}^0$  and mitigates the quenching of the metastable states. Thus, loss processes – mainly diffusion towards the plasma reactor walls in low- $n_i$  conditions [34] – become dominant and all parameters decrease to their *plasma-off* value. Note that  $n(\text{Ar}^*)$  severely drops due to the limited radiation trapping occurring at such pressure and thus low  $\text{Ar}^0$  density. This effect is greatly enhanced by the relatively high neutral gas temperature  $T_{\text{gas}}$  in H-mode (closely related to the plasma density). Indeed, a greater  $T_{\text{gas}}$  accentuates gas rarefaction and reduces the absorption coefficients due to wider Doppler broadening profiles of the lines. The  $n(\text{Ar}^*)$  variations observed after the drop are due to the detection limit of the OAS technique. Finally, the low  $T_e$  value in the temporal afterglow enhances ion recombination, notably through three-body recombination, which accentuates the decline of the ion density while feeding the argon metastable and ground states [34]. This explains the slow decrease of the long lived  $1s^3$  and  $1s^5$  states (respectively 1.3 and 38 s [38]).

Similar parameters are plotted for *c2* in Figures 3.2.1c and 1d.  $T_e$  and  $(V_p - V_f)$  share similar values and evolutions as in *c1* even though  $T_e$  is higher ( $\sim 4$  eV during the pulse,  $\sim 0.8$  eV otherwise). Knowing that increasing pressure in argon discharges is associated with a decrease in electron temperature [39], a greater  $T_e$  reveals that the plasma is confined to the source region. In these conditions, the substrate is immersed in a flowing afterglow leading to such a high electron temperature. It results in a smaller plasma volume, which leads to a rise in  $T_e$ . Regarding the energetic species densities presented in Figure 3.2.1d, a steep increase is observed for both  $n_i$  and  $n(\text{Ar}^*)$  as the electron quenching processes are mitigated at such low plasma density. This is also evidenced by the constant population of metastable states, which have only diffusive losses that are significantly reduced at higher pressure. While radiation trapping is better with rising pressure, the weak drop of  $n(\text{Ar}^*)$  is probably due to atom-atom collision processes [33].

Figures 3.2.1e and 3.2.1f also display the plasma characteristics of *c3* where DC = 50%. After plasma ignition,  $T_e$  and  $E_{ion}$  quickly stabilize around 2.5 and 9 eV (steady state regime).  $T_e$  is slightly lower than in *c1* since increasing power leads to a slow rise in electron temperature [39]. As seen in Figure 3.2.1f, the increased DC has a great impact on the population of resonant states since the number density value stays relatively constant around  $2 \times 10^9 \text{ cm}^{-3}$  throughout the whole period of the RF power. This may be explained by the low plasma density during the temporal afterglow, which prevents any electron-impact losses.

Based on this exhaustive characterization of the pulsed argon plasma, it is possible to extract the power density transferred to the graphene sample by each energetic species, namely, positive ions, metastable and resonant species [24,40]. The ion contribution to the total power density can be described by the following equation:

$$P_{ion} = \frac{1}{T} \int_0^T \mathbf{n}_i(\mathbf{t}) \sqrt{\frac{kT_e(t)}{M}} [\mathbf{C} \times \mathbf{E}_{ion}(\mathbf{t}) + \xi_i(\epsilon_i - \phi)] d\mathbf{t}, \quad (1)$$

where  $n_i$  is the number density of positive ions,  $\sqrt{\frac{kT_e(t)}{M}}$  is the Bohm velocity at the sheath edge (linked to the electron temperature  $T_e$  and the positive ion mass  $M = 40$  amu for argon),  $C$  is the energy transfer coefficient of the elastic collisions between argon ions and the graphene substrate [41],  $E_{ion}$  is the average kinetic energy of positive ions following their acceleration in the sheath voltage ( $V_p - V_f$ ),  $\xi_i$  is the probability of heterogeneous surface recombination of positive ions following their interaction with the graphene substrate,  $\epsilon_i$  is the energy released to the graphene lattice by heterogeneous surface recombination of positive ions (15.76 eV for argon ions),  $\phi$  is the work function of graphene ( $\sim 4.6$  eV) [42], and  $T$  is the period of the applied RF power.

Piejak *et al* [40] proposed an estimation of the power density provided by the heterogeneous surface de-excitation of metastable species following their interaction with a surface, as follows:

$$P_{ex} = \frac{1}{T} \int_0^T \frac{1}{4} (N_m(t) + N_*(t)) \sqrt{\frac{8kT_g}{\pi M}} \xi_m \epsilon_m dt, \quad (2)$$

where  $N_m$  and  $N_*$  are the number densities of metastable and resonant atoms, respectively,  $\sqrt{\frac{8kT_g}{\pi M}}$  is the average speed of neutral atoms impinging onto the substrate (linked to the neutral gas temperature  $T_g$  (assumed  $\sim 300$  K)),  $\xi_m$  is the probability of heterogeneous surface de-excitation of metastable and resonant atoms following their interaction with the graphene substrate, and  $\epsilon_m$  is the energy released to the graphene lattice by heterogeneous surface de-excitation of metastable and resonant atoms ( $\sim 11.7$  eV for argon species). It is worth highlighting than in optically-thick plasma conditions, resonant states are characterized by lifetimes comparable to those of metastable species [33] and can thus be included in the calculations of  $P_{ex}$ .

Finally, VUV-photons input to the total power density in a cylindrical geometry (characterized by  $z_{max}=20$  cm and  $r_{max}=10$  cm) can be estimated from [33]:

$$P_{re} = \frac{1}{4\pi T} \int_0^{z_{max}} \int_0^{r_{max}} \int_0^T A_{ij} N_*(t) \xi_u \epsilon_u e^{-k_0 \sqrt{r^2+z^2}} \times \frac{z}{(r^2+z^2)^{3/2}} dt 2\pi r dr dz, \quad (3)$$

where  $A_{ij}$  is the Einstein coefficient for spontaneous emission,  $N_*$  is the number density of resonant atoms,  $\xi_u$  is the probability of absorption of VUV photons following their interaction with the graphene substrate,  $\epsilon_u$  is the energy released to the graphene lattice by VUV-photons absorption ( $\sim 11.4$  eV for argon), and  $k_0$  is the absorption coefficient at the center of the line.

All energy transfer coefficients ( $\xi_i$ ,  $\xi_m$ ,  $\xi_u$ ) are first assumed equal to unity, i.e. that the probability of heterogeneous surface recombination of argon ions and heterogeneous surface de-excitation of metastable and resonant argon atoms is 100% and that VUV photons are fully absorbed. The assumption yields the percent contribution of each energetic species presented in Figure 3.2.2. In conditions *c1*, a significant fraction of the power density comes from ion irradiation, which is expected for a low-pressure plasma operated in H-mode. This aspect is

even more prominent when  $\xi_i = 1$ ,  $\xi_m = 0.085$  and  $\xi_u = 0.07$  (see details below). In conditions *c2*, a significant contribution from metastable atoms can be seen for  $\xi_i = \xi_m = \xi_u = 1$ ; this remains valid for  $\xi_i = 1$ ,  $\xi_m = 0.085$  and  $\xi_u = 0.07$ . Lastly, for condition *c3*, VUV photons dominate the power density provided to the graphene lattice for both  $\xi_i = \xi_m = \xi_u = 1$  and  $\xi_i = 1$ ,  $\xi_m = 0.085$  and  $\xi_u = 0.07$ .

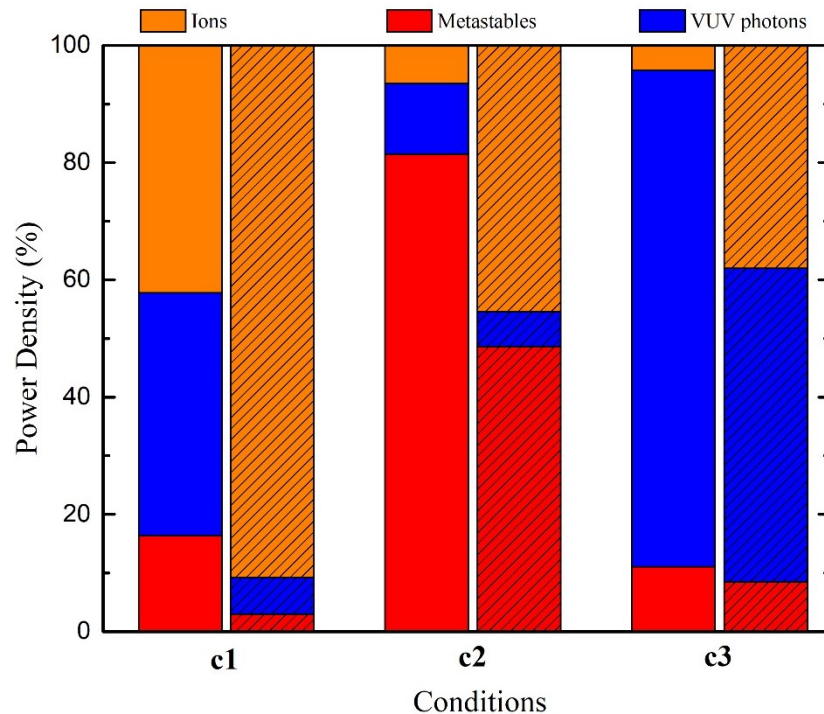


Figure 3.2.5 Percent contribution of positive ions, VUV-photon and metastable atoms in the total power density provided to the graphene lattice for conditions *c1*, *c2* and *c3*. The results are shown for  $\xi_i = \xi_m = \xi_u = 1$  and  $\xi_i = 1$ ,  $\xi_m = 0.085$  and  $\xi_u = 0.07$ .

Raman spectroscopy is a versatile technique for probing the fundamental properties of plasma-treated graphene. This study considers the D, G, D' and 2D bands at respectively 1350, 1580, 1610, and 2690  $\text{cm}^{-1}$  for a laser energy of  $E_L = 2.33$  eV (532 nm). The D and D' bands arise from lattice disorder induced by the plasma treatment, while the other two are intrinsic features of pristine graphene. The parameters of these bands are dependent on lattice perturbations such as strain, doping, number of layers, defects and so on. Their influence on the local on the band parameters such as the full width at half maximum (FWHM),  $\Gamma$ , the position of the band maximum,  $\omega$ , the maximum band intensity,  $I$ , and the band area,  $A$ , is summarized

elsewhere [13]. Here we adopt the same procedure to extract the Raman signatures linked with the presence of features such as the grain boundaries (GBs) in CVD-grown graphene films. Following the plasma characterization described above, we apply the procedure to each subsequent plasma treatment and analyze the results using a Cançado-type plot [43], *i.e.* laser-corrected  $A_D/A_G$  ratio as a function of  $\Gamma_G$ . While both of these parameters are dependent on the defect density in the graphene lattice, the  $A_D/A_G$  ratio is more sensitive to 0D-type defects (carbon adatoms and vacancies) and  $\Gamma_G$  is more prone to grow with 1D-type defects (boundaries and dislocations).

Raman measurements are performed, from  $t = 0$  s (pristine) to  $t = 1005$  s, 10340 s and 2370 s for conditions *c1*, *c2* and *c3*, respectively. These total cumulative treatment times are chosen such that each graphene sample is exposed to a comparable total energy fluence by positive ions (between 0.1 and 0.3  $J \cdot cm^{-2}$ ). One can see that the pristine values for both graphene domains (GDs) and GBs are similar ( $A_D/A_G \times E_L^4 \sim 8 \text{ eV}^4$ ,  $\Gamma_G \sim 12 \text{ cm}^{-1}$ ) for *c1*, *c2* and *c3*; this denotes the good reproducibility of the graphene film production method and allows for a reliable comparison of the results for these 3 samples. The *c1* graph reports the data for which the plasma-graphene interaction is dominated by ion irradiation [13]. This condition is used as a control to highlight the contributions of metastable argon species and VUV photons in *c2* and *c3*, respectively. For *c1*, it can be seen that the GDs follow the 0D-type defect curve. More specifically, the defect density  $\sigma = 1/L_D^2$ , where  $L_D$  is the average distance between nearest defects ( $L_D \rightarrow \infty$  for pristine graphene and  $L_D \rightarrow 0$  for fully disordered graphene), increases from about  $\sigma \sim 0$  at  $t = 0$  to  $\sigma \sim 10^{13} \text{ cm}^{-2}$  at  $t = 1005$  s, while no significant change is noted in the average crystallite size  $L_a$  ( $L_a \rightarrow \infty$  for pristine graphene and  $L_a \rightarrow 0$  for fully disordered graphene) [43]. Regarding *c2*, the subsequent treatments lead to very weak damage for the first 4 treatments (up to  $t = 1840$  s) before a rise is observed (from  $t = 3840$  s to  $t = 10340$  s). When comparing with *c1*, the defects seem to be more 1D-oriented. In particular, the defect density also increases from about  $\sigma \sim 0$  at  $t = 0$  to  $\sigma \sim 10^{13} \text{ cm}^{-2}$  at  $t = 10340$  s, but the average crystallite size now significantly decreases from  $L_a \rightarrow \infty$  at  $t = 0$  to  $L_a \sim 30 \text{ nm}$  at  $t = 10340$  s [43]. The condition *c3* results in a damage generation closer to the one observed in *c1*, *i.e.*  $\sigma \sim 10^{13} \text{ cm}^{-2}$  and no significant modification of  $L_a$  at  $t = 2370$  s.

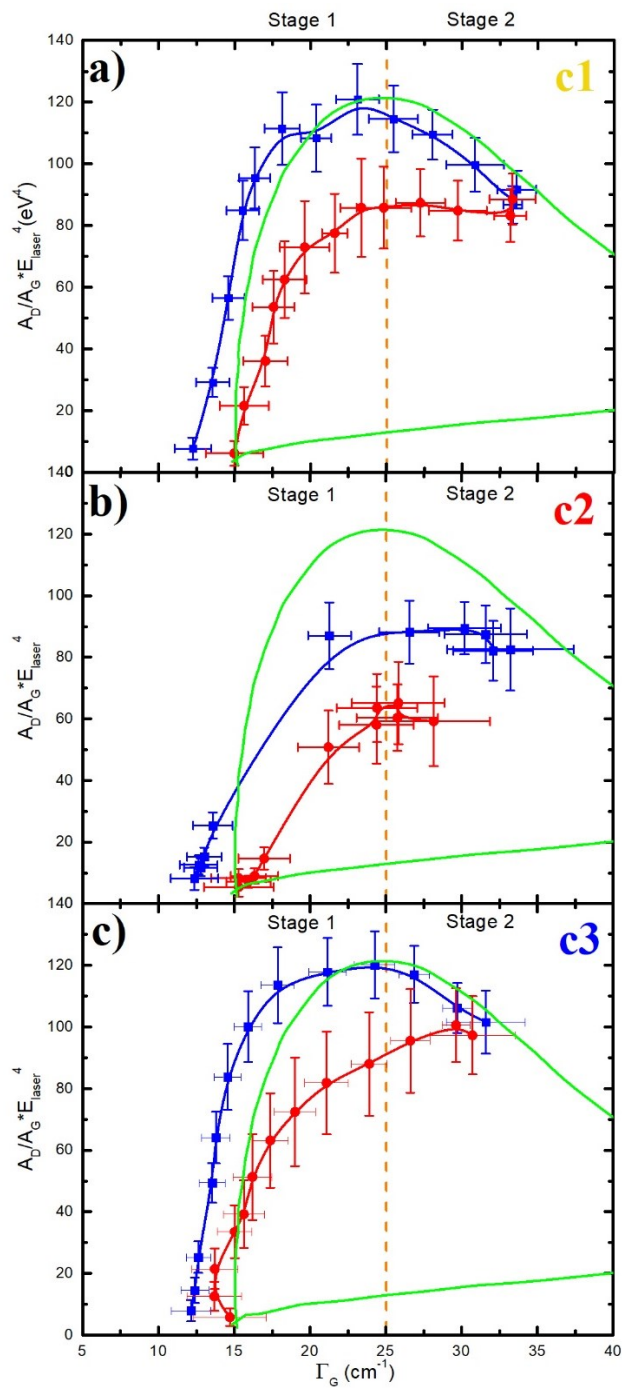


Figure 3.2.6. Cançado-type graphs extracted from RIMA mappings with distinctions between GDs (blue) and GBs (red) in conditions c1, c2 and c3. Lines are guide to the eye only. Green lines delimit the 0D and 1D defect type evolutions. A vertical dotted line marks the limit between stage 1 and stage 2 of the amorphization trajectory.

For all of these conditions, Figure 3.2.3 further shows that GBs are more prone to develop 1D-type defects, with  $L_a$  values lower than in GDs. For example, in *c1* at  $t = 645$  s,  $L_a \sim 35$  nm at GBs ( $A_D/A_G \times E_L^4 \sim 80$  eV<sup>4</sup>,  $\Gamma_G \sim 25$  cm<sup>-1</sup>) and  $L_a > 500$  nm in GDs ( $A_D/A_G \times E_L^4 \sim 115$  eV<sup>4</sup>,  $\Gamma_G \sim 26$  cm<sup>-1</sup>) [43]. In addition, the defect density is also lower at GBs than in GDs. Again, using the example of *c1* at  $t = 645$  s,  $\sigma \sim 0.4 \times 10^{13}$  cm<sup>-2</sup> at GBs and  $\sigma \sim 10^{13}$  cm<sup>-2</sup> in GDs. This latter result implies that GBs are less affected than GDs by the plasma-induced damage. Such effect was previously observed after a careful analysis of various Raman band parameters and was ascribed to a preferential self-healing of radiation damage at GBs [13]. Noteworthy, a peculiarity in this behavior is observed for the first 2 treatments in *c3* since the GBs show a reduced G band FWHM. We will come back to this point later on.

By using the same terminology introduced before to described disordered carbons [44], the graphs presented in Figure 3.2.3 are typical of a two-stage evolution, in which Stage 1 and Stage 2 correspond to a low- and high-defect concentration in graphene, respectively [45]. The transition between Stage 1 and Stage 2 is usually observed at  $A_D/A_G \times E_L^4 \sim 120$  eV<sup>4</sup>,  $\Gamma_G \sim 25$  cm<sup>-1</sup> [43]. In order to confirm some of the features deduced from Cançado-type graphs, other Raman signals linked to graphene lattice disorders are examined [46,47]. This includes the  $I_{2D}/I_G$  band ratio, which is commonly used to evaluate graphene quality [48] and it is also known to decrease with damage generation. Furthermore, the  $I_D/I_{2D}$  band ratio increases monotonously with damage generation without any dependency on strain or doping [49]. Figure 3.2.4 presents the evolution of  $I_{2D}/I_G$  and  $I_D/I_{2D}$  band ratios as a function of the energy fluence provided by positive ions to the graphene lattice in the three plasma conditions. Here, it is first assumed (see additional details below) that positive ions are the only vector of energy in the formation of plasma-induced damage.

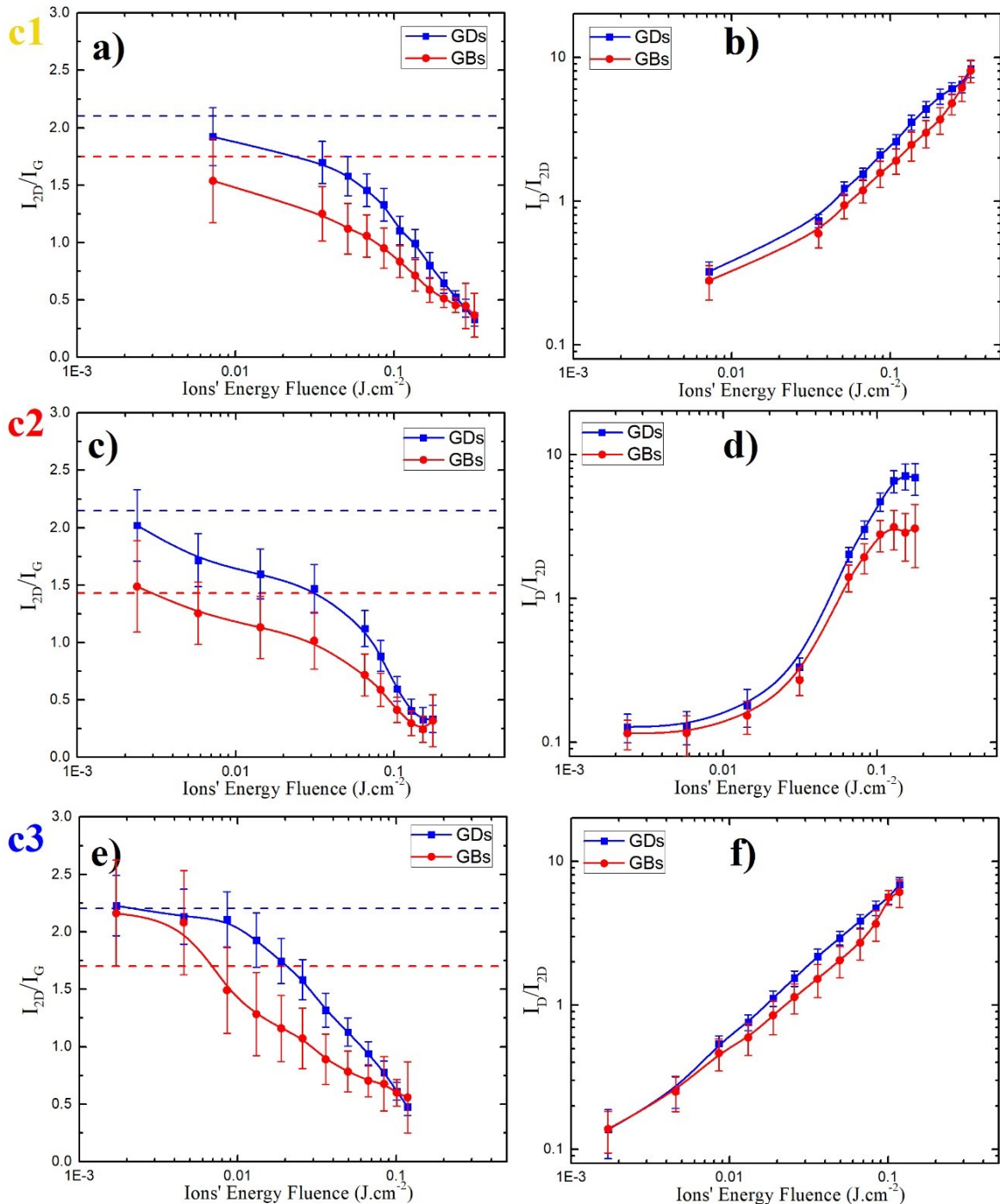


Figure 3.2.7. Evolution of  $I_{2D}/I_G$  (a-c-e) –related to the graphene quality– and  $I_D/I_{2D}$  (b-d-f) –related to the damage generation– as a function of the energy fluence provided by positive ions to the graphene lattice for conditions c1, c2 and c3. The results are shown for both graphene domains (blue) and graphene boundaries (red). For  $I_{2D}/I_G$ , the dashed lines correspond to the values in pristine graphene. For  $I_D/I_{2D}$ , pristine values were much below 0.1 (not shown) [13].

As seen in Figures 3.2.4a, 3.2.4c, and 3.2.4e, pristine graphene reveals a  $I_{2D}/I_G$  ratio lower at GBs (1.7) than in GDs (2.2) and this is due to their intrinsically imperfect nature. However, as the ions' energy fluence increases, GB values decrease with a lower slope than GD ones to reach similar values at the end of the plasma treatments. Using the arguments detailed by Eckmann *et al.*[50], the decrease of  $I_{2D}/I_G$  below 1 for the highest energy-fluences confirms the onset of graphene amorphization ( $I_{2D}/I_G > 2$  for pristine graphene). By comparing the results obtained in *c1* with the ones in *c2* and *c3*, it can be seen that the onset of graphene amorphization appears at a higher ions' energy fluence for *c1* than for *c2* and *c3*. For GD, the  $I_{2D}/I_G$  threshold of 1 is achieved for *c1*, *c2* and *c3* at 0.15, 0.07 and 0.05  $\text{J cm}^{-2}$ , respectively. As discussed below, this suggests that an additional energy source needs to be considered for *c2* and *c3*.

In Figure 3.2.4b, 3.2.4d, and 3.2.4f,  $I_D/I_{2D}$  ratios increase with the energy fluence provided by positive ions for both GDs and GBs. However, even though GBs and GDs have identical initial values (not shown in Figure 3.2.4, see all details in a previous study [13]), the ratios of GBs systematically stay below the ones of GDs for all conditions. This result is consistent with lower defect densities deduced from the Cançado-like graphs in Figure 3.2.3. Because of the positive enthalpy of GBs as compared with GDs [51], GBs have, however, been shown to be highly sensitive to irradiation processes, especially by positive ions[52,53], reactive atoms [54,55] or high-energy electrons [56]. Hence, the behavior is unexpected and reveals that a preferential adatoms-vacancies recombination at GBs is acting effectively to reduce defect densities induced by the treatments, giving a preferential self-healing of plasma-induced damage at GBs [13]. Here, the difference in defect densities seems to vanish for the last plasma treatments for conditions *c1* and *c3* but not for *c2*. Moreover, for *c3* in Figure 3.2.4e, despite a clear difference of the  $I_{2D}/I_G$  ratio for pristine graphene for GDs (2.2) and GBs (1.7), the first treatments increase the values at GBs and leave GDs unaffected to finally obtain a value of 2.2 for both regions. In such conditions,  $I_D/I_{2D}$  values for both GDs and GBs are surprisingly very similar (see Figure 3.2.4f).

In *c1*, the monotonous diminution of  $I_{2D}/I_G$  and the progressive increase of  $I_D/I_{2D}$  with the plasma treatment time can be understood as the direct consequence of a degradation of the graphene lattice by ion irradiation. This aspect is examined in more details for *c1*, *c2* and *c3* by

comparing all data sets presented in Figure 3.2.4 in a single plot of  $I_{2D}/I_G$  as a function of  $I_D/I_{2D}$ . Here, the objective is to examine the graphene quality using  $I_{2D}/I_G$  at comparable defect concentrations, which can be determined by  $I_D/I_{2D}$ . The results are shown in Figure 3.2.5a for GDs. Clearly,  $c1$  and  $c3$  have similar values and trends:  $I_{2D}/I_G$  decreases from about 2.2 down to about 0.25 as  $I_D/I_{2D}$  rises by almost two orders of magnitude. This trend is in very good agreement with the data presented in Figure 3.2.3, which follow the 0D-type defect curve [43]. Hence, both positive ions and VUV photons seem to have comparable effects in damage formation. In sharp contrast,  $c2$  indicates that a similar defect concentration associated to a given value of  $I_D/I_{2D}$  induces a more prominent decrease in graphene quality (lower  $I_{2D}/I_G$ ). Again, in addition to the deduced decrease of  $\sigma = 1/L_D^2$ , this trend is consistent with a decrease in the average crystallite size  $L_a$  in the  $c2$  condition after plasma treatment. This suggests that the presence of metastable argon atoms brings additional physics to the plasma-graphene interactions. Similar features for  $c1$ ,  $c2$  and  $c3$  were observed for GBs (not shown, for concision, in Figure 3.2.5a); as discussed above,  $I_{2D}/I_G$  and  $I_D/I_{2D}$  values are nonetheless lower for GBs than for GDs [13].

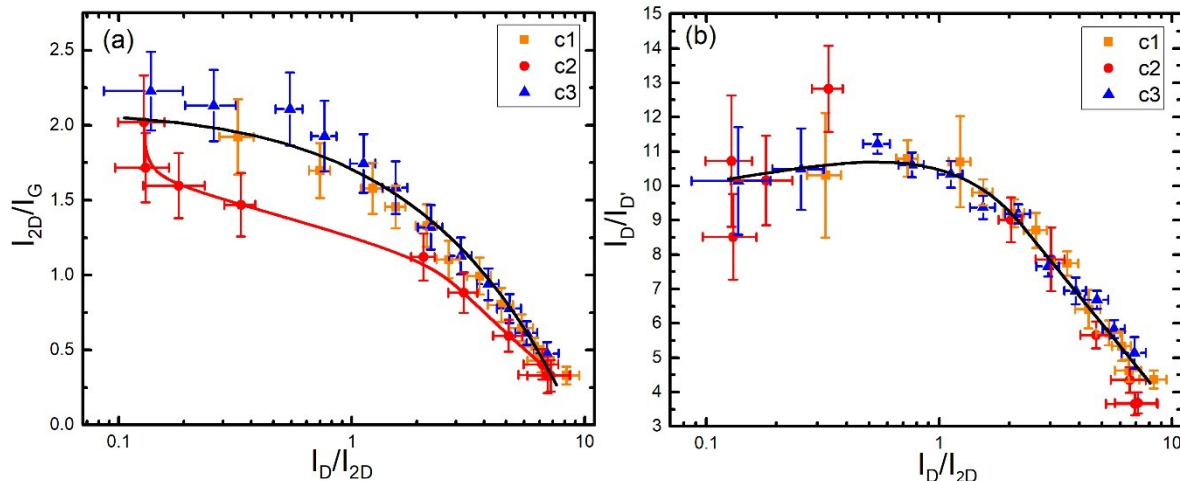


Figure 3.2.8. (a) Evolution of  $I_{2D}/I_G$  as a function of  $I_D/I_{2D}$  for conditions  $c1$ ,  $c2$  and  $c3$ . (b) Evolution of  $I_D/I_{D'}$  as a function of  $I_D/I_{2D}$  for conditions  $c1$ ,  $c2$  and  $c3$ . The results are for GDs only, but similar values were observed for GBs (not shown for concision).

It is worth highlighting that the nature of plasma-induced damage is comparable for  $c1$ ,  $c2$ , and  $c3$ . Based on the work of Eckmann *et al.* [50], the nature of defects in graphene can be

probed using the  $I_D/I_{D'}$  band ratio and these plots are presented in Figure 3.2.5b. At low defect concentrations, *i.e.* low values of  $I_D/I_{2D}$  (Stage 1 in Figure 3.2.3), the plasma-induced damage appears to be a combination of  $sp^3$  hybridization ( $I_D/I_{D'} \sim 13$ ) and vacancy-like ( $I_D/I_{D'} \sim 7$ ) defects. At higher defect concentrations – characterized by the onset of graphene amorphization (higher values of  $I_D/I_{2D}$ , Stage 2 in Figure 3.2.3), this Raman signature of damage decreases progressively and reaches a minimum for boundary-like defects in graphene ( $I_D/I_{D'} \sim 3.5$ ).

In order to better highlight the respective role of each species in the plasma-graphene interaction, the  $I_D/I_{2D}$  ratio is plotted in a single and unique graph in Figure 3.2.6a to correlate the evolution with the energy fluence provided by positive ions. Clearly, for a comparable value of the ions' energy fluence, *c3* systematically yields to more prominent damage than *c1*. This confirms additional energy uptake by plasma-generated VUV photons. In sharp contrast, the presence of metastable species in *c2* first retards damage generation with respect to *c1* and then speeds it up when the damage level becomes important. In line with these results, a total energy fluence is calculated for various values of  $\xi_m$  and  $\xi_u$  (assuming  $\xi_i = 1$ ) and fitted to the whole set of data. The best fit is obtained using  $\xi_m = 0.085$  and  $\xi_u = 0.07$ . While the heterogeneous surface recombination coefficient of metastable argon atoms on graphene is unknown, the  $\xi_m = 0.085$  value is comparable to the de-excitation coefficients expected for metastable states on metals ( $\xi_m = 0.1 - 1$  [40]). As for the absorption coefficient of VUV photons, the light emitted by resonant species is at precise wavelengths (104.8 and 106.7 nm), for which the graphene absorption coefficients are not clearly determined, albeit they appear to be even smaller than that for visible light, [57] which is around 2.3% [58]. Note that this absorption is increased further due to reflection on the  $SiO_2$  surface supporting the graphene film.

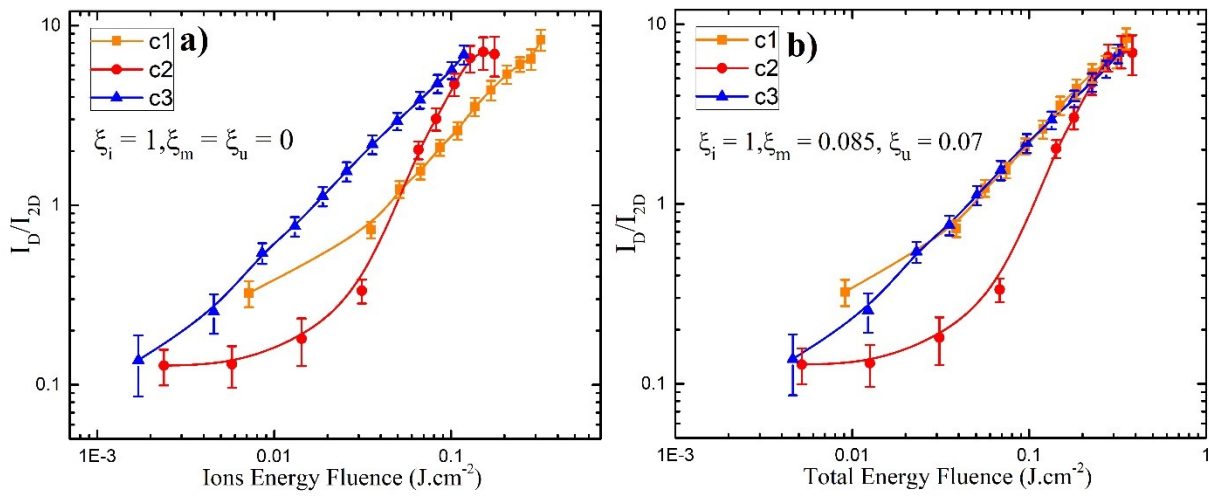


Figure 3.2.9. Damage generation analysis in graphene domains as a function of (a) the energy fluence provided by positive ions and (b) the total energy fluence assuming  $\xi_i = 1$ ,  $\xi_u = 0.085$  and  $\xi_u = 0.07$ . Similar results with lower  $I_D/I_{2D}$  values due to preferential self-healing were observed at graphene boundaries (not shown).

In this framework, the results in *c1* and *c3* presented in Figure 3.2.6b confirm that both positive ions and VUV photons contribute to damage formation. In such conditions, the onset of graphene amorphization (linked to  $I_D/I_{2D}$  ratios higher than about 1) appears for a total energy fluence of about  $0.1 \text{ J}\cdot\text{cm}^{-2}$ . With a carbon density of  $3.2\times 10^{15} \text{ cm}^{-2}$  for the graphene lattice, this corresponds to a total energy per carbon atom of about  $3.1\times 10^{-17} \text{ J}$  (195 eV). There is no plasma synergy effect in *c1* and *c3* because the respective contributions of positive ions and VUV photons are purely additive. In sharp contrast, Figure 3.2.6b for *c2* shows that the contribution of argon metastable species in the plasma-graphene interaction is not simply an additional energy uptake following their heterogeneous surface de-excitation. While  $I_D/I_{2D}$  ratios are lower in *c2* than the ones achieved in *c1* and *c3* at low defect concentrations, similar  $I_D/I_{2D}$  values are observed for all conditions at higher defect concentrations. Clearly, in low-damaged graphene, the presence of metastable species seems to inhibit damage formation by positive ion irradiation.

To fully understand the results presented in the previous section, the mechanism responsible for the defect generation in graphene must be recalled. In ion-irradiated graphene, it is well-established that the defect formation is governed by the knock-on collisions between positive ions and carbon atoms [44,45,59]. Over the range of experimental conditions investigated, however, the average energy obtained by positive ions following their acceleration in the plasma sheath is very low ( $\sim$ 10-14 eV with the RF power on and  $\sim$ 1-2 eV with the RF power off in pulsed plasma conditions, see Figure 3.2.1), *i.e.* lower than the displacement energy threshold for damage formation in graphene (18-22 eV [22]). Despite clear evidences of defect formation by Raman spectroscopy (see, for example, Figures 3.2.3 and 3.2.4), the kinetic energy of argon ions thus seems too small to produce any significant damage if ballistic ejection of carbon atoms is dominant. Of note, defect formation was also observed in graphene exposed to a beam of very-low-energy argon ions (1-2 eV range) with both single (15.8 eV) and double ionization (43.4 eV).[53] This indicates, as underlined by Equation (1), that the energy provided to the graphene lattice by positive ions does not only include knock-on collisions but also the heterogeneous surface recombination of positive ions with graphene electrons. While recombination surface processes leading to hot electron carriers in the graphene lattice are extremely fast ( $\sim$  fs),[60,61] electron energy relaxation phenomena (for example, through electron-phonon coupling) are comparatively much slower ( $\sim$  a few ps).[62,63] In presence of such highly transient energy input leading to momentarily “warm” graphene surfaces, molecular dynamics simulations have confirmed that the formation of carbon adatoms/vacancy pairs (Frenkel pairs) by ion irradiation can appear at energies below 18-22 eV [13].

Once created by ion irradiation, a single vacancy requires  $\sim$ 0.9-1.3 eV for migration along the graphene surface. On the other hand, a carbon adatom only needs 0.4 eV to diffuse [22]. Thus, carbon adatoms on graphene are typically considered as the most mobile species and can adopt different migration paths that should eventually cross 0D or 1D-type defects. In the first case scenario, annihilation typically occurs on a submicrosecond timescale after the ion impact [59]. Upon interaction with the boundaries of graphene domains (1D defects), carbon adatoms become highly mobile alongside the boundary [64,65], triggering an anisotropic transport responsible of an imbalance in the spatial distribution of carbon adatoms.[66] Hence, as discussed in a previous paper[13], a second scenario can be inferred in which an accumulation

or excess of carbon adatoms at the GBs combined with a so-called interstitial emission mechanism[67] enhances the annihilation probability of radiation damage near the GBs. This reaction pathway explains the preferential self-healing of plasma-induced damage, and thus lower  $I_D/I_{2D}$  values, at GBs with respect to GDs for all conditions investigated in this work (Figures 3.2.4b, 3.2.4d, and 3.2.4f). Such effect is expected to vanish as the graphene approaches the amorphous state due to limited carbon adatom transport at high defect density, as seen for the last plasma treatments in Figures 3.2.4b, 3.2.4d, and 3.2.4f.

In presence of an additional energy input provided by the heterogeneous surface de-excitation of metastable argon atoms, it is clear that additional electron excitation occurs [60,61,68]. Since the electron energy relaxation through electron-phonon coupling is more efficient at defect sites than in pristine graphene [69–71] and considering that the thermal conductance is significantly less at GBs than in GDs [72,73], high-frequency phonons become localized near defect site boundaries [74]. If the localized transient energy is high enough near vacancy sites, these defects can become mobile and hence prone to coalesce with other existing defects to form multivacancies and line defects in the GDs [22,75–77]. In such conditions, the average crystallite size  $L_a$  – obtained from  $A_D/A_G \times E_L^4$  vs  $\Gamma_G$  plot – and the graphene quality – linked to  $I_{2D}/I_G$  – are expected to decrease, which is consistent with the sets of data displayed in Figures 3.2.3b and 3.2.5a, respectively. In addition, the preferential self-healing of plasma-induced damage at GBs would no longer become limited to the boundary of GDs, but also to the boundaries of nanocrystallites within the GDs. This explain an apparent impediment in the plasma-induced formation of defects in presence of metastable argon atoms; again, this is consistent with the set of data presented in Figure 3.2.6b.

Treatments in conditions *c3* resemble the ones induced by ion irradiation only (condition *c1*) with an additional energy uptake provided by VUV photons. However, some peculiarities are observed at the GBs during the first few plasma treatments: an increase of  $I_{2D}/I_G$  (Figure 3.2.4e) up to the value of GDs and a decline of  $\Gamma_G$  (Figure 3.2.3c) down to the value of GDs. Knowing that the defect generation – evidenced by the  $I_{2D}/I_G$  versus  $I_D/I_{2D}$  plot (Figure 3.2.5a) and the  $I_D/I_{D'}$  versus  $I_D/I_{2D}$  plot (Figure 3.2.5b) – is very similar, the differences observed in the

evolution of  $I_{2D}/I_G$  and  $\Gamma_G$  most likely arises due to strain and/or doping effects caused by the presence of VUV photons. PMMA transfer of CVD-grown graphene on Si/SiO<sub>2</sub> substrates is well known to induce strain [78] and to affect the p-doping of the layer by the environment [79]. The evidence of such doping is seen in our pristine graphene films by the relatively high value of the G position ( $\sim 1591\text{ cm}^{-1}$ ), the low value of  $I_{2D}/I_G$  ( $\sim 2$ ) and narrow G band ( $\sim 12.5\text{ cm}^{-1}$ ), all typical of p-doping [80]. Additionally, PMMA residues may still remain on the film after transfer, especially at the GBs and surface defects [81]. A method to clean the film off of these residues is through irradiation by high-energy photons [82]. Thus, the VUV-assisted removal of PMMA residues could be the source of the differences observed on graphene domains and their boundaries between conditions *c1* (Figures 3.2.3a and 3.2.4a) and *c3* (Figures 3.2.3c and 3.2.4c). More specifically, the increase of  $I_{2D}/I_G$  at GBs seen in the first few treatments is rather astonishing since it should decrease with the introduction of damage, evidenced by the growing value of  $I_D/I_{2D}$ . Therefore, this is the clear indication that the graphene p-doping level due to the environment has been locally reduced, which is consistent with a removal of PMMA residues during the initial period of the plasma treatments. Moreover, the narrowing of the G-band at GBs is once again incoherent with growing lattice disorder [43,46]. As the G-band shifts with doping, this phenomenon is ascribed to a uniformization of the doping distribution resulting from the elimination of PMMA residues. VUV-photons could also help desorbing the trapped species (O<sub>2</sub>, H<sub>2</sub>O) at the interface between graphene and SiO<sub>2</sub> [83] since ion penetration is rather unlikely over the range of experimental conditions examined in this study ( $E_{ion} \sim 10\text{-}14\text{ eV}$  with the RF power on and  $\sim 1\text{-}2\text{ eV}$  with the RF power off in pulsed plasma conditions, see Figure 3.2.1). Lastly, the inherent structures such as ripples and wrinkles in graphene have enhanced reactivity and provide sites to stabilize functional groups [84] leading to a greater number of carbon atoms nearby in the sp<sup>3</sup> configuration. The removal of these groups through VUV irradiation would then reduce the sp<sup>3</sup> content resulting in the narrowing of the G band [85].

Recently, the preferential self-healing of GBs in polycrystalline monolayer graphene films under very low-energy ion irradiation in argon plasmas has been experimentally demonstrated [13]. In this study, graphene films were exposed to three different plasma conditions to isolate the respective roles of positive ions, VUV-photons and metastable atoms on the damage generation in graphene domains and their boundaries. Based on a detailed analysis of the D, G, D' and 2D Raman bands extracted from RIMA results, discrepancies between the three plasma treatments were highlighted. While defect formation remains mostly due to the interaction of positive argon ions with carbon atoms from the graphene lattice, the combination with either VUV-photons or metastable atoms has a very different impact. In the former, the photons are found to clean the films from PMMA residues and remove trapped dopants, as evidenced by the increase of  $I_{2D}/I_G$  and the decrease of  $\Gamma_G$  at the GBs. In addition, the small absorption of VUV-photons by the graphene lattice seems to provide an additional energy input during the formation of 0D-type defects. In such conditions, the defect density simply rises with the total energy fluence, with no significant change in the average crystallite size. In conditions with both positive ion and metastable state irradiation, the heterogenous de-excitation of the latter impedes the plasma-induced defect formation. In addition, the defect density also increases with the energy fluence as in other conditions, but the average crystallite size now significantly decreases. Here, the additional energy input provided by the heterogeneous surface de-excitation of metastable atoms induces a localization of high-frequency phonons near defect sites, which enhances the preferential self-healing at their boundaries.

## ACKNOWLEDGMENTS

This work was financially supported by the National Science and Engineering Research Council (NSERC), PRIMA-Québec, Plasmionique Inc., Photon Etc., the Fonds de Recherche du Québec - Nature et Technologies (FRQNT), and the Canada Research Chair (L. Stafford and R. Martel). The authors thank Carl Charpin for providing the CVD-grown graphene samples and Charlotte Allard for technical support with Raman imaging.

## REFERENCES

- [1] M. Meyyappan, Plasma nanotechnology: Past, present and future, *J. Phys. D. Appl. Phys.* 44 (2011). doi:10.1088/0022-3727/44/17/174002.
- [2] Z.F. Ren, Z.P. Huang, Synthesis of large arrays of well-aligned carbon nanotubes on glass, *Science* (80-. ). 282 (1998) 1105–1107. doi:10.1126/science.282.5391.1105.
- [3] Q. Wang, X. Wang, Z. Chai, W. Hu, Low-temperature plasma synthesis of carbon nanotubes and graphene based materials and their fuel cell applications, *Chem. Soc. Rev.* 42 (2013) 8821–8834. doi:10.1039/c3cs60205b.
- [4] Y. Kim, W. Song, S.Y. Lee, C. Jeon, W. Jung, M. Kim, C.Y. Park, Low-temperature synthesis of graphene on nickel foil by microwave plasma chemical vapor deposition, *Appl. Phys. Lett.* 98 (2011) 1–4. doi:10.1063/1.3605560.
- [5] G. Robert Bigras, X. Glad, P. Vinchon, R. Martel, L. Stafford, Selective nitrogen doping of graphene domains due to preferential healing of plasma-generated defects near grain boundaries, *Accept. NPJ 2D Mater. Appl.* (2020). doi:10.1038/s41699-020-00176-y.
- [6] G. Al Makdassi, X. Glad, S. Dap, M. Rojo, R. Clergereaux, J. Margot, Influence of a magnetic field on the formation of carbon dust particles in very low-pressure high-density plasmas, *J. Phys. D. Appl. Phys.* 50 (2017) 155203. doi:10.1088/1361-6463/50/15/155203.
- [7] I. Levchenko, K. Ostrikov, J. d. Long, S. Xu, Plasma-assisted self-sharpening of platelet-structured single-crystalline carbon nanocones, *Appl. Phys. Lett.* 91 (2007) 113115-1–3. doi:10.1063/1.2784932.
- [8] Z.L. Tsakadze, I. Levchenko, K. Ostrikov, S. Xu, Plasma-assisted self-organized growth of uniform carbon nanocone arrays, *Carbon N. Y.* 45 (2007) 2022–2030. doi:10.1016/j.carbon.2007.05.030.
- [9] A. Malesevic, R. Kemps, A. Vanhulsel, M.P. Chowdhury, A. Volodin, C. Van Haesendonck, Field emission from vertically aligned few-layer graphene, *J. Appl. Phys.* 104 (2008) 084301.
- [10] X. Glad, L. De Poucques, J.A. Jaszcak, M. Belmahi, J. Ghanbaja, J. Bougdira, Plasma synthesis of hexagonal-pyramidal graphite hillocks, *Carbon N. Y.* 76 (2014) 330–340. doi:10.1016/j.carbon.2014.04.084.
- [11] X. Glad, L. de Poucques, J. Bougdira, Formation mechanism of graphite hexagonal pyramids by argon plasma etching of graphite substrates, *J. Phys. D. Appl. Phys.* 48 (2015) 495304. doi:10.1088/0022-3727/48/49/495304.
- [12] Y. Shao, S. Zhang, M. H. Engelhard, G. Li, G. Shao, Y. Wang, J. Liu, I. A. Aksay, Y. Lin, Nitrogen -doped graphene and its electrochemical applications, *J. Mater. Chem.* 20 (2010) 7491–7496. doi:10.1039/C0JM00782J.

- [13] P. Vinchon, X. Glad, G. Robert Bigras, R. Martel, L. Stafford, Preferential self-healing at grain boundaries in plasma-treated graphene, *Nat. Mater.* (2020). doi:10.1038/s41563-020-0738-0.
- [14] G. Robert Bigras, X. Glad, L. Vandsburger, C. Charpin, P. Levesque, R. Martel, L. Stafford, Low-damage nitrogen incorporation in graphene films by nitrogen plasma treatment: Effect of airborne contaminants, *Carbon N. Y.* 144 (2019) 532–539. doi:10.1016/j.carbon.2018.12.095.
- [15] G. Robert Bigras, X. Glad, R. Martel, A. Sarkissian, L. Stafford, Treatment of graphene films in the early and late afterglows of N<sub>2</sub> plasmas: comparison of the defect generation and N-incorporation dynamics, *Plasma Sources Sci. Technol.* 27 (2018). doi:10.1088/1361-6595/aaedfd.
- [16] A. Horn, A. Schenk, J. Biener, B. Winter, C. Lutterloh, M. Wittmann, J. Küppers, H atom impact induced chemical erosion reaction at C: H film surfaces, *Chem. Phys. Lett.* 231 (1994) 193–198.
- [17] B. V. Mech, A.A. Haasz, J.W. Davis, Model for the chemical erosion of graphite due to low-energy H<sup>+</sup> and D<sup>+</sup> impact, *J. Appl. Phys.* 84 (1998) 1655–1669. doi:10.1063/1.368235.
- [18] J. Roth, C. Garcia-Rosales, Analytic description of the chemical erosion of graphite by hydrogen ions, *Nucl. Fusion*. 36 (1996) 1647.
- [19] E. Salonen, K. Nordlund, J. Keinonen, C.H. Wu, Carbon erosion mechanisms in tokamak divertor materials: insight from molecular dynamics simulations, *J. Nucl. Mater.* 290–293 (2001) 144–147. doi:10.1016/S0022-3115(00)00431-1.
- [20] Y. Takeguchi, M. Kyo, Y. Uesugi, Y. Tanaka, S. Masuzaki, Erosion and dust formation of graphite materials under low-energy and high-flux atomic hydrogen irradiation, *Phys. Scr.* 2009 (2009) 014056. doi:10.1088/0031-8949/2009/T138/014056.
- [21] F. Banhart, Irradiation effects in carbon nanostructures, *Reports Prog. Phys.* 62 (1999) 1181–1221. doi:10.1088/0034-4885/62/8/201.
- [22] F. Banhart, J. Kotakoski, A. V. Krasheninnikov, Structural Defects in Graphene, *ACS Nano.* 5 (2011) 26–41. doi:10.1021/nn102598m.
- [23] B. Rousseau, H. Estrade-Szwarckopf, A.L. Thomann, P. Brault, Stable C-atom displacements on HOPG surface under plasma low-energy argon-ion bombardment, *Appl. Phys. A Mater. Sci. Process.* 77 (2003) 591–597. doi:10.1007/s00339-002-1538-x.
- [24] P. Vinchon, X. Glad, G. Robert-Bigras, R. Martel, A. Sarkissian, L. Stafford, A combination of plasma diagnostics and Raman spectroscopy to examine plasma-graphene interactions in low-pressure argon radiofrequency plasmas, *J. Appl. Phys.* 126 (2019) 233302. doi:10.1063/1.5125143.
- [25] E. Gaufrès, S. Marcet, V. Aymong, N.Y.-W. Tang, A. Favron, F. Thouin, C. Allard, D. Rioux, N. Cottenye, M. Verhaegen, R. Martel, Hyperspectral Raman imaging using Bragg tunable filters of graphene and other low-dimensional materials, *J. Raman Spectrosc.* 49 (2018) 174–182.

doi:10.1002/jrs.5298.

- [26] G. Robert Bigras, P. Vinchon, C. Allard, X. Glad, R. Martel, L. Stafford, Probing plasma-treated graphene using hyperspectral Raman, *Rev. Sci. Instrum.* 91 (2020) 063903. doi:10.1063/5.0006556.
- [27] L. Maaloul, S. Morel, L. Stafford, Populations of metastable and resonant argon atoms in radio frequency magnetron plasmas used for deposition of indium-zinc-oxide films, *J. Vac. Sci. Technol. A Vacuum, Surfaces, Film.* 30 (2012) 021301. doi:10.1116/1.3674162.
- [28] D. Barton, D.J. Heason, R.D. Short, J.W. Bradley, The measurement and control of the ion energy distribution function at a surface in an RF plasma, *Meas. Sci. Technol.* 11 (2000) 1726–1731. doi:10.1088/0957-0233/11/12/312.
- [29] J.B. Boffard, R.O. Jung, C.C. Lin, A.E. Wendt, Measurement of metastable and resonance level densities in rare-gas plasmas by optical emission spectroscopy, *Plasma Sources Sci. Technol.* 18 (2009) 035017. doi:10.1088/0963-0252/18/3/035017.
- [30] S. Choubak, P.L. Levesque, E. Gaufres, M. Biron, P. Desjardins, R. Martel, Graphene CVD: Interplay between growth and etching on morphology and stacking by hydrogen and oxidizing impurities, *J. Phys. Chem. C.* 118 (2014) 21532–21540. doi:10.1021/jp5070215.
- [31] Y.-C. Lin, C.-C. Lu, C.-H. Yeh, C. Jin, K. Suenaga, P. Chiu, Graphene Annealing: How Clean Can It Be?, *Nano Lett.* 12 (2012) 414–419. doi:10.1021/nl203733r.
- [32] T. Bieber, X. Glad, L. de Poucques, R. Hugon, J.-L. Vasseur, J. Bougdira, Argon Ion and Neutral Metastable Levels Destruction in a Magnetically Enhanced Inductively Coupled Plasma Reactor, *Open Plasma Phys. J.* 6 (2013) 32–43. doi:10.2174/1876534301306010032.
- [33] J.B. Boffard, C.C. Lin, C. Culver, S. Wang, A.E. Wendt, S. Radovanov, H. Persing, Comparison of surface vacuum ultraviolet emissions with resonance level number densities. I. Argon plasmas, *J. Vac. Sci. Technol. A Vacuum, Surfaces, Film.* 32 (2014) 021304. doi:10.1116/1.4859376.
- [34] Y. Celik, T. V. Tsankov, M. Aramaki, S. Yoshimura, D. Luggenhölscher, U. Czarnetzki, Recombination and enhanced metastable repopulation in the argon afterglow, *Phys. Rev. E - Stat. Nonlinear, Soft Matter Phys.* 85 (2012) 1–12. doi:10.1103/PhysRevE.85.056401.
- [35] X. Tang, D.M. Manos, Time-resolved electrostatic probe studies of a pulsed inductively-coupled plasma, *Plasma Sources Sci. Technol.* 8 (1999) 594–602. doi:10.1088/0963-0252/8/4/311.
- [36] A. Durocher-Jean, E. Desjardins, L. Stafford, Characterization of a microwave argon plasma column at atmospheric pressure by optical emission and absorption spectroscopy coupled with collisional-radiative modelling, *Phys. Plasmas.* 26 (2019) 063516. doi:10.1063/1.5089767.
- [37] M. V Malyshev, V.M. Donnelly, Trace rare gases optical emission spectroscopy: nonintrusive

- method for measuring electron temperatures in low-pressure, low-temperature plasmas., Phys. Rev. E. Stat. Phys. Plasmas. Fluids. Relat. Interdiscip. Topics. 60 (1999) 6016–6029. doi:10.1103/PhysRevE.60.6016.
- [38] J.B. Boffard, G.A. Piech, M.F. Gehrke, L.W. Anderson, C.C. Lin, Measurement of electron-impact excitation cross sections out of metastable levels of argon and comparison with ground-state excitation, Phys. Rev. A - At. Mol. Opt. Phys. 59 (1999) 2749–2763. doi:10.1103/PhysRevA.59.2749.
- [39] P. Chabert, N. Braithwaite, Physics of Radio-Frequency Plasmas, Cambridge University Press, Cambridge, 2011. doi:10.1017/CBO9780511974342.
- [40] R. Piejak, V. Godyak, B. Alexandrovich, N. Tishchenko, Surface temperature and thermal balance of probes immersed in high density plasma, Plasma Sources Sci. Technol. 7 (1999) 590–598. doi:10.1088/0963-0252/7/4/016.
- [41] H. Kersten, H. Deutsch, H. Steffen, G.M.W. Kroesen, R. Hippler, The energy balance at substrate surfaces during plasma processing, Vacuum. 63 (2001) 385–431. doi:10.1016/S0042-207X(01)00350-5.
- [42] Y.-J. Yu, Y. Zhao, S. Ryu, L.E. Brus, K.S. Kim, P. Kim, Tuning the Graphene Work Function by Electric Field Effect, Nano Lett. 9 (2009) 3430–3434. doi:10.1021/nl901572a.
- [43] L. Cançado, M. Gomes de Silva, E.H.M. Ferreira, F. Hof, Disentangling contributions of point and line defects in the Raman spectra of graphene-related materials, 2D Mater. 4 (2017) 025039.
- [44] A.C. Ferrari, J. Robertson, Interpretation of Raman spectra of disordered and amorphous carbon, Phys. Rev. B. 61 (2000) 14095–14107. doi:10.1103/PhysRevB.61.14095.
- [45] M.M. Lucchese, F. Stavale, E.H.M. Ferreira, C. Vilani, M.V.O. Moutinho, R.B. Capaz, C.A. Achete, A. Jorio, Quantifying ion-induced defects and Raman relaxation length in graphene, Carbon N. Y. 48 (2010) 1592–1597. doi:10.1016/j.carbon.2009.12.057.
- [46] Y.-B. Zhou, Z.-M. Liao, Y.-F. Wang, G.S. Duesberg, J. Xu, Q. Fu, X.-S. Wu, D.-P. Yu, Ion irradiation induced structural and electrical transition in graphene, J. Chem. Phys. 133 (2010) 234703. doi:10.1063/1.3518979.
- [47] K. Jia, Y. Su, Y. Chen, J. Luo, J. Yang, P. Lv, Z. Zhang, H. Zhu, C. Zhao, T. Ye, Effects of defects and thermal treatment on the properties of graphene, Vacuum. 116 (2015) 90–95. doi:10.1016/j.vacuum.2015.03.003.
- [48] Y. Ogawa, K. Komatsu, K. Kawahara, M. Tsuji, K. Tsukagoshi, H. Ago, Structure and transport properties of the interface between CVD-grown graphene domains, Nanoscale. 6 (2014) 7288–7294. doi:10.1039/c3nr06828e.

- [49] M. Bruna, A.K. Ott, M. Ijäs, D. Yoon, U. Sassi, A.C. Ferrari, Doping Dependence of the Raman Spectrum of Defected Graphene, *ACS Nano.* 8 (2014) 7432–7441. doi:10.1021/nn502676g.
- [50] A. Eckmann, A. Felten, A. Mishchenko, L. Britnell, R. Krupke, K.S. Novoselov, C. Casiraghi, Probing the nature of defects in graphene by Raman spectroscopy, *Nano Lett.* 12 (2012) 3925–3930. doi:10.1021/nl300901a.
- [51] C. Ophus, A. Shekhawat, H. Rasool, A. Zettl, Large-scale experimental and theoretical study of graphene grain boundary structures, *Phys. Rev. B - Condens. Matter Mater. Phys.* 92 (2015). doi:10.1103/PhysRevB.92.205402.
- [52] T. Larionova, T. Koltsova, E. Bobrynska, A. Smirnov, I. Eliseyev, V. Davydov, O. Tolochko, Comparative characterization of graphene grown by chemical vapor deposition, transferred to nonconductive substrate, and subjected to Ar ion bombardment using X-ray photoelectron and Raman spectroscopies, *Diam. Relat. Mater.* 76 (2017) 14–20. doi:10.1016/j.diamond.2017.04.001.
- [53] P. Ahlberg, F.O.L. Johansson, Z.B. Zhang, U. Jansson, S.L. Zhang, A. Lindblad, T. Nyberg, Defect formation in graphene during low-energy ion bombardment, *APL Mater.* 4 (2016). doi:10.1063/1.4945587.
- [54] R. Yang, L. Zhang, Y. Wang, Z. Shi, D. Shi, H. Gao, E. Wang, G. Zhang, An anisotropic etching effect in the graphene basal plane, *Adv. Mater.* 22 (2010) 4014–4019. doi:10.1002/adma.201000618.
- [55] G. Diankov, M. Neumann, D. Goldhaber-Gordon, Extreme monolayer-selectivity of hydrogen-plasma reactions with graphene, *ACS Nano.* 7 (2013) 1324–1332. doi:10.1021/nn304903m.
- [56] S. Kurasch, J. Kotakoski, O. Lehtinen, V. Skákalová, J. Smet, C.E. Krill, A. V. Krasheninnikov, U. Kaiser, Atom-by-atom observation of grain boundary migration in graphene, *Nano Lett.* 12 (2012) 3168–3173. doi:10.1021/nl301141g.
- [57] P.E. Trevisanutto, M. Holzmann, M. Côté, V. Olevano, Ab initio high-energy excitonic effects in graphite and graphene, *Phys. Rev. B - Condens. Matter Mater. Phys.* 81 (2010) 3–6. doi:10.1103/PhysRevB.81.121405.
- [58] G. Imamura, K. Saiki, UV-irradiation induced defect formation on graphene on metals, *Chem. Phys. Lett.* 587 (2013) 56–60. doi:10.1016/j.cplett.2013.09.065.
- [59] A. V. Krasheninnikov, F. Banhart, Engineering of nanostructured carbon materials with electron or ion beams, *Nat. Mater.* 6 (2007) 723–733. doi:10.1038/nmat1996.
- [60] A. Tomadin, D. Brida, G. Cerullo, A.C. Ferrari, M. Polini, Nonequilibrium dynamics of photoexcited electrons in graphene: Collinear scattering, Auger processes, and the impact of screening, *Phys. Rev. B.* 88 (2013) 035430. doi:10.1103/PhysRevB.88.035430.

- [61] C. Su, M. Tripathi, Q.B. Yan, Z. Wang, Z. Zhang, C. Hofer, H. Wang, L. Basile, G. Su, M. Dong, J.C. Meyer, J. Kotakoski, J. Kong, J.C. Idrobo, T. Susi, J. Li, Engineering single-atom dynamics with electron irradiation, *Sci. Adv.* 5 (2019) 1–12. doi:10.1126/sciadv.aav2252.
- [62] M. Lazzeri, S. Piscanec, F. Mauri, A.C. Ferrari, J. Robertson, Electron Transport and Hot Phonons in Carbon Nanotubes, *Phys. Rev. Lett.* 95 (2005) 236802. doi:10.1103/PhysRevLett.95.236802.
- [63] S. Butscher, F. Milde, M. Hirtschulz, E. Malić, A. Knorr, Hot electron relaxation and phonon dynamics in graphene, *Appl. Phys. Lett.* 91 (2007) 17–20. doi:10.1063/1.2809413.
- [64] L.F. Huang, M.Y. Ni, G.R. Zhang, W.H. Zhou, Y.G. Li, X.H. Zheng, Z. Zeng, Modulation of the thermodynamic, kinetic, and magnetic properties of the hydrogen monomer on graphene by charge doping, *J. Chem. Phys.* 135 (2011) 064705. doi:10.1063/1.3624657.
- [65] B. Wang, Y. Puzyrev, S.T. Pantelides, Strain enhanced defect reactivity at grain boundaries in polycrystalline graphene, *Carbon N. Y.* 49 (2011) 3983–3988. doi:10.1016/j.carbon.2011.05.038.
- [66] A. Hashimoto, K. Suenaga, A. Gloter, K. Urita, S. Iijima, Direct evidence for atomic defects in graphene layers, *Nature*. 430 (2004) 870–873. doi:10.1038/nature02817.
- [67] X.M. Bai, A.F. Voter, R.G. Hoagland, M. Nastasi, B.P. Uberuaga, Efficient annealing of radiation damage near grain boundaries via interstitial emission, *Science (80-. ).* 327 (2010) 1631–1634. doi:10.1126/science.1183723.
- [68] J. Afonso Ferreira, L. Stafford, R. Leonelli, a. Ricard, Electrical characterization of the flowing afterglow of N<sub>2</sub> and N<sub>2</sub>/O<sub>2</sub> microwave plasmas at reduced pressure, *J. Appl. Phys.* 115 (2014) 163303. doi:10.1063/1.4872468.
- [69] J.C.W. Song, L.S. Levitov, Energy flows in graphene: Hot carrier dynamics and cooling, *J. Phys. Condens. Matter.* 27 (2015). doi:10.1088/0953-8984/27/16/164201.
- [70] M.W. Graham, S.F. Shi, D.C. Ralph, J. Park, P.L. McEuen, Photocurrent measurements of supercollision cooling in graphene, *Nat. Phys.* 9 (2013) 103–108. doi:10.1038/nphys2493.
- [71] K.L. Grosse, V.E. Dorgan, D. Estrada, J.D. Wood, I. Vlassiouk, G. Eres, J.W. Lyding, W.P. King, E. Pop, Direct observation of resistive heating at graphene wrinkles and grain boundaries, *Appl. Phys. Lett.* 105 (2014). doi:10.1063/1.4896676.
- [72] A. Bagri, S.P. Kim, R.S. Ruoff, V.B. Shenoy, Thermal transport across twin grain boundaries in polycrystalline graphene from nonequilibrium molecular dynamics simulations, *Nano Lett.* 11 (2011) 3917–3921. doi:10.1021/nl202118d.
- [73] A.Y. Serov, Z.Y. Ong, E. Pop, Effect of grain boundaries on thermal transport in graphene, *Appl. Phys. Lett.* 102 (2013). doi:10.1063/1.4776667.
- [74] M.M. Hollick, M. Arjomandi, B.S. Cazzolato, An investigation into the sensory application of DBD

- plasma actuators for pressure measurement, Sensors Actuators A Phys. 171 (2011) 102–108. doi:10.1016/j.sna.2011.07.011.
- [75] J. Chen, T. Shi, T. Cai, T. Xu, L. Sun, X. Wu, D. Yu, Self healing of defected graphene, Appl. Phys. Lett. 102 (2013) 103–107. doi:10.1063/1.4795292.
- [76] A. V. Krasheninnikov, K. Nordlund, Ion and electron irradiation-induced effects in nanostructured materials, J. Appl. Phys. 107 (2010). doi:10.1063/1.3318261.
- [77] K. Nordlund, S.J. Zinkle, A.E. Sand, F. Granberg, R.S. Averback, R.E. Stoller, T. Suzudo, L. Malerba, F. Banhart, W.J. Weber, F. Willaime, S.L. Dudarev, D. Simeone, Primary radiation damage: A review of current understanding and models, J. Nucl. Mater. 512 (2018) 450–479. doi:10.1016/j.jnucmat.2018.10.027.
- [78] M.B.B.S. Larsen, D.M.A. Mackenzie, J.M. Caridad, P. Bøggild, T.J. Booth, Transfer induced compressive strain in graphene: Evidence from Raman spectroscopic mapping, Microelectron. Eng. 121 (2014) 113–117. doi:10.1016/j.mee.2014.04.038.
- [79] A. Pirkle, J. Chan, A. Venugopal, D. Hinojos, C.W. Magnuson, S. McDonnell, L. Colombo, E.M. Vogel, R.S. Ruoff, R.M. Wallace, The effect of chemical residues on the physical and electrical properties of chemical vapor deposited graphene transferred to SiO<sub>2</sub>, Appl. Phys. Lett. 99 (2011) 2009–2012. doi:10.1063/1.3643444.
- [80] A. Das, S. Pisana, B. Chakraborty, S. Piscanec, S.K. Saha, U. V. Waghmare, K.S. Novoselov, H.R. Krishnamurthy, A.K. Geim, A.C. Ferrari, A.K. Sood, Monitoring dopants by Raman scattering in an electrochemically top-gated graphene transistor, Nat. Nanotechnol. 3 (2008) 210–215. doi:10.1038/nnano.2008.67.
- [81] H.J. Jeong, H.Y. Kim, S.Y. Jeong, J.T. Han, K.J. Baeg, J.Y. Hwang, G.W. Lee, Improved transfer of chemical-vapor-deposited graphene through modification of intermolecular interactions and solubility of poly(methylmethacrylate) layers, Carbon N. Y. 66 (2014) 612–618. doi:10.1016/j.carbon.2013.09.050.
- [82] Z. Li, Y. Wang, A. Kozbial, G. Shenoy, F. Zhou, R. McGinley, P. Ireland, B. Morganstein, A. Kunkel, S.P. Surwade, L. Li, H. Liu, Effect of airborne contaminants on the wettability of supported graphene and graphite, Nat. Mater. 12 (2013) 925–931. doi:10.1038/nmat3709.
- [83] G. Imamura, K. Saiki, Modification of graphene/SiO<sub>2</sub> interface by UV-irradiation: Effect on electrical characteristics, ACS Appl. Mater. Interfaces. 7 (2015) 2439–2443. doi:10.1021/am5071464.
- [84] D.W. Boukhvalov, M.I. Katsnelson, Enhancement of chemical activity in corrugated graphene, J. Phys. Chem. C. 113 (2009) 14176–14178. doi:10.1021/jp905702e.

- [85] K.N. Kudin, B. Ozbas, H.C. Schniepp, R.K. Prud'homme, I.A. Aksay, R. Car, Raman Spectra of Graphite Oxide and Functionalized Graphene Sheets, *Nano Lett.* 8 (2008) 36–41. doi:10.1021/nl071822y.

# **Chapitre 4. Dopage du graphène par plasma d'argon au diborane**

## **1 Dopage du graphène par plasma**

L'étude des interactions plasma-graphène dans les plasmas d'argon en régimes continu et pulsé a permis de cerner la gamme d'énergie nécessaire pour exposer le graphène à un plasma tout en limitant les dommages induits par irradiation ionique. De plus, nous avons pu mieux comprendre les rôles respectifs des ions, des métastables et des photons VUV. L'introduction de  $B_2H_6$ , même en faible quantité (5%), change énormément la dynamique du plasma. En effet, dès les premiers instants de ce plasma, un dépôt se forme sur les parois et sur la fenêtre de quartz du réacteur. Ainsi, les plasmas produits aux conditions de pression et de puissance utilisées dans les sections précédentes se révèlent maintenant très différents. Cependant, il reste possible de caractériser le plasma suivant la même méthodologie. En plus de la détermination classique des paramètres fondamentaux du plasma d'argon, une étude plus approfondie est réalisée par spectrométrie de masse afin de déterminer le degré de dissociation des espèces réactives du  $B_2H_6$ . A ceci, inspiré de travaux précédent dans la littérature, se rajoute une méthode optique pour évaluer la densité absolue de bore atomique dans le plasma. Afin d'obtenir des énergies comparables à celles obtenues dans le plasma d'argon en régime pulsé (Chapitre 3), le graphène est exposé seulement 22 secondes au plasma en régime continue contenant le diborane. Ceci permet de conserver le graphène tout en altérant de manière finement contrôlé son environnement chimique. En effet, des mesures XPS mettent en lumière qu'entre 2 et 3 % de bore sont incorporés directement dans le graphène. L'analyse RIMA confirme une incorporation et un bon état du graphène mais il est difficile d'obtenir une réelle confirmation du dopage due à l'hydrogénéation, même très limitée, du graphène. Ces résultats sont présentés sous la forme d'un article en préparation finale pour soumission au journal *Carbon*. Dans cet article, j'ai réalisé l'étude du plasma, préparé et traité par plasma l'échantillon de graphène ainsi qu'effectué les mesures et analyse RIMA et XPS. J'ai enfin écrit un premiers jet d'article. X.Glad et G.R

Bigras ont participé à l'interprétation des données. Les travaux ont été supervisé par R. Martel et L. Stafford, en collaboration avec le partenaire industriel A. Sarkissian

# **POST-GROWTH MODIFICATION OF MONOLAYER GRAPHENE FILMS BY LOW-PRESSURE DIBORANE-ARGON PLASMA**

P. Vinchon<sup>1</sup>, X. Glad<sup>1</sup>, G. Robert Bigras<sup>1</sup>, A. Sarkissian<sup>2</sup>, R. Martel<sup>3</sup>, L. Stafford<sup>1\*</sup>

<sup>1</sup>Département de physique, Université de Montréal, Montréal, Québec, Canada

<sup>2</sup>Département de chimie, Université de Montréal, Montréal, Québec, Canada

<sup>3</sup>Plasmionique inc., Varennes, Québec, Canada

## **ABSTRACT**

Polycrystalline monolayer graphene films grown by chemical vapor deposition were exposed to a low-pressure inductively-coupled plasma operated in argon-diborane gas mixtures. Optical emission spectroscopy combined with plasma sampling mass spectrometry reveals high B<sub>2</sub>H<sub>6</sub> fragmentation leading to significant populations of both boron and hydrogen species in the gas phase. X-ray photoelectron spectroscopy indicates surface formation of a boron-containing layer and substitutional incorporation of boron atoms within the graphene lattice. Graphene doping by graphitic boration is confirmed by Hyperspectral Raman Imaging of graphene domains. These results demonstrate that diborane-containing plasmas are efficient tools for boron substitutional incorporation in graphene with minimal domain hydrogenation.

Unveiling a few of the numerous promising properties of graphene can be achieved through selective incorporation of foreign atoms into the honeycomb lattice. For example, fine tuning of the electronic properties of graphene can be realized through carbon atom substitution with nitrogen or boron atoms, leading to n- or p-type semiconductor, respectively [1,2]. Boron-doped graphene has been less studied than its nitrogen counterpart [3,4]. Besides direct applications to electronics and optoelectronics [5,6], B-doped graphene is also considered for electrochemical energy storage [7] and sensing [8,9], as well as for biomedical applications [10].

Modification of graphene films grown by chemical vapor deposited (CVD) can be performed either during growth [2,11] or by post-growth treatment techniques [12,13]. Among the latter, plasma treatment is a promising method due to its versatility and simplicity [12,14,15]. While mostly argon plasmas are known to significantly damage graphene films [16,17], recent studies have shown that more delicate treatments can be obtained in pulsed plasma conditions [18]. Selective incorporation of foreign atoms in the graphene lattice is usually realized by the addition of a reactive species in the argon-based plasma. For graphene nitrogenation, N<sub>2</sub>-based plasmas are typically used [19–24], while for graphene boration, only trimethylborane (TMB)-based plasmas were examined [13].

This work reports the post-growth modification of graphene films in diborane (B<sub>2</sub>H<sub>6</sub>)-containing plasmas. With respect to TMB, diborane has the advantage to prevent the deposition of amorphous hydrogenated carbon films [25]. By introducing B<sub>2</sub>H<sub>6</sub> into the argon gas, plasma-induced fragmentation obviously leads to boron species but also to hydrogen atoms, molecules, and ions. Such plasma mixture can induce a number of mechanisms following their interaction with the graphene surface, including hydrogenation [15,26,27], ion-assisted chemical etching [28,29], and boration [13]. The latter is typically assessed by X-ray photoelectron spectroscopy (XPS), which is an excellent method to estimate boron-to-carbon ratios [11]. However, plasma-generated B atoms incorporated through carbon atom substitution in the graphene lattice can be difficult to determine. XPS is thus usually coupled with Raman Spectroscopy (RS), which is a powerful technique to probe plasma-induced damage and dopants in graphene [30,31]. However, carbon atom substitution by boron atoms can induce strain within the graphene lattice such that reliable analysis of boron content by RS becomes complex [32].

With the objective to substitute carbon atoms by boron species using a post-growth plasma treatment, polycrystalline monolayer graphene films grown by chemical vapor deposition were

exposed to a 5% diborane - 95% argon inductively-coupled plasma (ICP) at low pressure. The graphene was synthesized on a 25- $\mu\text{m}$ -thick polycrystalline copper foil in a CH<sub>4</sub>/H<sub>2</sub> environment [33] and then transferred to a SiO<sub>2</sub>(100 nm)/Si substrate using a standard PMMA transfer method [34]. The ICP reactor (with load lock for sample injection into the plasma chamber) was described in previous work [17,35]. The diborane-argon gas mixture was obtained with 10 SCCM (standard cubic centimeters per minute) from a 10% B<sub>2</sub>H<sub>6</sub> (balance Ar) bottle and 10 SCCM from an Ar bottle; both bottles were ultra-high-purity grade. For the sake of reproducibility, a 30-min B<sub>2</sub>H<sub>6</sub>-Ar plasma in the same conditions of pressure and power was carried out before injecting the sample into the plasma chamber. The substrate-holder was at floating potential and was placed at the center of the reactor at 20 cm below the ICP antenna (in the diffused plasma region). After plasma treatment and before exposing the substrate to ambient air conditions, ultra-high-purity nitrogen was slowly injected in the load lock chamber up to 1 atm.

In order to analyze plasma-generated species interacting with the graphene surface, the discharge was characterized by various tools. This includes: (i) a Langmuir probe (LP, Scientific Systems) to obtain the positive ion number density  $n_i$  (equivalent to the electron density  $n_e$ , assuming quasi-neutrality) and the average ion energy at the substrate surface  $E_{ion}$  (assuming a monoenergetic ion energy distribution within the approximation  $E_{ion} = e \cdot (V_p - V_f)$ , where  $e$  is the elementary charge,  $V_p$  is the plasma potential, and  $V_f$  is the floating potential [17]), (ii) an Optical Absorption Spectroscopy (OAS) system to determine the populations of argon metastable (Ar<sup>m</sup>: 1s<sup>3</sup> and 1s<sup>5</sup> at  $\sim$ 11.6 eV above the fundamental state Ar<sup>0</sup>) and argon resonant (Ar\*: 1s<sup>2</sup> and 1s<sup>4</sup> at  $\sim$ 11.7 eV above Ar<sup>0</sup>) states (using the argon 2p-1s lines from an argon low-pressure lamp and a Princeton Instruments Isoplane equipped with a Vis-blazed 300 gr·mm<sup>-1</sup> grating and a PI-MAX4 camera [36]), (iii) a high-resolution Optical Emission Spectroscopy (OES) system to gather the population of boron atoms (using the emission lines of the resonance boron doublet recorded at 249.68 and 249.77 nm thanks to a Princeton Instruments SpectraPro 2750 spectrometer equipped with an UV-blazed 3000 gr·mm<sup>-1</sup> grating and a PI-MAX4 camera [37]), and (iv) a Plasma Sampling Mass Spectrometer (PSMS, HAL EQP from Hiden Analytical Ltd) to analyze plasma-induced fragmentation of diborane in the Residual Gas Analysis (RGA) mode.

Plasma-treated graphene was characterized by XPS and Hyperspectral Raman IMAGING (RIMA) [38]. XPS measurements were carried out over a 400- $\mu\text{m}$  spot with a Thermo Scientific Al K-Alpha system. A pass energy of 200 eV and 50 eV was used for the surveys and the high-resolution (HR) XPS spectra, respectively. As for the step energy, it was set to 1eV and 0.05 eV for the surveys and the HR XPS spectra, respectively. Wagner sensitivity factor were used for the quantitative analysis. Three different locations were probed by XPS: (i) the same zone as the one analyzed by RIMA (see details below), (ii) another area, 1 mm away from the first one, to ensure reproducibility and uniformity of the plasma-treated graphene, and (iii) a spot on the silicon sample with no graphene to examine possible plasma deposition after exposure to the diborane-argon plasma. Peak deconvolution of the C1s band was done by multiple peaks fitting using a 1:1 Lorentzian-Gaussian (LG) product and the same full width at half maximum (FWHM) for all carbon moieties with the exceptions of  $sp^2$  C-C and C-B peaks. To account for the metallic properties of graphene, these two contributions were fitted using an asymmetric Doniach-Sunjic peak [39] with an asymmetry factor  $\alpha = 0.05$ . As for B1s band, again multiple peaks with 1:1 LG product were fitted, keeping a fixed FWHM for all contributions with the exceptions of  $sp^2$  B-C peak. Again, an asymmetric Doniach-Sunjic peak with an asymmetry factor  $\alpha = 0.05$  was used to fit the  $sp^2$  B-C moiety in the B1s spectra [5,11].

The plasma-induced modification of the graphene lattice was assessed by RS using the RIMA system [38,40]. This system enables RS analysis over a wide area (up to 130x130  $\mu\text{m}^2$ ) with high spectral ( $3 \text{ cm}^{-1}$ ) and spatial (pixel size = 130 nm, or 390 nm with 3x3 binning) resolutions. From the measured Raman spectra recorded at different locations across the graphene sample, a detailed mapping of the most relevant Raman band parameters can be extracted [40]. This includes the position ( $\omega$ ), the full-width at half maximum ( $\Gamma$ ), the peak intensity (I) and peak area (A) of the G ( $\sim 1580 \text{ cm}^{-1}$ ) and 2D ( $\sim 2700 \text{ cm}^{-1}$ ) bands that are the prominent features of the untreated sample, as well as of the D ( $\sim 1350 \text{ cm}^{-1}$ ) and D' ( $\sim 1600 \text{ cm}^{-1}$ ) bands that appear with the formation of plasma-induced disorders [41]. As highlighted in recent studies [35,40], because of their distinct Raman signatures, RIMA analysis can probe different regions of the polycrystalline monolayer graphene films, including graphene domains, grain boundaries, and contaminants introduced either during the growth and/or through the transfer process.

The discharge conditions were selected to be as mild as possible to avoid significant damage formation [17]. Moreover, preliminary tests have shown that the pressure in the plasma reactor

had to be kept low enough to prevent dust formation, commonly seen in argon plasmas containing silane [42], acetylene [43] or hexamethyldisiloxane [44,45] and enhanced by heterogeneous surface reactions at contaminated reactor walls [46]. Hence, conditions have been selected as such: a pressure of 10 mTorr and a RF power of 50 W in a 5% diborane - 95% argon gas mixture.

Inspired by previous studies [17,35], LP and OAS measurements were used to analyze the power density provided to the graphene lattice by: (i) positive ions following their acceleration in the plasma sheath, (ii) positive ions following their heterogenous recombination at the graphene surface (assuming a surface recombination probability of 1), (iii) metastable argon atoms following their heterogeneous deexcitation at the graphene surface (assuming a surface deexcitation probability of 1), and (iv) vacuum-ultraviolet (VUV) photons following their interaction with the graphene surface (assuming an absorption coefficient of 1). The results are presented in Figure 4.1.1 for conditions with (gas mixture detailed above) and without (20 SCCM Ar) diborane in the low-pressure argon plasma. With diborane introduction, the number density of charged species drops to 50% of the value in nominally pure argon plasmas. This effect is commonly seen with the addition of a molecular gas in argon [47] since a significant part of the power absorbed by electrons becomes consumed by the electron-impact excitation of rotational and vibrational states of the molecule and by the electron-impact dissociation of the molecule [48,49]. A more significant decrease is observed on the population of metastable argon atoms. Similar findings were reported by other authors in argon with minor additions of molecules [50] and was ascribed to the quenching of metastable argon atoms by interactions with the parent molecule as well as its plasma-generated fragments [44,51]. Globally, the total power density sees a 72% decrease from 3.5 to 1.0  $\text{mW}\cdot\text{cm}^{-2}$  and, in diborane-argon plasmas, is almost solely governed by argon ions.

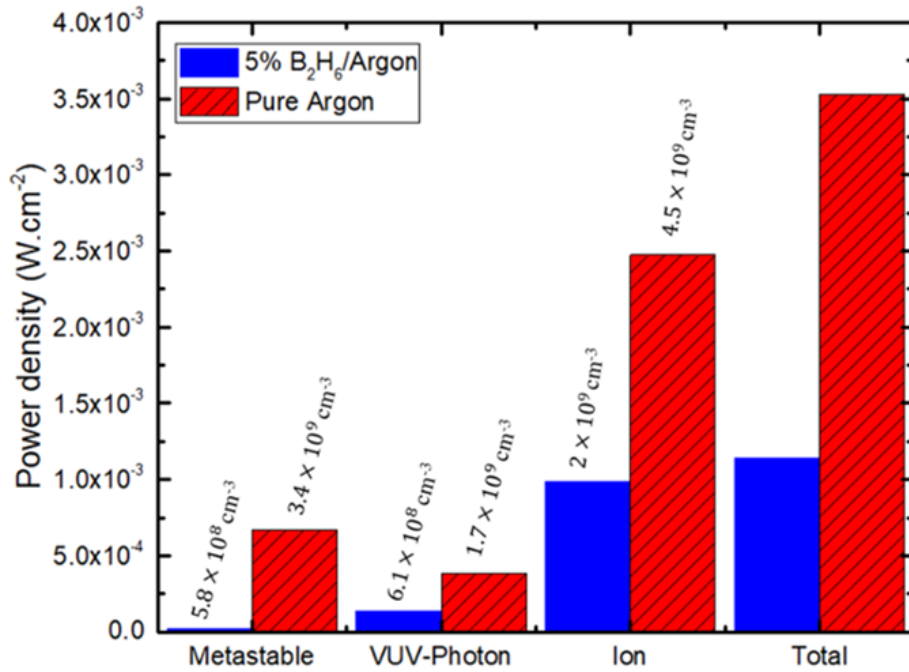


Figure 4.1.1 : Effect of the addition of 5%  $\text{B}_2\text{H}_6$  in a nominally pure argon plasma on the power density provided to the graphene lattice. The respective contributions of positive ions, argon metastable and resonant atoms, and VUV photons are also shown. Populations of each species obtained from LP and OAS are provided in  $\text{cm}^{-3}$ .

In order to analyze  $\text{B}_2\text{H}_6$  fragmentation, PSMS measurements were performed in RGA mode with 20 eV of electron energy [44]. Figure 4.1.2 presents ion count ratios of the main species observed at plasma *on* over the ones at plasma *off*. Low values obtained for  $\text{B}_2\text{H}_x$  are the evidence of plasma dissociation of the boron precursor. The cracking pattern of diborane can be used to extract a fragmentation degree. For example, using the  $\text{B}_2\text{H}_4^+$  signal (at  $m/z=26$ ) [52], we obtain  $(1 - 26_{on}/26_{off}) \times 100 = 95.5\%$ . Similar values were found from the  $\text{B}_2\text{H}_5^+$  and  $\text{B}_2\text{H}_2^+$  signals. Such precursor fragmentation levels suggest very high populations of boron and hydrogen atoms. For example, assuming a 100% fragmentation of  $\text{B}_2\text{H}_6$  to produce 2 boron and 6 hydrogen atoms, one obtains  $n_{\text{B},\text{max}} = 3.2 \times 10^{13} \text{ cm}^{-3}$  for B atoms and  $n_{\text{H},\text{max}} = 9.6 \times 10^{13} \text{ cm}^{-3}$  for H atoms (assuming a neutral gas temperature of 300 K, the number density of  $\text{B}_2\text{H}_6$  with the plasma off is  $1.6 \times 10^{13} \text{ cm}^{-3}$  in the 5%  $\text{B}_2\text{H}_6 - 95\% \text{ Ar}$  plasma at 10 mTorr). This corresponds to boron and hydrogen partial pressures of 1 and 3 mTorr, respectively. However, high-resolution OES analysis combined with the approach provided by Lavrov *et al.* [37] reveals that the population of boron atoms was below the detection limit of  $3 \times 10^{10} \text{ cm}^{-3}$  at 50 W and rose to

$3.2 \times 10^{10} \text{ cm}^{-3}$  at 100 W. Similarly, OES analysis of hydrogen and argon emission lines by actinometry coupled with the method provided by Barshilia and Vanka [53] determines that the population of hydrogen atoms was below the detection limit of  $3.1 \times 10^{12} \text{ cm}^{-3}$  at 50 W (hydrogen-to-argon line ratio of 0.01) and rose to  $1.9 \times 10^{13} \text{ cm}^{-3}$  at 300 W (hydrogen-to-argon line ratio of 0.06). This indicates that, over the range of the experimental conditions investigated,  $\text{B}_2\text{H}_6$  fragmentation is incomplete implying that the populations of  $\text{B}_x\text{H}_y$  are significant. This aspect can be confirmed by PSMS. For example,  $\text{BH}^+$  and  $\text{BH}_2^+$  fragments (mostly linked to  $\text{BH}_3$ ) show *on/off* ratios below unity but much higher than the ones of  $\text{B}_2\text{H}_3^+$ ,  $\text{B}_2\text{H}_4^+$ , and  $\text{B}_2\text{H}_5^+$ (mostly linked to  $\text{B}_2\text{H}_6$ ).

Additionally, a net increase of the *on/off* ratio of  $\text{B}^+$  up to 1.6 is observed in Figure 4.1.2. The presence of boron species in PSMS analysis also inevitably indicates that hydrogen atoms are present since the preferred diborane dissociation pathways induce H formation:  $\text{B}_2\text{H}_5-\text{H}$  at 4.42 eV or  $\text{H}_3\text{B}-\text{BH}_3$  then  $\text{BH}_2-\text{H}$  at 1.6 and 4.62 eV, respectively [54,55]. In such conditions, in addition to the power density provided to the graphene lattice by argon species (Figure 4.1.1), the plasma also contains boron atoms for graphene boration [13] and hydrogen atoms for graphene hydrogenation [15,26,27]. Other positive ions are also created in the discharge such as  $\text{ArH}^+$ ,  $\text{H}^+$ ,  $\text{H}_2^+$ and  $\text{H}_3^+$  [47,56] suggesting that ion-assisted chemical etching also occurs [28,29].

Plasma-induced modification of graphene films after 22-s exposure to the diborane-argon plasma was first examined by XPS. Figure 4.1.3a compares the XPS survey of pristine and plasma-treated graphene. For the latter, two regions are shown, the boron-treated graphene (BTG) and the boron-treated silicon (BTSi). Of note, similar signals were observed on both regions of BTG probed by XPS. On all spectra, carbon, oxygen and silicon peaks can be observed. After plasma treatment, features characteristic of N and B species appear. Here, nitrogen most likely arises from the airlock purge before exposing the substrate to ambient air conditions. Such nitrogen contamination is very limited (%at survey N below 1% for BTG and BTSi) and is additionally expected to be contained in the airborne hydrocarbon contaminants on the topmost surface [12,57]. Figure 4.1.3a further shows boron signals on both BTG and BTSi; this reveals plasma-induced modification of both graphene and silicon regions.

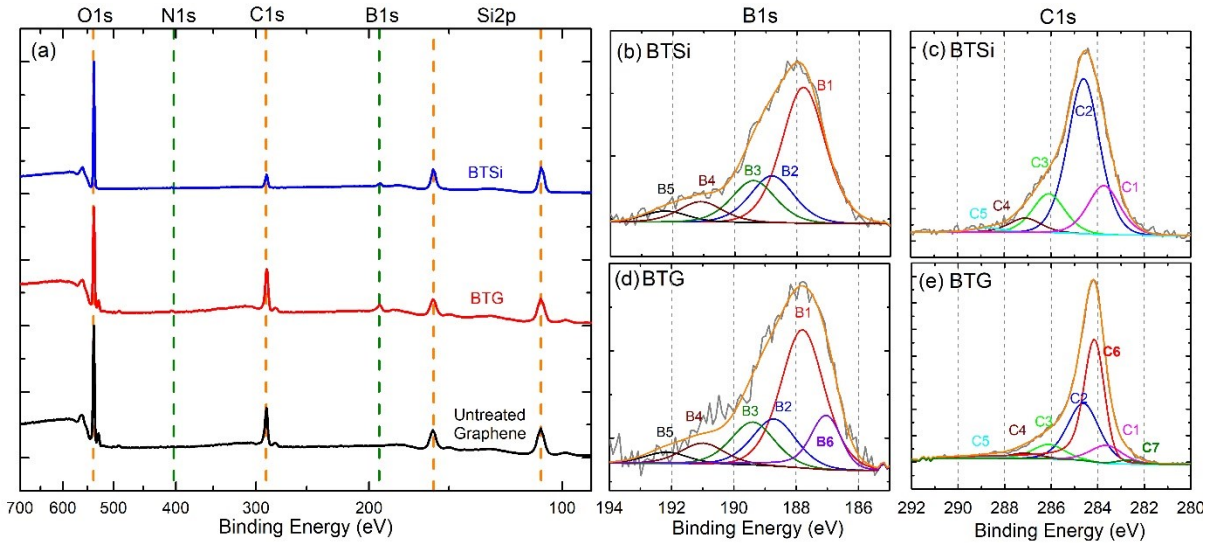


Figure 4.1.3. (a) Normalized XPS surveys of pristine (black), BTSi (blue) and BTG (red) samples. (b) B1s and (c) C1s HR scans of BTSi. (d) B1s and (e) C1s HR scans of BTG.

Figures 4.1.3b-3e present the XPS HR scans of boron (B1s; 3b, 3d) and carbon (C1s; 3c, 3e). The results are shown for both the BTSi (3b and 3c) and BTG (3d and 3e) regions. To account for any potential charge shift between the two sets of measurements, all peaks were shifted such that HR Si2p peaks were perfectly aligned for all samples (not shown in Figure 4.1.3). On the silicon substrate, the B1s HR spectra displayed in Figure 4.1.3b can be decomposed in several sub-peaks. The main contribution at 187.8 eV can be attributed to amorphous boron (B1) [58,59]. At higher binding energy, peaks associated to B-C at 188.7 eV (B2) [58,59] and B-H at 189.4 eV (B3) [60] are the signature of boron species in amorphous, boron-containing, hydrocarbon layers. Finally, two peaks at 191 eV (B4) and 192.4 eV (B5) reveal the presence of oxidized boron linked to carbon ( $C_2BO$  and  $CB_2O$ , respectively) [61,62]. On the other hand, in the C1s HR spectrum, the  $sp^3$  C-C component appears a 284.6 eV (C2), 0.4 eV lower than what is typically observed in amorphous carbon [63]. Such feature was observed by other authors with boron incorporation [58,60]. The peak at lower binding energy (283.7 eV) can be attributed to  $sp^3$  B-C bonds (C1) [58,60]. A few minor contributions can also be seen at higher binding energies due to C-OH (286.1 eV), O-C=O (287.1 eV) and C=O (288.7 eV) [12,64,65]. From such deconvolution of the B1s and C1s peaks on the BTSi, it is clear that an amorphous, boron-containing, hydrocarbon layer is formed on the plasma-treated sample. Similar films were

observed during tokamak wall boration by diborane plasmas [60]. The respective percent contributions of B1-B5 and C1-C6 are provided in Table 4.1.1.

Table 4.1.1: Percent contribution of each sub-peak in the XPS HR scans of B1s and C1s. For B1s, the sub-peaks are: B1 (B-B), B2 (B-C), B3 (B-H), B4 ( $C_2BO$ ), B5 ( $CB_2O$ ), B6 (B-C  $sp^2$ ). For C1s, the sub-peaks are: C1(B-C  $sp^3$ ), C2(C-C  $sp^3$ ), C3(C-O), C4(C=O), C5(O-C=O),, C6(C-C  $sp^2$ ), C7(B-C  $sp^2$ )

<b>B1s</b>	<b>B1</b>	<b>B2</b>	<b>B3</b>	<b>B4</b>	<b>B5</b>	<b>B6</b>	
BTG	45.5	16.5	14.2	11.3	0	13.6	
BTSi	53.2	18.3	16.3	8.0	4.1	0	
<b>C1s</b>	<b>C1</b>	<b>C2</b>	<b>C3</b>	<b>C4</b>	<b>C5</b>	<b>C6</b>	<b>C7</b>
BTG	8.9	28.2	7.1	2.6	0.8	50.8	1.7
BTSi	18.8	59.4	14.8	5.4	1.6	0	0

From the survey spectra, an amorphous, boron-containing, hydrocarbon layer is formed on both silicon and graphene after exposure to the diborane-argon plasma. Hence, all deconvoluted peaks from the B1s and C1s spectra recorded on BTSi were conserved and directly applied to the analysis of the B1s and C1s spectra recorded on BTG. However, to correctly deconvolute the B1s HR spectrum presented in Figure 4.1.3d, it is necessary to add an additional peak at lower binding energy (187 eV) linked to in-plane boron atoms in different geometries, including ( $C_2CB$ ,  $CCB_2$ , and  $CB_3$ ) (B6) [5,11]. This B6 contribution is 13% of the whole B1s contribution (see Table 1) or 1.8% of the total B1s+C1s signals. Similarly, for the proper deconvolution of the C1s HR spectrum presented in Figure 4.1.3e, it is necessary to add two supplementary peaks at 284.1 eV and 282.7 eV associated to  $sp^2$  C-C (C6) and  $sp^2$  B-C (C7), respectively. The former, related to the monolayer graphene layer, is shifted toward lower binding energy due to difference in boron electronegativity with respect to carbon [4,5,11,13,66]. Here, the C6 contribution is 52% of the whole C1s or 43% of the total B1s+C1s signals. As for the latter, it is of particular interest since it is the direct consequence of carbon atom substitution with boron atoms [4,11,61]. Over the range of experimental conditions investigated, the C7 contribution is at most 1.7% of the whole C1s contribution or at most 1.5% of the total B1s+C1s signals.

Considering that one boron atom is linked to three carbon atoms in graphitic configuration, this reveals an upmost amount of 0.5% of graphitic moiety in plasma-treated graphene. It is worth highlighting that this 0.5% value is lower than the one obtained from the B1s signal (1.8%); this is because B6 includes C<sub>2</sub>CB, CCB<sub>2</sub>, and CB<sub>3</sub> and not only the sp<sup>2</sup> B-C (C7) moiety [5]. Since the average excess charge is -0.5 electron per boron atom in the graphene lattice [67], this corresponds to hole doping level of 0.25%.

Inspired by the work of Cançado *et al.*[68], a powerful approach to monitor modification in graphene is to plot the area ratio of the D and G bands ( $A_D/A_G$ ) –corrected by the laser energy  $E_{\text{laser}}$  to the power 4– as a function of the full width at half maximum of the G band ( $\Gamma_G$ ). In this case, it is also possible to distinguish zero- (0D) and one-dimensional (1D) defects. For the former, a strong increase of  $A_D/A_G \times E_{\text{laser}}^4$  with weak change in  $\Gamma_G$  is observed. With further damage,  $A_D/A_G \times E_{\text{laser}}^4$  decreases while  $\Gamma_G$  increases more significantly before complete graphene amorphization. 1D defects produce a weak-slope linear increase of  $A_D/A_G \times E_{\text{laser}}^4$  with  $\Gamma_G$ . All data obtained from RIMA analysis are plotted in Figure 4.1.4 for both the pristine and BTG samples. As a comparison, data sets obtained from treatments in nominally pure argon plasmas are also shown in Figure 4.1.4 (Argon-Treated Graphene, ATG)[35]. The results are presented as a function of the total energy fluence provided to the graphene lattice, namely  $E_{\text{ATG}1} = 33 \text{ mJ}\cdot\text{cm}^{-2}$ ,  $E_{\text{ATG}2} = 83 \text{ mJ}\cdot\text{cm}^{-2}$  and  $E_{\text{ATG}3} = 120 \text{ mJ}\cdot\text{cm}^{-2}$ . As a reference, the energy fluence of the BTG sample is  $E_{\text{BTG}} = 25 \text{ mJ}\cdot\text{cm}^{-2}$ .

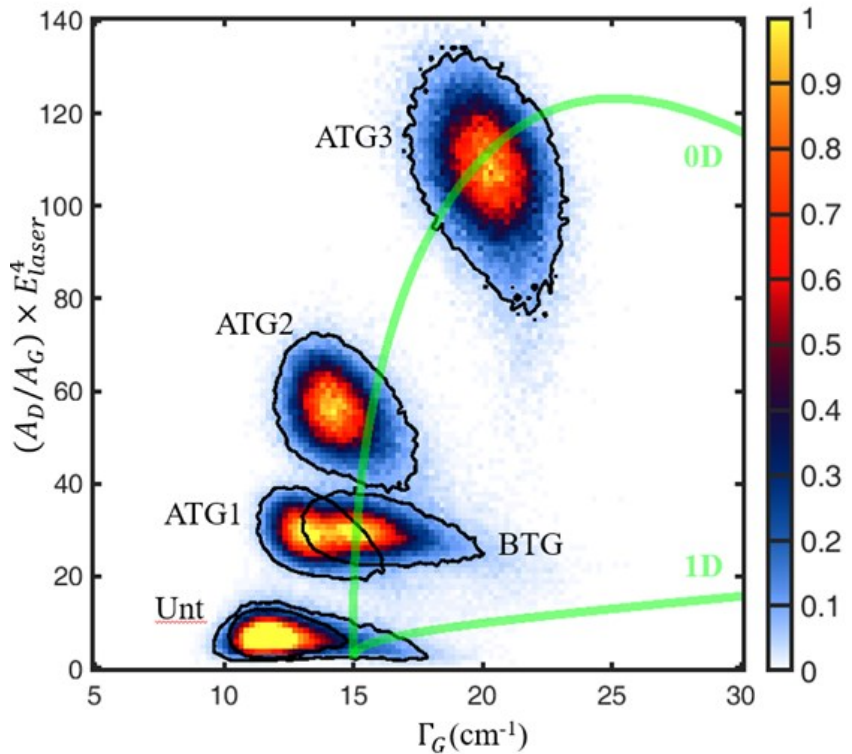


Figure 4.1.4 : BTG and subsequent ATG data extracted from RIMA measurements plotted in a Cançado-like<sup>68</sup> graph: evolution of  $A_D/A_G \times E_{laser}^4$  in function of  $\Gamma_G$ . Distributions for untreated graphene films are also displayed. The colored scale is density-normalized. Green lines delimit the 0D and 1D defect type evolutions<sup>68</sup>. For clarity, black outlines highlight the 6 different sets of data.

With rising energy fluence, Figure 4.1.4 reveals that ATG follows fairly well the predicted curve for 0D-type defect generation [35]. In such conditions, the defect density monotonously increases with the energy fluence, with no significant change in the average crystallite size [68]. As for BTG, a larger value of  $\Gamma_G \sim 15 \text{ cm}^{-1}$  (averaged over the whole graphene sample) combined with an  $A_D/A_G \times E_{laser}^4$  value comparable to that of ATG1 ( $A_D/A_G \times E_{laser}^4 \sim 30$ ) is observed. Due to the small difference in energy fluence between the two conditions (33 mJ·cm<sup>-2</sup> for ATG1 versus 25 mJ·cm<sup>-2</sup> for BTG), this suggests a small effect on the damage generation by plasma-generated B- and H-containing species. However, this interpretation is not trivial since incorporation of boron atoms into the graphene lattice would lead to p-doping and thus to a decrease of  $A_D/A_G$  [69]. On the other hand, hydrogenation of the graphene lattice would imply an increase of  $A_D/A_G$  [14,70]. Both features could therefore counterbalance each

other leading to rather constant  $A_D/A_G$  values between ATG and BTG samples. As for  $\Gamma_G$ , p-doping yields to relatively constant values for typical dopant concentrations between about  $2 \times 10^{12} \text{ cm}^{-2}$  and  $1 \times 10^{13} \text{ cm}^{-2}$  [69]. Hence, the rise of  $\Gamma_G$  observed in Figure 4.1.4 suggests some level of hydrogenation [14,69,70]. Based on the data presented in Figure 4.1.2d from reference [14],  $\Gamma_G$  rises from  $10 \text{ cm}^{-1}$  to  $15 \text{ cm}^{-1}$  for hydrogen doses in the  $\text{H}_2$  RF plasma between 0 and  $10 \text{ W}\cdot\text{Torr}\cdot\text{min}$  (here, W is the RF plasma power, Torr is the hydrogen plasma pressure and min is the plasma treatment time in minutes). This  $10 \text{ W}\cdot\text{Torr}\cdot\text{min}$  value corresponds to the stage 1 of graphene hydrogenation (very low hydrogen coverage). As a comparison, the upmost hydrogen dose that can be estimated in this work is only  $50 \text{ W} - 3 \text{ mTorr} - 0.37 \text{ min}$  which gives  $0.06 \text{ W}\cdot\text{Torr}\cdot\text{min}$ .

Typically, doping can be confirmed through a shift in the position of the G band ( $\omega_G$ ) which increases with both p- or n-doping [71]. Aiming at confirming the XPS data, Figure 4.1.5 presents raw averaged spectra of a large area within the graphene domains (red square in the inset of Fig. 4.1.5a) before (blue) and after (red) treatment in the diborane-argon plasma. A  $4\text{-cm}^{-1}$  blueshift (rise of  $\omega_G$ ) is observed for the G band after plasma treatment. Additionally, the 2D band frequency is also known to increase with rising concentration of holes [69] and a  $2\text{-cm}^{-1}$   $\omega_{2D}$  blueshift (rise of  $\omega_{2D}$ ) is observed in BTG. Such variations of  $\omega_G$  and  $\omega_{2D}$  cannot be linked to hydrogenation of the graphene lattice as the former remains constant and the latter decreases with increasing hydrogen doses (see Figure 4.1.2d for  $\omega_G$  and Figure 4.1.5b for  $\omega_{2D}$  of reference [14]). Since both  $\omega_G$  and  $\omega_{2D}$  are also sensitive to strain, Lee *et al.* [30] have developed a method to differentiate one from the other, as shown in Figure 4.1.5b for the whole  $100 \times 100 \mu\text{m}^2$  area. According to these results, the pristine graphene film is already p-doped (hole concentration  $\sim 5 \times 10^{12} \text{ cm}^{-2}$ ) and under compressive strain ( $\varepsilon = -0.20\%$ ). This can be explained by an unintentional p-doping due to PMMA residues and substrate interaction [72,73]. After diborane-argon plasma treatment, the mean hole concentration doubles ( $< c_h > \sim 10^{13} \text{ cm}^{-2}$ ), while the compressive strain slightly decreases ( $\varepsilon \sim -0.18\%$ ). Considering a graphene surface atomic density of  $3.2 \times 10^{15} \text{ cm}^{-2}$ , this corresponds to a dopant concentration of 0.13%, which is rather similar to the value obtained in XPS analysis (0.25%).

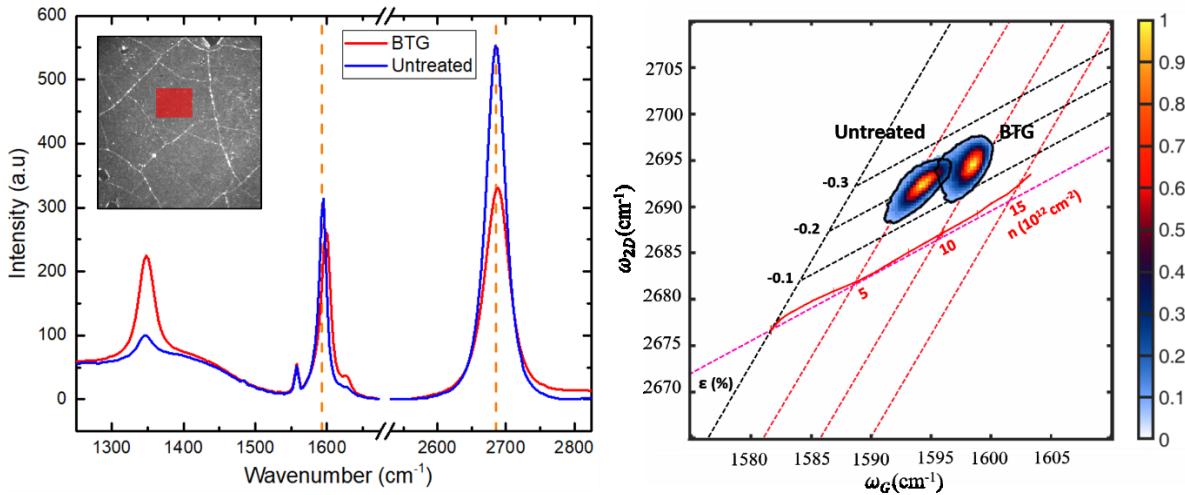


Figure 4.1.5. (Left) Raw averaged spectra from the same graphene domain area ( $18 \times 22 \mu\text{m}^2$ , red rectangle in the inset) for pristine and BTG. (right) Plot of  $\omega_{2D}$  in function of  $\omega_G$  to separate strain and p-doping levels. The  $\epsilon$  and  $n$  scales are derived from [30].

As highlighted elsewhere [32], the use of  $\omega_G$  as a marker for p-doped graphene might be tricky in the case of B-incorporation where a significant tensile strain is expected. This is especially true in damaged graphene since the G band frequency typically increases with disorder [69]. A complimentary approach based on tensile strain effect in Raman was examined. Here, the peak intensity ratio of the D and 2D bands ( $I_D/I_{2D}$ ) is compared to the full width at half maximum of the 2D band ( $\Gamma_{2D}$ ). While  $I_D/I_{2D}$  rises with damage formation and remains independent of doping and strain effects [74–76],  $\Gamma_{2D}$  rises with both damage and tensile strain and is independent of doping [77,78]. Figure 4.1.6 presents  $I_D/I_{2D}$  vs  $\Gamma_{2D}$  plots for graphene domains for both BTG and ATG. In ATG,  $I_D/I_{2D}$  increases with  $\Gamma_{2D}$ . For comparable energy fluences ( $33 \text{ mJ}\cdot\text{cm}^{-2}$  for ATG1 versus  $25 \text{ mJ}\cdot\text{cm}^{-2}$  for BTG), Figure 4.1.6 reveals that  $I_D/I_{2D}$  only slightly rises from 0.32 to 0.48 between the argon and diborane-argon plasma treatments. Most of this increase can be linked to hydrogenation. Indeed, based on the data presented in Figure 4.1.2d from reference [14],  $I_D/I_{2D}$  rises from 0.02 to 0.66 for hydrogen doses in the  $\text{H}_2$  RF plasma between 0 and 10  $\text{W}\cdot\text{Torr}\cdot\text{min}$ . Of note, the hydrogen dose required to match the  $\Gamma_G$  data presented in Figure 4.1.4 and the  $I_D/I_{2D}$  values presented in Figure 4.1.6 are comparable [14]. As for  $\Gamma_{2D}$ , when taking into consideration the initial  $1 \text{ cm}^{-1}$  gap between the two untreated samples, an increase of  $4 \text{ cm}^{-1}$  is obtained for BTG with respect to ATG. Based on the set of

data presented in reference [14], such increase cannot be due solely to hydrogenation effects ( $\Gamma_{2D}$  only rises from 28 to 30  $\text{cm}^{-1}$  for hydrogen doses in the  $\text{H}_2$  RF plasma between 0 and 10  $\text{W}\cdot\text{Torr}\cdot\text{min}$ ). The observed 4- $\text{cm}^{-1}$  rise thus seems mostly related to tensile strain effects brought by surface formation of a boron-containing layer and/or substitutional incorporation of boron atoms within the graphene lattice.

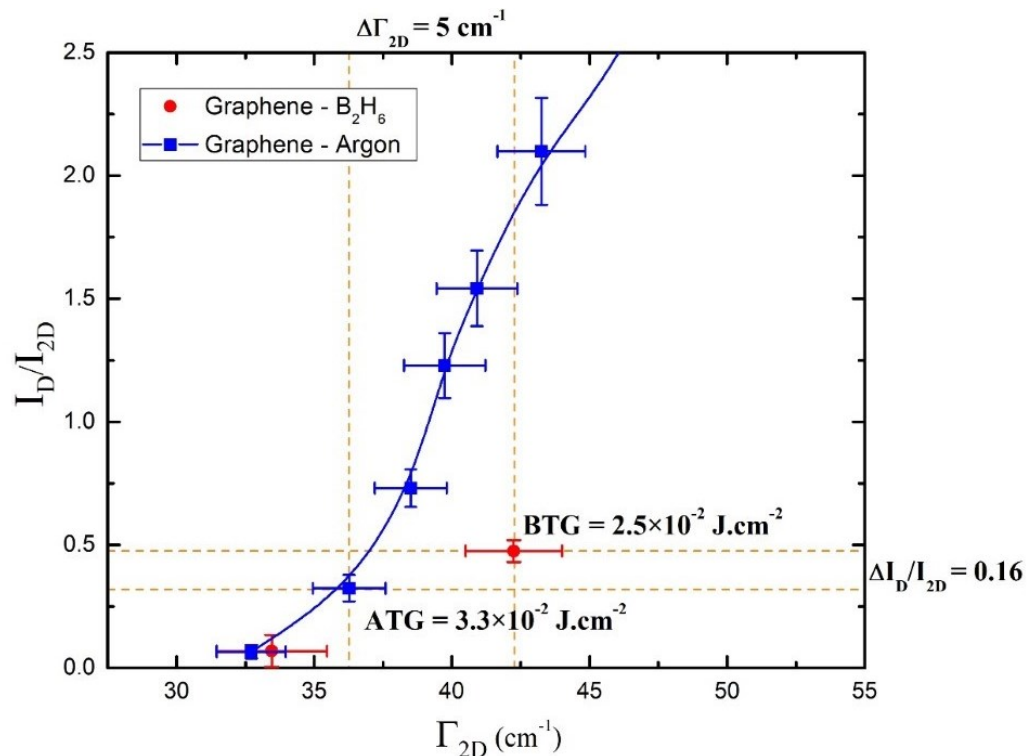


Figure 4.1.6. Evolution of  $I_D/I_{2D}$  as a function of  $\Gamma_{2D}$  in ATG and BTG samples

According to Frank *et al.* [77], the strain is directly proportional to  $\Gamma_{2D}$  with a slope depending on the laser energy. Following their data and accounting for the  $\lambda_{\text{laser}}$  used in RIMA measurements, the observed  $\Gamma_{2D}$  rise is linked to an increase of 0.4% in tensile strain. In the case of this strain being purely due to substitutional boron incorporation, it is possible to estimate a boron concentration from the change in bond length from C-C to C-B. Assuming C-C<sub>2</sub>B as the dominant moiety, a rise of 0.4% in tensile strain implies a 2.5% incorporation of boron atoms in the graphene lattice [2]. Clearly, this value is higher than the one obtained by XPS and RIMA measurements; the observed tensile strain is thus not only due to graphitic boration but also due to the surface formation of a boron-containing layer [79].

In summary, a low concentration of diborane was added to a nominally pure argon plasma as a mean to functionalize graphene films. After careful plasma characterization, the presence of B- and H-bearing species in the gas phase was confirmed. Due to the great affinity between hydrogen and carbon, hydrogenation and ion-assisted chemical etching were expected to play an important role before any significant boration would occur. However, by carefully tuning the discharge parameters, XPS and RIMA analysis confirmed the possibility to rely on a mild plasma treatment and a diborane precursor for efficient substitution of carbon atoms by plasma-generated boron atoms, with only low hydrogenation of the graphene domains. Nonetheless, it appears that boron incorporation is not limited to the graphene lattice but also involved surface formation of a boron-containing layer.

## ACKNOWLEDGMENTS

Figure 1 : This work was financially supported by the National Science and Engineering Research Council (NSERC), PRIMA-Québec, Plasmionique Inc., Photon Etc., the Fonds de Recherche du Québec - Nature et Technologies58 (FRQNT), and the Canada Research Chair program (L. Stafford and R. Martel).

## REFERENCES

- [1] A. Lherbier, X. Blase, Y.-M. Niquet, F. Triozon, S. Roche, Charge Transport in Chemically Doped 2D Graphene, *Phys. Rev. Lett.* 101 (2008) 036808. doi:10.1103/PhysRevLett.101.036808.
- [2] L.S. Panchakarla, K.S. Subrahmanyam, S.K. Saha, A. Govindaraj, H.R. Krishnamurthy, U. V. Waghmare, C.N.R. Rao, Synthesis, Structure, and Properties of Boron- and Nitrogen-Doped Graphene, *Adv. Mater.* 21 (2009) 4726–4730. doi:10.1002/adma.200901285.
- [3] M. Telychko, P. Mutombo, P. Merino, P. Hapala, M. Ondráček, F.C. Bocquet, J. Sforzini, O. Stetsovych, M. Vondráček, P. Jelínek, M. Švec, Electronic and Chemical Properties of Donor, Acceptor Centers in Graphene, *ACS Nano.* 9 (2015) 9180–9187. doi:10.1021/acsnano.5b03690.
- [4] S. Agnoli, M. Favaro, Doping graphene with boron: a review of synthesis methods, physicochemical characterization, and emerging applications, *J. Mater. Chem. A.* 4 (2016) 5002–5025. doi:10.1039/C5TA10599D.
- [5] J. Gebhardt, R.J. Koch, W. Zhao, O. Höfert, K. Gotterbarm, S. Mammadov, C. Papp, A. Görling, H.-P. Steinrück, T. Seyller, Growth and electronic structure of boron-doped graphene, *Phys. Rev.*

- B. 87 (2013) 155437. doi:10.1103/PhysRevB.87.155437.
- [6] M. Wu, C. Cao, J.Z. Jiang, Light non-metallic atom (B, N, O and F)-doped graphene: a first-principles study, *Nanotechnology*. 21 (2010) 505202. doi:10.1088/0957-4484/21/50/505202.
  - [7] Z.S. Wu, W. Ren, L. Xu, F. Li, H.M. Cheng, Doped graphene sheets as anode materials with superhigh rate and large capacity for lithium ion batteries, *ACS Nano*. 5 (2011) 5463–5471. doi:10.1021/nn2006249.
  - [8] K.H. Hui, A. Ambrosi, Z. Sofer, M. Pumera, A. Bonanni, The dopant type and amount governs the electrochemical performance of graphene platforms for the antioxidant activity quantification, *Nanoscale*. 7 (2015) 9040–9045. doi:10.1039/c5nr01045d.
  - [9] Y. Zhang, R. Sun, B. Luo, L. Wang, Boron-doped graphene as high-performance electrocatalyst for the simultaneously electrochemical determination of hydroquinone and catechol, *Electrochim. Acta*. 156 (2015) 228–234. doi:10.1016/j.electacta.2014.12.156.
  - [10] S. Jahan, F. Mansoor, S. Naz, J. Lei, S. Kanwal, Oxidative synthesis of highly fluorescent boron/nitrogen Co-doped carbon nanodots enabling detection of photosensitizer and carcinogenic dye, *Anal. Chem.* 85 (2013) 10232–10239. doi:10.1021/ac401949k.
  - [11] D.Y. Usachov, A. V. Fedorov, A.E. Petukhov, O.Y. Vilkov, A.G. Rybkin, M.M. Otrokov, A. Arnau, E. V. Chulkov, L. V. Yashina, M. Farjam, V.K. Adamchuk, B. V. Senkovskiy, C. Laubschat, D. V. Vyalikh, Epitaxial B-Graphene: Large-Scale Growth and Atomic Structure, *ACS Nano*. 9 (2015) 7314–7322. doi:10.1021/acsnano.5b02322.
  - [12] G. Robert Bigras, X. Glad, L. Vandsburger, C. Charpin, P. Levesque, R. Martel, L. Stafford, Low-damage nitrogen incorporation in graphene films by nitrogen plasma treatment: Effect of airborne contaminants, *Carbon N. Y.* 144 (2019) 532–539. doi:10.1016/j.carbon.2018.12.095.
  - [13] Y.B. Tang, L.C. Yin, Y. Yang, X.H. Bo, Y.L. Cao, H.E. Wang, W.J. Zhang, I. Bello, S.T. Lee, H.M. Cheng, C.S. Lee, Tunable band gaps and p-type transport properties of boron-doped graphenes by controllable ion doping using reactive microwave plasma, *ACS Nano*. 6 (2012) 1970–1978. doi:10.1021/nn3005262.
  - [14] Z. Luo, T. Yu, Z. Ni, S. Lim, H. Hu, J. Shang, L. Liu, Z. Shen, J. Lin, Electronic Structures and Structural Evolution of Hydrogenated Graphene Probed by Raman Spectroscopy, *J. Phys. Chem. C*. 115 (2011) 1422–1427. doi:10.1021/jp107109h.
  - [15] E. Despiau-Pujo, A. Davydova, G. Cunge, L. Delfour, L. Magaud, D.B. Graves, Elementary processes of H<sub>2</sub> plasma-graphene interaction: A combined molecular dynamics and density functional theory study, *J. Appl. Phys.* 113 (2013). doi:10.1063/1.4794375.
  - [16] X. Glad, L. de Poucques, J. Bougdira, Formation mechanism of graphite hexagonal pyramids by

argon plasma etching of graphite substrates, *J. Phys. D. Appl. Phys.* 48 (2015) 495304. doi:10.1088/0022-3727/48/49/495304.

- [17] P. Vinchon, X. Glad, G. Robert-Bigras, R. Martel, A. Sarkissian, L. Stafford, A combination of plasma diagnostics and Raman spectroscopy to examine plasma-graphene interactions in low-pressure argon radiofrequency plasmas, *J. Appl. Phys.* 126 (2019) 233302. doi:10.1063/1.5125143.
- [18] G. Robert Bigras, X. Glad, P. Vinchon, R. Martel, L. Stafford, Selective nitrogen doping of graphene domains due to preferential healing of plasma-generated defects near grain boundaries, *Accept. NPJ 2D Mater. Appl.* (2020). doi:10.1038/s41699-020-00176-y.
- [19] N. Bundaleska, N. Bundaleski, A. Dias, F.M. Dias, M. Abrashev, G. Filipič, U. Cvelbar, Z. Rakočević, Z. Kissovski, J. Henriques, E. Tatarova, Microwave N<sub>2</sub>-Ar plasmas applied for N-graphene post synthesis, *Mater. Res. Express.* 5 (2018) 095605. doi:10.1088/2053-1591/aad7e9.
- [20] M. Baraket, R. Stine, W.K. Lee, J.T. Robinson, C.R. Tamanaha, P.E. Sheehan, S.G. Walton, Aminated graphene for DNA attachment produced via plasma functionalization, *Appl. Phys. Lett.* 100 (2012) 233123. doi:10.1063/1.4711771.
- [21] A. Dey, A. Chroneos, N.S.J. Braithwaite, R.P. Gandhiraman, S. Krishnamurthy, Plasma engineering of graphene, *Appl. Phys. Rev.* 3 (2016). doi:10.1063/1.4947188.
- [22] Y.P. Lin, Y. Ksari, J. Prakash, L. Giovanelli, J.C. Valmalette, J.M. Themlin, Nitrogen-doping processes of graphene by a versatile plasma-based method, *Carbon N. Y.* 73 (2014) 216–224. doi:10.1016/j.carbon.2014.02.057.
- [23] S.H. Park, J. Chae, M.-H. Cho, J.W.J.H. Kim, K.-H. Yoo, S.W. Cho, T.G. Kim, J.W.J.H. Kim, High concentration of nitrogen doped into graphene using N<sub>2</sub> plasma with an aluminum oxide buffer layer, *J. Mater. Chem. C.* 2 (2014) 933–939. doi:10.1039/C3TC31773K.
- [24] M. Rybin, A. Pereyaslavtsev, T. Vasilieva, V. Myasnikov, I. Sokolov, A. Pavlova, E. Obraztsova, A. Khomich, V. Ralchenko, E. Obraztsova, Efficient nitrogen doping of graphene by plasma treatment, *Carbon N. Y.* 96 (2016) 196–202. doi:10.1016/j.carbon.2015.09.056.
- [25] T. Teraji, K. Arima, H. Wada, T. Ito, High-quality boron-doped homoepitaxial diamond grown by high-power microwave-plasma chemical-vapor deposition, *J. Appl. Phys.* 96 (2004) 5906–5908. doi:10.1063/1.1805180.
- [26] M. Wojtaszek, N. Tombros, A. Caretta, P.H.M. Van Loosdrecht, B.J. Van Wees, A road to hydrogenating graphene by a reactive ion etching plasma, *J. Appl. Phys.* 110 (2011). doi:10.1063/1.3638696.
- [27] J.S. Burgess, B.R. Matis, J.T. Robinson, F.A. Bulat, F. Keith Perkins, B.H. Houston, J.W. Baldwin, Tuning the electronic properties of graphene by hydrogenation in a plasma enhanced chemical

- vapor deposition reactor, Carbon N. Y. 49 (2011) 4420–4426. doi:10.1016/j.carbon.2011.06.034.
- [28] A. Horn, A. Schenk, J. Biener, B. Winter, C. Lutterloh, M. Wittmann, J. Küppers, H atom impact induced chemical erosion reaction at C: H film surfaces, Chem. Phys. Lett. 231 (1994) 193–198.
- [29] J. Roth, C. Garcia-Rosales, Analytic description of the chemical erosion of graphite by hydrogen ions, Nucl. Fusion. 36 (1996) 1647.
- [30] J.E. Lee, G. Ahn, J. Shim, Y.S. Lee, S. Ryu, Optical separation of mechanical strain from charge doping in graphene, Nat. Commun. 3 (2012) 1024. doi:10.1038/ncomms2022.
- [31] A. Das, S. Pisana, B. Chakraborty, S. Piscanec, S.K. Saha, U. V. Waghmare, K.S. Novoselov, H.R. Krishnamurthy, A.K. Geim, A.C. Ferrari, A.K. Sood, Monitoring dopants by Raman scattering in an electrochemically top-gated graphene transistor, Nat. Nanotechnol. 3 (2008) 210–215. doi:10.1038/nnano.2008.67.
- [32] Y.A. Kim, K. Fujisawa, H. Muramatsu, T. Hayashi, M. Endo, T. Fujimori, K. Kaneko, M. Terrones, J. Behrends, A. Eckmann, C. Casiraghi, K.S. Novoselov, R. Saito, M.S. Dresselhaus, Raman spectroscopy of boron-doped single-layer graphene, ACS Nano. 6 (2012) 6293–6300. doi:10.1021/nn301728j.
- [33] S. Choubak, P.L. Levesque, E. Gaufres, M. Biron, P. Desjardins, R. Martel, Graphene CVD: Interplay between growth and etching on morphology and stacking by hydrogen and oxidizing impurities, J. Phys. Chem. C. 118 (2014) 21532–21540. doi:10.1021/jp5070215.
- [34] Y.-C. Lin, C.-C. Lu, C.-H. Yeh, C. Jin, K. Suenaga, P. Chiu, Graphene Annealing: How Clean Can It Be?, Nano Lett. 12 (2012) 414–419. doi:10.1021/nl203733r.
- [35] P. Vinchon, X. Glad, G. Robert Bigras, R. Martel, L. Stafford, Preferential self-healing at grain boundaries in plasma-treated graphene, Nat. Mater. (2020). doi:10.1038/s41563-020-0738-0.
- [36] L. Maaloul, S. Morel, L. Stafford, Populations of metastable and resonant argon atoms in radio frequency magnetron plasmas used for deposition of indium-zinc-oxide films, J. Vac. Sci. Technol. A Vacuum, Surfaces, Film. 30 (2012) 021301. doi:10.1116/1.3674162.
- [37] B.P. Lavrov, M. Osiac, A. V Pipa, J. Ropcke, On the spectroscopic detection of neutral species in a low-pressure plasma containing boron and hydrogen, Plasma Sources Sci. Technol. 12 (2003) 576–589.
- [38] E. Gaufrès, S. Marcet, V. Aymong, N.Y.-W. Tang, A. Favron, F. Thouin, C. Allard, D. Rioux, N. Cottenye, M. Verhaegen, R. Martel, Hyperspectral Raman imaging using Bragg tunable filters of graphene and other low-dimensional materials, J. Raman Spectrosc. 49 (2018) 174–182. doi:10.1002/jrs.5298.
- [39] S. Doniach, M. Sunjic, Many-electron singularity in X-ray photoemission and X-ray line spectra

- from metals, *J. Phys. C Solid State Phys.* 3 (1970) 285–291. doi:10.1088/0022-3719/3/2/010.
- [40] G. Robert Bigras, P. Vinchon, C. Allard, X. Glad, R. Martel, L. Stafford, Probing plasma-treated graphene using hyperspectral Raman, *Rev. Sci. Instrum.* 91 (2020) 063903. doi:10.1063/5.0006556.
- [41] R. Beams, L. Gustavo Cançado, L. Novotny, Raman characterization of defects and dopants in graphene, *J. Phys. Condens. Matter.* 27 (2015) 083002. doi:10.1088/0953-8984/27/8/083002.
- [42] L. Boufendi, A. Bouchoule, Particle nucleation and growth in a low-pressure argon-silane discharge, *Plasma Sources Sci. Technol.* 3 (1994) 262. doi:10.1088/0963-0252/3/3/004.
- [43] G. Al Makdassi, X. Glad, S. Dap, M. Rojo, R. Clergereaux, J. Margot, Influence of a magnetic field on the formation of carbon dust particles in very low-pressure high-density plasmas, *J. Phys. D. Appl. Phys.* 50 (2017) 155203. doi:10.1088/1361-6463/50/15/155203.
- [44] V. Garofano, R. Bérard, X. Glad, C. Joblin, K. Makasheva, L. Stafford, Time-resolved analysis of the precursor fragmentation kinetics in an hybrid PVD/PECVD dusty plasma with pulsed injection of HMDSO, *Plasma Process. Polym.* (2019) 1–12. doi:10.1002/ppap.201900044.
- [45] V. Garofano, L. Stafford, B. Despax, R. Clergereaux, K. Makasheva, Cyclic evolution of the electron temperature and density in dusty low-pressure radio frequency plasmas with pulsed injection of hexamethyldisiloxane, *Appl. Phys. Lett.* 107 (2015). doi:10.1063/1.4935030.
- [46] C. Hollenstein, The physics and chemistry of dusty plasmas, *Plasma Phys. Control. Fusion.* 42 (2000) R93. doi:10.1088/0741-3335/42/10/201.
- [47] M. Sode, T. Schwarz-Selinger, W. Jacob, Ion chemistry in H<sub>2</sub>-Ar low temperature plasmas, *J. Appl. Phys.* 114 (2013). doi:10.1063/1.4817526.
- [48] J.-S. Yoon, M.-Y. Song, J.-M. Han, S.H. Hwang, W.-S. Chang, B.J. Lee, Y. Itikawa, Cross Sections for Electron Collisions with Hydrogen Molecules, *J. Phys. Chem. Ref. Data.* 37 (2008) 913–931. doi:doi:10.1063/1.2838023.
- [49] A. Durocher-Jean, N. Delnour, L. Stafford, Influence of N<sub>2</sub>, O<sub>2</sub>, and H<sub>2</sub> admixtures on the electron power balance and neutral gas heating in microwave Ar plasmas at atmospheric pressure, *J. Phys. D. Appl. Phys.* 52 (2019) 475201. doi:10.1088/1361-6463/ab373a.
- [50] B.K. McMillin, M.R. Zachariah, Two-dimensional laser-induced fluorescence imaging of metastable density in low-pressure radio frequency argon plasmas with added O<sub>2</sub>, Cl<sub>2</sub> 2, and CF<sub>4</sub>, *J. Appl. Phys.* 79 (1996) 77–85. doi:10.1063/1.360793.
- [51] V. Garofano, R. Bérard, S. Boivin, C. Joblin, K. Makasheva, L. Stafford, Multi-scale investigation in the frequency domain of Ar/HMDSO dusty plasma with pulsed injection of HMDSO, *Plasma Sources Sci. Technol.* 28 (2019) 055019. doi:10.1088/1361-6595/ab07cc.

- [52] R. Basner, M. Schmidt, K. Becker, Absolute total and partial cross sections for the electron impact ionization of diborane ( $B_2H_6$ ), *J. Chem. Phys.* 118 (2003) 2153–2158. doi:10.1063/1.1533013.
- [53] H.C. Barshilia, V.D. Vankar, Concentration of atomic hydrogen in the ground state in a  $CH_4$ - $H_2$  microwave plasma, *J. Appl. Phys.* 80 (1996) 3694–3698. doi:10.1063/1.363318.
- [54] P.R. Rablen, J.F. Hartwig, Accurate borane sequential bond dissociation energies by high-level ab initio computational methods, *J. Am. Chem. Soc.* 118 (1996) 4648–4653. doi:10.1021/ja9542451.
- [55] T.P. Fehlner, G.W. Mappes, A mass spectrometric investigation of the low-pressure pyrolysis of borane carbonyl. The bond dissociation energy of diborane, *J. Phys. Chem.* 73 (1969) 873–882. doi:10.1021/j100724a020.
- [56] M. Sode, T. Schwarz-Selinger, W. Jacob, Quantitative determination of mass-resolved ion densities in  $H_2$ -Ar inductively coupled radio frequency plasmas, *J. Appl. Phys.* 113 (2013). doi:10.1063/1.4794165.
- [57] Z. Li, Y. Wang, A. Kozbial, G. Shenoy, F. Zhou, R. McGinley, P. Ireland, B. Morganstein, A. Kunkel, S.P. Surwade, L. Li, H. Liu, Effect of airborne contaminants on the wettability of supported graphene and graphite, *Nat. Mater.* 12 (2013) 925–931. doi:10.1038/nmat3709.
- [58] J.I. Oñate, A. García, V. Bellido, J.L. Viviente, Deposition of hydrogenated B-C thin films and their mechanical and chemical characterization, *Surf. Coatings Technol.* 49 (1991) 548–553. doi:10.1016/0257-8972(91)90115-D.
- [59] C. Ronning, D. Schwen, S. Eyhusen, U. Vetter, H. Hofsäss, Ion beam synthesis of boron carbide thin films, *Surf. Coatings Technol.* 158–159 (2002) 382–387. doi:10.1016/S0257-8972(02)00248-7.
- [60] F. Ghezzi, L. Laguardia, R. Caniello, A. Canton, S. Dal Bello, B. Rais, M. Anderle, XPS, SIMS and FTIR-ATR characterization of boronized graphite from the thermonuclear plasma device RFX-mod, *Appl. Surf. Sci.* 354 (2015) 408–419. doi:10.1016/j.apsusc.2015.04.109.
- [61] T. Susi, T. Pichler, P. Ayala, X-ray photoelectron spectroscopy of graphitic carbon nanomaterials doped with heteroatoms, *Beilstein J. Nanotechnol.* 6 (2015) 177–192. doi:10.3762/bjnano.6.17.
- [62] G. Panomsuwan, N. Saito, T. Ishizaki, Electrocatalytic oxygen reduction activity of boron-doped carbon nanoparticles synthesized via solution plasma process, *Electrochim. Commun.* 59 (2015) 81–85. doi:10.1016/j.elecom.2015.07.005.
- [63] J.C. Lascovich, R. Giorgi, S. Scaglione, Evaluation of the  $sp_2/sp_3$  ratio in amorphous carbon structure by XPS and XAES, *Appl. Surf. Sci.* 47 (1991) 17–21. doi:10.1016/0169-4332(91)90098-5.
- [64] G. Robert Bigras, X. Glad, R. Martel, A. Sarkissian, L. Stafford, Treatment of graphene films in

the early and late afterglows of N<sub>2</sub> plasmas: comparison of the defect generation and N-incorporation dynamics, *Plasma Sources Sci. Technol.* 27 (2018). doi:10.1088/1361-6595/aaedfd.

- [65] J.I. Mendez-Linan, E. Ortiz-Ortega, M.F. Jimenez-Moreno, M.I. Mendivil-Palma, E. Martínez-Guerra, F.S. Aguirre-Tostado, S.O. Martinez-Chapa, S. Hosseini, M.J. Madou, Aging effect of plasma-treated carbon surfaces: An overlooked phenomenon, *Carbon N. Y.* 169 (2020) 32–44. doi:10.1016/j.carbon.2020.06.085.
- [66] T. Shirasaki, A. Derré, M. Ménétrier, A. Tressaud, S. Flandrois, Synthesis and characterization of boron-substituted carbons, *Carbon N. Y.* 38 (2000) 1461–1467. doi:10.1016/S0008-6223(99)00279-1.
- [67] D. Liu, D. Tománek, Effect of Net Charge on the Relative Stability of 2D Boron Allotropes, *Nano Lett.* 19 (2019) 1359–1365. doi:10.1021/acs.nanolett.8b04968.
- [68] L. Gustavo Cançado, M. Gomes da Silva, E.H. Martins Ferreira, F. Hof, K. Kampioti, K. Huang, A. Pénicaud, C. Alberto Achete, R.B. Capaz, A. Jorio, L. Cançado, M. Gomes de Silva, E.H.M. Ferreira, F. Hof, Disentangling contributions of point and line defects in the Raman spectra of graphene-related materials, *2D Mater.* 4 (2017) 025039. doi:10.1088/2053-1583/aa5e77.
- [69] M. Bruna, A.K. Ott, M. Ijäs, D. Yoon, U. Sassi, A.C. Ferrari, Doping Dependence of the Raman Spectrum of Defected Graphene, *ACS Nano.* 8 (2014) 7432–7441. doi:10.1021/nn502676g.
- [70] Z. Luo, J. Shang, S. Lim, D. Li, Q. Xiong, Z. Shen, J. Lin, T. Yu, Modulating the electronic structures of graphene by controllable hydrogenation, *Appl. Phys. Lett.* 97 (2010) 233111. doi:10.1063/1.3524217.
- [71] L. Zhao, R. He, A. Zabet-Khosousi, K.S. Kim, T. Schiros, M. Roth, P. Kim, G.W. Flynn, A. Pinczuk, A.N. Pasupathy, Dopant segregation in polycrystalline monolayer graphene, *Nano Lett.* 15 (2015) 1428–1436. doi:10.1021/nl504875x.
- [72] A. Pirkle, J. Chan, A. Venugopal, D. Hinojos, C.W. Magnuson, S. McDonnell, L. Colombo, E.M. Vogel, R.S. Ruoff, R.M. Wallace, The effect of chemical residues on the physical and electrical properties of chemical vapor deposited graphene transferred to SiO<sub>2</sub>, *Appl. Phys. Lett.* 99 (2011) 2009–2012. doi:10.1063/1.3643444.
- [73] J. Zabel, R.R. Nair, A. Ott, T. Georgiou, A.K. Geim, K.S. Novoselov, C. Casiraghi, Raman Spectroscopy of Graphene and Bilayer under Biaxial Strain: Bubbles and Balloons, *Nano Lett.* 12 (2012) 617–621. doi:10.1021/nl203359n.
- [74] Y.-B. Zhou, Z.-M. Liao, Y.-F. Wang, G.S. Duesberg, J. Xu, Q. Fu, X.-S. Wu, D.-P. Yu, Ion irradiation induced structural and electrical transition in graphene, *J. Chem. Phys.* 133 (2010) 234703. doi:10.1063/1.3518979.

- [75] K. Jia, Y. Su, Y. Chen, J. Luo, J. Yang, P. Lv, Z. Zhang, H. Zhu, C. Zhao, T. Ye, Effects of defects and thermal treatment on the properties of graphene, Vacuum. 116 (2015) 90–95. doi:10.1016/j.vacuum.2015.03.003.
- [76] P. Venezuela, M. Lazzeri, F. Mauri, Theory of double-resonant Raman spectra in graphene: Intensity and line shape of defect-induced and two-phonon bands, Phys. Rev. B - Condens. Matter Mater. Phys. 84 (2011) 1–25. doi:10.1103/PhysRevB.84.035433.
- [77] O. Frank, M. Mohr, J. Maultzsch, C. Thomsen, I. Riaz, R. Jalil, K.S. Novoselov, G. Tsoukleri, J. Parthenios, K. Papagelis, L. Kavan, C. Galiotis, Raman 2D-band splitting in graphene: Theory and experiment, ACS Nano. 5 (2011) 2231–2239. doi:10.1021/nn103493g.
- [78] Y. Wang, Y. Wang, C. Xu, X. Zhang, L. Mei, M. Wang, Y. Xia, P. Zhao, H. Wang, Domain-boundary independency of Raman spectra for strained graphene at strong interfaces, Carbon N. Y. 134 (2018) 37–42. doi:10.1016/j.carbon.2018.03.069.
- [79] M.A. Bissett, M. Tsuji, H. Ago, Strain engineering the properties of graphene and other two-dimensional crystals, Phys. Chem. Chem. Phys. 16 (2014) 11124–11138. doi:10.1039/c3cp55443k.

## Conclusion et perspectives

Les travaux de recherche réalisés dans le cadre de cette thèse de doctorat se sont penchés sur les interactions plasma-surface appliquées au cas du graphène exposé à un plasma de diffusion produit par un champ RF dans des conditions de basse pression ( $5 \text{ mTorr} < P < 80 \text{ mTorr}$ ). L'étude d'un plasma d'argon pur en mode continu et pulsé a permis l'identification des espèces vecteurs d'énergie au substrat, incluant des ions positifs, les métastables et les photons VUV. Ceci a permis également de lier la dose d'énergie apportée au graphène par spectroscopie Raman. De plus, en présence de diborane dans le plasma d'argon, ces travaux ont permis de déterminer des conditions opératoires du plasma idéales pour l'incorporation atomique de bore dans le graphène, tout en minimisant efficacement les dommages générés.

Dans un premier temps, les interactions plasma-graphène ont été étudiées par l'exposition du graphène à un plasma continu d'argon. L'exposition à un plasma basse densité (mode E) permet de se rendre effectivement compte du lien entre la densité de dommage et le temps de traitement. L'étude minutieuse du plasma opéré en mode H permet de trouver des conditions de pressions et de puissances dans lesquelles l'énergie des ions accélérées dans la gaine varie tout en conservant la fluence des ions totale constante. Malgré l'énergie des ions très faible et le faible temps de traitement, des dommages importants sont observés. Une dépendance de la densité de défauts à l'énergie des ions est clairement visible alors que celle-ci reste inférieure au seuil de pulvérisation du graphène ( $\sim 18\text{-}22 \text{ eV}$ ). Ceci implique nécessairement un mécanisme de gravure à deux étapes qui a pour conséquence de réduire fortement les seuils nécessaires pour provoquer des dégâts. Le traitement par le plasma en mode E avec un temps de traitement très long semble indiquer que les métastables jouent un rôle important dans la production de dommage.

Cependant, nos premiers travaux obtenus par spectroscopie Raman confocale ont montré une forte inhomogénéité à la surface des films de graphène. Afin de mieux étudier la physique des interactions plasma-graphène en lien avec l'état initiale du graphène, une méthode est mise au point pour adapter la spectroscopie Raman Hyperspectrale (RIMA) à des études quantitatives des dommages d'irradiation.

Afin d'obtenir un meilleur contrôle sur la densité de puissance délivrée par le plasma au graphène, la puissance RF a été pulsée à une fréquence de 1 kHz. Une étude temporelle du plasma a ainsi permis de déterminer une condition où les ions sont majoritaires et représentent le principal vecteur d'énergie. De ce résultat, en capitalisant sur le potentiel d'innovation immense du RIMA, l'exposition successive d'un échantillon de graphène au plasma a permis de mettre en lumière les évolutions différentes selon les régions du graphène étudiées. En effet, le graphène obtenu par CVD présente des joints de grains que l'on ne retrouve pas dans le même matériau obtenu par exfoliation. Étonnamment, ces joints sont plus résistants que les domaines de graphène au plasma d'argon. La faible énergie des ions obtenues dans nos conditions ne permet pas la pulvérisation. Cependant, des défauts peuvent tout de même être générés, les atomes de carbones libérés de la matrice graphitiques pouvant alors diffuser sur la surface. Ils peuvent alors être stoppés dans leurs diffusions par les joints de grains. Ceux-ci sont en plus connus pour être moins bon conducteur électronique et thermique. Ils peuvent alors atteindre des températures supérieures à celle du graphène. La convergence des atomes de carbone due aux défauts combinée à l'élévation des températures déclenche un processus d'autoréparation qui permet aux joints d'être moins endommagés. Ce phénomène d'autoréparation préférentielle aux joints de grains était en principe bien connu dans le cas des matériaux 3D n'avait pas été jusqu'à présent observé expérimentalement sur les matériaux 2D.

En changeant la puissance et la pression dans un plasma pulsé d'argon, il a aussi été possible de favoriser un certain type d'espèces par rapport aux autres. Ainsi, des conditions ont été déterminées dans lesquels les métastables puis les photons VUV sont les médiateurs principaux pour le transfert d'énergie au graphène. Des différences significatives sont observées dans l'évolution de l'état du graphène en fonction de l'énergie déposée selon l'espèce vecteur. Lorsque l'énergie est transmise via les metastables, les défauts générés sont plus de type 1D alors que dans le cas des ions et des photons VUV, les défauts sont de nature 0D. Une autre surprise réside dans la résistance supérieure des joints de grains lorsque l'énergie est fournie majoritairement par les métastables. Ceci peut s'expliquer par une augmentation notable des températures sous l'effet des métastables et donc une réparation préférentiellement des joints de grains accrus. L'effet des photons VUV est quant à lui remarqué lors des premiers traitements par un changement de l'interaction entre le graphène et le substrat ainsi qu'une nette

amélioration des joints de grains. En effet, les photons VUV très peu absorbés par le graphène lui-même, peuvent cependant affecter les résidus de PMMA associés aux transferts ainsi que les espèces situées entre le graphène et le substrat de SiO<sub>2</sub>. Il est alors possible de conclure que le phénomène de synergie observé dans de nombreux travaux d’interaction plasma-surface pourrait être principalement due aux métastables.

Finalement, la méthode pour déterminer l’énergie peut être utilisée afin de prédire l’état du graphène après un traitement plasma gouverné principalement par le bombardement ionique, métastable et photon VUV en provenance de l’argon. Ainsi, bien qu’un changement conséquent des paramètres fondamentales du plasma a été observé, l’introduction de seulement 5% de diborane dans un plasma d’argon a permis de conserver une cinétique de dégât gouvernée par l’argon. Ainsi, le graphène exposé par ce plasma est globalement très peu endommagé. Cependant, l’environnement chimique du graphène après traitement a varié considérablement avec l’incorporation notable d’atomes de bore ainsi qu’une faible hydrogénéation. De plus, les joints de grains ont cette fois-ci un comportement à l’opposé de celui démontré lors des traitements par plasma d’argon pur. De plus, il est possible qu’une accumulation d’atomes de bores avec des configurations différentes aient lieu.

À l’évidence, les travaux présentés dans cette thèse constituent une contribution majeure à la physique des interactions plasma-graphène et même plus généralement à celle des interactions entre le plasma et toutes les surfaces. De plus, ces travaux ouvrent la voie à plusieurs perspectives de recherche. Nous en détaillons quelques-unes ci-dessous :

- Tout au long de ces travaux, la distribution en énergie des ions Ar<sup>+</sup> est supposée (et vérifiée) mono-énergétique. Il serait cependant intéressant de considérer le cas où cela n’est plus vrai et qu’une distribution bi-modale soit obtenue. Un bombardement de la surface par des ions avec des énergies très variées aurait alors lieu, fournissant une contribution différente à la génération de dommage.
- Il serait intéressant de vérifier l’exactitudes des énergies estimées pour la contribution des ions, des metastables et des photons VUV. Ceci pourrait être réalisé via des études de calorimétrie à la place du substrat. Il serait alors possible de lier une augmentation éventuelle de la température du substrat au flux des métastables ou d’autres espèces énergétiques issues du plasma

- Dans cette continuité, le rôle des métastables dans le phénomène de synergie demande à être confirmé par des travaux de modélisation. En effet, les chemins de désexcitation aux surfaces possibles peuvent varier selon la nature du substrat et peuvent gérer des phonons et/ou des électrons Auger. Bien que la production de phonons pourrait effectivement provoquer une élévation de température et abaisser les seuils d'énergies pour provoquer des défauts, l'émission d'électrons Auger pourrait également temporairement affaiblir la matrice graphitique. Dans ce cours laps de temps, un ion pourrait provoquer bien plus de dégâts qu'observé habituellement pour la même énergie. Ceci reste donc à approfondir.
- L'étude de la dynamique d'incorporation atomique de bore par l'exposition du graphène à un plasma contenant du diborane dilué dans l'argon est remarquablement complexe. En plus de l'insertion de bore dans le graphène, des défauts, un dépôt ainsi que de l'hydrogénéation sont générés. La distinction de ces phénomènes est nécessaire pour obtenir le contrôle de l'état du graphène. Aussi, dans le cas du graphène dopé à haut niveau par des atomes de bore, il est supposé que celui-ci soit supraconducteur à basse température. Ceci reste à vérifier.
- Enfin, lors de l'étude de plasma contenant du diborane, on a pu observer des signes de production de poudre pour certaines conditions de pression en mode E. En effet, des mesures en spectrométrie de masse (en mode RGA) a permis d'identifier des oscillations temporelles de certaines espèces comme la molécule d'hydrogène. La figure suivante présente l'évolution temporelle des valeurs On/Off pour plusieurs espèces dans un plasma généré en mode E (30W) pour plusieurs pressions.

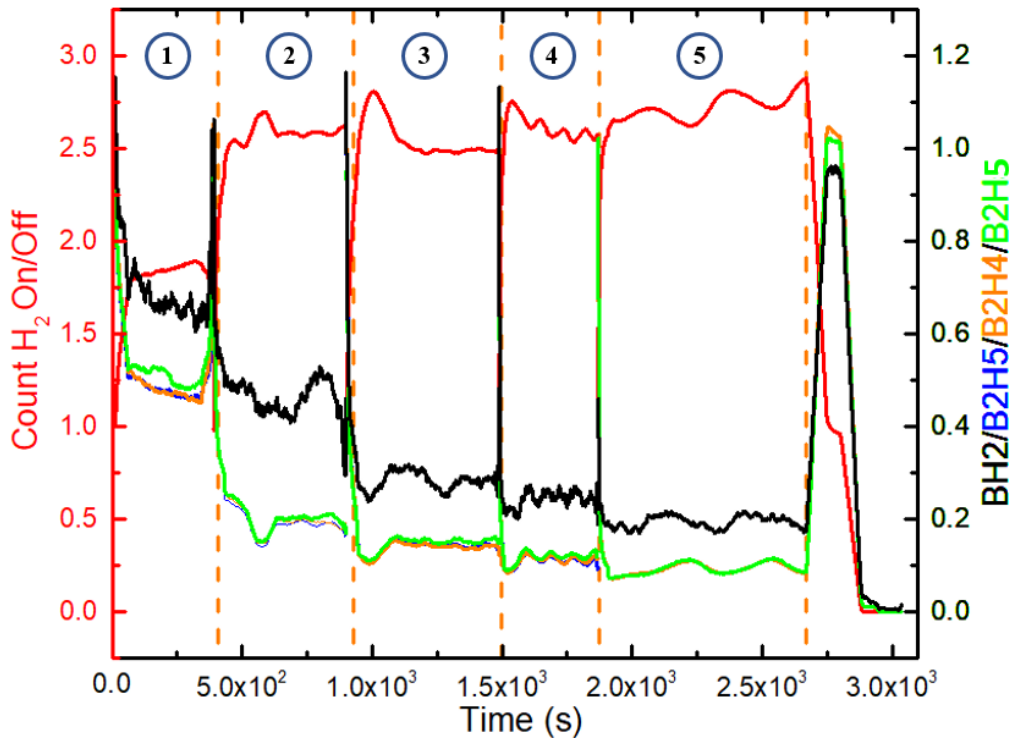


Figure C.1 : Évolution temporelle en spectrométrie de masse des ratios plasma allumé et éteint de  $\text{H}_2^+$ ,  $\text{BH}_2^+$ ,  $\text{B}_2\text{H}_2^+$ ,  $\text{B}_2\text{H}_4^+$ ,  $\text{B}_2\text{H}_5^+$  pour un plasma généré en mode E à 30W et (1) 10 mTorr, (2) 20 mTorr, (3) 30 mTorr, (4) 40 mTorr et (5) 50 mTorr.

Il est difficile d'observer de variations périodiques pour des pressions entre 10 et 30 mTorr mais on constate aisément pour  $\text{H}_2$  des oscillations dans le cas de plasma générés à 40 et 50mTorr. Celles-ci peuvent également être observées pour les espèces de type  $\text{B}_2\text{H}_y$  et plus difficilement pour  $\text{B}_2\text{H}$ . De telles variations périodiques sont typiquement observées lors de la formation de nanoparticules en phase gaz. Ainsi l'exploration de leurs dynamiques de formation en phase gaz permettrait de maîtriser leurs tailles et possiblement, leurs structures. Des mesures préliminaires montrent que celles-ci sont composées principalement de bore (et d'hydrogène) et qu'elles sont très poreuses, permettant des réactions avec l'oxygène et l'azote de l'air ambiant.

À suivre...